TU/e EINDHOVEN UNIVERSITY OF TECHNOLOGY

Plasma-assisted atomic layer deposition of conductive HfNx

Citation for published version (APA):
Karwal, S. (2020). *Plasma-assisted atomic layer deposition of conductive HfNx: on the role of plasma chemistry and ions in tailoring film properties*. [Phd Thesis 1 (Research TU/e / Graduation TU/e), Applied Physics and Science Education]. Technische Universiteit Eindhoven.

Document status and date:
Published: 06/02/2020

Document Version:
Publisher’s PDF, also known as Version of Record (includes final page, issue and volume numbers)

Please check the document version of this publication:

• A submitted manuscript is the version of the article upon submission and before peer-review. There can be important differences between the submitted version and the official published version of record. People interested in the research are advised to contact the author for the final version of the publication, or visit the DOI to the publisher's website.
• The final author version and the galley proof are versions of the publication after peer review.
• The final published version features the final layout of the paper including the volume, issue and page numbers.

Link to publication

General rights
Copyright and moral rights for the publications made accessible in the public portal are retained by the authors and/or other copyright owners and it is a condition of accessing publications that users recognise and abide by the legal requirements associated with these rights.

• Users may download and print one copy of any publication from the public portal for the purpose of private study or research.
• You may not further distribute the material or use it for any profit-making activity or commercial gain
• You may freely distribute the URL identifying the publication in the public portal.

If the publication is distributed under the terms of Article 25fa of the Dutch Copyright Act, indicated by the “Taverne” license above, please follow below link for the End User Agreement:

www.tue.nl/taverne

Take down policy
If you believe that this document breaches copyright please contact us at:

openaccess@tue.nl

providing details and we will investigate your claim.

Download date: 04. Oct. 2023

Plasma-assisted atomic layer deposition of conductive HfN_x: on the role of plasma chemistry and ions in tailoring film properties

PROEFSCHRIFT

ter verkrijging van de graad van doctor aan de Technische Universiteit Eindhoven, op gezag van de rector magnificus prof.dr.ir. F.P.T. Baaijens, voor een commissie aangewezen door het College voor Promoties, in het openbaar te verdedigen op donderdag 6 februari 2020 om 16:00 uur

door

Saurabh Karwal

geboren te Delhi, India

Dit proefschrift is goedgekeurd door de promotoren en de samenstelling van de promotiecommissie is als volgt:

voorzitter:	prof.dr.ir. G.M.W. Kroesen
1e promotor:	prof.dr. M. Creatore
2e promotor:	prof.dr.ir. W.M.M. Kessels
copromotor:	dr. M.A. Verheijen
leden:	prof.dr.ir. J.R. van Ommen (TUD)
	prof.dr. H. Pedersen (Linköping University)
	dr.ir. S. Nijdam
	prof.dr.ir. A.H.M. Smets (TUD)

Het onderzoek dat in dit proefschrift wordt beschreven is uitgevoerd in overeenstemming met de TU/e Gedragscode Wetenschapsbeoefening.

This research has been financially supported by Technologiestichting STW through the project LIMIET programma 13316 and Netherlands Organization for Scientific Research NWO through project HTSM programma 15352.

Printed and bound by Ipskamp Printing, Enschede

Cover brief by: Saurabh Karwal

Cover design by: Anurag Bhattacharya

A catalogue record is available from the Eindhoven University of Technology Library,

ISBN: 978-90-386-4946-7

Table of contents

1 General Introduction **1**

1.1 Evolution of field-effect-transistors: requirements 2

1.2 Atomic layer deposition 4

1.3 Framework of the project 5

1.4 Research questions and thesis outline 6

2 Synthesis of conductive transition metal nitrides: an overview **10**

2.1 Transition metal nitride material properties 11

2.2 Transition metal nitride synthesis 14

2.3 Effect of energetic ions on material properties 19

Appendix 2 32

3 Plasma-assisted ALD of HfNx: Tailoring the film properties by the plasma gas composition **38**

3.1 Introduction 39

3.2 Experimental section 41

3.3 Results and discussion 44

3.4 Conclusions 53

Appendix 3 58

4 Low resistivity HfNx grown by plasma-assisted ALD with external rf substrate biasing **59**

4.1 Introduction 60

4.2 Experimental section 62

4.3 Results and discussion 66

4.4 Conclusions 78

Appendix 4 84

5 Atomic Insights into the Oxygen Incorporation in Atomic Layer Deposited Conductive Nitrides and its Mitigation by Energetic Ions **93**

5.1 Introduction 94

5.2 Experimental section 95

5.3 Results and discussion 96

5.4 Conclusions 105

Appendix 5 111

6 Plasma-assisted ALD of highly conductive HfNx: on the effect of energetic ions on film microstructure **133**

6.1 Introduction 134

6.2 Experimental section 135

6.3 Results and discussion 138

6.4 Conclusions 147

Appendix 6 154

7 Conclusions and Outlook **165**

Thesis appendix **174**

Summary **192**

List of publications **195**

Acknowledgements **198**

Curriculum Vitae **204**

Chapter 1

General Introduction

Abstract

This introductory chapter outlines the progress in nano-electronic industry. The recently introduced state-of-the-art gate-all-around field effect transistor (FET) is the epitome of the advancements in nano-electronics. The realization of such a device has been made possible by the combined progress in thin film deposition techniques and lithography techniques. This chapter highlights atomic layer deposition (ALD) as the key enabling technique for the deposition of thin films with excellent conformality and uniformity in these high aspect ratio 3D nanostructures. Since the conductive transition metal nitride films play a pivotal role in the manufacturing line of advanced FETs, this dissertation uses the growth of HfN_x thin films by ALD as a model system to address, in the form of research questions, the various challenges that are encountered in the synthesis of high quality and low resistivity HfN_x films.

1.1 Evolution of field-effect-transistors: requirements

The tremendous progress in micro- and nano-electronics over the last few decades is the combined result of the advancements in the field of thin film (oxide, nitride and metal) deposition techniques and the lithography techniques. Gordon Moore in 1965 observed that the number of transistors per unit area on a microprocessor chip doubled every 18-24 months [1]. Henceforth, the so-called 'Moore's law' has been adopted by the semiconductor industry as the roadmap for further development of integrated circuits and downscaling of transistor size [2]. The shrinkage of device features has resulted in remarkable increase in the computation power and the clock speed, responsible for the affordable development of advanced computers and smartphones.

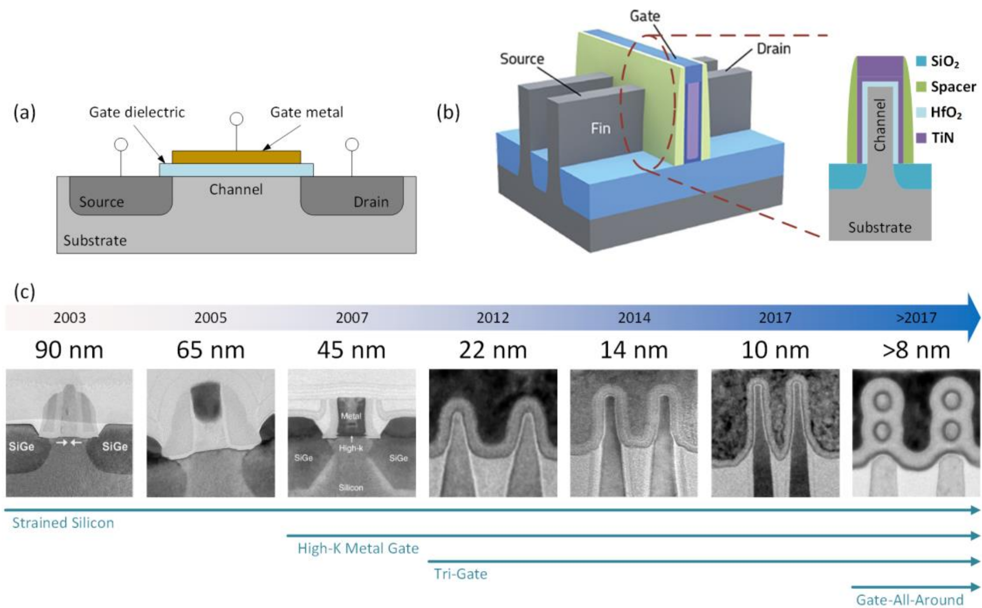

Figure 1.1. (a) A schematic illustration of a planar metal-oxide-semiconductor field-effect-transistor (MOSFET). The highly doped source and drain regions are separated by a semi-conducting channel. The current flow from source to drain depends on the capacitance of the gate dielectric and the voltage applied to the metallic gate. (b) A schematic illustration of the 3D FinFET device architecture with corresponding thin layers of functional materials. (c) The evolution of the metal-oxide-semiconductor-field-effect-transistors (MOSFETs) in integrated circuits in order to keep up with Moore's law [3, 4].

For instance, Figure 1.1a shows a schematic of a silicon-based planar metal-oxide-semiconductor field-effect-transistor (MOSFET), i.e. the elementary component of an integrated circuit (IC). The conducting source and drain regions

are separated by a semiconducting channel. The extent of the electronic conduction through the semiconducting channel and appropriate switching of the transistor is controlled by the voltage applied to the metallic gate and the capacitance of the dielectric layer. In order to address the shrinking feature sizes and, at the same time, suppress the flow of unnecessary current between the source and the drain, a better control over the electrostatics of the semiconducting channel is required. The latter can be achieved by increasing the capacitance of the dielectric layer, either by reducing the thickness of the layer or by adopting a material with higher dielectric constant (*k*) value. This was the primary reason behind the replacement of silicon oxide (SiO_2) with high-*k* hafnium oxide (HfO_2) since 2007 [4]. In order to further improve the control over the electrostatics, another exemplary leap was taken by Intel in 2012 by introducing the revolutionary 3D Fin Field-Effect-Transistor (22 nm node FinFET, also referred to as Tri-Gate) design [3] (Figure 1b). This non-planar transistor consists of Si fins serving as channel, around which a layer of HfO_2 is deposited on three sides. A thin, conformal and conductive titanium nitride (TiN) layer is subsequently grown on HfO_2, serving as the gate metal electrode. Further reduction in the feature size led to the introduction of the 10 nm node technology in 2017, characterized by an aspect ratio of 7.5:1 for the fin structures. As a major step forward, IMEC introduced a novel state-of-the-art gate-all-around FET (GAAFET) structure in 2016 in order to further improve the electrostatic control over the channel and to reduce the channel width to ≤ 8 nm [5, 6]. In this FET device, the Si nanowire channel is uniformly covered with HfO_2 whereas a thin layer of TiN serves as the gate metal.

The nitrides of group 4-6 transition metals have received considerable attention due to their outstanding electronic and physical properties, making them technologically essential in the front-end-of-line (FEOL) fabrication of the state-of-the-art devices, as aforementioned. In addition to the FEOL, transition metal nitride (TMN) films are also a vital component in the back-end-of-line (BEOL) fabrication. Specifically, TMN films are used as copper diffusion barriers when the FETs gets interconnected by Cu metallization. In addition to TiN, tantalum nitride (TaN) films have been also employed as gate metal in advanced FETs [7, 8]. However, both TiN and TaN tend to form undesirable oxy-nitrides at the interface with the HfO_2, thereby reducing the 'effective' *k* value [9, 10]. Yu *et al.* showed that the low-resistivity hafnium nitride (HfN) is highly compatible and thermally stable material when used in combination with the high-*k* HfO_2, in contrast to its counterparts TiN and TaN [9, 10].

The introduction of high-*k* metal oxides and conductive transition metal nitrides is, however, not the only key element to the successful development towards the 10 nm node technology. As aforementioned, notable advancement in

lithography techniques such as spacer-defined double patterning (SDDP) and/or self-aligned double pattering (SADP) should be acknowledged too, as responsible for the device evolution from a relatively simple planar structure to a complex 3D architecture (Figure 1c).

In parallel with the advancement in lithography, the deposition of ultra-thin films with good conformality and step coverage on such complex 3D device structures is equally relevant and urgent. With the onset of 22 nm node technology, these requirements in thin film deposition have been met by atomic layer deposition (ALD). The latter delivers ultra-thin films with precise control over thickness, excellent uniformity and unparalleled conformality on high aspect ratio 3D structures [11-14].

1.2 Atomic layer deposition

ALD is a vapour-phase deposition technique [11-17]. In an ideal ALD process, the reactions between the surface and the precursor or the co-reactant do not proceed any further (i.e. are self-limiting) once saturation is achieved. Figure 1.2 shows the growth per cycle (GPC) as a function of the precursor dose, co-reactant exposure and the intermediate purge steps involved in an ALD process.

In a **thermal** ALD process involving only vapours, the time of saturation for each half reaction is determined by the reaction kinetics, adsorbate's partial pressure and the number of available surface sites, in accordance to the Langmuir adsorption model. A **plasma-assisted** ALD process typically employs reactive plasma species as the co-reactant during the second half cycle, instead of gaseous vapours. A plasma is a collection of electrons, ions, atomic and/or molecular radical species and photons. The saturation behaviour of the plasma step is then controlled by parameters such as the plasma exposure time, plasma operating pressure, gas composition, reaction kinetics and the availability of surface sites. The use of plasma as a co-reactant in an ALD process has burgeoned in the recent years as it allows more freedom in the processing conditions. Plasma processing enables low film growth temperatures, tuning of film stoichiometry and crystallinity and lower ALD cycle times.

The growth of films by an ALD process, in saturation, is independent of the flux of reactant species on the surface. Furthermore, the self-limiting nature of ALD allows uniform layer-by-layer growth of the desired material, even over large areas and also on high aspect ratio structures [11-14]. The latter is schematically represented in Figure 1.3.

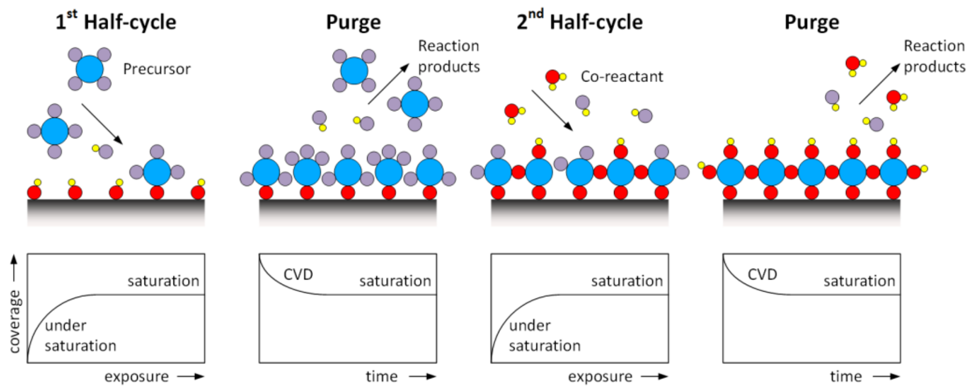

Figure 1.2. A schematic representation of an ALD process consisting of two self-limiting half reactions. The first half cycle consists of dosing the metal precursor and the second half cycle consists of a co-reactant exposure. The purge steps after the precursor dose and co-reactant exposure are placed to prevent unwanted reactions between the precursor and co-reactant. The resulting coverage, or growth per cycle (GPC), as a function of the exposure and purge time is indicated as well. The exposure steps and purge steps are sufficiently long in order to achieve the saturated growth for the self-limiting reactions and prevent any reaction between the precursor and the co-reactant.

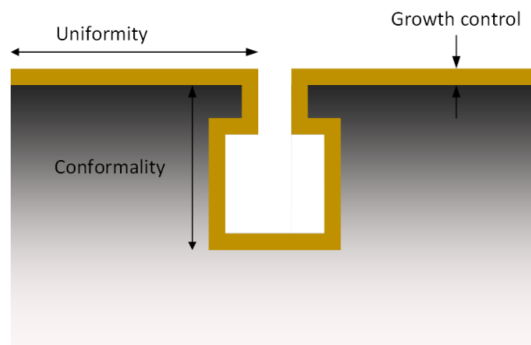

Figure 1.3. An illustration showing the merits of ALD: high wafer-scale uniformity, precise control over growth and excellent step coverage.

1.3 Framework of the project

This dissertation work was carried out in the Plasma & Materials Processing (PMP) group at the Eindhoven University of Technology in the Netherlands. The project was financially supported by Stichting Technische Weterschappen (STW) through the project entitled 'Light Management and Interface Engineering for Highly Efficient and Ultra-Thin CIGS Solar Cells (LIMIET 13316)' and by Netherlands

Organization for Scientific Research (NWO) through the project entitled 'Taking Plasma Atomic Layer Deposition to the Next Level (HTSM 15352)'.

This dissertation focuses on exploring the routes towards the synthesis of low resistivity TMN films. Although TMN films are highly relevant in modern nano-electronics, the growth of low-resistivity TMN films by ALD is challenging and non-trivial. The challenge lies in the efficient reduction of the metal atom, present in a higher oxidation state in the precursor, to the M(III) oxidation state in the deposited film. Next to this, the suppression of impurity incorporation (such as oxygen or carbon) in the grown films is also a major challenge. Furthermore, the growth of TMN films with a high crystallinity and low nanoporosity at typically low ALD operating temperatures is difficult to attain. This dissertation addresses the case-study of plasma-assisted ALD of HfN_x thin films to elucidate these challenges in detail. As it will be discussed in the Chapter 2, the choice of the reducing co-reactant is essential in promoting the Hf(III) oxidation state in the film and, therefore, the development of the conductive δ-HfN phase. Since a plasma is a highly reactive medium, plasma chemistry (specifically, H· radicals generated in an H_2 plasma) is expected to efficiently reduce the Hf(IV) state in the metal precursor. Moreover, the ions impinging the surface of the growing film are expected to affect the film microstructure. In this respect, Chapter 2 also reviews the literature works which have investigated the impact of energy, flux and mass of impinging ions, incident on the surface of the growing film, in tailoring the microstructure of the films.

1.4 Research questions and thesis outline

This thesis addresses the plasma-assisted ALD process of conductive HfN_x films. The research questions covered through Chapters 2-6 are here summarized:

What are the challenges in vapour-based deposition techniques when synthesizing conductive metal nitrides?

One of the key aspects toward the synthesis of conductive HfN_x and, in general, TMN films is the efficient reduction of the oxidation state of the metal atom to +3 in the deposited film, when adopting metal (-organic or -halide) precursors with the metal atoms present in a higher oxidation state. Chapter 2 briefly reviews the synthesis of conductive TMN films by various vapour-based techniques (PVD, CVD and ALD). It is inferred that, when adopting CVD or ALD, the reduction of some atoms (Zr, Hf, Ta) from a higher oxidation state in the metal precursor to +3 in the film is challenging to achieve. Furthermore, Chapter 2 highlights that the application of highly reactive H_2 plasma as the co-reactant in

CVD and ALD processes enables the reduction of metal atoms to +3 oxidation state in the film. However, the extent of reduction of metal atom to +3 oxidation state and the correlation between +3 oxidation state fraction and the resistivity is missing in literature.

How does a selected plasma chemistry (N_2 plasma vs H_2 plasma) contribute in promoting the reduction of the Hf(IV) state in the metal precursor to Hf(III) in the deposited film?

Chapter 3 addresses the role of the plasma feed gas composition (N_2 plasma versus H_2 plasma) in affecting the stoichiometry of the HfN layers, including the fraction of Hf(III) oxidation state in the deposited films. It is found that the highly reducing nature of H_2 plasma leads to larger Hf(III) fraction than the N_2 plasma. A correlation between the Hf(III) fraction and the film electrical resistivity is reported, which also serves as figure of merit for the research carried out in the subsequent chapters. This chapter also elucidates the effect of the presence of oxygen impurities in the deposited film on the Hf(III) fraction.

How does the energy of the impinging ions on the HfN_x surface during the film growth affect its Hf(III) oxidation state fraction and microstructure?

Chapter 4 reports on the application of an external rf substrate bias during the H_2 plasma step in the plasma-assisted ALD of HfN_x. An increase in time-averaged substrate bias from 0V to -130V leads to a major decrease in O content, an increase in Hf(III) fraction from 0.65 to 0.82 and a major decrease in HfN_x film resistivity by two orders of magnitude from 0.9 Ωcm down to $3.3 \cdot 10^{-3}$ Ωcm.

Can we gain insights into the chemical reactions taking place at the HfN_x film surface in the presence of impinging energetic ions?

Chapter 5 focusses on the application of theoretical first principles density functional theory (DFT) calculations to the case study of HfN_x thin films. Specifically, DFT calculations are found to provide insight into: I. the thermodynamically and kinetically favoured oxygen incorporation in HfN_x films in the form of OH groups; II. the thermodynamic affinity of plasma cationic species (H^+, H_2^+ and H_3^+) towards the surface -OH groups; III. the removal of oxygen in form of volatile H_2O by the scission of the surface Hf-OH bonds by energetic cations and a subsequent reduction of the surface Hf(IV) to Hf(III) by H· radicals.

How does the incident ions with larger mass affects the structural properties of HfN_x films?

Chapter 6 addresses the impact of energetic ions with larger mass (i.e. ArH^+ vs. H_3^+) on the chemical composition, microstructure and the associated electrical properties of the HfN_x films. Heavier ions are generated in an Ar-H_2 plasma and are found to be responsible for further decrease in resistivity by an order of magnitude down to $4.1 \cdot 10^{-4}$ Ωcm with respect to the case of H_2 plasma. The decrease in resistivity is primarily attributed to the major decrease of in-grain nano-porosity in the film, whereas the Hf(III) fraction is similar to the case of the H_2 plasma process. It is concluded that the impinging ions with a larger lead to a greater extent of energy and momentum transfer to the HfN_x surface.

References

1. Moore, G.E., *Cramming more components onto integrated circuits, Reprinted from Electronics.* Electroniics, 1965. **38**(8): p. 114-117.
2. ITRS. *International Technology Roadmap for Semiconductors*. 2015; Available from: https://en.wikipedia.org/wiki/International_Technology_Roadmap_for_Semiconductors.
3. *Intel Announces New 22 nm 3D Tri-gate Transistors*. 2011; Available from: https://www.intel.com/content/dam/www/public/us/en/documents/backgrounders/standards-22nm-3d-tri-gate-transistors-presentation.pdf.
4. *Intel 32 nm disclosure*. [cited 2009; Available from: https://newsroom.intel.com/press-kits/intel-32nm-disclosure/.
5. Mertens, H., et al. *Gate-all-around MOSFETs based on vertically stacked horizontal Si nanowires in a replacement metal gate process on bulk Si substrates*. in *2016 IEEE Symposium on VLSI Technology*. 2016.
6. *Imec demonstrates gate-all-around MOSFETs with lateral silicon nanowires at scaled dimensions*. 2017; Available from: https://phys.org/news/2016-06-imec-gate-all-around-mosfets-lateral-silicon.html.
7. Franklin, A.D., et al., *Carbon Nanotube Complementary Wrap-Gate Transistors.* Nano Letters, 2013. **13**(6): p. 2490-2495.
8. Liu, Y., et al., *Channel shape and interpoly dielectric material effects on electrical characteristics of floating-gate-type three-dimensional fin channel flash memories.* Japanese Journal of Applied Physics, 2015. **54**(4).

9. Yu, H.Y., et al., *Robust High-Quality HfN-HfO 2 Gate Stack for Advanced MOS Device Applications.* IEEE Electron Device Letters, 2004. **25**(2): p. 70-72.

10. Yu, H.Y., M.F. Li, and D.L. Kwong, *Thermally robust HfN metal as a promising gate electrode for advanced MOS device applications.* IEEE Transactions on Electron Devices, 2004. **51**(4): p. 609-615.

11. Elam, J.W., et al., *Atomic layer deposition of aluminum oxide in mesoporous silica gel.* Journal of Physical Chemistry C, 2010. **114**(41): p. 17286-17292.

12. Haukka, S., et al., *Dispersion and distribution of titanium species bound to silica from TiCl4.* Langmuir, 1993. **9**(12): p. 3497-3506.

13. Lakomaa, E.L., A. Root, and T. Suntola, *Surface reactions in Al2O3 growth from trimethylaluminium and water by atomic layer epitaxy.* Applied Surface Science, 1996. **107**: p. 107-115.

14. Keranen, J., et al., *Surface-controlled gas-phase deposition and characterization of highly dispersed vanadia on silica.* Journal of Physical Chemistry B, 2003. **107**(39): p. 10773-10784.

15. Suntola, T. and J. Antson, *Method for producing compound thin films*. 1974: Finland.

16. L., P.R., *A Short History of Atomic Layer Deposition: Tuomo Suntola's Atomic Layer Epitaxy.* Chemical Vapor Deposition, 2014. **20**(10-11-12): p. 332-344.

17. *The principle of ALD was first developed by Tuomo Suntola in mid-1970 under the name of 'Atomic Layer Epitaxy' of ZnS films for electroluminescent flat panel displays.*

Chapter 2

Synthesis of conductive transition metal nitrides: an overview

Abstract

Conductive nitrides of group 4-6 transition metals are a class of materials known for their mechanical stability and chemical inertness. Moreover, their excellent electrical and physical properties make them essential for various applications in the semiconductor industry. This chapter provides a short review on the relevant structural and chemical properties of transition metal nitrides (TMNs). Furthermore, the growth of TMN films, together with their material properties, by various vapour-based deposition techniques is reviewed. In general, very low film resistivity can be achieved by physical vapour deposition techniques. However, the growth of low-resistivity TMN films, when adopting deposition methods such as chemical vapour deposition or atomic layer deposition, presents some challenges. Specifically, the metal precursors generally contain the metal atom in a high oxidation state of +4 or +5, which requires to undergo reduction to +3 oxidation state in order to deposit conductive TMN films. The selection of reducing co-reactants is, therefore, essential to achieve conductive films. Among the reducing agents, plasmas fed with several gases (H_2, H_2/N_2, NH_3) are taken into consideration in this review. Together with the plasma chemistry, other plasma parameters are expected to play a major role in controlling film properties, such as energy, flux, and mass of the ions impinging on the surface of growing film. In particular, the influence of ion energy and ion flux on the structural properties of the films prepared by various vapour-based deposition techniques is reviewed in terms of the theoretical aspects as well as experimental observations. The concepts summarized in this chapter will be of support when discussing the experimental and computational results addressed in Chapters 3-6.

2.1 Transition metal nitride material properties

I. Crystal properties

The conductive nitrides of group 4-6 transition metals are often referred to as interstitial alloys [1, 2], prepared by inserting the nitrogen atoms into the interstitial sites of the parent metal lattice [3]. Generally, transition metal nitrides are found to crystallize in either the face-centered cubic (fcc) or hexagonal-closed packed (hcp) [2, 4] structure. The two representations of a unit cell of the TMN crystal structure are shown in Figure 2.1b, where the larger cations of transition metal (M) are shown in cyan and smaller nitrogen anions (N) are shown in blue. The crystal structure is determined by the Hägg rule and depends on the ratio (r) between the radius of nitrogen atoms (r_n) and transition metal atoms (r_m) [4]. Compounds with r exceeding 0.59 typically exhibit hcp crystal structure, while those with r less than 0.59 crystallizes usually in fcc structure. Nitrides of Ti and W metals yield unique MN stoichiometry, whereas Zr, Hf, V, Nb and Ta may also form sub-stoichiometric nitrides with formula MN_{1-x} [2].

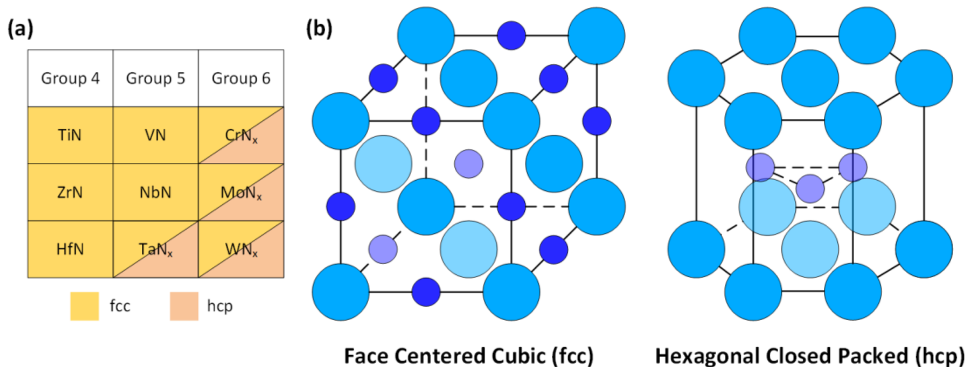

Figure 2.1. (a) Typical crystal structures exhibited by the conductive nitrides of different transition metals, adapted from ref. [2] and (b) representation of a unit cell of face centered cubic (fcc) and hexagonal closed packed (hcp) crystal structure for TMN compounds. Transition metal atoms are in cyan and nitrogen atoms are in blue.

II. Electronic properties

Table 2.1 quantitatively summarizes various properties of conductive nitrides of group 4 transition metals [1, 2]. These TMNs are also often referred to as refractory nitrides, due to their high melting point, high hardness and excellent chemical stability [1]. Furthermore, TMN films also exhibit high electrical

conductivity, making them technologically relevant for the semiconductor industry. The electronic states in TMNs are dictated by the distribution of charge between the transition metal atom and nitrogen. Numerous efforts have been devoted to comprehend the electronic structure of TMNs [4-10], as it is of fundamental importance for the electronic and optical properties of the solid. Figure 2.2a shows the density of states (DOS) for stoichiometric TiN, ZrN and HfN, deduced by means of density functional theory (DFT) calculations [4, 7, 8]. The low-lying bands at ~5 eV below the Fermi energy (E_F) originate from the N 2p states. The higher-lying bands near and above the E_F are predominantly due to the d states of the respective parent metal atom, illustrating the presence of a non-zero DOS at the E_F. It should be noted that the N 2p band also contains small contributions from the d states of the metal atom and similarly the d states above the E_F also have minor contributions from the N 2p states. The presence of a finite DOS at E_F and an associated metal-like behaviour of TMNs is attributed to the presence of the metal atom in the +3 oxidation state [11, 12]. As a consequence, the unpaired *free* d orbital electrons of the transition metal atoms contribute to film conductivity [13, 14]. Figure 2.2b shows the DOS for Zr_3N_4 and Hf_3N_4 for comparison purposes [9, 10]. As can be observed, the DOS goes to zero at the E_F, implying an insulating behaviour for these super-stoichiometric nitrides. This is due to the presence of the +4 oxidation state of the parent metal atom, as highlighted in Chapter 1.

Table 2.1. Properties of conductive nitrides of group 4 transition metals. Values are for room temperature and stoichiometric composition. Adapted from ref. [1, 15-20]. '-' denotes 'not reported'.

Compound	Density (g cm^{-3})	Melting point (°C)	Lattice parameter *a* (Å)	Epitaxial film resistivity (Ωcm)	Screened plasma energy E_p (eV)
TiN	5.4	2950	4.24	$1.25 \cdot 10^{-5}$	2.6
ZrN	7.3	2980	4.57	$1.2 \cdot 10^{-5}$	3.2
HfN	13.8	3387	4.52	$1.42 \cdot 10^{-5}$	3.7

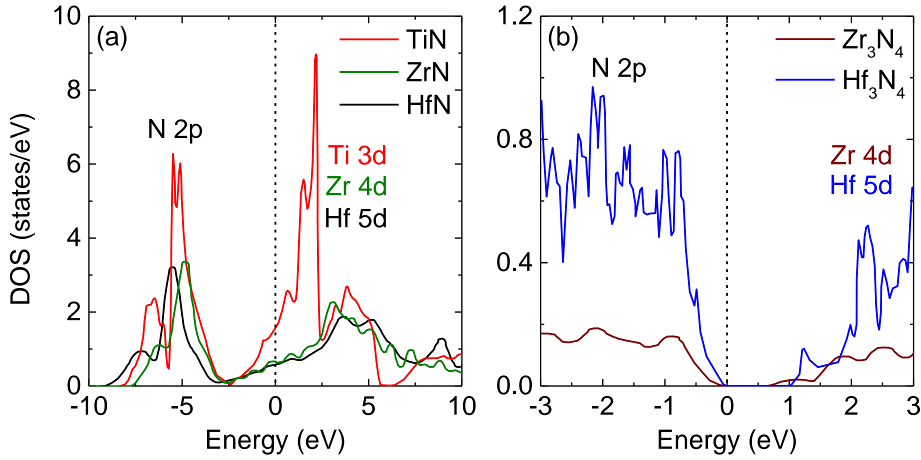

Figure 2.2. Total density of states of conductive nitrides (a) and insulating nitrides (b) of group 4 transition metals, calculated by means of density functional theory (DFT) calculations. Perpendicular dashed line at 0 eV denotes the Fermi level (E_F). Adapted from ref. [7-10].

III. Opto-electronic properties

TMN films have very high near-IR reflectivity. These properties enable their application as reflective back contacts in thin film CIGS solar cells and/or heat mirrors [21-23]. The opto-electronic properties of conductive TMN films, in general, can be inferred by using one free-electron Drude oscillator and two Lorentz oscillators [14, 16]. The Drude oscillator represents the intra-band low energy transitions whereas two Lorentz represents the inter-band transitions at low and high photon energy [14].

$$\varepsilon(E) = \varepsilon_1(E) + i\varepsilon_2(E) = \varepsilon_\infty - \overbrace{\frac{E_p^2}{E^2 - i\Gamma_D E}}^{Drude} + \sum_{j=1}^{2} \overbrace{\frac{S_j E_{0j}^2}{E_{0j}^2 - E_j^2 + iE_j\Gamma_j}}^{Lorentz} \quad (1)$$

where ε_∞ represents transitions at higher energy, E_p is plasma energy and Γ_D is the damping factor for a Drude oscillator. The Lorentz oscillators are centered at E_o which corresponds to the resonance frequency, while S indicates the strength of the oscillators and Γ is the damping factor for the Lorentz oscillators. The screened plasma frequency (ω_p) is given by

$$\omega_p = \sqrt{\frac{e^2 \cdot N}{\varepsilon_o \varepsilon_r m^*}} \quad (2)$$

where ε_o is the vacuum permittivity, ε_r is the relative permittivity at ω_p, m^* is the effective electron mass and N is the density of electrons. TMN films usually have high values of ω_p (Table 2.1), the reason for high near-IR reflectivity.

2.2 Transition metal nitride synthesis

I. Physical vapour deposition (PVD)

Physical vapour deposition (PVD) is definitely the most reported and investigated method for the deposition of TMN films in literature. In a typical PVD process for the growth of TMN films, a highly pure metallic pellet (ca. ~99.9%) is used as the target and either Ar or N_2 plasma or combination thereof is employed. A bias is usually employed to enhance the energy of impinging ions onto the metallic target. Consequently, the atoms are sputtered from the metallic target and contribute to the development of a closed film on the substrate. High vacuum processing, high purity of the target material and the process gases, and high temperature processing of 500-650°C allows for the deposition of TMN films with very low impurity content and high crystallinity by PVD. For instance, epitaxial and stoichiometric TMN films have been grown using PVD on MgO(001) substrates by employing pure metallic targets in combination with either N_2 plasma for TiN or Ar-N_2 plasma for ZrN, HfN and TaN respectively [17-19, 24]. In regards to the electrical properties, the epitaxial films of TiN [17], ZrN [18], HfN [19] and TaN [24] exhibit a very low room temperature resistivity of $1.25 \cdot 10^{-5}$ Ωcm, $1.2 \cdot 10^{-5}$ Ωcm, $1.42 \cdot 10^{-5}$ Ωcm and $1.85 \cdot 10^{-4}$ Ωcm, respectively. Furthermore, these films also displayed superconductivity below a critical temperature (T_c) of ca. ~5-10 K [20]. It should be noted that in the case of PVD, nitridation occurs that oxidizes the metal atom from M(0) oxidation state in the pellet to M(III) oxidation state in the grown film. Since stoichiometric films are obtained, the M(III) oxidation state fraction of ca. 1 is expected in the grown films. This combination of high M(III) fraction and high crystallinity of the films leads to the very low film resisitivities. Although PVD can yield films with high material quality, it suffers from issues such as poor step coverage on trench structures with high aspect ratios of more than 2.5:1, since

the film growth is limited by the line-of-sight of sputtered atoms from the metallic target. Typically, a PVD process also leads to non-uniformity over large surface areas and precise control over film thickness is a challenge, as schematically illustrated in Figure 2.3.

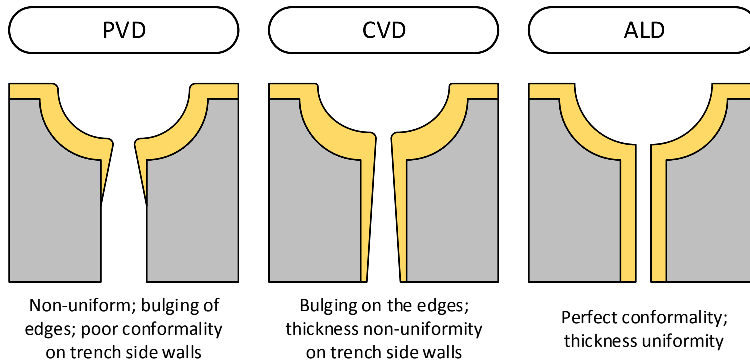

Figure 2.3. A schematic representation of the step-coverage and uniformity of thin films prepared by either PVD, CVD or ALD on high aspect ratio trench structures. Films grown by PVD have poor step coverage in 3D trench nanostructures since the deposition is limited by the line-of-sight of sputtered atoms. CVD leads to an improved step coverage, however the imperfect diffusion of reactive species into the trench nanostructures is still an issue. ALD leads to excellent conformality due to layer-by-layer deposition process.

II. Chemical vapour deposition (CVD)

Chemical vapour deposition (CVD) is a vapour-based deposition technique, aimed at overcoming the shortcomings of PVD processing and therefore improving the conformality and uniformity of the grown thin films. However, achieving a high conformality and uniformity for the films grown by CVD can still be a challenge, especially on the high aspect ratio trench nanostructures as shown in Figure 2.3. In a typical CVD process, a metal (-halide or -organic) precursor and the co-reactant (gas vapours or plasma) are dosed simultaneously. In some cases, such as, the growth of graphene or carbon nanotubes, where the decomposition of metal precursor is required, only the metal precursor is required. The reactions that lead to film formation can occur either in the gaseous phase or on the surface of the substrate [25-27]. A CVD process for the growth of conductive phase of TMN films typically employs precursors with metal atoms present in a higher oxidation state, and therefore a reducing co-reactant is essential to achieve the M(III) oxidation state in the grown films, as highlighted in Chapter 1. As can be anticipated, the growth of low-resistivity TMN films by means of CVD is challenging and the reduction potential of the metal atom determines the choice of reducing co-reactant [28]. A typical CVD process for the growth of TMN films

either employs NH_3 or N_2H_4 gases as reducing co-reactants. Often, a CVD process leads to the growth of polycrystalline TMN films. Therefore, the film resistivity also depends on numerous other factors, such as, film crystallinity, film thickness, grain size and nanoporosity. Furthermore, the presence of impurities in the film (leading to e.g. M-O bonds instead of M-N bonds) increases the oxidation state of the metal atoms and film resistivity.

Fix *et al.* reported the CVD growth of conductive phase of TiN_x and NbN_x films with a resistivity of ca. ~$1.0 \cdot 10^{-3}$ Ωcm by employing $Ti(NMe_2)_4$ and $Nb(NMe_2)_5$ respectively as the metal precursors [29, 30]. On the other hand, the growth of insulating Zr_3N_4, Hf_3N_4 and Ta_3N_5 phase was observed by respectively employing $Zr(NEt_2)_4$, $Hf(NEt_2)_4$ and $Ta(NMe_2)_5$ as the metal precursors [29, 30]. In all cases, NH_3 gas was adopted as co-reactant. Relevantly, the impurity content in the films was below the detection limit of Rutherford backscattering (RBS) measurements. The reported results signify that the Ti(IV) and Nb(V) atoms in the respective metal precursors can be effectively reduced by NH_3 gas such that the conductive phases of TMN films are obtained. On the other hand, the reducing potential of NH_3 gas is insufficient to reduce the Zr(IV), Hf(IV) and Ta(V) atoms in the respective metal precursors. Therefore, it can be anticipated that stronger reducing co-reactants are needed for the deposition of conductive phases of ZrN, HfN and TaN.

In regards to plasma-enhanced CVD, Intemann *et al.* reported the growth of conductive TiN_x phase and the polycrystalline films exhibited a resistivity of $5.5 \cdot 10^{-4}$ Ωcm and a small grain size of ~5 nm using $Ti(NMe_2)_4$ and H_2-N_2 plasma [31]. The as-deposited films contained low oxygen contamination of 0.1 at.%. Furthermore, Liu *et al.* showed the growth of superconductive and highly textured NbN(200) films using $Nb(NEt_2)_5$ and N_2H_4 plasma [32]. The as-deposited films contained 3.2 at.% O and 11 at.% C and exhibited a T_c of 9.25 K. Interestingly, plasma-enhanced CVD growth of conductive ZrN_x phase using $Zr(NEt_2)_4$ and H_2 plasma was demonstrated by Wendel and Suhr [33]. Specifically, a film resistivity of ~$1.1 \cdot 10^{-3}$ Ωcm was achieved. Furthermore, Kim *et al.* reported the plasma-enhanced CVD growth of conductive HfN_x phase using $Hf(NMe_2)_4$ and H_2 plasma and a film resistivity value of ~$5.0 \cdot 10^{-3}$ Ωcm was achieved [34]. The as-deposited films were polycrystalline in nature with a predominant growth of HfN(111) direction and the films were found to contain 18 at.% C and 2 at.% O. Ganin *et al.* showed the formation of insulating orthorhombic Ta_3N_5 phase using $TaCl_5$ and N_2 plasma at temperature of 650°C - 700°C [35], whereas lower temperature of 600°C - 650°C led to synthesis of Ta_2N_3 phase with an optical bandgap of ~2.5 eV.

Based on the above reported results, it can be concluded that a stronger reducing agent, such as H_2 plasma, can enable the reduction of Zr(IV) and Hf(IV) atoms in the metal precursor and thus lead to synthesis of conductive phase of

ZrN and HfN films. However, the extent of reduction, i.e. the fraction of M(III) oxidation state in the grown films, is not reported in the above mentioned works. Even though the grown films contain low O impurity content, the information on the chemical bonding environment of oxygen is missing. Furthermore, the data on microstructure, such as, the crystalline fraction, nanoporosity, and grain size is lacking. Therefore, a clear relation between the film resistivity and the material properties cannot be accomplished and the deviations in the resistivity of CVD grown films from the resistivity of PVD grown films cannot be explained. In addition, it can be inferred that the N_2 plasma is inadequate to reduce the Ta(V) atoms in the metal precursor. As a result, insulating Ta_3N_5 phase was obtained.

III. Atomic layer deposition (ALD)

Similar to CVD, a typical thermal ALD process for the growth of TMN films employs either NH_3 or N_2H_4 gases as reducing co-reactants [36-43]. When processing at low temperature is sought, plasma offers the opportunity to process at low thermal budget because of the high chemical and physical reactivity of the plasma medium [44], in terms of generated radicals and ions impinging on the surface of growing film (see thesis appendix Section B for more discussion on plasma, Pg. 174). Furthermore, the use of plasma as the co-reactant also allows the fine tuning of material properties in terms of film stoichiometry and crystallinity [45, 46]. Typical plasmas used for the growth of TMN films are those generated in H_2, N_2 or NH_3 gases or their combinations [36, 47-61]. It should be noted that in the case of H_2 plasma, the N atoms in TMN films originate from the metal precursor itself. Due the greater reduction potential of plasma radicals (H·, NH_x·) in comparison to the molecular NH_3 or N_2H_4 species, it can be anticipated that the extent of reduction to the M(III) oxidation state may be higher in plasma-assisted ALD, as compared to thermal ALD.

Numerous approaches have been explored and reported in literature to synthesize the TMN films by ALD by employing diverse alkylamide or halide metal precursors in combination with various reducing co-reactants. Figure 2.4 presents an overview of metal nitrides prepared by ALD, whereas Table A2.1 in the appendix provides a comprehensive summary of the material properties of only the group 4-6 transition metal nitride films prepared by both thermal and plasma-assisted ALD routes.

H																	He
^{T}Li	Be											$^{T/P}$B	C	N	O	F	Ne
Na	Mg											$^{T/P}$Al	$^{T/P}$Si	P	S	Cl	Ar
K	Ca	Sc	$^{T/P}$Ti	$^{T/P}$V	Cr	Mn	^{T}Fe	Co	Ni	$^{T/P}$Cu	^{T}Zn	$^{T/P}$Ga	Ge	As	Se	Br	Kr
Rb	Sr	Y	$^{T/P}$Zr	$^{T/P}$Nb	$^{T/P}$Mo	Tc	Ru	Rh	Pd	Ag	Cd	$^{T/P}$In	^{P}Sn	Sb	Te	I	Xe
Cs	Ba	*	$^{T/P}$Hf	$^{T/P}$Ta	$^{T/P}$W	^{T}Re	Os	Ir	Pt	Au	Hg	Tl	Pb	Bi	Po	At	Rn
Fr	R	**	Rf	Db	Sg	Bh	Hs	Mt	Ds	Rg	Cn	Uut	Fl	Uup	Lv	Uus	Uuo
		*	La	Ce	Pr	Nd	Pm	Sm	Eu	^{P}Gd	Tb	Dy	Ho	Er	Tm	Yb	Lu
		**	Ac	Th	Pa	U	Np	Pu	Am	Cm	Bk	Cf	Es	Fm	Md	No	Lr

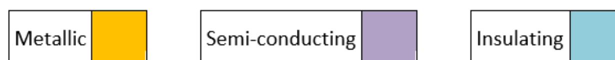

Figure 2.4. Overview of the metal nitrides grown by ALD. Classification is based on the fundamental electrical properties exhibited by films of these metal nitrides (i.e. conductive, semi-conductive or insulating). The superscripts T and P represent thermal and plasma ALD processes, respectively. Conductive transition metal nitrides are depicted in golden colour.

Addressing the thermal ALD first, Tetsuro *et al.* achieved the growth of conductive phase of TiN_x films with a resistivity of $4.0 \cdot 10^{-3}$ Ωcm by using $Ti(NMe_2)_4$ metal precursor and NH_3 gas as the reducing co-reactant [37]. Similarly, the growth of conductive phases of VN_x and WN_x films was shown by employing $V(NEt_2)_4$ and $W(NMe_2)_2(NCMe_3)_2$ metal precursors, and NH_3 gas as the reducing agent [39, 43]. A resistivity of ~$1.2 \cdot 10^{-4}$ Ωcm was obtained for VN_x films, whereas WN_x films exhibited a resistivity of ~$2.0 \cdot 10^{-3}$ Ωcm. These results signify that the reduction of above mentioned metal atoms to M(III) oxidation state can be achieved by NH_3 gas and thus the conductive phases of the metal nitrides have been obtained, similar to the aforementioned CVD processes. On the other hand, the growth of insulating phases of Zr_3N_4, Ta_3N_5, Hf_3N_4 phases was observed by employing $Zr(NMe_2)_4$, $Ta(NEt_2)_3NCMe_3$ and $Hf(NMe_2)_4$ metal precursors and NH_3 as the reducing gas [38, 40].

Based on the above works, it can be again concluded that more effective reducing agents are required to obtain conductive phases of ZrN_x, HfN_x and TaN_x films, in particular. These observations are also in-line with the material properties obtained for the aforementioned thermal CVD grown films.

In regards to the plasma-assisted ALD, the material properties and growth of only ZrN_x, TaN_x and HfN_x films are discussed here, whereas the material properties of other TMN films can be found in Table A2.1. Muneshwar and Cadien showed that conductive ZrN_x phase with a resistivity of $5.6 \cdot 10^{-4}$ Ωcm can be obtained by employing $Zr(NMe_2)_4$ metal precursor and N_2/H_2 plasma [49]. Similarly, Langereis *et al.* reported the growth of conductive TaN_x phase with a resistivity of $3.9 \cdot 10^{-4}$ Ωcm by employing $Ta(NMe_2)_5$ metal precursor and H_2 plasma [57]. In the same work, the application of N_2/H_2 plasma or NH_3 plasma, instead, resulted in the deposition of insulating Ta_3N_5 phase [57]. Consiglio *et al.* reported the growth of conductive HfN_x phase, with films exhibiting a resistivity of $2.3 \cdot 10^{-3}$ Ωcm, by a combination of $Hf(NMeEt)_4$ metal precursor and H_2 plasma [51]. Similarly, Kim *et al.* also achieved the deposition of conductive HfN_x phase with a film resistivity of $6.7 \cdot 10^{-3}$ Ωcm by using $Hf(NMe_2)_4$ metal precursor and H_2 plasma [52].

Based on the results obtained in above reported works, it can be clearly inferred that H_2 plasma is capable of providing highly reducing species that allow the reduction of Zr(IV), Ta(V) and Hf(IV) atoms to the M(III) state, in line with the results of plasma-enhanced CVD processes discussed above. However, even though H_2 plasma can lead to the synthesis of conductive phases of ZrN_x, HfN_x and TaN_x films, the information on the effectiveness of H_2 plasma in reducing the metal atoms (i.e. M(III) oxidation state fraction) is missing. Moreover, the effect of presence of impurities (M-O bonds) on the M(III) is also not reported. Next to the chemical composition, the data on the aforementioned key microstructural parameters is also lacking. Therefore, the resistivities of the TMN films grown by ALD cannot be compared with that of the PVD grown films. As will be shown later in Chapters 3-6, a step-by-step improvement in the Hf(III) fraction and HfN_x film microstructure by systematically varying the different co-reactant plasma parameters leads to major decrease in the resistivity values of the grown HfN_x films. Furthermore, the HfN_x film resistivity values even approach the resistivity values of HfN_x films prepared by PVD.

2.3 Effect of energetic ions on material properties

So far, we have discussed that H_2 plasma is capable of providing a reducing environment that can enable the synthesis of conductive phases of ZrN_x, TaN_x and HfN_x films. During film growth by a plasma process, the surface of the growing film is not only interacts with the plasma radicals as aforementioned, but also with the impinging ions, photons and electrons. One of the important parameters that can be manipulated during the plasma exposure is the energy and flux of impinging ions [45, 62]. Smets *et al.* described the various ion-surface interaction processes that may occur during growth of thin films [63]. They are schematically illustrated

in Figure 2.5. The incoming ions gets accelerated in the plasma sheath. Ions with low energy may get assimilated in the near-surface region through in-elastic collisions or back-scattered. Energy transfer to the surface may occur in form of local heating, which may promote adatom migration or lattice vibrations (enhancement of surface reactivity). On the other hand, ions with an energy above a certain threshold may penetrate below the surface and get trapped as interstitials or may also displace the lattice atoms of the surface or bulk [64-67]. At even higher energies of impinging ions, sputtering or ion implantation processes may initiate, where ions can kick out the atoms of the target material.

Figure 2.6 shows the ranges of ion energies and ion fluxes that determine the nature of ion-surface interactions. The latter allows to define the so-called 'operating windows' for various plasma-based processes. As we will learn, the ion energy and flux values that are suitable and also beneficial for film growth and various material properties can vary significantly and also depend on the material system of interest and the growth technique (PVD, CVD or ALD). In regards to the plasma-assisted ALD, the film growth by an ALD process typically employs an ion energy of ca. 10 - 100 eV and an ion flux of ca. 10^{13} - 10^{15} cm^{-2} s^{-1}. In a remote plasma ALD reactor, which has been used for performing the experiments in this dissertation, the plasma parameters (ion flux, radical density) can be varied fairly independently from the ion energy. By biasing the substrate with an external rf power source, energies of the impinging ions can be increased up to ca. 400 eV upon increasing the bias power applied to the substrate up to 100W. A detailed discussion on the various aspects of rf substrate biasing can be found in the thesis appendix (Section C, Pg. 177).

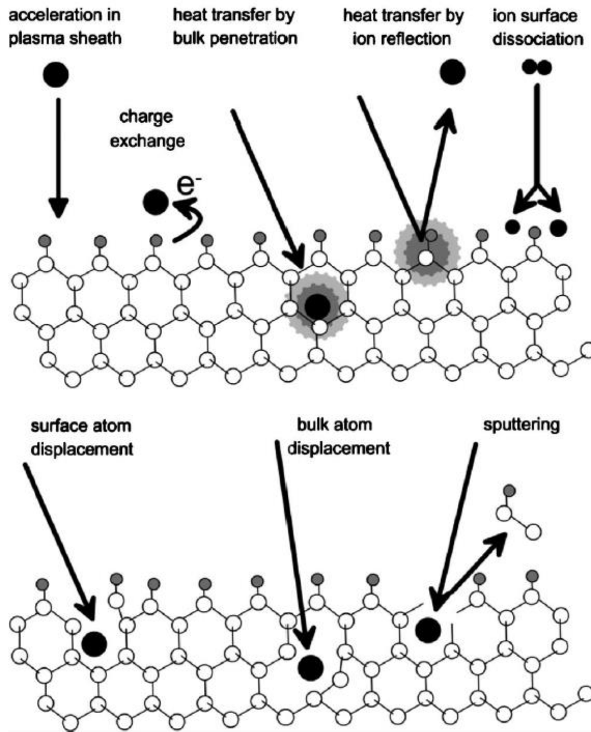

Figure 2.5. A schematic of energetic ion-surface and ion-bulk interactions with a crystalline lattice during thin film growth. Adapted from ref. [63].

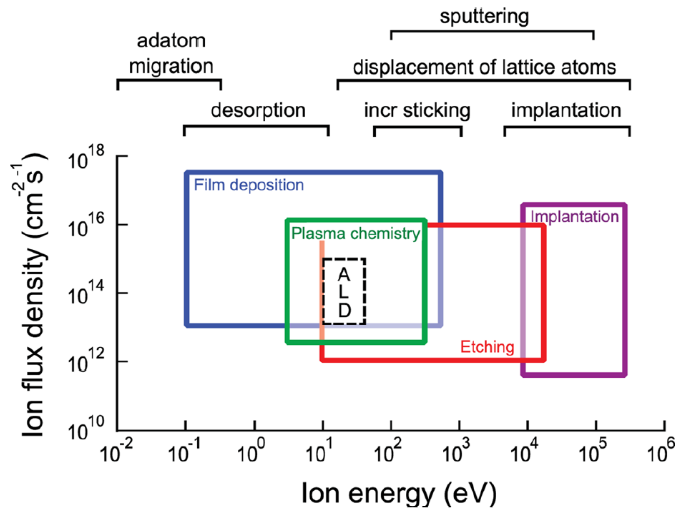

Figure 2.6. Ion-surface interactions in terms of ion energy and ion flux during various plasma processes. The typical operating windows for various plasma-based processes are indicated. Adapted from ref. [45, 62].

It is relevant here to briefly review the effect of ion energy and ion flux on the material properties of the films prepared by PVD, plasma-enhanced CVD and plasma-assisted ALD. The effects of energetic ions on the structural properties of films has been most extensively studied for the PVD technique [18, 24, 64, 66-72]. Addressing the nanoporosity first, Hultman *et al.* showed that the nanoporosity in the sputtered TiN films grown using pure Ti target and N_2 plasma decreased rapidly and monotonically with an increase in the absolute value of time-averaged substrate potential ($|V_{bias}|$) from 0V to 300V [72]. Increasing the $|V_{bias}|$ value above 300V led to ion-induced degradation and an increase in the nanoporosity. The reduction in the nanoporosity was attributed to the enhanced near-surface and/or sub-surface diffusion processes as a result of energetic ion bombardment [72]. In a follow-up study, Petrov *et al.* showed the growth of sputtered TiN films with a dense microstructure and a large grain size below a $|V_{bias}|$ value of 120V in an Ar-N_2 plasma discharge, whereas an increase in the value of $|V_{bias}|$ above 200V led to incorporation of defects and nanoporosity in the films [71].

In regards to crystallinity and chemical composition, Adibi *et al.* demonstrated that increasing either the energy or flux of bombarding N_2^+ ions can alter the microstructural properties of the sputtered $Ti_{0.5}Al_{0.5}N$ films in quite distinct ways [68]. Specifically, it was demonstrated that while keeping the J_i/J_{Me} (ratio of the flux of impinging ions J_i to flux of the metal atoms J_{Me}) at 1 and increasing the $\langle E_{ion} \rangle$ from 20 eV to 85 eV resulted in a minor change in the film texture, whereas a significant variation in the film stoichiometry (N/(Ti+Al) ratio increased from 1.0 to 1.2) and the lattice parameter (a_o increased from 0.415 to 0.419) was observed. Alternatively, a constant $\langle E_{ion} \rangle$ of 20 eV and an increase in J_i/J_{Me} from 1 to 7 led to an abrupt change in preferential growth orientation from <111> to <200>, while only a slight variation in the stoichiometry and the lattice parameter was observed. Furthermore, Villamayor *et al.* demonstrated an increase in the crystalline quality of sputtered HfN films by adopting Kr-N_2 plasma, instead of Ar-N_2 plasma [73].

In the case of plasma-enhanced CVD, Kuhr *et al.* reported that a variation in $|V_{bias}|$ significantly alters the nucleation and growth of insulating *h*-BN films [74]. In particular, a predominant growth of in-plane *h*-BN is observed at $|V_{bias}|$ = 0V, whereas the growth of out-of-plane *h*-BN is also observed $|V_{bias}|$ value above 30V. Burke and Pomot demonstrated the plasma-enhanced CVD growth of epitaxial Si below $\langle E_{ion} \rangle$ of 25 eV, whereas the epitaxial growth was lost above an $\langle E_{ion} \rangle$ of 25 eV [75]. Smets *et al.* showed a reduction in nanosized void density and defect density in *a*-Si:H films upon increasing $|V_{bias}|$ up to ca. 50V, above which the void density increased [63]. Considering the plasma-assisted ALD, Profijt *et al.* reported a modification in the crystalline structure of TiO_2 thin films from anatase-TiO_2 to rutile-TiO_2 by increasing the $\langle E_{ion} \rangle$ from 50 eV to 250 eV [76]. Furthermore, the

mass density Co_3O_4 thin films consistently increased with an increase in $<E_{ion}>$ from 50 eV to 210 eV [76]. In a follow-up work, Faraz *et al.* showed that energetic ions can induce crystallization of amorphous TiO_2 and HfO_2 films even at a low stage temperature of 150°C [61]. In the same work, variations in refractive index, density and the residual stress values with the $|V_{bias}|$ value for TiO_2 and HfO_2 films was also reported [61].

Based on the above reported works, it can be concluded that the energetic ions may play an analogous role to the increase in growth temperature up to a certain ion energy threshold, thereby overcoming the activation energy barrier for near-surface atomic diffusion processes and thus leading to defect annihilation and associated decrease in nanoporosity. Above this ion energy threshold, ion induced damage occurs that leads to defect incorporation and increase in nanoporosity. Moreover, ion bombardment can also induce crystallization in films at low temperatures, which are otherwise amorphous in the absence of energetic ions. Furthermore, the average energy deposited per metal atom ($<E_d> = <E_{ion}>\cdot J_i/J_{Me}$) and the associated ion energy dose cannot be used as a universal parameter to describe the effects of impinging ions on the growth and microstructure of the polycrystalline films. The same ion energy dose can be achieved by either increasing the ion energy or ion flux independently, however, the effects of either of the two parameter on the microstructure of the grown films can be completely different. Next to the ion energy and ion flux, the mass of impinging ions is of equal importance. Increasing the mass of impinging ions may lead to a greater extent of energy and momentum transfer to the atoms of growing film, which may also promote the near-surface atomic diffusion processes and lead to decrease in defects and nanoporosity. In short, the interaction between the impinging ions and the growing film can affect the microstructure and the growth process of thin films in several ways. These different topics will be treated in more detail in Chapters 4 and 6.

Lastly, it should be noted that the range of ion energies reported for plasma-assisted ALD that have a positive influence on the film properties may significantly differ from those observed for the PVD or plasma-enhanced CVD processes. This may pertain to the so-called 'duty cycle' of the substrate bias application. In a typical PVD or plasma-enhanced CVD process, the energetic ion bombardment is usually present during the entire time of the material growth. On the other hand, in the case of plasma-assisted ALD, the external rf substrate bias may be applied for the entire duration of the plasma half cycle or a small part of it. This means that the surface of the growing film may be exposed to energetic ions for only a small fraction of the entire ALD cycle of the material growth. Therefore, the threshold limit of the $<E_{ion}>$ and the ion energy dose above which the defect incorporation and/or ion-induced degradation initiates might significantly vary

between the different techniques. Furthermore, since the metal precursor dose and the plasma exposure step are well separated in an ALD process, an ALD process allows to distinctly study the effects of energetic ions and other plasma parameters on the material properties of the grown films. This imparts a higher degree of control on various process parameters. In short, as aforementioned, the nature of ion-surface interaction depends on the ion energy, ion flux, mass of impinging ions and the associated energy and momentum transfer to the surface of growing film, duration of energetic ion bombardment and the target material system of interest.

The above observations on material properties signify that the energetic ions play a crucial role in affecting wide range of material properties. These include microstructural properties (i.e. nanoporosity, crystallinity, and preferred orientation), film nucleation (i.e. epitaxy, grain size), residual film stress and also the chemical composition (i.e. stoichiometry). Figure 2.7 summarizes some of these key aspects, which will also be highlighted in the following chapters. As mentioned in Chapter 1, in this dissertation, we use plasma-assisted ALD of HfN_x films as a case study to illustrate the effect of the impingement of energetic ions on the chemical composition, microstructural properties and associated electrical properties of the grown HfN_x films.

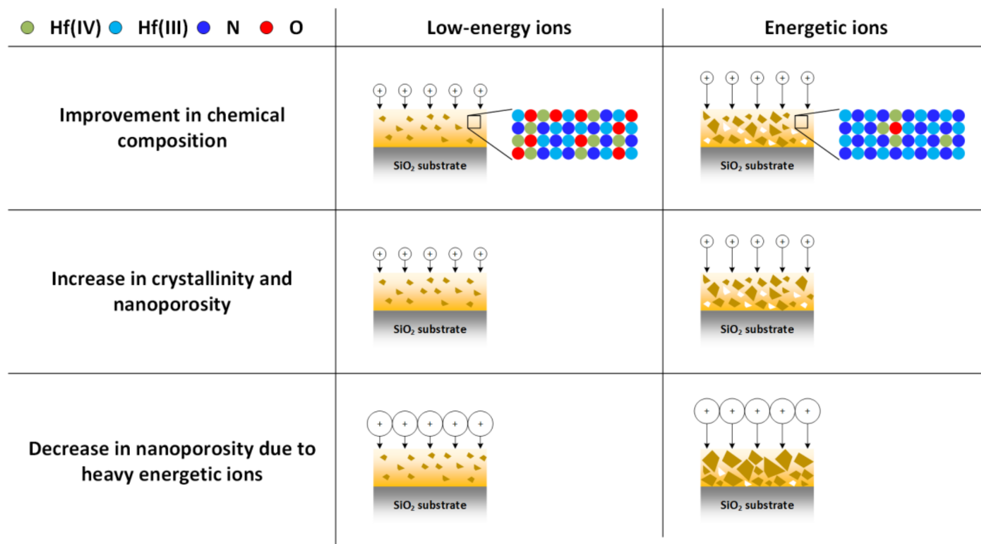

Figure 2.7. A schematic representation of the different material properties of HfN_x films that can be modified by impingement of energetic ions.

References

1. Pierson, H.O., *Handbook of Refractory Carbides and Nitrides: Properties, Characteristics, Processing and Apps*. 1996: Elsevier Science.
2. Zhong, Y., et al., *Transition metal carbides and nitrides in energy storage and conversion.* Advanced Science, 2015. **3**(5).
3. Freer, R., *The Physics and Chemistry of Carbides, Nitrides and Borides*. 2012: Springer Netherlands.
4. Schwarz, K., *Band structure and chemical bonding in transition metal carbides and nitrides.* Critical Reviews in Solid State and Materials Sciences, 1987. **13**(3): p. 211-257.
5. Johansson, L.I., *Electronic and structural properties of transition-metal carbide and nitride surfaces.* Surface Science Reports, 1995. **21**(5): p. 177-250.
6. Lengauer, W., *Nitrides: Transition Metal Solid-State Chemistry*, in *Encyclopedia of Inorganic and Bioinorganic Chemistry, R. A. Scott (Ed.)*. 2015.
7. Saha, B., et al., *Electronic structure, phonons, and thermal properties of ScN, ZrN, and HfN: A first-principles study.* Journal of Applied Physics, 2010. **107**(3): p. 033715.
8. Marlo, M. and V. Milman, *Density-functional study of bulk and surface properties of titanium nitride using different exchange-correlation functionals.* Physical Review B, 2000. **62**(4): p. 2899-2907.
9. Yu, S., et al., *First-principles study of Zr–N crystalline phases: phase stability, electronic and mechanical properties.* RSC Advances, 2017. **7**(8): p. 4697-4703.
10. Huang, H.H., et al., *Transformation of electronic properties and structural phase transition from HfN to Hf3N4.* Journal of Physics: Condensed Matter, 2015. **27**(22): p. 225501.
11. Knoops, H.C.M., et al., *Reaction mechanisms of atomic layer deposition of TaNx from Ta(NMe2)5 precursor and H2-based plasmas.* Journal of Vacuum Science & Technology A, 2012. **30**(1): p. 01A101.
12. Leskelä, M. and M. Ritala, *Atomic layer deposition (ALD): from precursors to thin film structures.* Thin Solid Films, 2002. **409**(1): p. 138-146.
13. Farrell, I.L., et al., *Tunable electrical and optical properties of hafnium nitride thin films.* Applied Physics Letters, 2010. **96**(7).

14. Hu, C., et al., *Nature of tunable optical reflectivity of rocksalt hafnium nitride films.* Journal of Physical Chemistry C, 2014. **118**(35): p. 20511-20520.

15. Kang, J.H. and K.J. Kim, *Structural, optical, and electronic properties of cubic TiNx compounds.* Journal of Applied Physics, 1999. **86**(1): p. 346-350.

16. Strømme, M., R. Karmhag, and C.G. Ribbing, *Optical constants of sputtered hafnium nitride films. Intra- and interband contributions.* Optical Materials, 1995. **4**(5): p. 629-639.

17. Karr, B.W., et al., *Effects of high-flux low-energy ion bombardment on the low-temperature growth morphology of TiN(001) epitaxial layers.* Physical Review B, 2000. **61**(23): p. 16137-16143.

18. Mei, A.B., et al., *Physical properties of epitaxial ZrN/MgO(001) layers grown by reactive magnetron sputtering.* Journal of Vacuum Science & Technology A, 2013. **31**(6): p. 061516.

19. Seo, H.S., et al., *Growth and physical properties of epitaxial HfN layers on MgO(001).* Journal of Applied Physics, 2004. **96**(1): p. 878-884.

20. Mei, A.B., et al., *Electron/phonon coupling in group-IV transition-metal and rare-earth nitrides.* Journal of Applied Physics, 2013. **114**(19): p. 193708.

21. Andersson, K.E., M. Veszelei, and A. Roos, *Zirconium nitride based transparent heat mirror coatings —preparation and characterisation.* Solar Energy Materials and Solar Cells, 1994. **32**(2): p. 199-212.

22. Karlsson, B. and C.G. Ribbing. *Optical Properties Of Transparent Heat Mirrors Based On Thin Films Of TiN, ZrN, And HfN*. in *Optical Coatings for Energy Efficiency and Solar Applications*. 1982. Proc. SPIE.

23. Malmström, J., S. Schleussner, and L. Stolt, *Enhanced back reflectance and quantum efficiency in Cu(In,Ga)Se 2 thin film solar cells with a ZrN back reflector.* Applied Physics Letters, 2004. **85**(13): p. 2634-2636.

24. Shin, C.-S., et al., *Epitaxial growth of metastable δ-TaN layers on MgO(001) using low-energy, high-flux ion irradiation during ultrahigh vacuum reactive magnetron sputtering.* Journal of Vacuum Science & Technology A, 2002. **20**(6): p. 2007-2017.

25. Pierson, H.O., *3 - The Chemistry of CVD*, in *Handbook of Chemical Vapor Deposition (CVD) (Second Edition)*, H.O. Pierson, Editor. 1999, William Andrew Publishing: Norwich, NY. p. 68-83.

26. Pierson, H.O., *2 - Fundamentals of Chemical Vapor Deposition*, in *Handbook of Chemical Vapor Deposition (CVD) (Second Edition)*, H.O. Pierson, Editor. 1999, William Andrew Publishing: Norwich, NY. p. 36-67.

27. Liu, Z., et al., *Chapter 2 - CVD Synthesis of Graphene*, in *Thermal Transport in Carbon-Based Nanomaterials*, G. Zhang, Editor. 2017, Elsevier. p. 19-56.

28. Kim, Y., et al., *Metal-organic CVD of conductive and crystalline hafnium nitride films.* Chemical Vapor Deposition, 2005. **11**(6-7): p. 294-297.

29. Fix, R., R.G. Gordon, and D.M. Hoffman, *Chemical vapor deposition of titanium, zirconium, and hafnium nitride thin films.* Chemistry of Materials, 1991. **3**(6): p. 1138-1148.

30. Fix, R., R.G. Gordon, and D.M. Hoffman, *Chemical vapor deposition of vanadium, niobium, and tantalum nitride thin films.* Chemistry of Materials, 1993. **5**(5): p. 614-619.

31. Intemann, A., H. Koerner, and F. Koch, *Film Properties of CVD Titanium Nitride Deposited with Organometallic Precursors at Low Pressure Using Inert Gases, Ammonia, or Remote Activation.* Journal of The Electrochemical Society, 1993. **140**(11): p. 3215-3222.

32. Liu, X., et al., *Plasma-Assisted MOCVD Growth of Superconducting NbN Thin Films Using Nb Dialkylamide and Nb Alkylimide Precursors.* Chemical Vapor Deposition, 2001. **7**(1): p. 25-28.

33. Wendel, H. and H. Suhr, *Thin zirconium nitride films prepared by plasma-enhanced CVD.* Applied Physics A, 1992. **54**(4): p. 389-392.

34. Kim, E.-J., H.-G. Woo, and D.-H. Kim, *Effect of Deposition Temperature on the Characteristics of HfNx Thin Films Prepared by Plasma Assisted Cyclic Chemical Vapor Deposition.* Journal of Nanoscience and Nanotechnology, 2010. **10**(5): p. 3463-3466.

35. Ganin, Alexei Y., L. Kienle, and Grigori V. Vajenine, *Plasma-Enhanced CVD Synthesis and Structural Characterization of Ta2N3.* European Journal of Inorganic Chemistry, 2004. **2004**(16): p. 3233-3239.

36. Musschoot, J., et al., *Atomic layer deposition of titanium nitride from TDMAT precursor.* Microelectronic Engineering, 2009. **86**(1): p. 72-77.

37. Tetsuro, H., et al., *Investigation of Thermal Stability of TiN Film Formed by Atomic Layer Deposition Using Tetrakis(dimethylamino)titanium Precursor for Metal-Gate Metal–Oxide–Semiconductor Field-Effect Transistor.* Japanese Journal of Applied Physics, 2010. **49**(4S): p. 04DA16.

38. Becker, J.S., E. Kim, and R.G. Gordon, *Atomic Layer Deposition of Insulating Hafnium and Zirconium Nitrides.* Chemistry of Materials, 2004. **16**(18): p. 3497-3501.

39. Mayumi, B.T., et al., *Atomic Layer Deposition of Thin VN x Film from Tetrakis(diethylamido)vanadium Precursor.* Japanese Journal of Applied Physics, 2011. **50**(5S1): p. 05EA06.

40. Burton, B.B., A.R. Lavoie, and S.M. George, *Tantalum nitride atomic layer deposition using (tert-butylimido) tris(diethylamido)tantalum and hydrazine.* Journal of the Electrochemical Society, 2008. **155**(7): p. D508-D516.

41. Miikkulainen, V., M. Suvanto, and T.A. Pakkanen, *Atomic Layer Deposition of Molybdenum Nitride from Bis(tert-butylimido)-bis(dimethylamido)molybdenum and Ammonia onto Several Types of Substrate Materials with Equal Growth per Cycle.* Chemistry of Materials, 2007. **19**(2): p. 263-269.

42. Klaus, J.W., S.J. Ferro, and S.M. George, *Atomic layer deposition of tungsten nitride films using sequential surface reactions.* Journal of the Electrochemical Society, 2000. **147**(3): p. 1175-1181.

43. Becker, J.S., et al., *Highly Conformal Thin Films of Tungsten Nitride Prepared by Atomic Layer Deposition from a Novel Precursor.* Chemistry of Materials, 2003. **15**(15): p. 2969-2976.

44. Profijt, H.B., et al., *Plasma-assisted atomic layer deposition: Basics, opportunities, and challenges.* Journal of Vacuum Science and Technology A: Vacuum, Surfaces and Films, 2011. **29**(5).

45. Profijt, H.B., et al., *Plasma-Assisted Atomic Layer Deposition: Basics, Opportunities, and Challenges.* Journal of Vacuum Science & Technology A: Vacuum, Surfaces, and Films, 2011. **29**(5): p. 050801.

46. Knoops, H.C.M., et al., *Status and prospects of plasma-assisted atomic layer deposition.* Journal of Vacuum Science & Technology A, 2019. **37**(3): p. 030902.

47. Kim, J.Y., et al., *Remote plasma enhanced atomic layer deposition of TiN thin films using metalorganic precursor.* Journal of Vacuum Science and Technology A: Vacuum, Surfaces and Films, 2004. **22**(1): p. 8-12.

48. Kim, J.Y., et al., *Remote plasma-enhanced atomic-layer deposition of tiN by using TDMAT with a NH 3 plasma.* Journal of the Korean Physical Society, 2004. **45**(6): p. 1639-1643.

49. Muneshwar, T. and K. Cadien, *Low temperature plasma enhanced atomic layer deposition of conducting zirconium nitride films using tetrakis (dimethylamido) zirconium and forming gas (5% H2 + 95% N2) plasma.* Journal of Vacuum Science & Technology A: Vacuum, Surfaces, and Films, 2015. **33**(3): p. 031502.

50. Seungchan, C., et al., *Barrier Characteristics of ZrN Films Deposited by Remote Plasma-Enhanced Atomic Layer Deposition Using Tetrakis(diethylamino)zirconium Precursor.* Japanese Journal of Applied Physics, 2007. **46**(7R): p. 4085.

51. Consiglio, S., et al., *Plasma-assisted atomic layer deposition of conductive hafnium nitride using tetrakis(ethylmethylamino)hafnium for CMOS gate electrode applications.* Journal of the Electrochemical Society, 2008. **155**(3): p. H196-H201.

52. Kim, E.J. and D.H. Kim, *Highly conductive HfN x films prepared by plasma-assisted atomic layer deposition.* Electrochemical and Solid-State Letters, 2006. **9**(8): p. C123-C125.

53. Jeong, W., et al., *Characteristics of HfN films deposited by using remote plasma-enhanced atomic layer deposition.* Journal of the Korean Physical Society, 2010. **56**(3): p. 905-910.

54. Rampelberg, G., et al., *Low temperature plasma-enhanced atomic layer deposition of thin vanadium nitride layers for copper diffusion barriers.* Applied Physics Letters, 2013. **102**(11): p. 111910.

55. Mario, Z., et al., *Superconducting niobium nitride thin films deposited by metal organic plasma-enhanced atomic layer deposition.* Superconductor Science and Technology, 2013. **26**(2): p. 025008.

56. Sowa, M.J., et al., *Plasma-enhanced atomic layer deposition of superconducting niobium nitride.* Journal of Vacuum Science & Technology A: Vacuum, Surfaces, and Films, 2017. **35**(1): p. 01B143.

57. Langereis, E., et al., *Synthesis and in situ characterization of low-resistivity Ta Nx films by remote plasma atomic layer deposition.* Journal of Applied Physics, 2007. **102**(8).

58. Bertuch, A., et al., *Plasma enhanced atomic layer deposition of molybdenum carbide and nitride with bis(tert-butylimido)bis(dimethylamido) molybdenum.* Journal of Vacuum Science & Technology A: Vacuum, Surfaces, and Films, 2017. **35**(1): p. 01B141.

59. Jang, Y., et al., *Highly-conformal nanocrystalline molybdenum nitride thin films by atomic layer deposition as a diffusion barrier against Cu.* Journal of Alloys and Compounds, 2016. **663**(Supplement C): p. 651-658.

60. Sowa, M.J., et al., *Plasma-enhanced atomic layer deposition of tungsten nitride.* Journal of Vacuum Science & Technology A: Vacuum, Surfaces, and Films, 2016. **34**(5): p. 051516.

61. Faraz, T., et al., *Tuning Material Properties of Oxides and Nitrides by Substrate Biasing during Plasma-Enhanced Atomic Layer Deposition on Planar and 3D Substrate Topographies.* ACS Applied Materials & Interfaces, 2018. **10**(15): p. 13158-13180.

62. Takagi, T., *Ion–surface interactions during thin film deposition.* Journal of Vacuum Science & Technology A, 1984. **2**(2): p. 382-388.

63. Smets, A.H.M., W.M.M. Kessels, and M.C.M.v.d. Sanden, *The effect of ion-surface and ion-bulk interactions during hydrogenated amorphous silicon deposition.* Journal of Applied Physics, 2007. **102**(7): p. 073523.

64. Auciello, O. and R. Kelly, *Ion bombardment modification of surfaces: fundamentals and applications*. 1984: Elsevier Science Publishers.

65. Kaufman, H.R. and J.M.E. Harper, *Ion doses for low-energy ion-assist applications.* Journal of Vacuum Science & Technology A: Vacuum, Surfaces, and Films, 2004. **22**(1): p. 221-224.

66. Greene, J.E. and S.A. Barnett, *ION-SURFACE INTERACTIONS DURING VAPOR PHASE CRYSTAL GROWTH BY SPUTTERING, MBE, AND PLASMA-ENHANCED CVD: APPLICATIONS TOSEMICONDUCTORS.* PROC OF THE ANNU CONF ON THE PHYS AND CHEM OF SEMICOND INTERFACES, 9TH, 1982. **V 21**(N 2): p. 285-302.

67. Anders, A., *A structure zone diagram including plasma-based deposition and ion etching.* Thin Solid Films, 2010. **518**(15): p. 4087-4090.

68. Adibi, F., et al., *Effects of high-flux low-energy (20–100 eV) ion irradiation during deposition on the microstructure and preferred orientation of Ti0.5Al0.5N alloys grown by ultra-high-vacuum reactive magnetron sputtering.* Journal of Applied Physics, 1993. **73**(12): p. 8580-8589.

69. Johansson, B.O., et al., *Reactively magnetron sputtered Hf-N films. I. Composition and structure.* Journal of Applied Physics, 1985. **58**(8): p. 3104-3111.

70. Petrov, I., et al., *Microstructural evolution during film growth.* Journal of Vacuum Science & Technology A, 2003. **21**(5): p. S117-S128.

71. Petrov, I., et al., *Microstructure modification of TiN by ion bombardment during reactive sputter deposition.* Thin Solid Films, 1989. **169**(2): p. 299-314.

72. Hultman, L., et al., *Low-energy ion irradiation during film growth for reducing defect densities in epitaxial TiN(100) films deposited by reactive-magnetron sputtering.* Journal of Applied Physics, 1987. **61**(2): p. 552-555.

73. Villamayor, M.M.S., et al., *Low temperature (Ts/Tm < 0.1) epitaxial growth of HfN/MgO(001) via reactive HiPIMS with metal-ion synchronized substrate bias.* Journal of Vacuum Science & Technology A, 2018. **36**(6): p. 061511.

74. Kuhr, M., S. Reinke, and W. Kulisch, *Nucleation of cubic boron nitride (c-BN) with ion-induced plasma-enhanced CVD.* Diamond and Related Materials, 1995. **4**(4): p. 375-380.

75. Burke, R.R. and C. Pomot, *Microwave multipolar plasma for etching and deposition.* Applied Surface Science, 1989. **36**(1): p. 267-277.

76. Profijt, H.B., M.C.M. Van De Sanden, and W.M.M. Kessels, *Substrate-biasing during plasma-assisted atomic layer deposition to tailor metal-oxide thin film growth.* Journal of Vacuum Science and Technology A: Vacuum, Surfaces and Films, 2013. **31**(1).

Appendix 2

Table A2.1. Overview of the material properties of various transition metal nitride (TMN) films prepared by either the thermal or plasma-assisted ALD route. The growth material, metal precursor, co-reactant, the plasma source configuration (‘*d*’ is direct plasma, ‘*r*’ is remote plasma and ‘-’ is ‘not specified’), stage temperature (T_s), crystalline phase, chemical composition ([N]/[M] is ratio between nitrogen and metal content), lowest reported film electrical resistivity and the corresponding references are given. Me = methyl (CH_3), Et = ethyl (C_2H_5), Cp = cyclopentadienyl (C_6H_5), ‘-’ = ‘not specified’.

Material	Precursor	Co-reactant	Reactor	Substrate	Optimum T_s (°C)	Crystalline phase	[N]/[M]	C at.%	O at.%	Resistivity (Ωcm)	Refs.
TiN	$Ti(NMe_2)_4$	H_2 plasma	*r*	SiO_2/Si	250	δ-TiN	1.1	15	15	$7.0\cdot10^{-4}$	[1]
		N_2 plasma					1.3	5	5	$3.0\cdot10^{-4}$	
	$Ti(NMe_2)_4$	NH_3 plasma	*r*	SiO_2/Si	200	δ-TiN	1.0	<1	5	$1.8\cdot10^{-4}$	[2]
		NH_3 gas					0.5	9	37	$5.3\cdot10^{-2}$	
	$Ti(NMe_2)_4$	NH_3 plasma	*r*	SiO_2/Si	250	-	1.2	2	20	$1.2\cdot10^{-3}$	[3]
	$Ti(NMe_2)_4$	NH_3 gas	-	Si	200	-	1.0	5	20	$4.0\cdot10^{-3}$	[4]
ZrN	$Zr(NMe_2)_4$	NH_3 gas	-	Si	200	Zr_3N_4	1.3	<1	<2	$>10^{2}$	[5]
	$Zr(NMe_2)_4$	N_2/H_2 plasma	*r*	SiO_2/Si	150	-	-	-	-	$5.6\cdot10^{-4}$	[6]
	$Zr(NEt_2)_4$	N_2 plasma	*r*	Si	300	-	0.4	10	10	$4.0\cdot10^{-4}$	[7]

HfN	$Hf(NMe_2)_4$	NH_3 gas	-	Si	200	Hf_3N_4	1.3	<1	<2	$>10^{2}$	[5]
	$Hf(NMeEt)_4$	Ar/H_2 plasma	*d*	SiO_2/Si	250	δ-HfN	1.0	10.1	2	$2.3\cdot10^{-3}$	[8]
	$Hf(NMe_2)_4$	H_2 plasma	*d*	SiO_2/Si	175	δ-HfN	0.6	21	2	$6.7\cdot10^{-3}$	[9]
	$Hf(NMe_2)_4$	N_2 plasma	*r*	Si	250	Hf_3N_4	1.25	2	5	$>10^{2}$	[10]
	$HfCp(NMe_2)_3$	H_2 plasma	*r*	SiO_2/Si	450	δ-HfN	0.86	<2	20.1	$>10^{2}$	[11]
	$HfCp(NMe_2)_3$	H_2 plasma	*r+RF sub. bias*	SiO_2/Si	450	δ-HfN	1.0	11	<2	$3.3\cdot10^{-3}$	[12]
	$HfCp(NMe_2)_3$	Ar/H_2 plasma	*r+RF sub. bias*	SiO_2/Si	450	δ-HfN	0.85	8.4	<2	$4.1\cdot10^{-4}$	[13]
VN	$V(NEt_2)_4$	NH_3 gas	-	SiO_2/Si	190	-	0.4	6.3	-	$1.2\cdot10^{-4}$	[14]
	$V(NMeEt)_4$	NH_3 plasma	*r*	SiO_2/Si	150	δ-VN	1.0	<2	<2	$2.0\cdot10^{-4}$	[15]
NbN	$Nb(NMeEt)_3NCMe_3$	H_2 plasma	*r*	Si	350	-	0.8	<2	27.5	$9.0\cdot10^{-4}$	[16]
TaN	$Ta(NEt_2)_3NCMe_3$	N_2H_4 gas	-	SiO_2/Si	225	Ta_3N_5	0.8	<2	5	$>10^{2}$	[17]
	$Ta(NMe_2)_5$	H_2 plasma	*r*	Si	225	δ-TaN	0.45	12	8	$3.9\cdot10^{-4}$	[18]
	$Ta(NMe_2)_5$	NH_3 plasma	*r*	Si	225	Ta_3N_5	1.67	-	-	$>10^{2}$	[18]
MoN	$Mo(NMe_2)_2(NCMe_3)_2$	H_2 plasma	*r*	SiO_2/Si	150	γ-Mo_2N	<0.1	30	8	$1.7\cdot10^{-4}$	[19]

	$Mo(NCMe_3)_2(SCMe_3)_2$	H_2 plasma	*d*	SiO_2/Si	300	γ-Mo_2N	0.7	2.6	-	$3.5 \cdot 10^{-4}$	[20]
WN	$W(NMe_2)_2(NCMe_3)_2$	NH_3 gas	-	Si	300	-	1	<1	<2	$2.0 \cdot 10^{-3}$	[21]
	$W(NMe_2)_2(NCMe_3)_2$	N_2/H_2 plasma	*r*	SiO_2/Si	400	-	0.4	<1	8	$4.0 \cdot 10^{-4}$	[22]

References

1. Kim, J.Y., et al., *Remote plasma enhanced atomic layer deposition of TiN thin films using metalorganic precursor.* Journal of Vacuum Science and Technology A: Vacuum, Surfaces and Films, 2004. **22**(1): p. 8-12.
2. Musschoot, J., et al., *Atomic layer deposition of titanium nitride from TDMAT precursor.* Microelectronic Engineering, 2009. **86**(1): p. 72-77.
3. Kim, J.Y., et al., *Remote plasma-enhanced atomic-layer deposition of tiN by using TDMAT with a NH 3 plasma.* Journal of the Korean Physical Society, 2004. **45**(6): p. 1639-1643.
4. Tetsuro, H., et al., *Investigation of Thermal Stability of TiN Film Formed by Atomic Layer Deposition Using Tetrakis(dimethylamino)titanium Precursor for Metal-Gate Metal–Oxide–Semiconductor Field-Effect Transistor.* Japanese Journal of Applied Physics, 2010. **49**(4S): p. 04DA16.
5. Becker, J.S., E. Kim, and R.G. Gordon, *Atomic Layer Deposition of Insulating Hafnium and Zirconium Nitrides.* Chemistry of Materials, 2004. **16**(18): p. 3497-3501.
6. Muneshwar, T. and K. Cadien, *Low temperature plasma enhanced atomic layer deposition of conducting zirconium nitride films using tetrakis (dimethylamido) zirconium and forming gas (5% H2 + 95% N2) plasma.* Journal of Vacuum Science & Technology A: Vacuum, Surfaces, and Films, 2015. **33**(3): p. 031502.
7. Seungchan, C., et al., *Barrier Characteristics of ZrN Films Deposited by Remote Plasma-Enhanced Atomic Layer Deposition Using Tetrakis(diethylamino)zirconium Precursor.* Japanese Journal of Applied Physics, 2007. **46**(7R): p. 4085.
8. Consiglio, S., et al., *Plasma-assisted atomic layer deposition of conductive hafnium nitride using tetrakis(ethylmethylamino)hafnium for CMOS gate electrode applications.* Journal of the Electrochemical Society, 2008. **155**(3): p. H196-H201.
9. Kim, E.J. and D.H. Kim, *Highly conductive HfN x films prepared by plasma-assisted atomic layer deposition.* Electrochemical and Solid-State Letters, 2006. **9**(8): p. C123-C125.
10. Jeong, W., et al., *Characteristics of HfN films deposited by using remote plasma-enhanced atomic layer deposition.* Journal of the Korean Physical Society, 2010. **56**(3): p. 905-910.

11. Karwal, S., et al., *Plasma-assisted atomic layer deposition of HfNx: Tailoring the film properties by the plasma gas composition.* Journal of Vacuum Science and Technology A: Vacuum, Surfaces and Films, 2017. **35**(1).

12. Karwal, S., et al., *Low resistivity HfNx grown by plasma-assisted ALD with external rf substrate biasing.* Journal of Materials Chemistry C, 2018. **6**(15): p. 3917-3926.

13. Karwal, S., et al., *Plasma-assisted ALD of highly conductive HfNx: on the effect of energetic ions on film microstructure.* to be submitted.

14. Mayumi, B.T., et al., *Atomic Layer Deposition of Thin VN x Film from Tetrakis(diethylamido)vanadium Precursor.* Japanese Journal of Applied Physics, 2011. **50**(5S1): p. 05EA06.

15. Rampelberg, G., et al., *Low temperature plasma-enhanced atomic layer deposition of thin vanadium nitride layers for copper diffusion barriers.* Applied Physics Letters, 2013. **102**(11): p. 111910.

16. Hinz, J., A.J. Bauer, and L. Frey, *Analysis of NbN thin film deposition by plasma-enhanced ALD for gate electrode application.* Semiconductor Science and Technology, 2010. **25**(7): p. 075009.

17. Burton, B.B., A.R. Lavoie, and S.M. George, *Tantalum nitride atomic layer deposition using (tert-butylimido) tris(diethylamido)tantalum and hydrazine.* Journal of the Electrochemical Society, 2008. **155**(7): p. D508-D516.

18. Langereis, E., et al., *Synthesis and in situ characterization of low-resistivity Ta Nx films by remote plasma atomic layer deposition.* Journal of Applied Physics, 2007. **102**(8).

19. Bertuch, A., et al., *Plasma enhanced atomic layer deposition of molybdenum carbide and nitride with bis(tert-butylimido)bis(dimethylamido) molybdenum.* Journal of Vacuum Science & Technology A: Vacuum, Surfaces, and Films, 2017. **35**(1): p. 01B141.

20. Jang, Y., et al., *Highly-conformal nanocrystalline molybdenum nitride thin films by atomic layer deposition as a diffusion barrier against Cu.* Journal of Alloys and Compounds, 2016. **663**(Supplement C): p. 651-658.

21. Becker, J.S., et al., *Highly Conformal Thin Films of Tungsten Nitride Prepared by Atomic Layer Deposition from a Novel Precursor.* Chemistry of Materials, 2003. **15**(15): p. 2969-2976.

22. Sowa, M.J., et al., *Plasma-enhanced atomic layer deposition of tungsten nitride.* Journal of Vacuum Science & Technology A: Vacuum, Surfaces, and Films, 2016. **34**(5): p. 051516.

Chapter 3

Plasma-assisted ALD of HfN_x: Tailoring the film properties by the plasma gas composition*

Abstract

We synthesized HfN_x ($x \geq 1$) thin films by plasma-assisted atomic layer deposition (ALD) at stage temperatures of 350°C-450°C by using the high-thermal-stability $CpHf(NMe_2)_3$ monomer as Hf precursor and either H_2 plasma or N_2 plasma as co-reactant. Most notably, the selection of the plasma gas composition enabled us to tune the film properties: films fabricated using N_2 plasma led to formation of highly resistive and amorphous Hf_3N_4 films ($6 \cdot 10^2$ Ωcm), while the use of the strongly reducing H_2 plasma generated conductive (resistivity of $6 \cdot 10^{-1}$ Ωcm) films with the signature of the δ-HfN fcc crystal structure. Via X-ray photoelectron spectroscopy, we observed that the use of the H_2 plasma facilitates the reduction of the oxidation state of Hf from Hf(IV) to Hf(III). This result was corroborated by the simultaneous increase in the free carrier absorption observed in the infrared range via spectroscopic ellipsometry. The δ-HfN_x films fabricated via the present route are promising as highly reflective back contacts for thin films solar cells, Cu diffusion barriers and as a gate metal for MOS capacitors, provided that the resistivity values can be further decreased by suppressing the formation of the resistive Hf_2ON_2 impurity phase and grain-boundary scattering of the charge carriers.

*Saurabh Karwal, Benjamin L. Williams, Janne-P Niemelä, Marcel A. Verheijen, Wilhelmus M. M. Kessels and Mariadriana Creatore, J. Vac. Sci. Technol. A 35, 01B129 (2017)

3.1 Introduction

Transition metal nitrides (TMNs) are of great interest for semiconductor devices owing to their low electrical resistivity and excellent oxygen [1] and copper diffusion barrier properties [2-4]. Two envisioned applications are the combination of HfO_2 with HfN as gate dielectric and gate metal in a MOS configuration as reported by Yu *et al.* [1, 5] and HfN as back reflector electrode for CIGS solar cells, due to its high reflectivity (>85%) in the low energy photon region (1 eV ≤ hv ≤ 2.4 eV) for semi-infinite films [6-8]. Both applications require low resistivity of HfN layers ($\rho = 10^{-4} – 10^{-5}$ Ωcm) [9].

Low resistivity epitaxial single crystal fcc δ-HfN films have been developed by physical vapour deposition (PVD) with a resistivity of $1.4 \cdot 10^{-5}$ Ωcm for a thickness of 650 nm [10]. Moreover, chemical vapour deposition (CVD) of δ-HfN_x at a stage temperature of 800°C employing akylamide Hf precursor and N,N-dimethylhydrazine as reducing agent led to a grain size of ~170 nm and a resistivity of $1 \cdot 10^{-3}$ Ωcm for a film thickness of ~1 µm [11]. An increase in the stage temperature was shown to increase the film conductivity and was attributed to an increase in crystallinity and grain size [11]. In the same work, NH_3 was demonstrated to yield non-conductive Hf_3N_4 films marking the requirement of a highly reducing co-reactant (N,N-dimethylhydrazine) to obtain the conductive δ-HfN_x films [11].

Many of the applications mentioned above require conformal films on 3D structured surfaces with precise thickness control. Supreme thickness controllability and conformality achieved by ALD has been demonstrated on high surface area materials such as silica gel [12-15], and nanopowders [16-18]. Some works on ALD of HfN_x have already been reported in the literature [19-21] and are summarized in the Table 3.1 below. Becker *et al.* reported the growth of insulating Hf_3N_4 films by employing TEMAH as the precursor and NH_3 as the co-reactant in a thermal ALD process, demonstrating the low reduction potential of NH_3 [19]. Note that thermal decomposition of TEMAH was observed at a stage temperature above 250°C [19]. On the other hand, low resistivity δ-HfN_x films ($2.3 \cdot 10^{-3}$ Ωcm) were obtained by Consiglio *et al.* using Ar-H_2 mixed plasma and the same precursor (TEMAH) in a plasma-assisted ALD processes [20]. Using TDMAH, similar results were also reported by Kim *et al.* with a N_2-H_2 mixed plasma yielding a resistivity of $6.7 \cdot 10^{-3}$ Ωcm for 14 nm film [21]. These studies demonstrate the requirement of highly reducing H_2 plasma species to achieve the conductive fcc δ-HfN phase [20, 21].

Table 3.1. Overview of HfN_x film properties as reported for some ALD processes using several metal precursors and co-reactants. The selected reports are chosen in order to highlight the importance of reductive H_2 plasma essential to fabricate δ-HfN_x fcc phase.

Hf precursor	Co-reactant	Stage temperature (°C)	N/Hf	C (at.%)	O (at.%)	Resistivity (Ωcm)	GPC (nm/cycle)	Ref.
TEMAH $Hf[N(CH_3)(C_2H_5)]_4$	NH_3	200	1.3	0.5	5	$>10^2$	0.11-0.12	[19]
TEMAH $Hf[N(CH_3)(C_2H_5)]_4$	15s Ar-H_2 plasma	250	1	10.1	2.2	$2.3\cdot10^{-3}$	0.12	[20]
TDMAH $Hf[N(CH_3)_2]_4$	60s H_2-N_2 plasma	175	0.6	21	2	$6.7\cdot10^{-3}$	0.085	[21]

The extent of Hf(IV) reduction (in the precursor) to Hf(III) (in the film) by H_2 plasma species was not specifically addressed, and thus far, a comprehensive study of the influence of variable plasma conditions and gas composition on the chemical, microstructural and optical material properties of HfN_x thin films is lacking. Furthermore, the deposition of the HfN_x films has been limited to rather low temperatures due to the thermal self-decomposition of the used homoleptic alkylamide precursors for Hf. Fortunately, the alkylamide precursor chemistry can be tailored by replacing one of the original ligands with a cyclopentadienyl ligand (Cp = C_5H_5). In such heteroleptic precursors the Cp functional group imparts high thermal stability to the precursor, thus enabling a larger temperature window while minimizing precursor decomposition [22].

In this contribution, we studied the effect of plasma gas composition for the plasma-assisted ALD of HfN_x at 350°C and 450°C by adopting a thermally stable novel heteroleptic metal precursor tris(dimethylamino)cyclopentadienylhafnium [$CpHf(NMe_2)_3$] [TDMACpH] and using it together with H_2 or N_2 -fed plasma as the co-reactant. In particular, a detailed study on the influence of plasma gas composition on the opto-electronic, chemical and micro-structural properties is presented. The material properties were shown to fundamentally depend on the plasma composition: highly resistive (ρ = $6\cdot10^2$ Ωcm) amorphous Hf_3N_4 films are obtained by using N_2 plasma, whereas use of highly reducing H_2 plasma enables synthesis of conductive (ρ = $6\cdot10^{-1}$ Ωcm) δ-HfN_x films. Using X-ray photoelectron spectroscopy, these improved film properties for the H_2 plasma are shown to

stem from a large increase in Hf(III)/(Hf(III)+ Hf(IV)) fraction. In addition, the factors limiting the film conductivity were identified and quantified.

3.2 Experimental section

I. Film deposition

HfN_x thin films of ~50 nm in thickness were deposited on 100 mm Si(100) substrates with 450 nm SiO_2 using an Oxford Instruments FlexAL ALD reactor [23, 24], equipped with an inductively coupled remote plasma (ICP) source with an alumina dielectric tube. The deposition chamber of the ALD reactor was pumped down by a turbo-molecular pump to a base pressure of $1.6{\cdot}10^{-6}$ Torr before every deposition and thereafter the substrate was transferred to the chamber from the load-lock. The stage temperature was controlled in the range 350°C - 450°C and the reactor walls were maintained at 145°C during all the depositions. Note that via SE, a substrate temperature of 270°C and 340°C was measured for a stage temperature 350°C and 450°C, respectively [23].

The Hf precursor TDMACpH [$CpHf(NMe_2)_3$] (Air Liquide, >99.99% purity) was placed in a stainless steel container kept at 60°C and bubbled by an Ar flow of 100 sccm. During the precursor dosage, an Ar flow rate of 100 sccm was also injected from the ICP chamber in order to suppress the deposition on the ICP tube, thereby setting up the chamber pressure of 200 mTorr as illustrated in Figure 3.1. Furthermore, during the plasma exposure, N_2 (>99.999% purity, working pressure ~12 mTorr) or H_2 (>99.999% purity, working pressure ~30 mTorr) was first introduced into the chamber and thereafter the plasma was ignited for the desired exposure time. The excess precursor, reaction byproducts and plasma species were purged with Ar at 200 sccm with full valve opening. The ALD step sequence is presented in Figure 3.1 including the optimum exposure times for the N_2 and H_2 plasma cases.

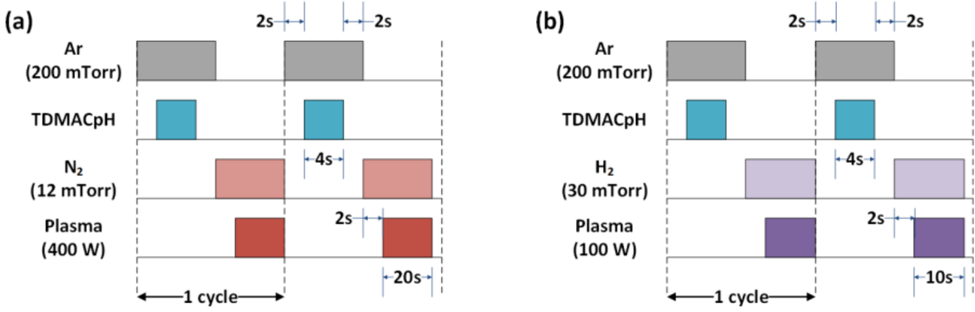

Figure 3.1. Time sequence for two complete ALD cycles of HfN_x based on (a) N_2 plasma and (b) H_2 plasma. Time intervals are not drawn to scale.

II. Film analysis

Spectroscopic ellipsometry (SE) was employed to monitor the ALD growth every 10 ALD cycles. Pseudo-dielectric functions were determined in the photon energy range of 0.75-5.0 eV by employing a visible and near-infrared rotating compensator ellipsometer (J.A. Woollam, Inc., M2000U) fitted to two optical viewports on the reactor. Subsequently, a model was set up for HfN_x films on SiO_2 (450 nm)/c-Si substrates. In addition to the HfN_x film thickness, key material parameters such as optical resistivity and optical bandgap could be extracted by parametrizing the complex dielectric function $\varepsilon = \varepsilon_1 + i\varepsilon_2$ [25, 26].

High resistivity Hf_3N_4 with an N/Hf ratio of 1.3 behaves as an insulator [27], for which the imaginary dielectric function (ε_2^{T-L}) can be described by a Tauc-Lorentz relation [26]:

$$\varepsilon_2^{T-L}(E) = \begin{cases} \dfrac{AE_oC\left(E-E_g\right)^2}{(E^2-E_o^2)^2+C^2E^2}\cdot\dfrac{1}{E};\ \left(E>E_g\right) \\ 0;\ \left(E\le E_g\right) \end{cases} \quad (1)$$

where A is the peak amplitude, E_o is the natural transition energy, E_g is the band gap, C is the full width half maximum (FWHM) of the ε_2 peak and E represents the photon energy. Then, once the imaginary part is known, the real part of the dielectric function (ε_1^{T-L}) can be deduced using the Kramers-Kronig relation:

$$\varepsilon_1^{T-L}(\omega) = 1 + \frac{2}{\pi} P \int_0^{\infty} \frac{\omega' \varepsilon_2(\omega')}{\omega'^2 - \omega^2} d\omega' \quad (2)$$

where P is the Cauchy principle value, ω' is the complex angular frequency and ε_2 is the imaginary dielectric function as defined above.

On the other hand, the resistivity of the epitaxial fcc δ-HfN thin films can be as low as 14.2 μΩcm [10] and can be modelled by a combinatorial approach using one Drude and two Lorentz oscillators as described by Hu *et al.* [7]. In our case, due to the coexistence of two phases, δ-HfN_x (x≤1) and Hf_2ON_2, the dielectric function can be modelled using one Drude, one Lorentz and one Tauc-Lorentz oscillator:

$$\varepsilon(E) = \varepsilon_1(E) + i\varepsilon_2(E) = \varepsilon_\infty - \overbrace{\frac{E_p^2}{E^2 - i\Gamma_D E}}^{Drude} + \overbrace{\frac{S E_0^2}{E_0^2 - E^2 + iE\Gamma}}^{Lorentz} + \overbrace{\varepsilon_1^{T-L} + i\varepsilon_2^{T-L}}^{Tauc-Lorentz} \quad (3)$$

where, ε_∞ represents transitions at higher energy which are not accounted in Lorentz oscillators, E_p is plasma energy and Γ_D is the damping factor for Drude oscillator. The Lorentz oscillator is centered at E_o which corresponds to the resonance frequency, while S indicates the strength of the oscillator and Γ is the damping factor for the Lorentz oscillator.

The deposited films were analyzed by X-ray photoelectron spectroscopy (XPS) using a Thermoscientific K-Alpha KA1066 system equipped with a monochromatic Al Kα ($h\nu$ = 1486.6 eV) source in order to determine the composition of the HfN_x layers. The films were first sputtered for 500 s by 200 eV Ar^+ ion gun prior to taking high resolution (pass energy = 50 eV) scans, in order to exclude the surface oxidation and adventitious carbon. Samples were continuously subjected to an electron flood gun during measurements in order to compensate for the charging. The sensitivity factors used for different elements in order to determine the chemical composition of HfN_x films were obtained from the Thermoscientific Avantage library [28].

The crystallinity of the films was studied by grazing-incidence X-ray diffraction (GIXRD). The experiments were conducted with a PanAlytical X'pert PRO MRD diffractometer operated at the incidence angle of 0.5° and using a Cu Kα (λ = 1.542 Å) X-ray source. The sheet resistance values (R_s) of HfN_x films deposited on 450 nm SiO_2/Si were determined by four-point probe measurements, using a Keithley 2400 SourceMeter and a Signaton probe. Electrical resistivity (ρ_e) at room temperature could subsequently be calculated using the film thickness deduced from SE modeling. The surface morphology was studied by scanning electron microscopy (SEM) using a ZeissSigma Nanolab operating at an acceleration voltage of 2 kV.

3.3 Results and discussion

I. ALD process with N_2 plasma

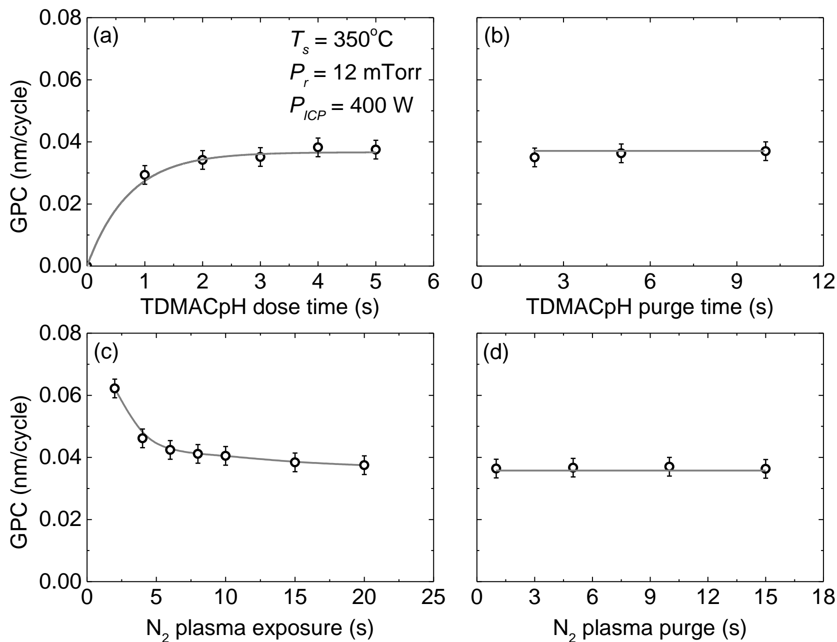

Figure 3.2. Growth-per-cycle (GPC) for the ALD process using N_2 plasma as the co-reactant as a function of (a) TDMACpH dose, (b) TDMACpH purge, (c) N_2 plasma exposure time, (d) N_2 plasma purge. On the basis of these results, a dosage sequence of 4-2-20-2 s was established for the ALD process with N_2 plasma. The gray lines serve as a guide to the eye.

The saturation of the growth-per-cycle (GPC) was studied at a stage temperature of 350°C by systematically varying the process parameters, i.e., TDMACpH dose, TDMACpH purge, N_2 plasma exposure, and N_2 plasma purge (Figure 3.2). Note that for all the depositions, a typical linear growth with no nucleation delay as a function of the number of ALD cycles was retrieved from in-situ SE (appendix, Figure A3.1).

During the variation of the TDMACpH dosing time, the N_2 plasma exposure was set to 20 s. Saturation of the GPC to a value of 0.038 nm/cycle was attained after 2 s of TDMACpH dosing (Figure 3.2a) and hence, a TDMACpH pulsing of 4 s was adopted for subsequent experiments. Purging of the unreacted species and reaction byproducts was found to be fast, as 1-2 s were already sufficient to obtain saturated growth (Figure 3.2b,d).

Table 3.2. The GPC and C at.% as a function of N_2 plasma exposure for the HfN_x films prepared at T_s = 350°C. The carbon content is retrieved via XPS and the GPC is obtained via SE. The corresponding error bars are indicated in the first row.

N_2 plasma exposure (s)	Thickness (nm)	GPC (nm/cycle)	C (at.%)
5	17.2	0.043±0.003	13.0±0.5
10	16.0	0.040	10.0
15	15.2	0.038	8.2
20	15.2	0.038	7.0

On the other hand, a peculiar decrease in the GPC with the increase in the N_2 plasma exposure was observed (Figure 3.2c). A very similar decrease in the GPC as a function of N_2 plasma exposure during the ALD of SiN_x was reported by Knoops *et al.*, attributed to the decrease in the C at.% [23]. In our case, closer inspection via X-ray photoelectron spectroscopy (XPS) revealed a relative decrease in the C at.% from 13 at.% for 5 s of N_2 plasma exposure to 7 at.% for 20 s of exposure (Table 3.2). It should be emphasized that C in the film results from either the re-deposition of the ligands that are dissociated in the plasma if the gas residence time is long [24] or from the incomplete removal of ligands by the N radicals. In order to verify whether the re-deposition is indeed occurring at T_s = 350°C, the gas residence time was systematically varied in a limited range (0.10 – 0.14 s) by adding Ar to the total gas flow during the plasma step (only for this experiment) (appendix, Table A3.1) and its effect on the GPC and C at.% was studied in a

similar fashion as reported by Knoops *et al.* [24]. A constant GPC and C at.% was obtained for 20 s of plasma exposure even for short residence time (0.10 s). This result suggests that the residual C of 7 at.% is due to the incomplete removal of the ligands at T_s = 350°C.

The decomposition of TDMACpH was observed at a stage temperature above 360°C for the thermal ALD process of HfO_2 with H_2O [29]. In our case, the self-limiting ALD obtained at a stage temperature of 350°C (substrate temperature = 270°C) suggests that we are well below the thermal decomposition temperature of TDMACpH. Subsequently, the stage temperature was raised to 450°C, which corresponds to a substrate temperature of 340°C as concluded from SE [29]. An increase in the stage temperature to 450°C enabled complete removal of C (Table 3.3), while maintaining a constant GPC of 0.038 nm/cycle for 20 s N_2 plasma exposure. This result corroborates that the 7 at.% residual C obtained at T_s = 350°C is a result of incomplete removal of ligands by N radicals.

Table 3.3. The properties of the ALD HfN_x films prepared using TDMACpH [$CpHf(NMe_2)_3$] for different deposition conditions. The chemical composition is determined by XPS, the resistivity by four-point probe and the thickness and GPC via SE. The corresponding error bars are indicated in the first row. The errors for the resistivity are less than 3% of their value.

Plasma condition	Stage temperature (°C)	N/Hf	C (at.%)	O (at.%)	Hf(III) / Hf(III)+Hf(IV)	Resistivity (Ωcm)	GPC (nm/cycle)	Thickness (nm)
20 s N_2	350	1.5±0.1	7.0±0.5	2.0±0.3	0.37±0.02	$7\cdot10^{2}$	0.038±0.003	35
20 s N_2	450	1.6	0	2.0	0.35	$6\cdot10^{2}$	0.038	45
10 s H_2	450	1.0	0	15.3	0.59	$6\cdot10^{-1}$	0.04	63
30 s H_2	450	1.0	0	20.2	0.53	$9\cdot10^{-1}$	0.04	33

The N_2 plasma process generated films with a high resistivity of $6\cdot10^2$ Ωcm for a film thickness ~45 nm at T_s = 450°C, measured via four-point probe. A closer inspection via XPS revealed a relatively high N/Hf ratio of 1.6±0.03 (Table 3.3). XPS was further used to study the oxidation state fraction Hf(III)/(Hf(III)+ Hf(IV)). In Figure 3.3a, the Hf 4f spectrum is presented: the Hf 4f7/2 peak centered at low binding energy of 14.9 eV is attributed to the Hf-N bond in *δ*-HfN. This peak is assigned as Hf(III), corresponding to the presence of the Hf(III) oxidation state

(Table 3.4) [30]. It should be noted that the spin orbit coupling of Hf 4f give rise to a doublet: Hf 4f7/2 and Hf 4f5/2, which is utilized in the peak deconvolution.

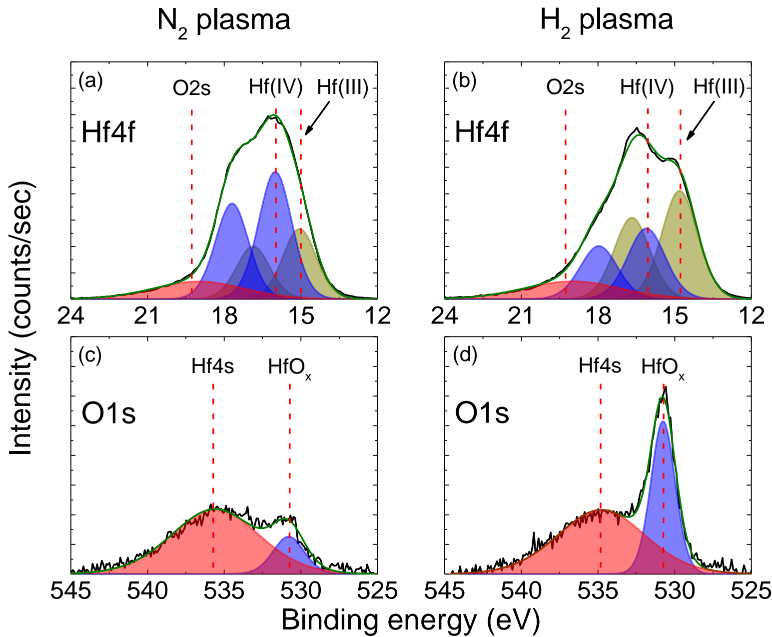

Figure 3.3. The Hf 4f XPS spectra depicting the peak deconvolution for (a) ~45 nm HfN_x deposited using the N_2 plasma at T_s = 450°C and (b) ~63 nm HfN_x deposited using 10 s H_2 plasma exposure at T_s = 450°C. The deconvoluted O 1s spectra for (c) N_2 plasma and (d) H_2 plasma.

Table 3.4. The corresponding XPS peak assignment, binding energies and full width half maximum for the Hf and O spectral lines used to de-convolute the peaks.

Spectral line	Peak assignment	Binding energy (eV)	FWHM (eV)	Ref.
Hf 4f7/2	Hf(IV)	16.0	1.6	[31, 32]
Hf 4f5/2	Hf(IV)	17.8	1.6	[31, 32]
Hf 4f7/2	Hf(III)	14.9	1.6	[34]
Hf 4f5/2	Hf(III)	16.7	1.6	[34]
O 1s	HfO_x	530.8	1.9	[33]

Kang *et al.* reported a Hf 4f7/2 peak shift to a higher binding energy of 16.0 eV due to the presence of O and the formation of HfN_xO_y [31]. Moreover, Arranz *et al.* reported the Hf 4f7/2 peak to be centered at 16.0 eV in the case of highly resistive Hf_3N_4 phase [32]. In both the above cases, the Hf 4f7/2 peak at 16.0 eV corresponds to the Hf(IV) oxidation state. Correspondingly, in our case, the Hf 4f7/2 peak at 16.0 eV has been assigned to Hf(IV) although the demarcation of the individual contributions of either Hf_3N_4 or HfO_xN_y is not possible due to overlap of the peaks (Table 3.4). In Figure 3.3c, the O 1s XPS spectrum is presented which consists of a small peak at 530.8 eV [33], corresponding to the Hf-O bond formation and a broad Hf 4s overlapping feature at 535.5 eV (Table 3.4). As a result of the formation of the Hf-O bond, the Hf oxidation state increases to +4. Altogether, it can be concluded that the N_2 plasma process yielded films with a low relative Hf(III) fraction of 0.35±0.02 (Table 3.3). The small peak area of Hf-O bond accounts for only ~2 at.% [O] in the films, suggesting that the low Hf(III) fraction is primarily related to the low reduction potential of N_2 plasma.

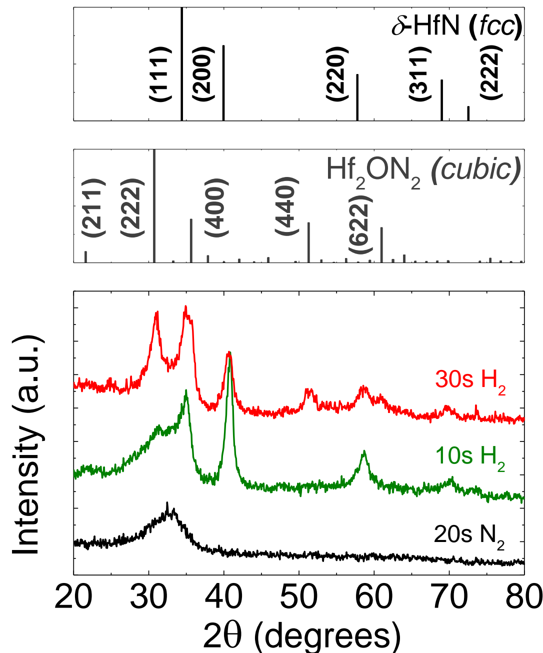

Figure 3.4. The GI-XRD spectra for the HfN_x films prepared by various ALD processes: the N_2 plasma process and the H_2 plasma process with varying exposure times. The powder δ-HfN_x and Hf_2ON_2 XRD spectra are shown for comparison.

The results of the X-ray diffraction studies were in line with the XPS studies. The N_2 plasma process generated amorphous films as no crystalline peak was observed (Figure 3.4). Moreover, only a broad feature was seen at 2θ = 33.6°. Wang *et al.* reported the presence of a broad feature at 2θ = 33.5° for N-rich $HfN_{1.39}$ films [34]. Hence for our films, the broad feature was attributed to over-stoichiometric $HfN_{1.6}$, thus corroborating the XPS results.

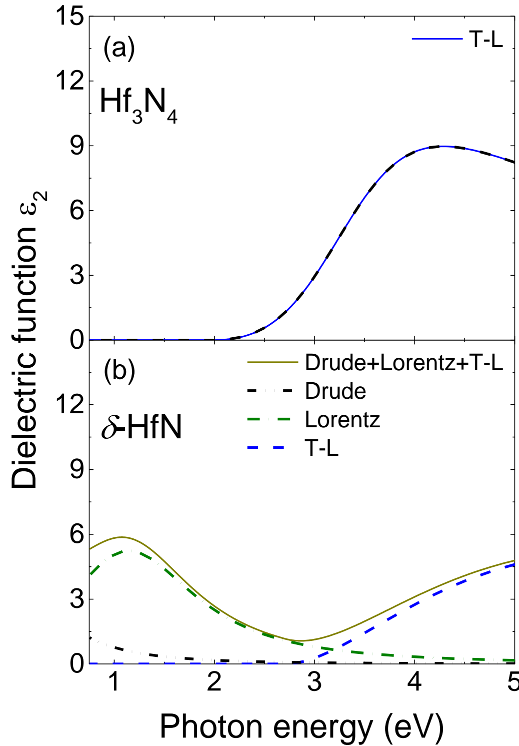

Figure 3.5. Imaginary dielectric function ε_2 for (a) the resistive Hf_3N_4 films prepared by the N_2 plasma process obtained via parameterization of the spectroscopic ellipsometric data using one Tauc-Lorentz oscillator, and (b) the conductive δ-HfN (x≤1) films prepared by the H_2 plasma process obtained via parameterization using one Drude, one Lorentz and one Tauc-Lorentz (T-L) oscillator.

The high film resistivity of the films ($6\cdot10^2$ Ωcm) is also reflected in the dielectric functions, obtained via the modeling of the spectroscopic ellipsometry data using a single Tauc-Lorentz (T-L) oscillator centered at 3.86 eV (Figure 3.5a). The Tauc-Lorentz behavior of the ε_2 is in-line with earlier reported optical studies

for Hf_3N_4 resistive phase in the given photon energy range [27]. Furthermore, the Tauc-Lorentz oscillator gives a band-gap of 2.26 eV which further corroborates the insulating properties of the material.

Altogether, the high resistivity of the films prepared with the N_2 plasma process is attributed to a relative over-stoichiometric $HfN_{1.6}$ phase with a small Hf(III) fraction, given the fact that the films only contain trace amounts of C and O as impurities. Furthermore, a low O content of 2 at.% is believed to be obtained for the N_2 plasma process due to the presence of a small Hf(III) fraction. In order to form an Hf-O bond, the oxidation state of Hf should increase from +3 to +4. Since a small Hf(III) fraction of 0.35±0.02 is obtained due to the low reduction potential of the N_2 plasma, the films are less susceptible to be oxidized by O.

II. ALD process with H_2 plasma

In the case of the H_2 plasma process, the GPC increased with the increase in plasma exposure using TDMACpH dosing of 4 s and a saturated GPC of 0.04 nm/cycle was obtained for a plasma exposure of 10 s or longer (Figure 3.6). Langereis *et al.* reported a soft-saturation in the GPC for the ALD of TaN_x using PDMAT and H_2 plasma [35], where the GPC continued to slightly increase after attaining a saturation for a plasma exposure of 5 s. This increase in the GPC after saturation is primarily attributed to the change in the N/Ta ratio with plasma exposure [35]. XPS studies of the HfN_x films revealed that the N/Hf ratio is consistent with the increase in plasma exposure whereas the material properties change due to an increase in the O at.% with the plasma exposure. The O content increased from 15.3 at.% to 20.2 at.% as the H_2 plasma exposure was increased from 10 s to 30 s respectively (Table 3.3). Note that the O in the film can result from either the ingress of H_2O or O_2 from the reactor background during the deposition, or from the post-deposition oxidation of the films which might arise due to potentially low film density. In order to demarcate the source of O in the HfN_x films, a thin layer of dense SiN_x (~10 nm) was deposited on top of the HfN_x film (~30 nm) in-situ, following the same recipe as reported by Andringa *et al.* for the deposition of gas/moisture barrier layers [36]. A decrease in the O content to 10.2 at.% was observed for the HfN_x films prepared with 10 s H_2 plasma exposure and SiN_x capping layer implying that the O primarily incorporates during the deposition itself. This can occur due to the background H_2O and/or O_2 (reactor base pressure = $1.6 \cdot 10^{-6}$ Torr) in the reactor which can get incorporated during the film growth for the complete cycle time, depending on the reactivity of the growing surface. Quite remarkably, an increase in the Hf(III)/(Hf(III) + Hf(IV)) fraction to 0.59±0.02 was observed via XPS for 10 s of plasma exposure as compared to the N_2 plasma process (Figure 3.3b). Due to the increased Hf(III)

oxidation state fraction as compared to the N_2 plasma process, the electrical resistivity decreased from $6\cdot10^{2}$ Ωcm prepared with the N_2 plasma process to $6\cdot10^{-1}$ Ωcm for 63 nm thick film prepared with 10 s H_2 plasma exposure.

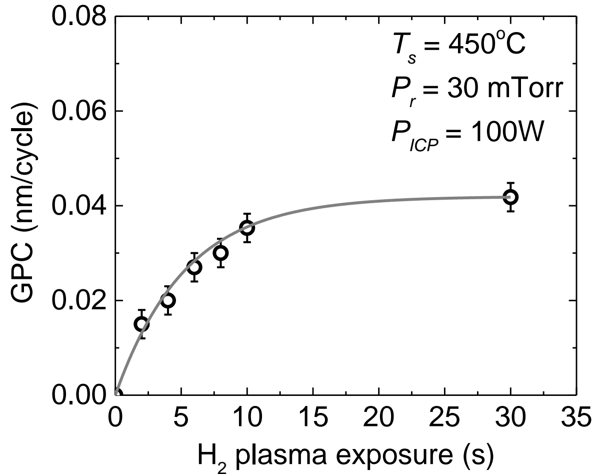

Figure 3.6. Growth-per-cycle (GPC) for the ALD process using H_2 plasma as the co-reactant as a function of H_2 plasma exposure time. The gray line serves as a guide to the eye.

The X-ray diffractogram revealed the development of the conductive δ-HfN fcc structure for the H_2 plasma process, in line with the decrease in electrical resistivity and the results from the XPS studies (Figure 3.4). Moreover, a shift in the peak position was observed for δ-HfN pattern when compared with the powder spectrum, as a result of the incorporation of O. In addition, a new peak could be discerned at 2θ = 31° for 30 s H_2 plasma exposure. This peak can be attributed to the (222) reflection of the resistive, cubic Hf_2ON_2 structure (Figure 3.4) [34], in-line with the XPS study suggesting Hf-O bond formation.

Although a polycrystalline δ-HfN fcc conductive phase is obtained, an electrical resistivity of $6\cdot10^{-1}$ Ωcm is rather high. In order to obtain more insight into the electrical properties, modelling of the SE data was performed. The dielectric function could be fitted with one Drude, one Lorentz oscillator centered at 1.41 eV and one Tauc-Lorentz oscillator centered at 4.88 eV as shown in Figure 3.5b. The Tauc-Lorentz oscillator reveals a band-gap of 2.7 eV which is higher as compared to 2.26 eV for the N_2 plasma process. This increase in the optical bandgap most probably arises due to the presence O in the form of Hf-O bonds.

The simultaneous presence of the Tauc-Lorentz and the Drude contributions indicates the synthesis of a mixed phase material composed of both conductive and resistive domains. The presence of the Drude absorption signifies the presence of free electrons contributing to the conductivity [37]. The optical resistivity can be deduced from the Drude absorption using:

$$\rho = \frac{\Gamma_D}{\varepsilon_o \cdot \omega_p^2} \quad (4)$$

where Γ_D is the damping factor for the Drude oscillator, ε_o is the permittivity of free space, ω_p is the plasma frequency and ρ is the resistivity of the deposited films as determined by SE. By using this equation, we obtained an optical resistivity of $5 \cdot 10^{-3}$ Ωcm – a value that is notably lower than the electrical resistivity value obtained via the four-point probe. The discrepancy between optical and electrical resistivity signifies prominent grain boundary (GB) scattering which dictates the electrical conductivity of the films [37]. In the simplified case with O in the films existing only in the Hf_2ON_2 lattice, 15 at.% O for 10 s H_2 plasma exposure would imply 75 at.% of Hf_2ON_2 and 25 at.% HfN. This result contradicts the Hf(III) fraction of 0.59±0.02, signifying that only a fraction of O exits in the Hf_2ON_2 lattice. Therefore it is expected that O is primarily bonded to Hf on the defect sites such as grain boundaries which can lead to prominent GB scattering. Furthermore, Hf-O bond formation would warrant an increase in the oxidation state of Hf to +4 which subsequently quenches the free electron density and limits the conductivity.

A scanning electron microscope (SEM) image is shown in Figure 3.7a reveals a lateral grain size of (24.5±2.5) nm for 63 nm thick film prepared with 10 s H_2 plasma exposure. This grain size increases with thickness due to the grain growth as apparent a from cross-sectional image (Figure 3.7b). The small grain size obtained via SEM, together with formation of resistive Hf-O bond further corroborates prominent grain-boundary scattering of the free electrons.

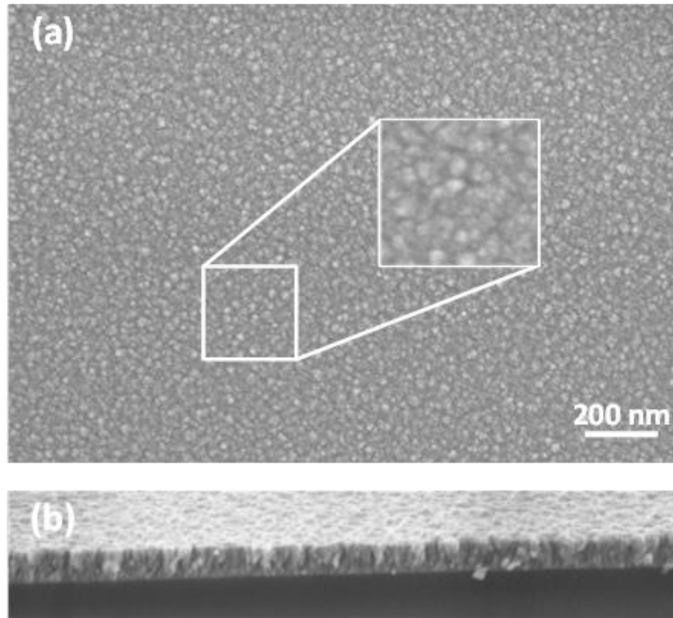

Figure 3.7. (a) Top-view and (b) cross-sectional SEM image for approx. 63 nm HfN_x film deposited by 10 s H_2 plasma exposure at T_s = 450°C. The images reveal a V-shaped grain growth mechanism [38].

Altogether, H_2 plasma is capable of efficiently reducing the Hf(IV) oxidation state to Hf(III), which is required to generate the conductive δ-HfN fcc structure. However, a limited conductivity is obtained due to the prominent grain-boundary scattering. Therefore, in order to further improve the conductivity of the HfN_x films (10^{-4} – 10^{-3} Ωcm), either the O should be reduced which would therefore promote the presence of the Hf(III) fraction [20, 21] and/or the grain size has be to increased.

3.4 Conclusions

A plasma-assisted ALD process for HfN_x thin films has been introduced and investigated using a novel metal precursor $CpHf(NMe_2)_3$ and a N_2 or H_2 plasma as the co-reactant. The growth-per-cycle and the material properties, such as chemical composition, electrical resistivity, optical properties and crystal structure, were presented in light of the reducing character of the chosen plasma gas. In case of the N_2 plasma, the films grown at stage temperatures of 350°C and 450°C showed a growth-per-cycle of 0.038 nm/cycle. An increase in the stage temperature from 350°C to 450°C led to a decrease in carbon content from 7 at.%

to below the XPS detection limit, for the N_2 plasma process. However, the N_2 plasma was found inefficient in reducing the Hf(IV) oxidation state to Hf(III), leading to high resistivity values of $6 \cdot 10^2$ Ωcm.

The process employing H_2 plasma as the co-reactant yielded conductive stoichiometric, fcc δ-HfN films. For this process, a higher Hf(III)/(Hf(III) + Hf(IV)) fraction of 0.59 was obtained which can be attributed to the high reduction potential of H_2 plasma species. The H_2 plasma based process markedly improved the electrical resistivity down to a value of $6 \cdot 10^{-1}$ Ωcm. We identified two predominant reasons for the yet limited conductivity. First, the presence of O, up to 15 at.% was observed for 10 s H_2 plasma exposure: O induces the formation of the resistive Hf_2ON_2 impurity phase. Second, prominent grain-boundary scattering as concluded from the discrepancy between the optical in-grain resistivity ($5 \cdot 10^{-3}$ Ωcm) and the electrical inter-grain resistivity ($6 \cdot 10^{-1}$ Ωcm) values accompanied with the small grain size of (24.5±2.5) nm.

In light of the results obtained in this study, we have demonstrated that the low Hf(III)/(Hf(III) + Hf(IV)) fraction is a bottleneck for the film conductivity, which is attributed to either the low reduction potential of the N_2 plasma or high O content in the case of H_2 plasma process. In the case HfN_x films reported earlier [20, 21], very low O at.% can justify the realization of conductive δ-HfN films with low resistivity. Furthermore, the presence of high C at.% leading to formation of Hf-C (Table 3.1) would not increase the resistivity, since Hf-C is a conductive phase [39]. In conclusion, highly reducing co-reactant is entailed in order to obtain conductive δ-HfN fcc crystal system. The Hf(III) oxidation state has high affinity towards O and therefore reduction of O impurity content is a requirement to further lower the resistivity of the films.

References

1. Yu, H.Y., M.F. Li, and D.L. Kwong, *Thermally robust HfN metal as a promising gate electrode for advanced MOS device applications.* IEEE Transactions on Electron Devices, 2004. **51**(4): p. 609-615.

2. Jeong, W., et al., *Characteristics of HfN films deposited by using remote plasma-enhanced atomic layer deposition.* Journal of the Korean Physical Society, 2010. **56**(3): p. 905-910.

3. Hu, C.K. and J.M.E. Harper, *Copper interconnections and reliability.* Materials Chemistry and Physics, 1998. **52**(1): p. 5-16.

4. Kim, H., et al., *Diffusion barrier properties of transition metal thin films grown by plasma-enhanced atomic-layer deposition.* Proceedings of the

29th Conference on the Physics and Chemistry of Semiconductor Interfaces, 2002. **20**(4): p. 1321-1326.

5. Yu, H.Y., et al., *Robust High-Quality HfN-HfO 2 Gate Stack for Advanced MOS Device Applications.* IEEE Electron Device Letters, 2004. **25**(2): p. 70-72.

6. Palik, E.D., *Handbook of Optical Constants of Solids II*. 1991: Academic Press.

7. Hu, C., et al., *Nature of tunable optical reflectivity of rocksalt hafnium nitride films.* Journal of Physical Chemistry C, 2014. **118**(35): p. 20511-20520.

8. Malmström, J., S. Schleussner, and L. Stolt, *Enhanced back reflectance and quantum efficiency in Cu(In,Ga)Se 2 thin film solar cells with a ZrN back reflector.* Applied Physics Letters, 2004. **85**(13): p. 2634-2636.

9. Farrell, I.L., et al., *Tunable electrical and optical properties of hafnium nitride thin films.* Applied Physics Letters, 2010. **96**(7).

10. Seo, H.S., et al., *Growth and physical properties of epitaxial HfN layers on MgO(001).* Journal of Applied Physics, 2004. **96**(1): p. 878-884.

11. Kim, Y., et al., *Metal-organic CVD of conductive and crystalline hafnium nitride films.* Chemical Vapor Deposition, 2005. **11**(6-7): p. 294-297.

12. Elam, J.W., et al., *Atomic layer deposition of aluminum oxide in mesoporous silica gel.* Journal of Physical Chemistry C, 2010. **114**(41): p. 17286-17292.

13. Haukka, S., et al., *Dispersion and distribution of titanium species bound to silica from TiCl4.* Langmuir, 1993. **9**(12): p. 3497-3506.

14. Lakomaa, E.L., A. Root, and T. Suntola, *Surface reactions in Al2O3 growth from trimethylaluminium and water by atomic layer epitaxy.* Applied Surface Science, 1996. **107**: p. 107-115.

15. Keranen, J., et al., *Surface-controlled gas-phase deposition and characterization of highly dispersed vanadia on silica.* Journal of Physical Chemistry B, 2003. **107**(39): p. 10773-10784.

16. Ferguson, J.D., A.W. Weimer, and S.M. George, *Atomic layer deposition of Al2O3 and SiO2 on BN particles using sequential surface reactions.* Applied Surface Science, 2000. **162**: p. 280-292.

17. Hakim, L.F., S.M. George, and A.W. Weimer. *Individual nanocoating of ceramic nanoparticles via atomic layer deposition*. 2006. Orlando, FL.

18. Beetstra, R., et al., *Atmospheric pressure process for coating particles using atomic layer deposition.* Chemical Vapor Deposition, 2009. **15**(7-9): p. 227-233.

19. Becker, J.S., E. Kim, and R.G. Gordon, *Atomic Layer Deposition of Insulating Hafnium and Zirconium Nitrides.* Chemistry of Materials, 2004. **16**(18): p. 3497-3501.

20. Consiglio, S., et al., *Plasma-assisted atomic layer deposition of conductive hafnium nitride using tetrakis(ethylmethylamino)hafnium for CMOS gate electrode applications.* Journal of the Electrochemical Society, 2008. **155**(3): p. H196-H201.

21. Kim, E.J. and D.H. Kim, *Highly conductive HfN x films prepared by plasma-assisted atomic layer deposition.* Electrochemical and Solid-State Letters, 2006. **9**(8): p. C123-C125.

22. Consiglio, S., et al., *Evaluation of high thermal stability cyclopentadienyl Hf precursors with H 2O as a co-reactant for advanced gate logic applications.* Journal of Vacuum Science and Technology A: Vacuum, Surfaces and Films, 2012. **30**(1).

23. Knoops, H.C.M., et al., *Atomic Layer Deposition of Silicon Nitride from Bis(tert-butylamino)silane and N<inf>2</inf> Plasma.* ACS Applied Materials and Interfaces, 2015. **7**(35): p. 19857-19862.

24. Knoops, H.C.M., K. De Peuter, and W.M.M. Kessels, *Redeposition in plasma-assisted atomic layer deposition: Silicon nitride film quality ruled by the gas residence time.* Applied Physics Letters, 2015. **107**(1).

25. Tompkins, H. and E.A. Irene, *Handbook of Ellipsometry*. 2005: Elsevier Science.

26. Fujiwara, H., *Spectroscopic Ellipsometry: Principles and Applications*. 2007: Wiley.

27. Xu, M., et al., *Optical properties of cubic Ti3N4, Zr3N4, and Hf3N4.* Applied Physics Letters, 2006. **89**(15).

28. Scientific, T.F., *K-Alpha™+ X-ray Photoelectron Spectrometer Avantage*. 2014.

29. Blasco, N., *Personal communication.* Air Liquide, 2014.

30. Wang, W., T. Nabatame, and Y. Shimogaki, *Interface structure of HfNx/SiO2 stack grown by MOCVD using TDEAHf precursor.* Surface Science, 2005. **588**(1-3): p. 108-116.

31. Kang, C.S., et al., *Bonding states and electrical properties of ultrathin HfOxN y gate dielectrics.* Applied Physics Letters, 2002. **81**(14): p. 2593-2595.

32. Arranz, A., *Synthesis of hafnium nitride films by 0.5-5 keV nitrogen implantation of metallic Hf: An X-ray photoelectron spectroscopy and factor analysis study.* Surface Science, 2004. **563**(1-3): p. 1-12.

33. Kirsch, P.D., et al., *Electrical and spectroscopic comparison of HfO 2/Si interfaces on nitrided and un-nitrided Si(100).* Journal of Applied Physics, 2002. **91**(7): p. 4353-4363.

34. Wang, W., T. Nabatame, and Y. Shimogaki, *Preparation of conductive HfN by post rapid thermal annealing-assisted MOCVD and its application to metal gate electrode.* Microelectronic Engineering, 2008. **85**(2): p. 320-326.

35. Langereis, E., et al., *Synthesis and in situ characterization of low-resistivity Ta Nx films by remote plasma atomic layer deposition.* Journal of Applied Physics, 2007. **102**(8).

36. Andringa, A.M., et al., *Low-Temperature Plasma-Assisted Atomic Layer Deposition of Silicon Nitride Moisture Permeation Barrier Layers.* ACS Applied Materials and Interfaces, 2015. **7**(40): p. 22525-22532.

37. Knoops, H.C.M., et al., *Optical modeling of plasma-deposited ZnO films: Electron scattering at different length scales.* Journal of Vacuum Science & Technology A, 2015. **33**(2): p. 021509.

38. Williams, B.L., et al., *Expanding Thermal Plasma Deposition of Al-Doped ZnO: On the Effect of the Plasma Chemistry on Film Growth Mechanisms.* Plasma Processes and Polymers, 2016. **13**(1): p. 54-69.

39. Pierson, H.O., *Handbook of Refractory Carbides and Nitrides: Properties, Characteristics, Processing and Apps*. 1996: Elsevier Science.

Appendix 3

Table A3.1. The carbon content and the GPC as a function of gas residence time during the N_2 plasma at T_s = 350°C. The carbon content is retrieved via XPS and the GPC is obtained via SE. The corresponding error bars are indicated in the first row.

N_2 plasma exposure (s)	N_2 flow (sccm)	Ar flow (sccm)	Total flow (sccm)	Plasma pressure (mTorr)	Residence time τ (s)	C (at.%)	GPC (nm/cycle)
20	100	0	100	12.5	0.14	7.0±0.5	0.038±0.003
20	100	100	200	20.3	0.11	7.0±0.5	0.038
20	100	200	300	28.3	0.10	6.9±0.5	0.038

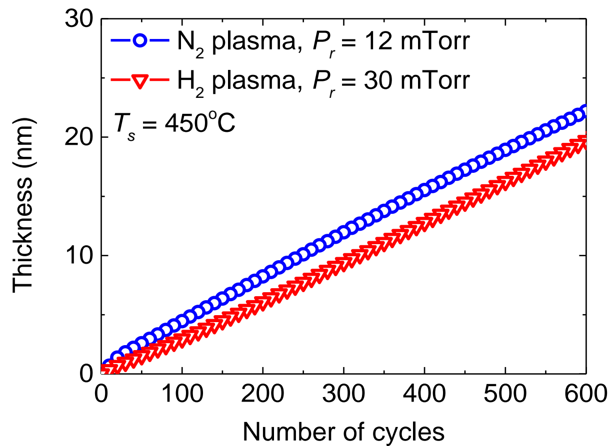

Figure A3.1. The thickness of HfN_x films prepared at T_s = 450°C as a function of ALD cycles obtained via in-situ SE. A typical linear ALD growth is obtained for the two ALD processes.

Chapter 4

Low resistivity HfN_x grown by plasma-assisted ALD with external rf substrate biasing*

Abstract

Plasma-assisted atomic layer deposition (ALD) of HfN_x thin films using tris(dimethylamino)cyclopentadienylhafnium [$CpHf(NMe_2)_3$] as the Hf precursor and H_2 plasma as reducing co-reactant is reported. We previously concluded that the HfN_x films prepared for a grounded substrate (0V substrate potential) exhibited a rather high electrical resistivity of $9.0\cdot10^{-1}$ Ωcm. In the present work, we show a steady decrease in electrical resistivity by two orders of magnitude to $3.3\cdot10^{-3}$ Ωcm upon increasing the time-averaged substrate potential up to -130V by externally biasing the substrate. A further increase in potential up to -187V led to an increase in electrical resistivity to $1.0\cdot10^{-2}$ Ωcm. The variations in electrical resistivity with the potential were found to correlate with the extent of grain boundary scattering in the films, which significantly decreased upon increasing the potential up to -130V, primarily due to major changes in film chemical composition. The latter consisted in a decrease in O content from 20.1 at.% under no bias to ≤2 at.% for a potential of -130V and an associated increase in Hf(III) fraction from 0.65 to 0.82. The latter is key to the development of low resistivity δ-HfN. A further increase in potential to -187V led to an increase in grain boundary scattering as a consequence of a major decrease in grain size as well as in-grain crystallinity. In view of advanced nanoelectronic devices, the HfN_x layers were also deposited on 3D trench nanostructures at a potential of -130V. A low oxygen content in the HfN_x film measured on both the planar and vertical topographies of the trenches. Overall, the time-averaged substrate potential has been shown to highly affect the chemical composition, microstructure and the associated electrical properties of the HfN_x layers and can be used to tailor the HfN_x film properties.

Saurabh Karwal, Marcel A. Verheijen, Benjamin L. Williams, Tahsin Faraz, Wilhelmus M. M. Kessels and Mariadriana Creatore, J. Mater. Chem. C 6, 3917 (2018)

4.1 Introduction

Conductive transition metal nitride (TMN) films are widely employed in microelectronics because of their low electrical resistivity [1, 2], and excellent diffusion barrier properties against oxygen and copper [3-6]. In particular, conductive titanium nitride and tantalum nitride films have been already implemented as gate metals in metal oxide semiconductor field-effect transistors (MOSFETs). One of the issues encountered in their implementation is the formation of oxy-nitrides at the interface with the gate oxide [1, 7, 8]. In photovoltaics, they are of interest due to the extended high near-IR reflectivity [9, 10]. Zirconium nitride has been employed as a back reflector electrode for thin-film copper-indium-gallium-selenide (CIGS) solar cells [11]. Recently, low resistivity hafnium nitride films (δ-HfN) have gained notable importance because of the superior stability when used in combination with HfO_2 [6]. Furthermore, a very-high reflectivity in the spectral region between 1 eV and 2.4 eV,2 allows applications such as back reflectors for CIGS solar cells and as heat mirrors [12, 13].

Hafnium nitride (HfN_x) exists in different crystal phases including highly resistive Hf_3N_4 [14, 15], and the conductive δ-HfN fcc phase [9, 16]. Therefore, it can be inferred that the oxidation state of Hf in the film (Hf(IV) vs. Hf(III)) and the stoichiometry fundamentally affect the HfN_x material properties. Thin films of δ-HfN_x have been grown by various methods, such as physical vapour deposition (PVD) [10, 17, 18], metal-organic chemical vapour deposition (MO-CVD) [19] and atomic layer deposition (ALD) [20-22]. Due to the stringent requirements posed by the semiconductor industry as a result of device shrinkage, especially ALD has emerged as a key deposition technique which holds promises of delivering ultra-thin films with precise thickness control, excellent uniformity, and unparalleled conformality on high surface area substrates [23-26].

Considering δ-HfN material properties, Seo *et al.* obtained a very low electrical resistivity (ρ_e) of $1.4 \cdot 10^{-5}$ Ωcm for a 650 nm thick single crystal δ-HfN film grown by PVD [18]. On the other hand, the preparation of low resistivity δ-HfN_x films by either CVD or ALD employing metal-organic Hf precursors and a reducing co-reactant, is challenging. This is primarily due to incomplete abstraction of ligands leading to impurities in the film and/or inefficient reduction of the Hf(IV) oxidation state (in the precursor) to Hf(III) (in the film). Kim *et al.* reported the MO-CVD growth of δ-HfN film with an ρ_e of $1.0 \cdot 10^{-3}$ Ωcm for a ~ 1 µm thick film using an alkylamide Hf precursor and N,N-dimethylhydrazine as reducing agent. On the contrary, non-conducting Hf_3N_4 films were obtained when NH_3 was used as the reducing agent [19]. This illustrates that the potential for the reduction of

M(IV) to M(III) (M = metal atom) dictates the choice in reducing co-reactant, which as such, can significantly alter the film properties [22].

The growth of ultra-thin δ-HfN_x films by ALD has been reported by Consiglio *et al.* and Kim *et al.* by employing a highly reducing H_2 plasma as co-reactant and using alkylamide Hf precursors [20, 21]. Consiglio *et al.* reported an ρ_e of $2.3\cdot10^{-3}$ Ωcm (film thickness is not reported) [20], whereas Kim *et al.* obtained an ρ_e of $6.7\cdot10^{-3}$ Ωcm for a film thickness of 14 nm [21]. For these films, the fraction of Hf(III) oxidation state in the layers was not reported. Moreover, next to the chemical composition, it can be expected that also the microstructure of the layer is crucial for HfN_x film resistivity. This effect has been only sparsely investigated so far.

Recently, we have shown the importance of selecting the composition of the plasma gas as co-reactant to control the chemical composition and microstructure of HfN_x thin films [22]. We demonstrated the necessity of a reducing H_2 plasma in order to fabricate the conductive δ-HfN_x phase [22]. However, the HfN_x films grown using H_2 plasma resulted in relatively high ρ_e values of $(9.0\pm0.2)\cdot10^{-1}$ Ωcm [22]. We observed that the film contained 20.1±0.7 O at.% leading to formation of Hf-O bonds and resistive films. In a conductive δ-HfN phase, the Hf exists in the +3 oxidation state with loosely bound 5d electrons serving as free carriers [10]. The presence of Hf-O bonds increased the oxidation state of Hf to +4, which limited the Hf(III) oxidation state fraction down to 0.65±0.02 for the aforementioned H_2 plasma case. This decreased the conduction electron density and increased the film resistivity [22].

Building on earlier studies, the seminal work of Anders showed that the mean energy of ion bombardment can play a central role in determining the film properties in case of PVD [27]. Furthermore, selected effects of energetic ion bombardment on the film properties during a PE-CVD processes have been reported [28, 29]. Regarding plasma-assisted ALD processes, Profijt *et al.* introduced the aspect of increasing the ion energy by externally biasing the substrate with an rf power source and studied the resulting ion energy distributions [30]. In this case, the bias was applied only during the plasma half cycle and it was found to tune the crystalline phase of TiO_2 films as well as increase the mass density of Co_3O_4 films [30].

In this work, we will address the impact of an external rf substrate bias during the H_2 plasma half cycle on the HfN_x films prepared by ALD. The time-averaged substrate potential (V_{bias}, developed upon application of external rf substrate bias) is shown to highly affect the material properties of HfN_x films. We observed a steady decrease in the ρ_e of the HfN_x films to a minimum of $(3.3\pm0.1)\cdot10^{-3}$ Ωcm upon increasing the $|V_{bias}|$ up to 130V. On the contrary, we observed an increase

in the ρ_e to $(1.0\pm0.3)\cdot10^{-2}$ Ωcm upon further increasing the $|V_{bias}|$ from 130V to 187V. We found that the variations in the ρ_e with $|V_{bias}|$ correlates with extent of grain boundary scattering in the films, which significantly decreased upon increasing the $|V_{bias}|$ up to 130V. The decrease in ρ_e and scattering is due to a substantial decrease in O content (down to ≤2 at.%) and an associated improvement in Hf(III) fraction to 0.82±0.02 since the HfN_x films grown at $|V_{bias}|$ = 130V are found to be considerably more porous than HfN_x films prepared with grounded electrode. A further increase in the $|V_{bias}|$ to 187V led to a major decrease in grain size as well as in-grain crystallinity, culminating in an increase in scattering and ρ_e of the films. The HfN_x was also deposited on 3D trench nanostructures to investigate the chemical composition at different regions (planar and vertical sidewalls), as is relevant for advanced nanoscale device architectures. The HfN_x layer grown at $|V_{bias}|$ = 130V showed a reduced O content on both the planar and vertical regions of the trench structures. The low O content on the vertical regions suggests that the ion bombardment reaches also the sidewalls, most certainly due to collisions between ions in the plasma sheath with background gas. The obtained results elucidate the importance of ions and their energy in improving the chemical composition/microstructure and the associated electrical properties of HfN_x layers.

4.2 Experimental section

I. Plasma-assisted ALD of HfN_x and Process Conditions

HfN_x thin films were deposited using an Oxford Instruments FlexAL ALD reactor [31, 32], equipped with an inductively coupled remote plasma (ICP) source with an alumina dielectric tube. A base pressure of $1.6\cdot10^{-6}$ Torr was achieved in the reactor chamber using a turbo-molecular pump before every deposition. The stage temperature was kept at 450°C (which corresponds to a substrate temperature of 340°C as determined using spectroscopic ellipsometry (SE)) [22]. The reactor walls were kept at 145°C during all the depositions.

A stainless steel bubbler contained the Hf precursor $CpHf(NMe_2)_3$ (Air Liquide, >99.99% purity) at 60°C and was bubbled by an Ar flow of 100 sccm. An Ar flow of 100 sccm was injected into the ICP alumina tube during the precursor dosage in order to suppress deposition on the ICP tube walls (the gate valve between the ICP source and reactor chamber was kept open during the full cycle). During the plasma exposure, H_2 (>99.999% purity, working pressure ~30 mTorr) at 100 sccm was introduced into the chamber and subsequently the plasma was ignited with 100W radio frequency (rf) ICP power (13.56 MHz) for the desired time (see Figure A4.1 for ALD recipe). The purge step for both half cycles consisted of a flow of 200

sccm Ar through the bubbling lines and 100 sccm Ar flow from the ICP source with the valve to the pump fully opened. As reported previously, a $CpHf(NMe_2)_3$ pulse length of 4 s and H_2 plasma exposure of 10 s was used, while keeping the purge step of 2 s after every half cycle (Figure A4.2) [22].

II. RF substrate biasing.

Employing the special feature of the latest Oxford Instruments FlexAL systems, an external substrate bias was applied during the H2 plasma exposure using a rf power source (13.56 MHz), attached to the substrate table (Figure A4.1). The magnitude of the developed time-averaged substrate potential with respect to ground is indicated by V_{bias}. During the H_2 plasma exposure, this value was regulated by varying the applied rf power.

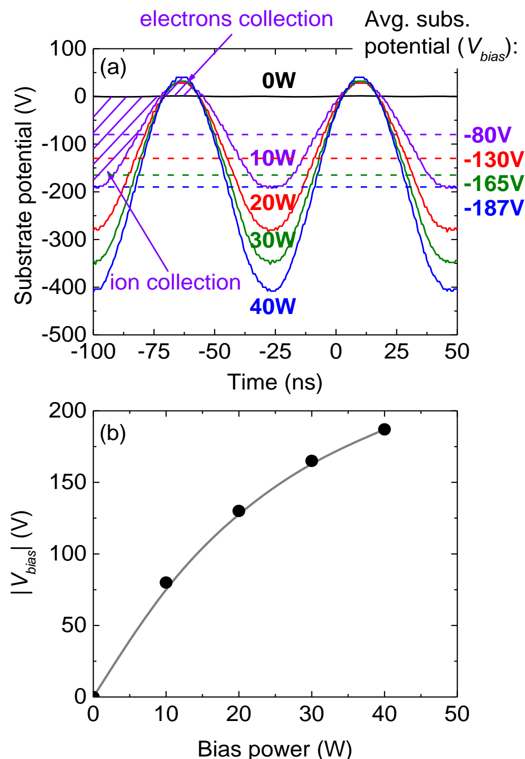

Figure 4.1. (a) Substrate potential waveforms as a function of time measured using an oscilloscope: the development of time-averaged substrate potential V_{bias} with respect to ground can be observed (b) Absolute values of V_{bias} as a function of the applied rf bias power. The line serves as a guide to the eye.

Shown in Figure 4.1a are the rf bias voltage waveforms as a function of time. These are measured using an oscilloscope connected to the substrate table via a high voltage probe. Figure 4.1a also shows that a time-averaged negative potential with respect to ground (V_{bias}) has developed at the substrate such that the flux of electrons equals the flux of ions, when integrated over one period of the rf waveform [30]. The amplitude of the voltage and V_{bias} can be regulated by varying the power applied to the substrate table. A V_{bias} = -80V is obtained when 10W rf bias power is applied, whereas V_{bias} = -187V results from 40W rf power. The plot of the absolute values of V_{bias} as a function of rf bias power (Figure 4.1b) shows a deviation from the ideal linear behaviour. This deviation may be due to heating of the electrons near the substrate generating an additional plasma which increases the ion current, as well as to other effects such as power dissipation by resistive losses at the substrate or in the matching network.

As a result of the voltage drop over the plasma sheath, the ions are accelerated towards the surface. For a collisionless sheath, the corresponding average ion energy (E_{ion}) is given by $E_{ion} = e(V_p - V_{bias})$, where V_p is the plasma potential [30]. Profijt *et al.* showed that the E_{ion} is 20-30 eV for a grounded electrode (no external substrate bias) using H_2 plasma in a similar FlexAL system and under similar experimental conditions [33]. This implies that the E_{ion} under rf substrate biasing conditions is expected to be approximately 20-30 eV higher than the value of $e|V_{bias}|$. We note however that the actual ion energy distribution function is bimodal [30], and that the plasma sheath is not fully collisionless as will be addressed in future work.

III. Substrates and material characterization

The HfN_x films were deposited on Si(100) substrates with a diameter of 100 mm and with 450 nm SiO_2 atop. The growth per cycle (GPC) and the dielectric functions of the HfN_x films were examined via spectroscopic ellipsometry (SE) (J.A. Woollam, Inc., M2000U). The dielectric functions ($0.75 \leq h\nu \leq 5.0$ eV) of HfN_x films were modelled using one Drude and two Lorentz oscillators as demonstrated by Hu *et al.* (see Figure A4.3a and Table A4.1 for details) [9]. Additionally, the optical resistivity (ρ_{op}) (at room temperature) was deduced from the free-carrier Drude parameterization, given by $\rho_{op} = \Gamma_D / \varepsilon_o \cdot \omega_p^2$, where Γ_D is the damping factor for the Drude oscillator, ε_o is the permittivity of free space, and ω_p is the screened plasma frequency [34]. The electrical resistivity (ρ_e) (at room temperature) was obtained via four-point probe measurements using a Keithley 2400 SourceMeter

and a Signaton probe by multiplying the sheet resistance of the HfN_x films with the film thickness as derived from SE.

The X-ray photoelectron spectroscopy (XPS) measurements were performed using a Thermoscientific K-Alpha KA1066 system equipped with a monochromatic Al Kα ($h\nu$ = 1486.6 eV) source in order to study the chemical bonding and the oxidation states of elements present in the film. The chemical composition and the mass density of the films was evaluated via Rutherford backscattering spectrometry (RBS) and elastic recoil detection (ERD) using 1900 keV $^4He^+$ ions (Detect99). For the ERD measurements, the recoil angle was 30° and the angle of incidence with the sample surface was kept at 15° whereas for the RBS, two detectors were used with scattering angles of 170° and 150°.

The HfN_x film microstructure was studied using transmission electron microscopy (TEM) using a JEOL ARM 200F, operated at 200 kV. Selected area electron diffraction (SAED) pattern of 1.3 µm diameter areas were acquired from HfN_x films with a similar film thickness (~15 nm), grown at various values of V_{bias}. The HfN_x films were grown on SiN_x TEM windows, coated with ~5 nm ALD SiO_2.

The crystallinity of the films was examined with a PANalytical X'pert PRO MRD X-ray diffractometer using a Cu $K\alpha$ (λ = 1.542 Å) X-ray source. The X-ray diffractograms were obtained in a θ-2θ configuration and were compared with the powder HfN and Hf_2ON_2 patterns [35, 36]. The crystallite sizes were computed using the X-ray line broadening in the Scherrer's equation. The broadening of peak in XRD primarily arises from the presence of stress and/or crystallite size [37]. For the computation of the crystallite size in our case, the film stress was neglected.

The surface morphology was studied using a Zeiss Sigma field emission scanning electron microscope (FE-SEM) operated at an acceleration voltage of 2 kV.

The residual film stress was calculated using a Tencor FLX-2320 by evaluating the laser deflection as a result of change in the curvature of the Si wafer using Stoney's equation [38].

The HfN_x films were also deposited on trench nanostructures with varying aspect ratio (height ~450 nm, width varying) in order to evaluate the chemical composition on 3D topographies. Coupons containing these trench nanostructures were prepared and provided by LAM Research [39]. The respective 3D trench nanostructures were formed by first depositing thick SiO_2 film on Si wafer via PECVD, which was then etched into trench structures. These structures were subsequently coated with a conformal SiN_x layer using a high-temperature CVD process, followed by deposition of a very thin layer of SiO_2 using

ALD [39]. Following the HfN_x ALD, a thin lamella (~100 nm) was prepared by a focused ion beam (FIB) using the lift-out preparation procedure. Scanning TEM combined with energy-dispersive X-ray spectroscopy (EDX) was used to study the chemical composition of the deposited HfN_x films.

4.3 Results and discussion

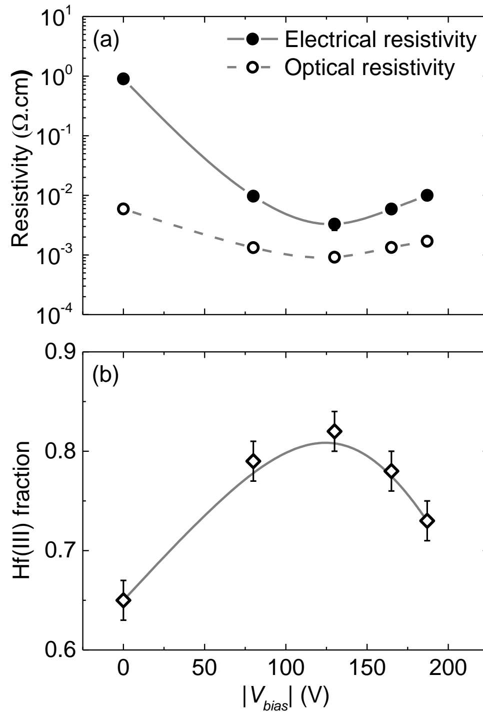

Figure 4.2. (a) Electrical and optical resistivity values and (b) Hf(III) oxidation state fraction of HfN_x films as a function of the absolute value of V_{bias}. Lines serve as a guide to the eye.

We previously reported on HfN_x films (~70 nm thick) prepared with a grounded electrode ($|V_{bias}|$ = 0V), reaching an ρ_e of (9.0±0.2)·10^{-1} Ωcm [22]. In addition, the opto-electronic properties of the HfN_x films were probed using SE. Figure A4.3b shows the imaginary part of the dielectric function ε_2 and the corresponding Drude absorption for the HfN_x films prepared at various values of $|V_{bias}|$. Using magnitude of the Drude absorption, we previously reported an

optical resistivity (ρ_{op}) of (5.9±0.1)·10^{-3} Ωcm for the HfN_x films prepared at $|V_{bias}|$ = 0V [22].

The effect of an external rf substrate bias on the HfN_x material properties was evaluated. For these experiments, only $|V_{bias}|$ was varied during the H_2 plasma half cycle, whereas the $CpHf(NMe_2)_3$ pulse length of 4 s and H_2 plasma exposure of 10 s was kept constant [22]. A comprehensive summary of several material properties of HfN_x films prepared on planar SiO_2/Si substrates for various values of $|V_{bias}|$ (constant film thickness ~70-80 nm) can be found in Table 4.1.

The variations in electrical and opto-electronic properties of the HfN_x films with $|V_{bias}|$ are discussed at first. Figure 4.2a shows the ρ_e and ρ_{op} for HfN_x films as a function of $|V_{bias}|$. Remarkably, the ρ_e decreased by two orders to a value of (3.3±0.1)·10^{-3} Ωcm at $|V_{bias}|$ = 130V, as compared to the films prepared with the grounded electrode. In parallel, an increase in the $|V_{bias}|$ to 130V led to an increase in Drude absorption resulting in a decrease of ρ_{op} to (9.0±0.2)·10^{-4} Ωcm (Figure A4.3b). On the other hand, a further increase in the $|V_{bias}|$ to 187V led to a subsequent increase in ρ_e to (1.0±0.3)·10^{-2} Ωcm and ρ_{op} to (1.7±0.1)·10^{-3} Ωcm.

By considering the rather small interaction distance of incident light with the HfN_x films (~2-3 nm) (see supplementary information), the difference between the ρ_e and ρ_{op} may provide insights in to the extent of grain boundary scattering phenomena as described by Knoops *et al.* [22, 34]. The large difference between ρ_e and ρ_{op} values at $|V_{bias}|$ = 0V suggests the presence of prominent grain boundary scattering in the HfN_x films. Interestingly, the resistivity difference decreased significantly by the application of external rf substrate bias and attained a minimum at $|V_{bias}|$ = 130V (Figure 4.2a). This indicates a decrease in the scattering at grain boundaries, which reduces the resistance in transport of the electrons between adjacent grains. On further increasing the $|V_{bias}|$ to 187V, the resistivity difference increased slightly, pointing out an increase in scattering in the film at high values of $|V_{bias}|$. The grain boundary scattering may arise from several factors such as a high barrier height at the grain boundaries and/or a low in-grain electron density [40]. Furthermore, smaller grains may result in larger grain boundary scattering if the grain boundaries are poorly passivated [34]. Therefore, in order to understand the variation in grain boundary scattering and the associated ρ_e with $|V_{bias}|$, the chemical composition and microstructure of the HfN_x films was studied.

The chemical composition of HfN_x films was investigated by means of RBS and XPS. We previously reported that HfN_x films grown at $|V_{bias}|$ = 0V contained <2.0 at.% C and that 10 s H_2 plasma exposure was sufficiently long for complete abstraction of the carbon groups from the adsorbed precursor (Table 4.1) [22]. Furthermore, the HfN_x film was found to contain 20.1±0.7 at.% O [22]. We showed

that oxygen was primarily incorporated during deposition and not because of post-deposition oxidation [22]. We also demonstrated that the O present in the films selectively formed Hf-O bonds (see the deconvolution of the O 1s XPS spectrum in Figure A4.4a) [41], which can be related to the high enthalpy of formation of HfO_2 (-1144.7 kJ/mol) and HfO (-564.8 kJ/mol) [42] as compared with the enthalpy of formation of HfN (-369 kJ/mol) [43]. This limited the Hf(III) oxidation state fraction to a relatively low value of 0.65±0.02 (Figure 4.2b, 4.3a and Table 4.1).

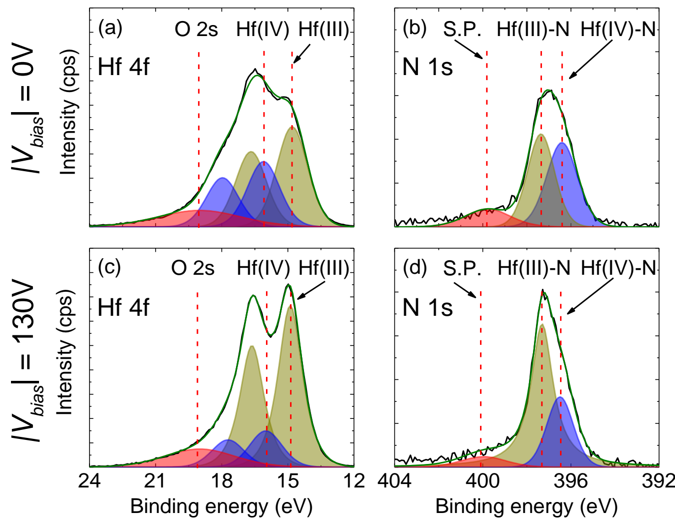

Figure 4.3. Deconvoluted XPS spectra for HfN_x films prepared at $|V_{bias}|$ = 0V and $|V_{bias}|$ = 130V for Hf 4f with Hf(III) and Hf(IV) oxidation states (a and c), N 1s with associated bonding to Hf atoms (c and d). Data for $|V_{bias}|$ = 0V is given in (a) and (b) and data for $|V_{bias}|$ = 130V is given in (c) and (d) S.P. represents the satellite peak.

Interestingly, the Hf(III) fraction steadily increased to 0.82±0.02 upon increasing the $|V_{bias}|$ value up to 130V as shown in Figures 4.2b and 4.3c, in-line with the aforementioned decrease in the ρ_{op}. On the other hand, when $|V_{bias}|$ is increased to 187V, the Hf(III) fraction decreases again to 0.73±0.02, in-line with the increase in the ρ_{op}. The increase in Hf(III) fraction with $|V_{bias}|$ up to 130V occurs in parallel with the decrease in O content to ≤2.0 at.% for $|V_{bias}|$ value of 130V or higher. Relevantly, preliminary density functional theory studies suggest that an increase in energy of bombarding ions may promote desorption of H_2O from the surface of the film, resulting in lower oxygen content upon increasing $|V_{bias}|$. The decrease in the Hf(III) fraction upon further increasing the $|V_{bias}|$ to

187V is speculated to arise from an increase in the H content (Table 4.1) and the associated Hf-H bonds, as the O content in the HfN_x films grown above $|V_{bias}|$ value of 130V remains similar. This may lead to an increase in the Hf(IV) relative content.

Nitrogen was also found to exist in two chemical environments, i.e. bonding with Hf(III) and Hf(IV) atoms as presented in Figures 4.3b,d (see Table A4.2 for a summary of the binding energies for different elements) [44, 45]. The application of external rf substrate bias ($|V_{bias}|$ = 130V) increased the number of N atoms bonded to Hf atoms that are present in +3 oxidation state, when compared with the grounded electrode condition. This result corroborates the increase in the fraction of the δ-HfN phase. In contrast to the O content, the C concentration increased by the application of external rf substrate bias (Table 4.1). Figure A4.5b shows the C 1s XPS spectra of the bulk HfN_x films as a function of $|V_{bias}|$. The peak at lower binding energy (282 eV) is attributed to Hf-C bonding [46].

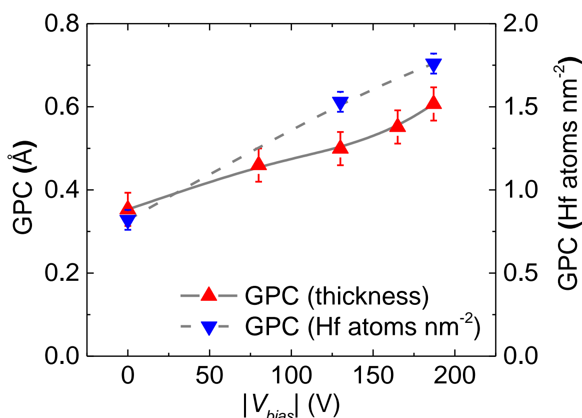

Figure 4.4. Growth per cycle (GPC) in terms of thickness and number of Hf atoms deposited per nm^2 as determined by SE and RBS as a function of absolute value of V_{bias}. Lines serve as a guide to the eye.

A steady increase in the Hf-C peak intensity is observed upon increasing the $|V_{bias}|$ from 0V up to 130V. These results suggest that carbon in the films may originate from the enhanced cracking of the ligands on the surface by energetic ion bombardment, followed by re-deposition [32]. Alternatively, carbon-containing cationic species in the plasma may also get accelerated towards the growing film (a kind of redeposition) that may also lead to carbon incorporation.

Figure 4.4 shows the effect of external rf substrate bias application on the GPC in terms of thickness (Å) and areal density of deposited Hf atoms (Hf atoms nm^{-2}), whereas an elaborate characterization of the ALD process (linear thickness increase, self-saturation behaviour and thickness uniformity maps for HfN_x films) as a function of $|V_{bias}|$ is shown in the appendix (Figure A4.3). The ALD process was found to saturate for all values of $|V_{bias}|$ investigated. A consistent increase in GPC (Å) with $|V_{bias}|$ was observed, which may result from an increase in precursor adsorption, decrease in film mass density and/or changes in chemical composition. By means of RBS, we found that the areal density of deposited Hf atoms per cycle also increased with $|V_{bias}|$. This indicates that the precursor adsorption increases with $|V_{bias}|$, which may occur due to the presence of a higher density of active sites for precursor adsorption after every ALD cycle. By plotting the GPC (Å) as a function of the areal density of Hf atoms deposited per cycle (Figure A4.6), we found roughly a linear dependence. Therefore, it can be concluded that the increase in the GPC (Å) with the $|V_{bias}|$ is primarily due to an increase in precursor adsorption. Furthermore, the application of external rf substrate bias resulted in N/Hf ratio of 1.00±0.07 and 0.98±0.06 at $|V_{bias}|$ = 130V and 187V respectively, which is higher than 0.86±0.05 obtained at $|V_{bias}|$ = 0V (Table 4.1). This result implies that the areal density of N atoms deposited per cycle increases in par with the areal density of Hf atoms when $|V_{bias}|$ increases.

In addition to the changes in Hf(III) fraction, the variations in microstructure with $|V_{bias}|$ might also contribute to the ρ_e as described by Ponomarev *et al.* [40]. The microstructure of the HfN_x films was studied by evaluating the in-grain film porosity, in-grain film crystallinity, lateral grain size and residual film stress as a function of $|V_{bias}|$ (for films with a similar thickness of ~75 nm).

Table 4.1. The properties of HfN_x films prepared at various values of $|V_{bias}|$, as determined by four-point probe (FPP), spectroscopic ellipsometry (SE), X-ray photoelectron spectroscopy (XPS), Rutherford backscattering (RBS) and elastic recoil detection (ERD). The electrical resistivity was obtained by a combination of FPP and SE whereas the optical resistivity, GPC and thickness were determined using SE. XPS was used to obtain the Hf(III) oxidation state fraction and the chemical composition and the GPC values in terms of number of deposited Hf at. nm^{-2} $cycle^{-1}$ were determined by RBS. The H content was determined using ERD. The mass density was calculated by dividing the areal mass density (obtained via RBS and ERD) with the film thickness. The errors for electrical resistivities and optical resistivities are less than 3% and 2% of their absolute values, respectively. The errors for the GPC, the Hf(III) fraction and the mass densities are mentioned in the first line unless otherwise mentioned.

$\|V_{bias}\|$ (V)	FPP	SE			XPS	RBS					ERD
	Electrical resistivity (Ωcm)	Optical resistivity (Ωcm)	GPC (Å)	Thickness (nm)	Hf(III) / Hf(III)+Hf(IV)	GPC (Hf at. nm^{-2} $cycle^{-1}$)	N/Hf	C (at.%)	O (at.%)	Mass density (g cm^{-3})	H (at.%)
0	$9.0 \cdot 10^{-1}$	$5.9 \cdot 10^{-3}$	0.35±0.03	71	0.65±0.02	0.82±0.04	0.86±0.05	<2.0	20.1±0.7	8.2±0.2	7.0±0.3
130	$3.3 \cdot 10^{-3}$	$9.0 \cdot 10^{-4}$	0.50	81	0.82	1.53±0.06	1.00±0.07	11.0±1.2	<2.0	8.6	12.6±0.6
187	$1.0 \cdot 10^{-2}$	$1.7 \cdot 10^{-3}$	0.60	83	0.73	1.76±0.06	0.98±0.06	10.3±1.1	<2.0	8.0	18.5±0.9

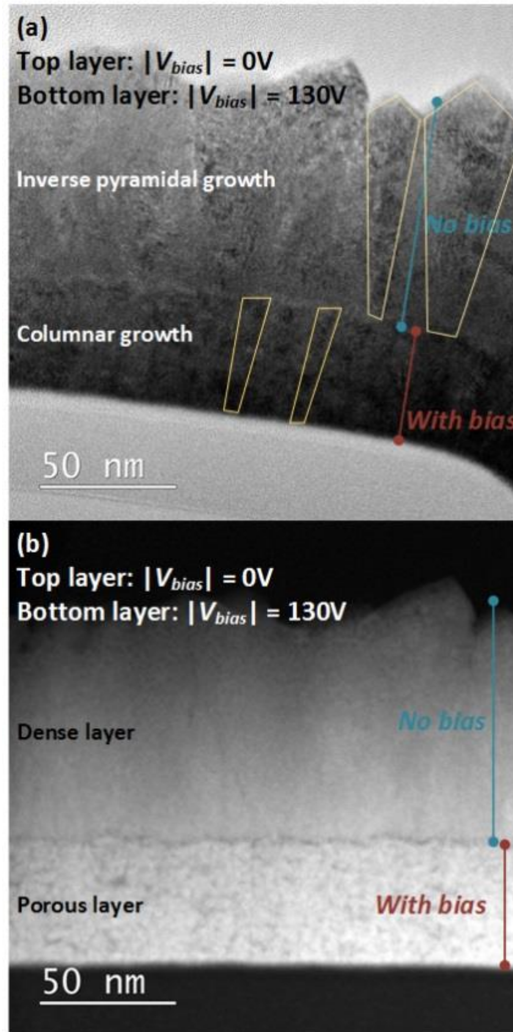

Figure 4.5. (a) Bright-field transmission electron microscope image (BF-TEM) and (b) high-angle annular dark-field scanning transmission electron microscopy (HAADF-STEM) image of the HfN_x film grown in two steps with different substrate potentials: bottom layer at $|V_{bias}|$ = 130V and top layer at $|V_{bias}|$ = 0V.

First, the microstructure of the HfO_yN_x and HfN_x films grown at $|V_{bias}|$ = 0V and $|V_{bias}|$ = 130V respectively are compared and the grain development was scrutinized. To serve our purposes, the HfN_x ALD was carried out under two conditions in a single run (without breaking the vacuum): a ~45 nm bottom layer grown at $|V_{bias}|$ = 130V and a ~85 nm top layer was grown at $|V_{bias}|$ = 0V. The bright-field TEM (BF-TEM) image of the stack of HfN_x films is presented in Figure

4.5a. The grain growth of HfN_x film prepared at $|V_{bias}|$ = 0V was found to be inverse pyramidal whereas a columnar growth of the HfN_x film was detected at $|V_{bias}|$ = 130V. Furthermore, the contrast variations within the crystals of the HfN_x film grown at $|V_{bias}|$ = 0V indicate the presence of many small defects such as dislocations and/or low-angle grain boundaries. In Figure 4.5b, the high-angle annular dark-field STEM (HAADF-STEM) image for the HfN_x film stack is presented elucidating that the HfN_x film grown at $|V_{bias}|$ = 130V is rich in nanopores whereas the HfN_x film prepared at $|V_{bias}|$ = 0V is relatively more dense.

The crystallinity of the HfN_x films was examined using XRD (θ-2θ mode) (Figure 4.6). The HfN_x films grown at $|V_{bias}|$ = 0V are polycrystalline with a mixture of two phases: δ-HfN and cubic Hf_2ON_2, as evident from previously reported grazing incidence XRD patterns [22, 36]. The θ-2θ scan of this sample in Figure 4.6 shows broad peaks, which can be explained by the defect-rich nature of the grains, in-line with the TEM study. Based on the chemical composition analysis, GIXRD patterns (Figure A4.7) and θ-2θ scans, we suggest a predominant growth of δ-HfN phase at $|V_{bias}|$ value of 130V and higher, whereas Hf_2ON_2 phase is below detection limit. The HfN_x films grown at $|V_{bias}|$ = 130V gave a strong HfN(200) reflection implying a preferred orientation, in-line with the columnar grain growth. Furthermore, the increase in HfN(111) and HfN(200) peak intensity suggests that the crystalline quality of XRD coherent domains increased upon increasing the $|V_{bias}|$ from 0V to 130V, despite the introduction of voids in the film. In contrast to the HfN_x films grown at $|V_{bias}|$ = 130V, HfN(111) is the preferred orientation at $|V_{bias}|$ = 187V. The development of a preferred orientation during film growth can be introduced by several factors, such as the minimization of strain or surface energy [47]. This was demonstrated by Pelleg *et al.* for TiN_x films grown by PVD [48]. It was reported that the growth of TiN(200) is favoured in order to minimize the surface energy whereas TiN(111) is the preferred growth direction to minimize the strain energy [48, 49]. Alternatively, the texture could already be different in the nucleation phase of the films. Interestingly, the crystallographic texture appeared to be similar for ~15 nm thick HfN_x films grown at $|V_{bias}|$ = 130V and $|V_{bias}|$ = 187V, as evident from the HAADF-STEM and SAED studies (see the discussion underneath in the appendix, Figure A4.8).

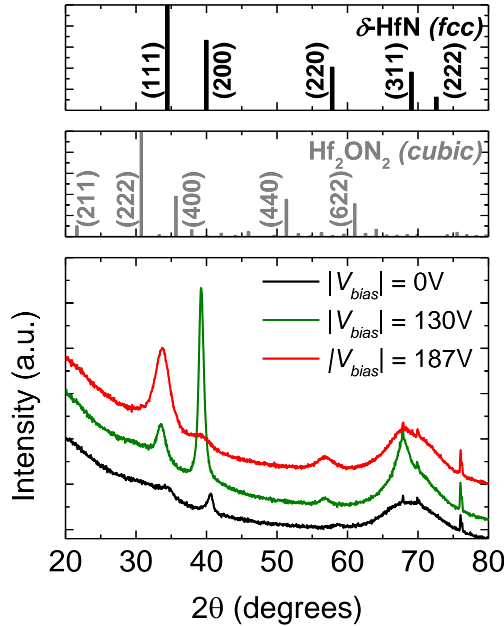

Figure 4.6. X-ray diffractograms (Gonio (θ-2θ) scans) for ~75 nm thick HfN_x films for various values of $|V_{bias}|$ referenced with powder fcc δ-HfN and cubic Hf_2ON_2 XRD patterns.

Subsequently, the lateral grain size of the HfN_x films was investigated for the relevant layer thickness of 75 nm by means of SEM. The HfN_x films grown with grounded electrode ($|V_{bias}|$ = 0V) displayed a lateral grain size of 25±3 nm (Figure 4.7a and Table 4.2). Interestingly, the 75 nm thick HfN_x layer grown at $|V_{bias}|$ value of 130V exhibits a similar grain size of 26±2 nm (Figure 4.7b).

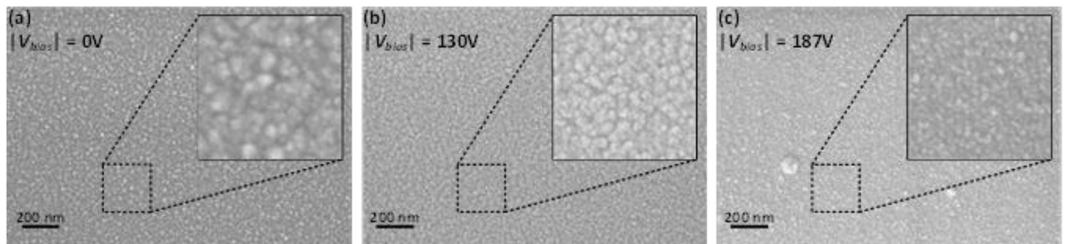

Figure 4.7. Scanning electron micrographs displaying top-view for HfN_x films (thickness ~75 nm) prepared at (a) $|V_{bias}|$ = 0V (b) $|V_{bias}|$ = 130V and (c) $|V_{bias}|$ = 187V. Insets depicts a magnified view of the surface morphology used to obtain lateral grain sizes.

Summarizing the first part, we can conclude that the HfN_x films grown at $|V_{bias}|$ of 130V are considerably more porous than HfO_yN_x films grown with grounded electrode even though the lateral grain sizes are similar for both layers. Therefore, the decrease in the ρe and grain boundary scattering upon increasing the $|V_{bias}|$ from 0V to 130V appears to be primarily a result of modification in the chemical composition. The latter stems from a decrease in O content and associated improvement in Hf(III) fraction.

Having established that the decrease in ρ_e up to $|V_{bias}|$ = 130V is primarily driven by modification in chemical composition, the microstructure of the HfN_x films grown at $|V_{bias}|$ = 130V and $|V_{bias}|$ = 187V with the same chemical composition was subsequently compared. An increment in the $|V_{bias}|$ from 130V to 187V led to a major decrease in the lateral grain size from 26±2 nm to 18±3 nm respectively (Figure 4.7c), as revealed from SEM analyses.

Complementary to the lateral grain size obtained from SEM analysis, the vertical crystallite sizes for the same films were deduced for the HfN(200) and HfN(111) reflections of the XRD patterns. The difference between the grain size from SEM and the crystallite size can have two reasons; firstly, SEM yields the lateral grain size as evident on the top surface, while XRD probes the vertical grain size. Secondly, a grain may contain many defects and small angle grain boundaries. The peaks widths in XRD scans represent the lengths of the coherent diffraction domains in a crystal. Therefore, crystallite size might be smaller or equal to the grain size. The data in Table 4.2 indicates the formation of relatively larger crystallites at $|V_{bias}|$ = 130V. On the other hand, an increment in the $|V_{bias}|$ to 187V gives an apparent broad peak for HfN(111) reflection yielding a relatively smaller crystallite size. A comparison with the BF-TEM image in Figure 4.5a shows that the crystallite size as determined from XRD is significantly smaller than the column height, which can be understood from the limited XRD coherence due to the porous and defect-rich nature of the layer. Furthermore, it should be also noted that the peak broadening may also result from the presence of residual stress in the layers [37].

The residual stress for the HfN_x films grown at varied $|V_{bias}|$ was determined by means of wafer curvature measurements and is presented in Table 4.2 [38]. The data displays a much higher compressive residual stress for the HfN_x films deposited at $|V_{bias}|$ = 130V as compared to that at $|V_{bias}|$ = 187V. Liao *et al.* demonstrated that the resistivity of HfN_x films, grown by PVD, can significantly depend on the residual stresses, i.e. high residual stress can lead to lower ρ_e [38]. Therefore the lower ρ_e at $|V_{bias}|$ = 130V may also partly arise from the high residual stress in the layer. Additionally, it can be concluded that the broadening of peaks in XRD at $|V_{bias}|$ = 187V is primarily due to decrease in the vertical

crystallite size. In addition, a discrete SAED pattern is obtained for ~15 nm thick HfN_x film prepared at $|V_{bias}|$ = 130V whereas HfN_x film grown at $|V_{bias}|$ = 187V exhibits a continuous pattern. This suggests that the lateral crystallite size is also smaller for HfN_x film grown at $|V_{bias}|$ = 187V (see appendix, Figure A4.8).

Table 4.2. Grain size and residual stress values for HfN_x films (thickness ~75 nm) prepared under various values of $|V_{bias}|$. The lateral grain sizes are determined via SEM. The crystallite size is obtained from XRD using Scherrer's equation for the corresponding diffracting planes (*h k l*). Typical errors associated with the measured quantities are indicated. The film stress has been determined by wafer curvature measurements.

$\lvert V_{bias}\rvert$ (V)	SEM	XRD		Residual compressive stress σ_{11} (GPa)
	Grain size (nm)	Peak (*h k l*)	Crystallite size (nm)	
0	25±3	200	-	-
		111	-	
130	26±2	200	10.6±0.1	2.00±0.05
		111	6.2±0.2	
187	18±3	200	-	0.34±0.03
		111	3.6±0.1	

Based on the microstructural characterization, it can be concluded that an increase in ρ_e and grain boundary scattering at $|V_{bias}|$ above 130V is primarily a consequence of a major decrease in lateral grain size as well as in-grain crystalline quality in both vertical and lateral directions, since the chemical composition of the HfN_x films grown above $|V_{bias}|$ = 130V is similar.

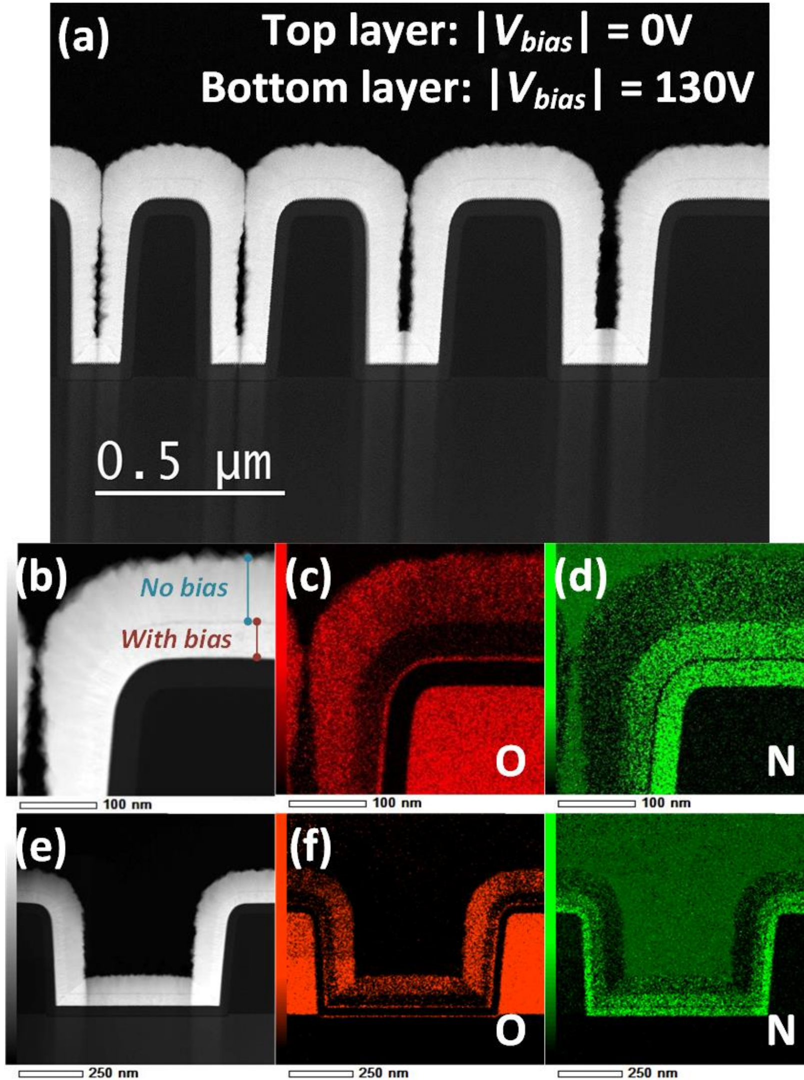

Figure 4.8. (a) High-angle annular dark-field scanning transmission electron microscopy (HAADF-STEM) image of the HfN_x film grown in two steps with different substrate potentials: bottom layer at $|V_{bias}|$ = 130V and top layer with grounded electrode ($|V_{bias}|$ = 0V) (b and e) higher magnification HAADF-STEM images containing both planar and vertical topography and EDX elemental mappings of (c and f) O and (d and g) N. The trench aspect ratio for (b,c and d) was 2:1 and 1:1 for (e,f and g).

Having established that the ρ_e is related to the chemical composition of the HfN_x films in the range of $|V_{bias}|$ up to 130V, the chemical composition of the HfN_x films was investigated on 3D topographies which is relevant for advanced

nanoscale device architectures. The HAADF-STEM image of HfN_x films grown on 3D trench nanostructures is presented in Figure 4.8. A stack of HfN_x films was prepared in a single run with ~45 nm bottom layer grown at $|V_{bias}|$ = 130V and a ~85 nm top layer was grown at $|V_{bias}|$ = 0V, as aforementioned. Magnified HAADF-STEM images for a trench with an aspect ratio of 2:1 and 1:1 are presented in Figure 4.8b,e. The difference in the chemical compositions of the two HfN_x films grown at different values of $|V_{bias}|$ is clearly evident from the EDX elemental mapping (Figure 4.8c,f and 4.8d,g), in agreement with Table 4.1. On planar surfaces, the HfN_x layer grown at $|V_{bias}|$ = 130V was found to contain no O, whereas O was present in abundance in the HfN_x layer grown at $|V_{bias}|$ = 0V (Figure 4.8c,f), in-line with the RBS findings. Moreover, the HfN_x layer grown at $|V_{bias}|$ = 130V was found to be relatively richer in N content as compared to the film grown at $|V_{bias}|$ = 0V (Figure 4.8d,g), also in-line with the RBS results.

Considering the sidewalls of the trenches, a higher O content and relatively lower N content was noted in comparison with planar surfaces at $|V_{bias}|$ = 0V. This relates to the fact that the sidewalls are exposed to a much lower ion flux as compared to the planar surfaces due to directionality of the ions. Strikingly, the sidewalls of HfN_x film grown at $|V_{bias}|$ = 130V appears to contain less oxygen than the planar surfaces of HfN_x film grown at $|V_{bias}|$ = 0V. Similarly, nitrogen appears to be higher in concentration on the sidewalls of the HfN_x film grown at $|V_{bias}|$ = 130V with respect to the planar surfaces of HfN_x film grown at $|V_{bias}|$ = 0V. This may be a consequence of ion bombardment present also on the sidewalls due to ions colliding in the plasma sheath which allows the ions to reach the sidewalls, but with a lower flux and energy. Indeed, the plasma sheath appears not to be fully collisionless as will be addressed in follow-up work on the basis of actual ion energy measurements.

4.4 Conclusions

A plasma-assisted HfN_x ALD process has been reported employing $CpHf(NMe_2)_3$ as the Hf precursor and H_2 plasma as the reducing co-reactant. The application of external rf substrate bias during H_2 plasma half cycle has been addressed in order to study the effects of increase in energy of ions impinging on the surface during film growth. It has been shown that the electrical resistivity of the HfN_x films decreased from $9.0 \cdot 10^{-1}$ Ωcm to $3.3 \cdot 10^{-3}$ Ωcm upon increasing the $|V_{bias}|$ from 0V to 130V respectively. A further increase in $|V_{bias}|$ to 187V led to an increase in film resistivity to $1.0 \cdot 10^{-2}$ Ωcm. Furthermore, we showed that the variations in electrical resistivity with $|V_{bias}|$ correlated with the grain boundary scattering in the films, which significantly decreased upon increasing $|V_{bias}|$ up to

130V. The decrease in electrical resistivity and scattering is the result of a major improvement in chemical composition. The latter stems from a major decrease in the O content from 20.1 at.% at no bias to ≤2 at.% at $|V_{bias}|$ of 130V or higher and associated increase in the Hf(III) oxidation state fraction from 0.65 to 0.82 respectively. Microstructural analyses revealed that the HfN_x films prepared at $|V_{bias}|$ = 130V are more porous than films grown with grounded electrode whereas the lateral grain sizes are similar. On the other hand, the grain boundary scattering increased at $|V_{bias}|$ above 130V primarily due to a major decrease in grain size as well as in-grain crystalline quality. Furthermore, the HfN_x was also deposited at $|V_{bias}|$ = 130V on 3D trench nanostructures. A low O content in the HfN_x film was obtained on the planar as well as vertical regions of the trench structures, attributed to collisions in plasma sheath leading to some ion bombardment on the sidewalls as well. In conclusions, we demonstrate that the energy of bombarding ions during plasma-assisted ALD play a vital role in improving the chemical composition, microstructure and electrical properties of the HfN_x films and may be extended to related nitrides.

References

1. Liu, Y., et al., *Channel shape and interpoly dielectric material effects on electrical characteristics of floating-gate-type three-dimensional fin channel flash memories.* Japanese Journal of Applied Physics, 2015. **54**(4).
2. Pierson, H.O., *Handbook of Refractory Carbides and Nitrides: Properties, Characteristics, Processing and Apps*. 1996: Elsevier Science.
3. Hu, C.K. and J.M.E. Harper, *Copper interconnections and reliability.* Materials Chemistry and Physics, 1998. **52**(1): p. 5-16.
4. Jeong, W., et al., *Characteristics of HfN films deposited by using remote plasma-enhanced atomic layer deposition.* Journal of the Korean Physical Society, 2010. **56**(3): p. 905-910.
5. Kim, H., et al., *Diffusion barrier properties of transition metal thin films grown by plasma-enhanced atomic-layer deposition.* Proceedings of the 29th Conference on the Physics and Chemistry of Semiconductor Interfaces, 2002. **20**(4): p. 1321-1326.
6. Yu, H.Y., et al., *Robust High-Quality HfN-HfO 2 Gate Stack for Advanced MOS Device Applications.* IEEE Electron Device Letters, 2004. **25**(2): p. 70-72.

7. Franklin, A.D., et al., *Carbon Nanotube Complementary Wrap-Gate Transistors.* Nano Letters, 2013. **13**(6): p. 2490-2495.

8. Yu, H.Y., M.F. Li, and D.L. Kwong, *Thermally robust HfN metal as a promising gate electrode for advanced MOS device applications.* IEEE Transactions on Electron Devices, 2004. **51**(4): p. 609-615.

9. Hu, C., et al., *Nature of tunable optical reflectivity of rocksalt hafnium nitride films.* Journal of Physical Chemistry C, 2014. **118**(35): p. 20511-20520.

10. Strømme, M., R. Karmhag, and C.G. Ribbing, *Optical constants of sputtered hafnium nitride films. Intra- and interband contributions.* Optical Materials, 1995. **4**(5): p. 629-639.

11. Malmström, J., S. Schleussner, and L. Stolt, *Enhanced back reflectance and quantum efficiency in Cu(In,Ga)Se 2 thin film solar cells with a ZrN back reflector.* Applied Physics Letters, 2004. **85**(13): p. 2634-2636.

12. Andersson, K.E., M. Veszelei, and A. Roos, *Zirconium nitride based transparent heat mirror coatings —preparation and characterisation.* Solar Energy Materials and Solar Cells, 1994. **32**(2): p. 199-212.

13. Karlsson, B. and C.G. Ribbing. *Optical Properties Of Transparent Heat Mirrors Based On Thin Films Of TiN, ZrN, And HfN*. in *Optical Coatings for Energy Efficiency and Solar Applications*. 1982. Proc. SPIE.

14. Xu, M., et al., *Optical properties of cubic Ti3N4, Zr3N4, and Hf3N4.* Applied Physics Letters, 2006. **89**(15).

15. Becker, J.S., E. Kim, and R.G. Gordon, *Atomic Layer Deposition of Insulating Hafnium and Zirconium Nitrides.* Chemistry of Materials, 2004. **16**(18): p. 3497-3501.

16. Farrell, I.L., et al., *Tunable electrical and optical properties of hafnium nitride thin films.* Applied Physics Letters, 2010. **96**(7).

17. Johansson, B.O., et al., *Reactively magnetron sputtered Hf-N films. I. Composition and structure.* Journal of Applied Physics, 1985. **58**(8): p. 3104-3111.

18. Seo, H.S., et al., *Growth and physical properties of epitaxial HfN layers on MgO(001).* Journal of Applied Physics, 2004. **96**(1): p. 878-884.

19. Kim, Y., et al., *Metal-organic CVD of conductive and crystalline hafnium nitride films.* Chemical Vapor Deposition, 2005. **11**(6-7): p. 294-297.

20. Consiglio, S., et al., *Plasma-assisted atomic layer deposition of conductive hafnium nitride using tetrakis(ethylmethylamino)hafnium for CMOS gate electrode applications.* Journal of the Electrochemical Society, 2008. **155**(3): p. H196-H201.

21. Kim, E.J. and D.H. Kim, *Highly conductive HfN x films prepared by plasma-assisted atomic layer deposition.* Electrochemical and Solid-State Letters, 2006. **9**(8): p. C123-C125.

22. Karwal, S., et al., *Plasma-assisted atomic layer deposition of HfNx: Tailoring the film properties by the plasma gas composition.* Journal of Vacuum Science and Technology A: Vacuum, Surfaces and Films, 2017. **35**(1).

23. Elam, J.W., et al., *Atomic layer deposition of aluminum oxide in mesoporous silica gel.* Journal of Physical Chemistry C, 2010. **114**(41): p. 17286-17292.

24. Haukka, S., et al., *Dispersion and distribution of titanium species bound to silica from TiCl4.* Langmuir, 1993. **9**(12): p. 3497-3506.

25. Lakomaa, E.L., A. Root, and T. Suntola, *Surface reactions in Al2O3 growth from trimethylaluminium and water by atomic layer epitaxy.* Applied Surface Science, 1996. **107**: p. 107-115.

26. Keranen, J., et al., *Surface-controlled gas-phase deposition and characterization of highly dispersed vanadia on silica.* Journal of Physical Chemistry B, 2003. **107**(39): p. 10773-10784.

27. Anders, A., *A structure zone diagram including plasma-based deposition and ion etching.* Thin Solid Films, 2010. **518**(15): p. 4087-4090.

28. Martinu, L., O. Zabeida, and J.E. Klemberg-Sapieha, *Chapter 9 - Plasma-Enhanced Chemical Vapor Deposition of Functional Coatings*, in *Handbook of Deposition Technologies for Films and Coatings (Third Edition)*. 2010, William Andrew Publishing: Boston. p. 392-465.

29. Walton, S.G. and J.E. Greene, *Chapter 2 - Plasmas in Deposition Processes A2 - Martin, Peter M*, in *Handbook of Deposition Technologies for Films and Coatings (Third Edition)*. 2010, William Andrew Publishing: Boston. p. 32-92.

30. Profijt, H.B., M.C.M. Van De Sanden, and W.M.M. Kessels, *Substrate-biasing during plasma-assisted atomic layer deposition to tailor metal-oxide thin film growth.* Journal of Vacuum Science and Technology A: Vacuum, Surfaces and Films, 2013. **31**(1).

31. Knoops, H.C.M., et al., *Atomic Layer Deposition of Silicon Nitride from Bis(tert-butylamino)silane and N<inf>2</inf> Plasma.* ACS Applied Materials and Interfaces, 2015. **7**(35): p. 19857-19862.

32. Knoops, H.C.M., K. De Peuter, and W.M.M. Kessels, *Redeposition in plasma-assisted atomic layer deposition: Silicon nitride film quality ruled by the gas residence time.* Applied Physics Letters, 2015. **107**(1).

33. Profijt, H.B., et al., *Plasma-assisted atomic layer deposition: Basics, opportunities, and challenges.* Journal of Vacuum Science and Technology A: Vacuum, Surfaces and Films, 2011. **29**(5).

34. Knoops, H.C.M., et al., *Optical modeling of plasma-deposited ZnO films: Electron scattering at different length scales.* Journal of Vacuum Science & Technology A, 2015. **33**(2): p. 021509.

35. Timofeeva, I.I. and L.K. Shvedova, *Microhardness and thermal expansion of transition metal nitrides within the 80-300K temperature range.* Izvestiya Akademii Nauk SSSR, Neorganicheskie Materialy, 1972. **8**(6): p. 1169-1170.

36. Wang, W., T. Nabatame, and Y. Shimogaki, *Preparation of conductive HfN by post rapid thermal annealing-assisted MOCVD and its application to metal gate electrode.* Microelectronic Engineering, 2008. **85**(2): p. 320-326.

37. Klug, H.P. and L.E. Alexander, *X-Ray Diffraction Procedures: For Polycrystalline and Amorphous Materials*. 1974: Wiley.

38. Liao, M.Y., et al., *Growth and stress evolution of hafnium nitride films sputtered from a compound target.* Journal of Vacuum Science and Technology A: Vacuum, Surfaces and Films, 2004. **22**(1): p. 214-220.

39. Ovanesyan, R.A., D.M. Hausmann, and S. Agarwal, *Low-Temperature Conformal Atomic Layer Deposition of SiN<inf>x</inf> Films Using Si<inf>2</inf>Cl<inf>6</inf> and NH<inf>3</inf> Plasma.* ACS Applied Materials and Interfaces, 2015. **7**(20): p. 10806-10813.

40. Ponomarev, M.V., et al., *Controlling the resistivity gradient in aluminum-doped zinc oxide grown by plasma-enhanced chemical vapor deposition.* Journal of Applied Physics, 2012. **112**(4): p. 043708.

41. Kirsch, P.D., et al., *Electrical and spectroscopic comparison of HfO 2/Si interfaces on nitrided and un-nitrided Si(100).* Journal of Applied Physics, 2002. **91**(7): p. 4353-4363.

42. Kornilov, A.N., et al., *The enthalpy of formation of hafnium dioxide.* The Journal of Chemical Thermodynamics, 1975. **7**(1): p. 21-26.

43. Mah, A.D. and N.L. Gellert, *Heats of formation of niobium nitride, tantalum nitride and zirconium nitride from combustion calorimetry.* Journal of the American Chemical Society, 1956. **78**(14): p. 3261-3263.

44. Shinkai, S. and K. Sasaki, *Influence of sputtering parameters on the formation process of high-quality and low-resistivity HfN thin film.* Japanese Journal of Applied Physics, Part 1: Regular Papers and Short Notes and Review Papers, 1999. **38**(4 A): p. 2097-2102.

45. Wang, W., T. Nabatame, and Y. Shimogaki, *Interface structure of HfNx/SiO2 stack grown by MOCVD using TDEAHf precursor.* Surface Science, 2005. **588**(1-3): p. 108-116.

46. Jang, J.H., et al., *Role of Carbon on Resistivity and Structure of Hf Cx Ny Films Grown by Low Temperature MOCVD.* Journal of the Electrochemical Society, 2009. **156**(1): p. H76-H79.

47. Thompson, C.V., *Structure evolution during processing of polycrystalline films.* Annual Review of Materials Science, 2000. **30**: p. 159-190.

48. Pelleg, J., et al., *Reactive-sputter-deposited TiN films on glass substrates.* Thin Solid Films, 1991. **197**(1-2): p. 117-128.

49. Oh, U.C. and J.H. Je, *Effects of strain energy on the preferred orientation of TiN thin films.* Journal of Applied Physics, 1993. **74**(3): p. 1692-1696.

Appendix 4

A. HfN_x ALD process

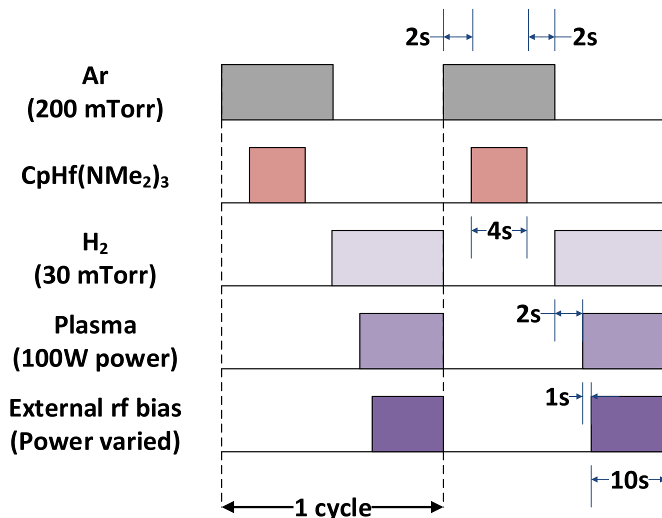

Figure A4.1. Time sequence for the complete ALD cycles of HfN_x using $CpHf(NMe_2)_3$ and H_2 plasma depicting the application of an external rf substrate bias during the H_2 plasma step. A plasma stabilization time of 1s was used and can be neglected. Time intervals are not drawn to scale.

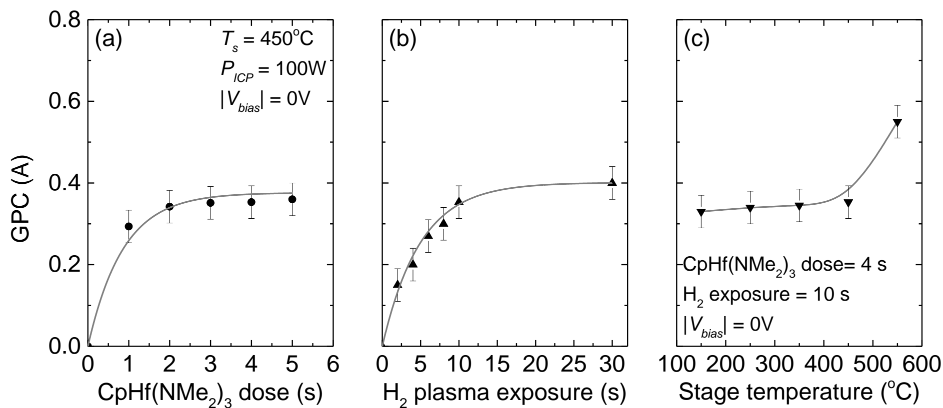

Figure A4.2. Growth per cycle (GPC) (Å) for HfN_x films prepared at $|V_{bias}|$ = 0V as a function of (a) $CpHf(NMe_2)_3$ dose time and (b) H_2 plasma exposure time. The $CpHf(NMe_2)_3$ dose, H_2 plasma exposure and purge times under saturation conditions were 4 s, 10 s and 2 s respectively. (c) GPC(Å) for the HfN_x films prepared under saturation conditions as a function of the stage temperature showing an abrupt increase above 450°C. Lines serve as a guide to the eye.

Figure A4.3a shows a linear thickness increase with number of ALD cycles for HfN_x films prepared at various values of $|V_{bias}|$. Furthermore, the ALD process was found to saturate using a $CpHf(NMe_2)_3$ dose time of 4 s at all values of $|V_{bias}|$ investigated (Figure A4.3b). Therefore, the application of external rf substrate bias does not affect the self-saturation behavior of the ALD process. The HfN_x films were also prepared at $|V_{bias}|$ = 0V and at $|V_{bias}|$ = 187V on 8-inch Si wafers and the thickness non-uniformity was evaluated (Figure A4.3c). The thickness non-uniformity was deduced by taking the ratio between standard deviation and average film thickness (1-sigma). A similar thickness non-uniformity of 9.1% and 7.8% was obtained for the HfN_x films prepared with grounded electrode and at $|V_{bias}|$ = 187V respectively.

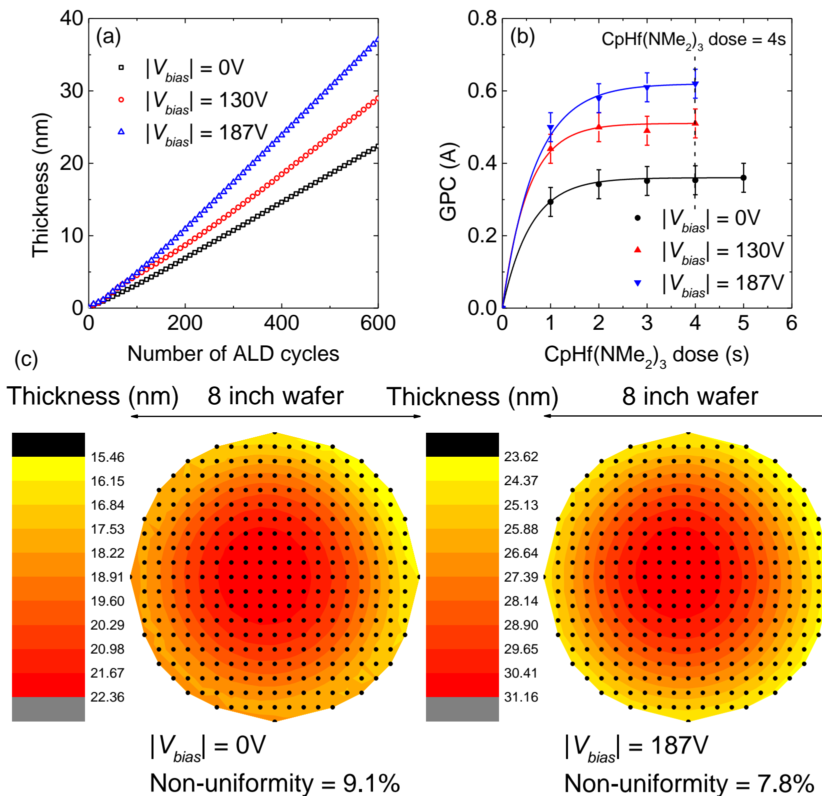

Figure A4.3. (a) HfN_x film thickness as a function of number of ALD cycles prepared for various values of $|V_{bias}|$; (b) GPC(Å) as a function of $CpHf(NMe_2)_3$ dose time for HfN_x films prepared at various values of $|V_{bias}|$; (c) thickness uniformity maps on 8-inch Si wafer for HfN_x films prepared with grounded electrode ($|V_{bias}|$ = 0V) and at $|V_{bias}|$ = 187V showing a similar thickness non-uniformity in both cases. The black points on the wafer are the actual measurement points with 5 mm edge exclusion.

B. Modeling of HfN_x dielectric functions using spectroscopic ellipsometry

The dielectric functions can be modelled using one Drude and two Lorentz oscillators:

$$\varepsilon(E) = \varepsilon_1(E) + i\varepsilon_2(E) = \varepsilon_\infty - \overbrace{\frac{E_p^2}{E^2 - i\Gamma_D E}}^{Drude} + \sum_{j=1}^{2} \overbrace{\frac{S_j E_{0j}^2}{E_{0j}^2 - E_j^2 + iE_j\Gamma_j}}^{Lorentz} \quad (1)$$

where, ε_∞ represents transitions at higher energy which are not accounted in Lorentz oscillators, E_p is plasma energy and Γ_D is the damping factor for Drude oscillator. The Lorentz oscillators are centered at E_o which corresponds to the resonance frequency, while S indicates the strength of the oscillators and Γ is the damping factor for the Lorentz oscillators.

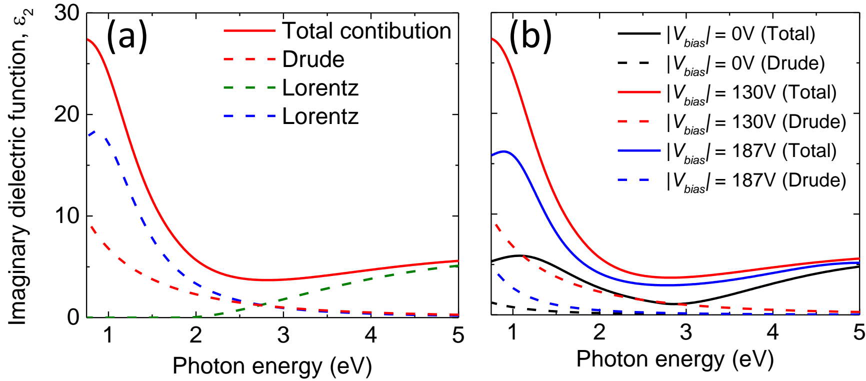

Figure A4.4. Imaginary dielectric function ε_2 for the δ-HfN_x films prepared at (a) $|V_{bias}|$ = 130V obtained *via* fitting of the ellipsometry data with parameterization including one Drude and two Lorentz oscillators and (b) various values $|V_{bias}|$. The individual Drude oscillators for the films are also given revealing an increase in Drude absorption by applying an external rf substrate bias.

Table A4.1. SE fitting parameter values for one Drude and two Lorentz oscillators for the δ-HfN film prepared at $|V_{bias}|$ = 130V.

$\lvert V_{bias}\rvert$ (V)		130
ε_∞		4.15
E_p (eV)		1.7
Lorentz oscillator 1	S (eV)	19.4
	Γ (eV)	1.2
	E_o (eV)	1.1
Lorentz oscillator 2	S (eV)	5.4
	Γ (eV)	4.3
	E_o (eV)	5.7

Knoops *et al.* described that the insights into grain boundary scattering can be gained by probing opto-electronic properties using SE [1]. In Figure A4.4, the imaginary part of the dielectric function ε_2 and the corresponding Drude absorption for the HfN_x films grown at various values of $|V_{bias}|$ are presented. An optical resistivity (ρ_{op}) of $(5.9\pm0.1)\cdot10^{-3}$ Ωcm was deduced from the magnitude of Drude absorption for the HfN_x film grown with grounded electrode ($|V_{bias}|$ = 0V). An increase in $|V_{bias}|$ to 130V led to an increase in the magnitude of Drude absorption, signifying an increase in the in-grain conduction electron density. An ρ_{op} of $(9.0\pm0.2)\cdot10^{-4}$ Ωcm was deduced for the HfN_x film grown at $|V_{bias}|$ = 130V. A further increase in the $|V_{bias}|$ to 187V led to a decrease in the magnitude of Drude absorption and an increase in ρ_{op} to $(1.7\pm0.1)\cdot10^{-3}$ Ωcm. In addition, the interaction distance (d_{int}) of the incident light with the HfN_x films was calculated using the HfN effective mass of 0.88 [2], the fermi velocity $\left(\nu_e = \hbar(3\pi^2 N)^{1/3}/m^*\right)$ and a photon energy of 0.75 eV (lower limit of SE) in the same manner as described by Knoops *et al.* [1]. An d_{int} of 2.3 nm, 3.3 nm and 2.9 nm were deduced for HfN_x films grown at $|V_{bias}|$ of 0V, 130V and 187V respectively. In-view of the small interaction distance as compared to the lateral grain size of ~20-25 nm of the HfN_x films (as will be explained in microstructural characterization section), it is plausible to use the difference between electrical

and optical resistivity in order to judge the extent of scattering at the grain boundaries as a function of $|V_{bias}|$.

C. Chemical composition analyses of HfN_x films using X-ray photoelectron spectroscopy

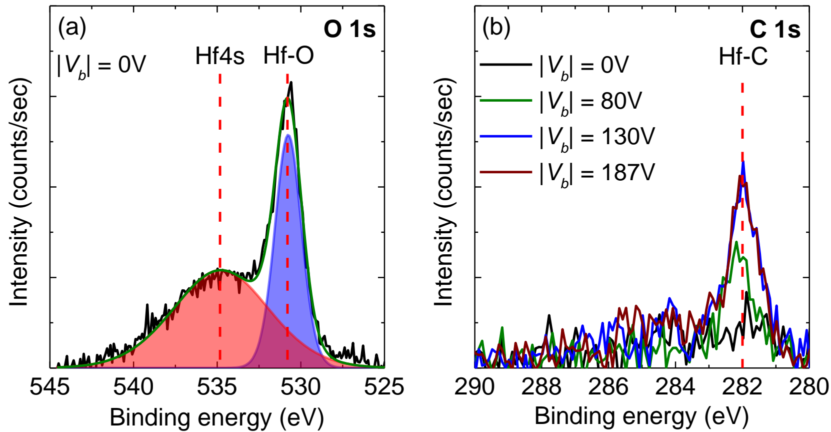

Figure A4.5. (a) De-convoluted O 1s XPS spectrum for HfN_x film prepared at $|V_{bias}|$ = 0V showing the presence of Hf-O bonds and (b) C 1s XPS spectra for HfN_x films prepared at various values of $|V_{bias}|$ showing an increase in the peak intensity of Hf-C bonds with an increase in $|V_{bias}|$.

Table A4.2. Corresponding peak assignment, binding energies and full width half maximum for the Hf, N, O and C spectral lines used to deconvolute the peaks, measured by XPS.

Spectral line	Peak designation	Binding energy (eV)	FWHM (eV)	Reference
Hf $4f_{7/2}$	Hf(IV)	16.0	1.6	[3, 4]
Hf $4f_{7/2}$	Hf(III)	14.9	1.6	[5]
N 1s	Hf(III)N	397.5	1.5	[6]
N 1s	Hf(IV)N	396.5	1.6	[7]
O 1s	HfO_x	530.8	1.9	[8]

C 1s	HfC_x	282	1.2	[9]

D. Variation of GPC (Å) with GPC (Hf atoms nm^{-2})

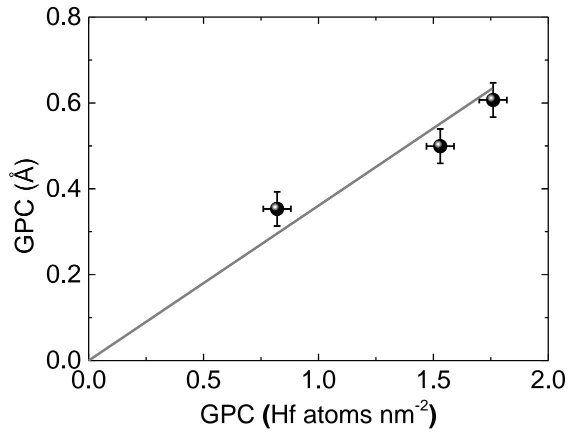

Figure A4.6. GPC in terms of thickness as a function of GPC in terms of Hf atoms deposited per nm^2 illustrating a proportional dependence.

E. GIXRD patterns for HfN_x films as a function of $|V_{bias}|$

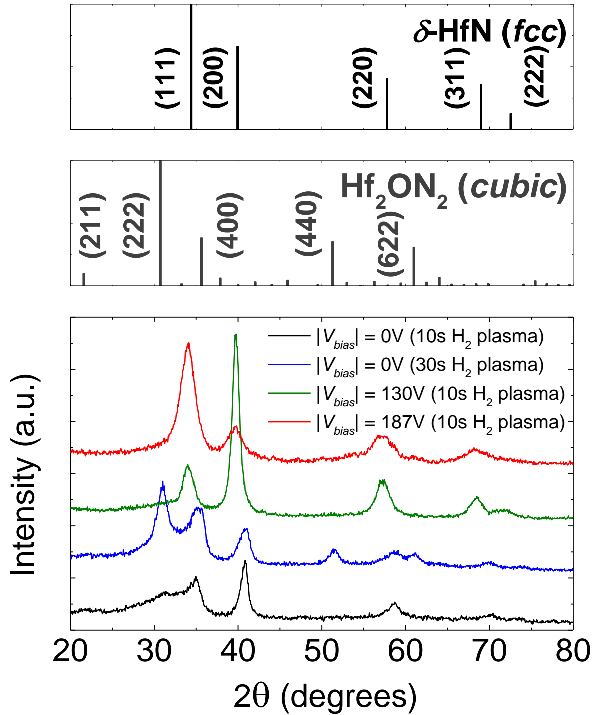

Figure A4.7. Grazing incindence X-ray diffractograms for ~75 nm thick HfN_x films prepared at various values of $|V_{bias}|$ referenced with powder fcc δ-HfN and *cubic* Hf_2ON_2 XRD patterns.

F. HAADF-STEM images for HfN_x films during nucleation phase

The development of microstructure was studied during the nucleation phase of film growth by preparing ~15 nm of HfN_x films on Si_3N_4 TEM windows that are coated with ~5 nm ALD SiO_2. Figure A4.8 shows the HAADF-STEM images of the HfN_x layers deposited at various values of $|V_{bias}|$. The HfN_x film grown at $|V_{bias}|$ = 130V exhibits a lateral grain size of 7.5±2.0 nm whereas the film grown at $|V_{bias}|$ = 187V was found to be nanocrystalline in nature. In addition, the selected area electron diffraction patterns (SAED) were acquired from 1.3 μm diameter areas for the corresponding HfN_x films (insets in Figure A4.8). Interestingly, no significant difference in crystallographic texture was observed in the nucleation layer for both the HfN_x films. However, the HfN_x film grown at $|V_{bias}|$ = 130V exhibits discontinuous diffraction rings signifying the formation of relatively *large* crystallites whereas a more continuous diffraction pattern was obtained for the

HfN_x film grown at $|V_{bias}|$ = 187V. This result implies that at $|V_{bias}|$ = 187V, relatively *small* lateral crystallites are formed.

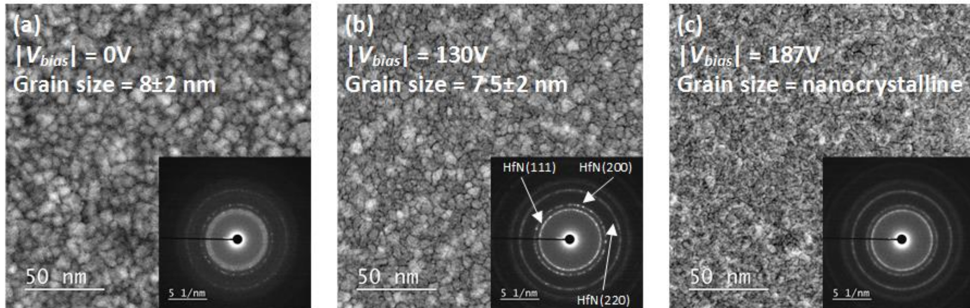

Figure A4.8. Top-view high-angle annular dark-field scanning transmission electron microscope (HAADF-STEM) images for ~15 nm thick HfN_x films prepared (a) $|V_{bias}|$ = 0V (b) $|V_{bias}|$ = 130V and (c) $|V_{bias}|$ = 187V. Inset depicts the corresponding selected area electron diffraction (SAED) patterns.

References

1. Knoops, H.C.M., et al., *Optical modeling of plasma-deposited ZnO films: Electron scattering at different length scales.* Journal of Vacuum Science & Technology A, 2015. **33**(2): p. 021509.
2. Strømme, M., R. Karmhag, and C.G. Ribbing, *Optical constants of sputtered hafnium nitride films. Intra- and interband contributions.* Optical Materials, 1995. **4**(5): p. 629-639.
3. Kang, C.S., et al., *Bonding states and electrical properties of ultrathin HfOxN y gate dielectrics.* Applied Physics Letters, 2002. **81**(14): p. 2593-2595.
4. Arranz, A., *Synthesis of hafnium nitride films by 0.5-5 keV nitrogen implantation of metallic Hf: An X-ray photoelectron spectroscopy and factor analysis study.* Surface Science, 2004. **563**(1-3): p. 1-12.
5. Wang, W., T. Nabatame, and Y. Shimogaki, *Preparation of conductive HfN by post rapid thermal annealing-assisted MOCVD and its application to metal gate electrode.* Microelectronic Engineering, 2008. **85**(2): p. 320-326.
6. Shinkai, S. and K. Sasaki, *Influence of sputtering parameters on the formation process of high-quality and low-resistivity HfN thin film.*

Japanese Journal of Applied Physics, Part 1: Regular Papers and Short Notes and Review Papers, 1999. **38**(4 A): p. 2097-2102.

7. Wang, W., T. Nabatame, and Y. Shimogaki, *Interface structure of HfNx/SiO2 stack grown by MOCVD using TDEAHf precursor.* Surface Science, 2005. **588**(1-3): p. 108-116.

8. Kirsch, P.D., et al., *Electrical and spectroscopic comparison of HfO 2/Si interfaces on nitrided and un-nitrided Si(100).* Journal of Applied Physics, 2002. **91**(7): p. 4353-4363.

9. Jang, J.H., et al., *Role of Carbon on Resistivity and Structure of Hf Cx Ny Films Grown by Low Temperature MOCVD.* Journal of the Electrochemical Society, 2009. **156**(1): p. H76-H79.

Chapter 5

Atomic Insights into the Oxygen Incorporation in Atomic Layer Deposited Conductive Nitrides and its Mitigation by Energetic Ions*

Abstract

Oxygen is often detected as impurity in metal and metal nitride films prepared by atomic layer deposition (ALD) and its presence has profound and adverse effects on the material properties. In this work, we present the case study of HfN_x films prepared by plasma-assisted ALD by alternating exposures of $CpHf(NMe_2)_3$ and H_2 plasma. First, we identify the primary source of O contamination in the film. Specifically, we find that the extent of O incorporation in HfN_x films is determined by the flux of background H_2O/O_2 residual gases reaching the HfN_x surface during the ALD process and leads to the formation of Hf-O bonds. Then, we report on the decrease in the concentration of Hf-O bonds in the film upon application of an external rf substrate bias during the H_2 plasma step. The experimental work is accompanied by first principles calculations to gain insights into the O incorporation and its mitigation upon the impingement of energetic ions on the surface. Specifically, we find that the dissociative binding of H_2O on a bare HfN surface is highly favoured, resulting in surface Hf–OH groups and concomitant increase in the oxidation state of Hf. We also show that energetic cations (H^+, H_2^+ and H_3^+) lead to the dissociation of surface Hf-OH bonds, H_2O formation, and its subsequent desorption from the surface. The latter is followed by reduction of the Hf oxidation state, presumably by H· radicals. The atomic-level understanding obtained in this work on O incorporation and its abstraction are expected to be crucial to prevent O impurities in the HfN_x films and contribute to the fabrication of other technologically relevant low resistivity ALD-grown transition metal nitride films.

---

* Saurabh Karwal, Bora Karasulu, Harm C. M. Knoops, Vincent Vandalon, Wilhelmus M.M. Kessels and Mariadriana Creatore (submitted)

5.1 Introduction

Atomic layer deposition (ALD) has emerged as the method of choice for the synthesis of ultra-thin, uniform and highly conformal layers, required in the fabrication of advanced nanoscale device architectures [1-4]. At the same time, control over the film properties in terms of chemical composition and microstructure is highly important. When specifically referring to the metal and metal nitride films prepared by ALD, oxygen is often detected as impurity [5-7]. An interesting class of materials to evaluate the effect of oxygen contamination is the one of conductive transition metal nitride (TMN) films, such as TiN_x, TaN_x, MoN_x, HfN_x. In fact, oxygen contamination can be directly related to the decrease in electrical conductivity [8-26], as illustrated in the literature over-view for various TMN films (appendix Section A, Table A5.1) [8-28]. In particular, Musschoot *et al.* and Langereis *et al.* reported on the inevitable oxygen incorporation in TiN_x and TaN_x films and suggested residual H_2O in the reactor background and/or process gases as potential sources of oxygen contamination in the films [18, 19]. However, these observations have not been followed by in-depth analysis of the surface reactivity of TMN films towards H_2O/O_2.

Recently, we have reported on the growth of the conductive phase of hafnium nitride (δ-HfN) by adopting $CpHf(NMe_2)_3$ as Hf(IV) precursor and H_2 plasma as co-reactant [29]. We observed that the HfN_x films contained 20 at.% oxygen [13]. Furthermore, due to the formation of Hf-O bonds, a low Hf(III) oxidation state fraction of 0.65 was detected, contributing to a rather high film resistivity of 0.9 Ω·cm [13]. Moreover, we have also reported a decrease in the film resistivity by two orders of magnitude down to $3.3 \cdot 10^{-3}$ Ω·cm upon the application of an external rf substrate bias during the H_2 plasma step with a time-averaged potential value (V_{bias}) of -130V [12]. This resulted from a decrease in oxygen content to below 2.0 at.% and a correlated increase in the Hf(III) fraction up to 0.82 [12]. These results suggest a correlation between the decrease in oxygen content in the films and the increase in the average energy of incident ions (E_{ion}). However, the mechanism of the suppression of oxygen content enabled by energetic ions was not explored.

In this work, we first elucidate the primary source of oxygen incorporation in the film and study the dependence of oxygen content as a function of the total ALD cycle time. We find a gradual increase in the oxygen content when the ALD cycle time is increased. Subsequently, we demonstrate a gradual decrease in the density of Hf-O bonds in the HfN_x films with an increase in E_{ion}, enabled by the application of external rf substrate bias. By means of first-principles density functional theory (DFT) calculations, we provide an atomistic insight into the kinetics of chemisorption of gaseous H_2O/O_2 on the pristine HfN surface that leads

to formation of surface Hf–OH groups. Subsequently, we show that energetic cations in the H_2 plasma trigger the dissociation of surface Hf-OH bonds and led to H_2O formation, followed by its desorption. In addition, we hypothesize that the H· radicals in the H_2 plasma reduce Hf(IV) to Hf(III) subsequent to H_2O desorption, in-line with our previous report [12]. The atomic-level understanding of the oxygen incorporation and the underlying mechanism of its removal provided here is expected to be key in devising efficient approaches for preventing oxygen impurities in the ALD-grown metal nitride and metal films.

5.2 Experimental section

The plasma-assisted ALD process of HfN_x films was carried out in an Oxford Instruments FlexAL ALD reactor that is equipped with an inductively coupled remote plasma (ICP) source with an alumina dielectric tube [6, 30]. A base pressure of 10^{-6} Torr was achieved in the reactor chamber using a turbo-molecular pump before every deposition. The metal-organic Hf(IV) precursor $CpHf(NMe_2)_3$ was used and an H_2 plasma served as the reducing co-reactant. The details of the recipe can be found elsewhere [13]. An ALD cycle under saturation conditions comprised of a $CpHf(NMe_2)_3$ pulse of 4 s and H_2 plasma exposure of 10 s, while keeping the purge steps of 2 s after every half cycle (appendix Section B, Figure A5.1). An external rf substrate bias was applied during the H_2 plasma exposure. As a result of bias application, a time-averaged negative potential with respect to ground develops at the substrate (V_{bias}) [12, 31]. The magnitude of the developed V_{bias} was tuned by varying the applied rf power transmitted to the substrate holder as previously reported [12]. Furthermore, as a result of negative substrate potential, the average energy of exclusively the cationic species in the plasma is enhanced by accelerating them towards the HfN surface. Si(100) with a diameter of 100 mm and with 450 nm SiO_2 atop was used as the substrate.

X-ray photoelectron spectroscopy (XPS) measurements were performed using a Thermoscientific K-Alpha KA1066 system equipped with a monochromatic Al Kα (hν = 1486.6 eV) source in order to study the chemical bonds and the oxidation states of the elements present in the film. Rutherford backscattering spectrometry (RBS) was performed using 1900 keV $^4He^+$ ions (Detect99) with two detectors at scattering angles of 170° and 150° in order to study the chemical composition of the HfN_x layers.

All electronic structure calculations were done using the projector augmented wavefunction (PAW) [32, 33] as implemented in Vienna Ab Initio Simulation Package (VASP, v.5.3.5) [34-37]. Generalized gradient approximation (GGA) to DFT [38, 39] was used jointly with the Perdew−Burke−Ernzerhof (PBE) exchange

correlation functional [40, 41]. DFT(PBE)-D3 corrections with Becke-Jonson damping [42] were employed to account for Van der Waals interactions on an empirical basis (see appendix section C1 for further computational details).

5.3 Results and discussion

Our initial experiments were focused on the investigation of the primary source of oxygen incorporation in the HfN_x films. This was probed by adding a pump-down step following the H_2 plasma exposure in order to bring the reactor down to the vacuum base pressure (appendix Section B, Figure A5.1). The duration of the pump-down step was varied from 0 s to 80 s, thereby increasing the total ALD cycle time from 20 s to 100 s. This additional pump-down step exposed the HfN_x surface only to the residual gases in reactor background. Figure 5.1a shows the O 1s XPS spectra of the HfN_x films as a function of total ALD cycle time. A gradual increase in Hf-O peak intensity is observed when increasing the total ALD cycle time, leading to a steady decrease in Hf(III) fraction from 0.65±0.02 to 0.47±0.02 . This result suggests that oxygen content in the HfN_x layers is determined by the total flux of residual H_2O/O_2 gases in the reactor background reaching the HfN_x surface. In every ALD cycle, this pristine HfN_x surface is exposed to the vacuum conditions for a relatively long time, making it susceptible to oxidation even at a vacuum base pressure of 10^{-6} Torr. Relevantly, Kroll *et al.* showed that the oxygen incorporation in a-Si:H films prepared by plasma-enhanced CVD was enhanced at lower deposition rates [17]. The reactor outgassing, i.e. release of residual gases, was identified as one of the primary reason for oxygen contamination [17]. The lower the deposition rate of a-Si:H films, the more important is the flux of outgassed residual gases. In our case, in order to illustrate that even very low background pressures can lead to significant oxygen incorporation in the film, the flux of H_2O molecules impinging on the HfN_x surface was calculated using the Hertz-Knudsen equation (see appendix Section B). This calculation reveals that a significant O content in the film can result even from a very low background H_2O partial pressure.

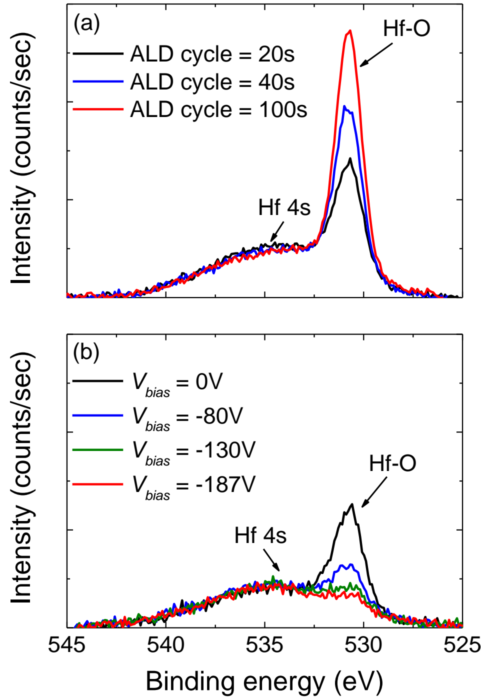

Figure 5.1. O 1s XPS spectra for the (a) HfN_x films prepared with grounded substrate (V_{bias} = 0V) showing an increase in the peak intensity of Hf-O bonds as a function of ALD cycle time. The difference in ALD cycle time is due to an extension of the pump-down time of the reactor. (b) HfN_x films grown at various values of V_{bias} illustrating a steady decrease in the Hf-O peak intensity upon increasing the V_{bias} from 0V to -130V and above.

The effect of application of external rf substrate bias on the oxygen content in the HfN_x films was subsequently investigated. The HfN_x films were prepared using a H_2 plasma exposure of 10 s (no pump-down step) and the magnitude of V_{bias} was gradually increased from 0V to -187V during the H_2 plasma half cycle. Figure 5.1b shows the Hf-O peak intensity as a function of the value of V_{bias}. Interestingly, the Hf-O peak intensity significantly decreased upon increasing the V_{bias} from 0V to -80V, suggesting a decrease in the density of Hf-O bonds. Moreover, an increase in the V_{bias} to -130V or higher led to a saturation in decrease of Hf-O peak intensity, yielding an oxygen content below 2.0 at.% as determined by RBS [12]. Energetic ions may lead to the physical sputtering of oxygen. In the case of sputtering, a decrease in the areal density of nitrogen atoms is also expected to occur in parallel. In contrast, we reported an increase in the areal density of nitrogen atoms per cycle from 0.71±0.03 atoms nm^{-2} at V_{bias} = 0V to 1.53±0.08 atoms nm^{-2}

at V_{bias} = -130V [12]. This cannot be simply explained by sputtering. Therefore, a preferential abstraction of oxygen (and containing groups) is expected as a result of the impingement of energetic ions on the surface of growing film. The seminal works of Sigmund and Steinbrüchel show that ca. 10 times higher ion energy values than the bond energy value is required in order to dissociate molecular bonds, due to the inefficient transfer of the ion energy to the film surface [43, 44]. Following this, Kanarik *et al.* recently reported on the requirement of Ar^+ ions with an E_{ion} of ca. 50 eV in order to enable the dissociation of Si-Si bonds with a bond energy of 2.3 eV in order to facilitate the atomic layer etching of Si [45, 46]. In our case, assuming a similar energy transfer factor, an E_{ion} of ~90-100 eV seems adequate to dissociate the Hf-O bonds with a high bond energy of 8.3 eV, as will be shown later [47].

In order to gain insights into the oxygen incorporation in the HfN_x films and its mitigation upon delivery of energetic ions to the surface, detailed DFT calculations were carried out. To this end, the dissociative binding of H_2O and O_2 on a bare HfN surface was simulated. Three δ-HfN models were generated for DFT simulations: one HfN(200) surface with equivalent N- and Hf- termination and two HfN(111) surface with either Hf- or N- termination (see appendix Section C2, Figure A5.2 for the discussion on HfN surface termination). These surfaces are in-line with our experimental observations on the growth of polycrystalline δ-HfN_x films, with the co-existence of HfN(200) and HfN(111) orientations at V_{bias} = 0V and V_{bias} = -130V [12]. For brevity, we discuss here the results for the case of HfN(200) surface, whereas similar results for Hf(111) surface can be found in the appendix (Section D2).

Ab initio molecular dynamics (AIMD) simulations were performed to generate canonical (NVT) ensembles at 1000 K in vacuum environment, using 1 fs time step for a set of at least 3.0 ps trajectories. The model system used for bare HfN(200) surface contained 32 Hf and 32 N atoms on the top-most surface (appendix, Section C2). A total of 16 H_2O molecules were placed atop the HfN(200) surface, providing a surface coverage ratio of one H_2O molecule per two surface Hf sites (i.e. Hf:O=2:1). MD simulations suggest that following a thermal adsorption process, H_2O molecules bind exclusively to Hf atoms, leading to the formation of Hf-OH bonds (appendix Section D2, Figure A5.3- A5.4), supporting the XPS results of Figure 5.1a. Furthermore, the dissociative adsorption of H_2O molecules could proceed via two routes. The first involves the combination of two H_2O molecules to yield a H_2 molecule, with the two -OH groups easily binding on two Hf(III) sites (Eqn. 1). The second route involves the binding of one -OH group at the Hf-site, whereas the additional H is transferred to the neighbouring N-site (Eqn. 2).

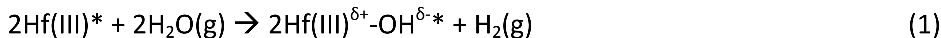

$$2Hf(III)^* + 2H_2O(g) \rightarrow 2Hf(III)^{\delta+}\text{-}OH^{\delta-*} + H_2(g) \quad (1)$$

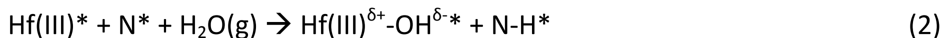

$$Hf(III)^* + N^* + H_2O(g) \rightarrow Hf(III)^{\delta+}\text{-}OH^{\delta-*} + N\text{-}H^* \quad (2)$$

*Denotes surface species, whereas partial charges are represented by $^{\delta+}$,$^{\delta-}$. Partial charges are only limited to the surface as Hf(III)-N bonds are present in the bulk.

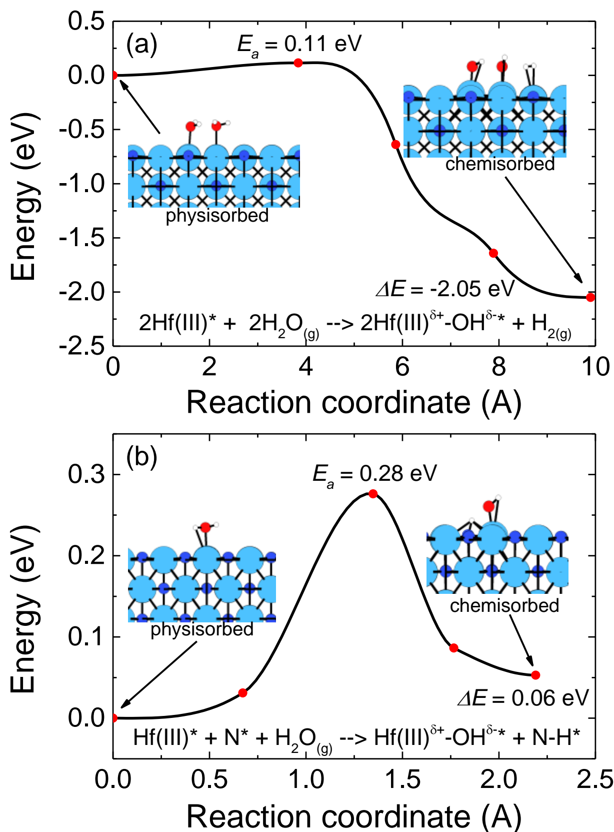

Figure 5.2. DFT/PBE-D3 level minimum-energy paths (MEPs) for the thermal adsorption of H_2O molecule(s) on the bare HfN(200) surface following the pathways as described in (a) Eqn. 1 and (b) Eqn. 2. Color code: cyan: Hf; blue: N; red: O; white: H.

AIMD simulations suggest route 1 is most likely to occur, as concluded from the released H_2 molecules and the absence of amine groups (N-H) (see appendix Section D2, Figures A5.3-A5.4 for snapshots from the relevant MD trajectories).

For a more quantitative comparison, the climbing-image nudged elastic band (CI-NEB) method was utilized for concerted binding of two H_2O molecules on a pristine HfN(200) surface following each pathway. Figure 5.2 shows the resulting minimum-energy paths (MEPs) revealing that unlike the second pathway (Eqn. 2), which has a high activation energy (E_a = 0.28 eV), the first one (Eqn. 1) is both kinetically and thermodynamically highly feasible (E_a = 0.11 eV and ΔE = -2.05 eV), in-line with the above AIMD results.

Based on the AIMD and NEB results, it can be concluded that the binding of H_2O on a pristine HfN surface is expected to proceed via route 1, leading to surface Hf-OH groups. Furthermore, the low E_a agrees well with the easy incorporation of oxygen in the HfN_x films prepared by plasma-assisted ALD with the grounded electrode as discussed earlier. It is worth mentioning that the reverse reaction (i.e. associative desorption of H_2O) is energetically unfeasible, involving high energy barriers and high endothermicity. The latter conclusion falls in line with the high bond energy for Hf-O bonds (i.e. 8.3 eV) [47], rendering surface -OH groups thermodynamically stable.

It should be noted that only the overall reaction for hydroxylation of bare HfN surface is presented in Eqn. 1, whereas the hypothesized redox half reactions and related discussion can be found in the appendix (Section D2, Eqns. S2-S5).

Alongside the background H_2O, the dissociative binding of gaseous O_2 on HfN surface was also investigated (see appendix Section D3 for detailed discussion, Figure A5.5). The dissociative binding of O_2 on HfN surface is found to be kinetically hindered (E_a = 0.25 eV) when compared to chemisorption of H_2O.

The effect of energetic ions on surface functionalization was investigated next. First, the binding energies of distinct species in a H_2 plasma towards surface –OH group was determined using static ab initio DFT calculations, wherein the plasma species are manually attached to the surface (i.e. without energetic ions). For simplicity, the HfN(200) surface was assumed to be fully hydroxylated (with Hf/O=1:1), along with a fully oxygenated one (with Hf/O=2:1) for comparison purposes (see appendix Section E1, Figure A5.6 for further discussion). Bader charge analysis [48, 49] reveals that the binding of 32 –OH groups leads to an increase in the total charge of HfN slab by ca. 16e, in-line with the partial oxidation of Hf(III) to $Hf(III)^{\delta+}$ (see note [50] for a detailed discussion).

Based upon the experimental work of Sode *et al.* [51], a H_2 plasma discharge is expected to contain H^-, H^+, H_2^+ and H_3^+ ions and H· radicals species. Table 5.1 summarizes the computed binding energies of all the possible H_2 plasma species with the surface –OH groups at the PBE-D3 level. Furthermore, the corresponding

reaction products as a result of their binding with surface –OH groups are also reported.

Table 5.1. DFT/PBE-D3 level binding energies (E_b) of various hydrogen-containing plasma species on a hydroxylated HfN surface and the type of volatile product(s) being formed. The most reactive species (i.e. cations), their E_b and type of products are given in bold. Only a single adsorbent species is considered for computing the E_b of each adsorbing species.

Species	E_b [eV][a]	Reaction product(s)
H^- / H / $\mathbf{H^+}$	0.64 / -1.61 / **-4.26**	H_2 / H_2 / $\mathbf{H_2O}$
H_2^- / H_2 / $\mathbf{H_2^+}$	1.90 / -0.21 / **-15.23**	— / — / $\mathbf{2H_2O}$
H_3^- / H_3 / $\mathbf{H_3^+}$	0.46 / -6.25 / **-16.65**	$2H_2$/$2H_2$/$\mathbf{H_2O+H_2}$

[a]Binding energies are computed using $E_b=E_p-E_H-E_s$, where E_p is the product energy, E_H and E_s energies of the isolated hydrogen-containing species and isolated hydroxylated HfN surface.

It can be concluded that the cationic species (H^+, H_2^+ and H_3^+) show the highest affinity for the surface –OH groups. Furthermore, the cationic species are predicted to form H_2O as a product upon reacting with surface -OH groups. In contrast, the anionic (H^-, H_2^- and H_3^-) and neutral (H, H_2 and H_3) species are (energetically) reluctant to react with the surface –OH groups. The anionic and neutral species in the H_2 plasma were found to yield volatile H_2 products, leaving the surface -OH groups intact (see appendix Section E2 for the results on fully oxygenated HfN surface).

Based on the energetics results, a set of redox half reactions that likely underlie the binding of H^+ ions on Hf-OH surface groups are proposed and can be found in the appendix (Section E3, Eqns. S8-S12). Moreover, we hypothesize that following the liberation of H_2O from the HfN surface, H· radicals in the plasma near the surface restore the pristine HfN surface via reduction of Hf(IV) to Hf(III) in a concerted reaction pathway (Eqns. S10-S11), in-line with the previously reported XPS results [13]. This hypothesis is also based on the application of H_2 plasma to reduce the Pt(IV) and Ta(V) in the precursor to synthesize metallic Pt(0) and Ta(III)N films with ALD [52, 53].

Based on the experimental observations of the mitigation of oxygen incorporation due to energetic ions, a set of AIMD simulations were designed to probe this effect at molecular level. As aforementioned, the average energy (E_{ion})

of the highly-reactive cationic species (H^+, H_2^+ and H_3^+) in our experimental work is controlled by the application of external rf substrate bias [12, 31]. In these simulations, the fully hydroxylated HfN surface model (as previously introduced, Figure A5.6) was again assumed. In addition, 16 hydrogen cations (H^+) were placed randomly 4.5 Å above the hydroxylated HfN surface in three separate tries (which differ in terms of initial H^+ positions), and all ions were assigned with the same initial velocities directed towards the surface. A sample simulation model is visualized in Figure 5.3a. Two cases with ion velocities of v_i=0.76 Ȧ/fs and v_i=1.75 Ȧ/fs were assumed in order to roughly model the resulting kinetic energy for the grounded electrode and rf substrate bias conditions (see appendix Section E4, Table A5.4 for a substantiation of these values). The ions with a lower initial velocity did not lead to dissociation of surface Hf-OH bonds. AIMD simulations point at the formation of intermediate surface $[H_2O]^+$ species, which remains chemisorbed on the surface, and later dissociates to yield again the Hf-OH surface bonds. On the other hand, the ions with a higher initial velocity lead to abstraction of -OH groups from the surface and H_2O liberation was observed within the same time frame (e.g. 350 fs simulation) (Figure 5.3b). It should also be noted here that the DFT calculations were performed only for the H^+ ions to limit the computational efforts, however the H_2^+ and H_3^+ ions are expected to yield similar results.

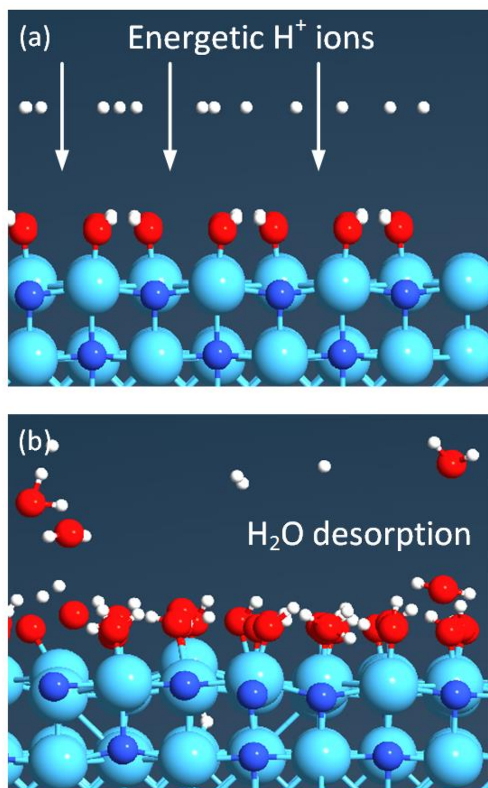

Figure 5.3. Ab initio molecular dynamics (AIMD) simulation snapshots illustrating the desorption of H_2O resulting from the impingement of energetic H^+ ions with a velocity of 1.75 Å fs^{-1} on a fully hydroxylated HfN(200) surface at (a) Δt = 0.0 fs and (b) 350.0 fs. Color code: cyan: Hf; blue: N; red: O; white: H. See appendix Section E4, Figure A5.7 for additional snapshots of the movies.

So far, we have discussed a one-off ion exposure event (i.e. a single layer of ions impacting the surface), while the HfN surface experiences a continuous flux of energetic ions in reality. In an attempt to crudely account for the continuous energetic ion flux, we performed analogous MD simulations with two layers of 16 H^+ ions (instead of one) in the simulation model (with 3.5 Ȧ interlayer separation, data not shown). An extra layer of H^+ ions with a v_i value of 1.75 Ȧ/fs indeed led to an increase in the number of removed surface -OH groups as volatile H_2O products with respect to a single layer H^+ ions, thus suggesting an enhanced removal of the surface -OH groups upon increasing ion flux (see appendix Section E5 for the discussion on surface termination subsequent to the abstraction of all surface –OH groups).

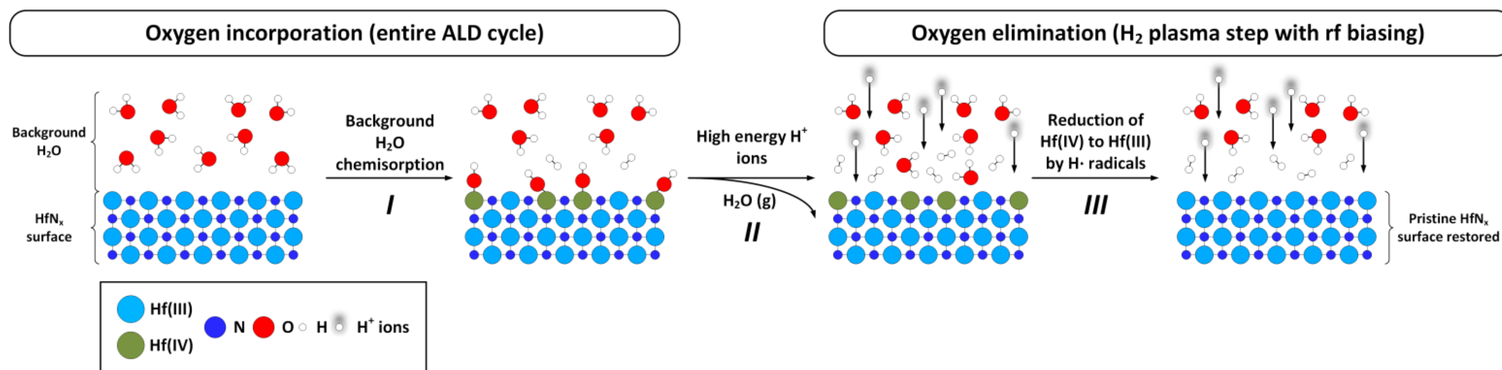

Figure 5.4. A schematic summary of the oxygen incorporation and elimination mechanisms proposed in this work. The H_2O chemisorption occurs during the entire ALD cycle and leads to the hydroxylation of HfN surface and the formation of Hf-OH bonds. The liberation of H_2O and subsequent reduction of Hf(IV) to Hf(III) takes place only during the H_2 plasma half cycle, resulting from the impingement of energetic cations. It should be noted that only a part of the entire ALD cycle is depicted.

5.4 Conclusions

Suppressing the oxygen contamination is a well-known challenge in the synthesis of conductive metal nitride and metal thin films by ALD, since oxygen limits their electrical conductivity. Here, we present a study on the O incorporation in conductive metal nitrides by using plasma-assisted ALD of HfN_x films as case study. We investigate the atomic-level processes that leads to the oxidation of the HfN_x surface by first principles DFT calculations. In addition, the kinetics of O elimination by energetic ions upon application of external rf substrate bias during the H_2 plasma step is addressed. The corresponding events of H_2O chemisorption on the HfN surface and Hf-O bond dissociation and H_2O formation due to impingement of energetic ions are schematically summarized in Figure 5.4.

We show that the O content in the HfN_x layers is determined by the total flux of H_2O/O_2 impinging on the HfN_x surface during the entire ALD cycle. Next, we observed that an increase in the time-averaged substrate potential from 0V to 130V leads to a decrease in the density of Hf-O bonds in HfN_x films due to the impingement of energetic ions.

By using DFT calculations, we found that the chemisorption of H_2O on the bare HfN surface is kinetically and thermodynamically highly feasible, creating hydroxyl (Hf-OH) surface groups (I, Figure 5.4). DFT calculations also revealed that only the cationic species (H^+, H_2^+, H_3^+) present in H_2 plasma are highly reactive towards the surface –OH groups. Moreover, an increase in the energy of incident cations was shown to not only dissociate Hf-OH surface bonds but also lead to H_2O formation and desorption (II, Figure 5.4). In addition, the H· radicals present in H_2 plasma are hypothesized to reduce Hf(IV) to Hf(III) subsequent to H_2O liberation (III, Figure 5.4), in line with previously reported increase in Hf(III) fraction. These reactions can be considered as contributing to a so-called atomic layer cleaning (ALC) process [54].

In perspective, these results shed light on the mechanism of oxygen incorporation and its mitigation for a wide range of ALD processes, where surfaces with high affinity towards oxidation are considered, such as TiN_x, HfN_x, MoC_x, Ta, and enable ALD of low resistivity films with potential application in nano-electronics [25, 26, 55].

References

1. Elam, J.W., et al., *Atomic layer deposition of aluminum oxide in mesoporous silica gel.* Journal of Physical Chemistry C, 2010. **114**(41): p. 17286-17292.
2. Haukka, S., et al., *Dispersion and distribution of titanium species bound to silica from TiCl4.* Langmuir, 1993. **9**(12): p. 3497-3506.
3. Lakomaa, E.L., A. Root, and T. Suntola, *Surface reactions in Al2O3 growth from trimethylaluminium and water by atomic layer epitaxy.* Applied Surface Science, 1996. **107**: p. 107-115.
4. Keranen, J., et al., *Surface-controlled gas-phase deposition and characterization of highly dispersed vanadia on silica.* Journal of Physical Chemistry B, 2003. **107**(39): p. 10773-10784.
5. Eom, D., et al., *Properties of aluminum nitride thin films deposited by an alternate injection of trimethylaluminum and ammonia under ultraviolet radiation.* Journal of the Electrochemical Society, 2006. **153**(4): p. C229-C234.
6. Knoops, H.C.M., et al., *Atomic Layer Deposition of Silicon Nitride from Bis(tert-butylamino)silane and N<inf>2</inf> Plasma.* ACS Applied Materials and Interfaces, 2015. **7**(35): p. 19857-19862.
7. Lee, H.B.R., et al., *High quality area-selective atomic layer deposition co using ammonia gas as a reactant.* Journal of the Electrochemical Society, 2010. **157**(1): p. D10-D15.
8. Bertuch, A., et al., *Plasma enhanced atomic layer deposition of molybdenum carbide and nitride with bis(tert-butylimido)bis(dimethylamido) molybdenum.* Journal of Vacuum Science & Technology A: Vacuum, Surfaces, and Films, 2017. **35**(1): p. 01B141.
9. Consiglio, S., et al., *Plasma-assisted atomic layer deposition of conductive hafnium nitride using tetrakis(ethylmethylamino)hafnium for CMOS gate electrode applications.* Journal of the Electrochemical Society, 2008. **155**(3): p. H196-H201.
10. Heil, S.B.S., et al., *Low-temperature deposition of TiN by plasma-assisted atomic layer deposition.* Journal of the Electrochemical Society, 2006. **153**(11): p. G956-G965.

11. Hinz, J., A.J. Bauer, and L. Frey, *Analysis of NbN thin film deposition by plasma-enhanced ALD for gate electrode application.* Semiconductor Science and Technology, 2010. **25**(7): p. 075009.

12. Karwal, S., et al., *Low resistivity HfNx grown by plasma-assisted ALD with external rf substrate biasing.* Journal of Materials Chemistry C, 2018. **6**(15): p. 3917-3926.

13. Karwal, S., et al., *Plasma-assisted atomic layer deposition of HfNx: Tailoring the film properties by the plasma gas composition.* Journal of Vacuum Science and Technology A: Vacuum, Surfaces and Films, 2017. **35**(1).

14. Kim, E.J. and D.H. Kim, *Highly conductive HfN x films prepared by plasma-assisted atomic layer deposition.* Electrochemical and Solid-State Letters, 2006. **9**(8): p. C123-C125.

15. Kim, J.Y., et al., *Remote plasma-enhanced atomic-layer deposition of tiN by using TDMAT with a NH 3 plasma.* Journal of the Korean Physical Society, 2004. **45**(6): p. 1639-1643.

16. Kim, J.Y., et al., *Remote plasma enhanced atomic layer deposition of TiN thin films using metalorganic precursor.* Journal of Vacuum Science and Technology A: Vacuum, Surfaces and Films, 2004. **22**(1): p. 8-12.

17. Kroll, U., et al., *Origins of atmospheric contamination in amorphous silicon prepared by very high frequency (70 MHz) glow discharge.* Journal of Vacuum Science & Technology A: Vacuum, Surfaces, and Films, 1995. **13**(6): p. 2742-2746.

18. Langereis, E., et al., *Synthesis and in situ characterization of low-resistivity Ta Nx films by remote plasma atomic layer deposition.* Journal of Applied Physics, 2007. **102**(8).

19. Musschoot, J., et al., *Atomic layer deposition of titanium nitride from TDMAT precursor.* Microelectronic Engineering, 2009. **86**(1): p. 72-77.

20. Rampelberg, G., et al., *Low temperature plasma-enhanced atomic layer deposition of thin vanadium nitride layers for copper diffusion barriers.* Applied Physics Letters, 2013. **102**(11): p. 111910.

21. Seungchan, C., et al., *Barrier Characteristics of ZrN Films Deposited by Remote Plasma-Enhanced Atomic Layer Deposition Using Tetrakis(diethylamino)zirconium Precursor.* Japanese Journal of Applied Physics, 2007. **46**(7R): p. 4085.

22. Sowa, M.J., et al., *Plasma-enhanced atomic layer deposition of tungsten nitride.* Journal of Vacuum Science & Technology A: Vacuum, Surfaces, and Films, 2016. **34**(5): p. 051516.

23. Sowa, M.J., et al., *Plasma-enhanced atomic layer deposition of superconducting niobium nitride.* Journal of Vacuum Science & Technology A: Vacuum, Surfaces, and Films, 2017. **35**(1): p. 01B143.

24. Ritala, M., et al., *Atomic layer epitaxy growth of TiN thin films from TiI 4 and NH 3.* Journal of the Electrochemical Society, 1998. **145**(8): p. 2914-2920.

25. Faraz, T., et al., *Tuning Material Properties of Oxides and Nitrides by Substrate Biasing during Plasma-Enhanced Atomic Layer Deposition on Planar and 3D Substrate Topographies.* ACS Applied Materials & Interfaces, 2018. **10**(15): p. 13158-13180.

26. Grady, E., et al., *Tailoring Molybdenum Carbide Properties by Plasma and Ion Energy Control during Plasma Enhanced ALD.* to be submitted.

27. Krylov, I., et al., *Properties of conductive nitride films prepared by plasma enhanced atomic layer deposition using quartz and sapphire plasma sources.* Journal of Vacuum Science & Technology A, 2019. **37**(1): p. 010906.

28. Knoops, H.C.M., et al., *Status and prospects of plasma-assisted atomic layer deposition.* Journal of Vacuum Science & Technology A, 2019. **37**(3): p. 030902.

29. Kornilov, A.N., et al., *The enthalpy of formation of hafnium dioxide.* The Journal of Chemical Thermodynamics, 1975. **7**(1): p. 21-26.

30. Knoops, H.C.M., K. De Peuter, and W.M.M. Kessels, *Redeposition in plasma-assisted atomic layer deposition: Silicon nitride film quality ruled by the gas residence time.* Applied Physics Letters, 2015. **107**(1).

31. Profijt, H.B., M.C.M. Van De Sanden, and W.M.M. Kessels, *Substrate-biasing during plasma-assisted atomic layer deposition to tailor metal-oxide thin film growth.* Journal of Vacuum Science and Technology A: Vacuum, Surfaces and Films, 2013. **31**(1).

32. Blöchl, P.E., *Projector augmented-wave method.* Physical Review B, 1994. **50**(24): p. 17953-17979.

33. Kresse, G. and D. Joubert, *From ultrasoft pseudopotentials to the projector augmented-wave method.* Physical Review B, 1999. **59**(3): p. 1758-1775.

34. Kresse, G. and J. Furthmüller, *Efficiency of ab-initio total energy calculations for metals and semiconductors using a plane-wave basis set.* Computational Materials Science, 1996. **6**(1): p. 15-50.

35. Kresse, G. and J. Furthmüller, *Efficient iterative schemes for ab initio total-energy calculations using a plane-wave basis set.* Physical Review B, 1996. **54**(16): p. 11169-11186.

36. Kresse, G. and J. Hafner, *Ab initio molecular dynamics for liquid metals.* Physical Review B, 1993. **47**(1): p. 558-561.

37. Kresse, G. and J. Hafner, *Ab initio molecular-dynamics simulation of the liquid-metal-amorphous-semiconductor transition in germanium.* Physical Review B, 1994. **49**(20): p. 14251-14269.

38. Hohenberg, P. and W. Kohn, *Inhomogeneous Electron Gas.* Physical Review, 1964. **136**(3B): p. B864-B871.

39. Kohn, W. and L.J. Sham, *Self-Consistent Equations Including Exchange and Correlation Effects.* Physical Review, 1965. **140**(4A): p. A1133-A1138.

40. Perdew, J.P., K. Burke, and M. Ernzerhof, *Generalized Gradient Approximation Made Simple.* Physical Review Letters, 1996. **77**(18): p. 3865-3868.

41. Perdew, J.P., K. Burke, and M. Ernzerhof, *Generalized Gradient Approximation Made Simple [Phys. Rev. Lett. 77, 3865 (1996)].* Physical Review Letters, 1997. **78**(7): p. 1396-1396.

42. Grimme, S., et al., *A consistent and accurate ab initio parametrization of density functional dispersion correction (DFT-D) for the 94 elements H-Pu.* The Journal of Chemical Physics, 2010. **132**(15): p. 154104.

43. Sigmund, P., *Theory of Sputtering. I. Sputtering Yield of Amorphous and Polycrystalline Targets.* Physical Review, 1969. **184**(2): p. 383-416.

44. Steinbrüchel, C., *Universal energy dependence of physical and ion-enhanced chemical etch yields at low ion energy.* Applied Physics Letters, 1989. **55**(19): p. 1960-1962.

45. Sakurai, S. and T. Nakayama, *Adsorption, diffusion and desorption of Cl atoms on Si(111) surfaces.* Journal of Crystal Growth, 2002. **237-239**: p. 212-216.

46. Kanarik, K.J., et al., *Overview of atomic layer etching in the semiconductor industry.* Journal of Vacuum Science & Technology A, 2015. **33**(2): p. 020802.

47. Luo, Y.R., *Comprehensive Handbook of Chemical Bond Energies*. 2007: CRC Press.

48. Tang, W., E. Sanville, and G. Henkelman, *A grid-based Bader analysis algorithm without lattice bias.* Journal of Physics: Condensed Matter, 2009. **21**(8): p. 084204.

49. Bader, R.F.W., *Atoms in Molecules: A Quantum Theory*. 1990, New York: Oxford University Press.

50. *Comparison of the Bader charges of the bare and hy-droxylated HfN models reveals that the binding of -OH groups (with a partial charge of ca. -0.52e per -OH moiety) triggers a charge transfer away from the surface Hf atoms (amounting to ca. 0.35e).*

51. Sode, M., T. Schwarz-Selinger, and W. Jacob, *Ion chemistry in H2-Ar low temperature plasmas.* Journal of Applied Physics, 2013. **114**(6).

52. Mackus, A.J.M., et al., *Room-Temperature Atomic Layer Deposition of Platinum.* Chemistry of Materials, 2013. **25**(9): p. 1769-1774.

53. Knoops, H.C.M., et al., *Reaction mechanisms of atomic layer deposition of TaNx from Ta(NMe2)5 precursor and H2-based plasmas.* Journal of Vacuum Science & Technology A, 2012. **30**(1): p. 01A101.

54. Faraz, T., et al., *Atomic Layer Etching: What Can We Learn from Atomic Layer Deposition?* ECS Journal of Solid State Science and Technology, 2015. **4**(6): p. N5023-N5032.

55. Kim, H. and S.M. Rossnagel, *Plasma-enhanced atomic layer deposition of tantalum thin films: the growth and film properties.* Thin Solid Films, 2003. **441**(1): p. 311-316.

Appendix 5

A. Literature overview of TMN films prepared by plasma-assisted ALD and O incorporation

Table A5.1. Overview of the material properties of various transition metal nitride (TMN) films prepared by plasma-assisted ALD as reported in the literature. The deposited material, metal precursor, co-reactant, the plasma source configuration (‘*d*’ is ‘direct plasma’, ‘*r*’ is ‘remote plasma’ and ‘-’ is ‘not specified’), stage temperature (T_s), chemical composition (‘[N]/[M]’ is ‘ratio of nitrogen-to-metal content’), lowest film electrical resistivity reported in respective works and the corresponding references are provided. Me = methyl (CH_3), Et = ethyl (C_2H_5), Cp = cyclopentadienyl (C_6H_5), ‘-’ = not reported.

Material	Precursor	Co-reactant	Reactor type	T_s (°C)	[O] at.%	[C] at.%	[N]/[M]	Resistivity (μΩcm)	Ref.
TiN	$Ti(NMe_2)_4$	H_2 plasma N_2 plasma	*r*	250	15 5	15 5	1.1 1.3	700 300	[1]
	$Ti(NMe_2)_4$	NH_3 plasma	*r*	200	5	<1	1.0	180	[2]
	$Ti(NMe_2)_4$	NH_3 plasma	*r*	250	20	2	1.2	1200	[3]
	$TiCl_4$	N_2/H_2 plasma	*r*	400	2	-	1.0	70	[4]
	$Ti(NMe_2)_4$	N_2 plasma NH_3 plasma H_2 plasma	*r*	300	2.5 2.5 7	<2 <2 8	1.0	110 75 125	[5]
ZrN	$Zr(NEt_2)_4$	N_2 plasma	*r*	300	10	10	0.4	400	[6]
HfN	$Hf(NMeEt)_4$	Ar/H_2 plasma	*d*	250	2	10.1	1.0	2327	[7]
	$Hf(NMe_2)_4$	H_2	*d*	175	2	21	0.6	6700	[8]

		plasma							
	$HfCp(NMe_2)_3$	H_2 plasma	*r*	450	20.1	<2.0	0.86	$9\cdot10^5$	[9]
	$HfCp(NMe_2)_3$	N_2 plasma	*r*	450	5	<2.0	1.25	$>10^5$	[9]
	$HfCp(NMe_2)_3$	H_2 plasma+rf substrate bias	*r*	450	<2	11	1.0	3300	[10]
VN	$V(NMeEt)_4$	NH_3 plasma	*r*	150	<2	<2	1.0	200	[11]
NbN	$Nb(NMeEt)_3NCMe_3$	H_2 plasma	*r*	350	27.5	<2	0.8	905	[12]
TaN	$Ta(NMe_2)_5$	H_2 plasma	*r*	150	15	10	0.55	1000	[13]
		H_2 plasma	*r*	225	8	12	0.45	390	[13]
		NH_3 plasma	*r*	225	<2	<2	1.67	$>10^5$	[13]
MoN	$Mo(NMe_2)_2(NCMe_3)_2$	H_2 plasma	*r*	150	8	30	<0.1	170	[14]
WN	$W(NMe_2)_2(NCMe_3)_2$	N_2/H_2 plasma	*r*	400	10	<1	0.4	405	[15]

A general observation is that the application of N_2 or N_2 containing plasma usually leads to less O incorporation in comparison to the H_2 plasma. The low O content in the case of N_2 plasma may be attributed to a lower fraction of M(III) oxidation state in the films and/or less affinity of the growing surface towards oxidation in comparison to the films grown with H_2 plasma.

B. Flux of H_2O and O incorporation in HfN_x films

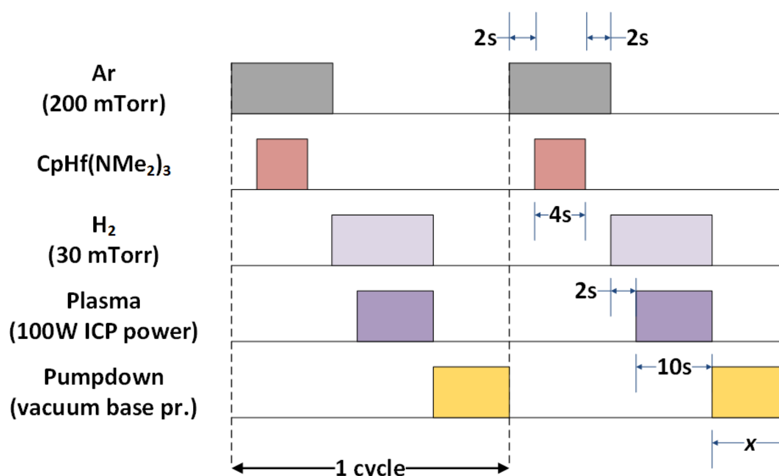

Figure A5.1. Layout of ALD cycles of HfN_x in which the duration of the pump-down step (with duration *x* s) following the H_2 plasma has been varied. The total cycle time ranges from 20 s (*x* = 0s) up to 100 s (*x* = 80 s). The figure shows 2 ALD cycles and the time intervals are not drawn to scale.

Oxygen contamination in the HfN_x films can result from various sources during the film growth even when oxygen is not intentionally introduced in the reactor, as highlighted by Ritala *et al.* and Knoops *et al.* [16, 17]. Specifically, oxygen in the HfN_x films can originate from the post-deposition oxidation when exposing the samples to air. Furthermore, oxygen in the HfN_x films can originate from the adsorption of H_2O/O_2 present as residual gases in the reactor background. Moreover, H_2O/O_2 impurities present in the precursor and in the process and purge gases used during the ALD process can also result in oxygen incorporation.

The residual H_2O/O_2 gases are present in the reactor due to inadequate sealing of the reactor. Even when pumped by a turbo-molecular pump, this results in approximately vacuum base pressure of 10^{-6} Torr for an O-ring sealed reactor. The residual gases present in reactor background mainly comprise of H_2, N_2, H_2O and O_2 [18]. Note that a constant partial pressure of the impurity gases may not be necessarily assumed since the reactor wall surfaces covered with the metal nitride film and metal precursor acts as a sink for the adsorption of H_2O/O_2 [16]. As a result, the partial pressure of the impurity gases can be anticipated to decrease with time. Furthermore, oxygen incorporation happens particularly when the reactivity of the growth surface is high towards H_2O/O_2 (e.g. when growing HfN, TiN etc.). Moreover, the ALD cycle time and/or the growth per cycle influences the O content as shown by Kroll *et al.* [19], i.e., a slower process gives a higher O content in the films.

In our case, the XPS experimental data presented in Figure 5.1 in the main text shows that the peak intensity of Hf-O bonds (and the associated oxygen concentration in the HfN_x films) increases significantly even when the HfN_x films are exposed to base vacuum conditions (10^{-6} Torr) for up to 100 s and the peak intensity does not saturate. Therefore, it can be concluded that under our experimental conditions, the primary source of oxygen contamination in the HfN_x films is from residual H_2O/O_2 gas in the reactor background.

To further support this conclusion, the O content in the HfN_x films as a consequence of the adsorption of residual H_2O/O_2 gas in the reactor background can be estimated by calculating the flux (*F*) of H_2O/O_2 molecules impinging on the pristine HfN_x surface using the Hertz-Knudsen equation [$F = P(2\pi mkT)^{-1/2}$], where *P* is the H_2O partial pressure; *m* is the mass of one H_2O molecule; *k* is the Boltzmann constant and *T* is the wall temperature. For calculation, a total ALD cycle time of 20 s, and a wall temperature of 145°C is considered. Furthermore, the total number of all the atoms (i.e. Hf, N, O, C and H) being deposited in each ALD cycle is considered to be 2.1 atoms cycle^{-1} nm^{-2} as obtained from RBS measurements [10]. For calculation purposes, the residual H_2O gas is assumed to be the primary source of oxygen contamination. In addition, the partial pressure of background H_2O and the density of surface sites for H_2O adsorption are assumed to be constant in the calculations. Making crude assumptions that each H_2O molecule delivers one O atom to the surface, Table A5.2 shows the calculated O content as a function of background H_2O partial pressure for a sticking probability of s = 1. In addition to that, the table shows the calculated O content as a function the *s* for a background H_2O partial pressure of 10^{-8} Torr. These calculations illustrates that even a relatively small amount of residual H_2O gas in reactor background can lead to a significant amount of oxygen incorporation. Although the calculation is simple and based on very crude assumptions, a reasonable estimation on the oxygen incorporation can be made. Experimentally, we determine an O content of 20.1±0.7 at.% by RBS analysis [10].

Table A5.2. The calculated O content as a function of the background H_2O partial pressure for a sticking probability (*s*) = 1 is shown. Furthermore, the O content as a function of *s* for a constant H_2O partial pressure of 10^{-8} Torr is reported. A total ALD cycle time of 20 s and a total number of atoms being deposited every cycle of approximately ~2.1 atoms cycle^{-1} nm^{-2} has been considered. The calculation was done for a wall temperature of 145°C during ALD.

H_2O partial pressure (Torr)	H_2O flux (nm^{-2} s^{-1})	H_2O fluence per cycle (nm^{-2})	Sticking probability of H_2O (*s*)	O content (%)

10^{-8}	0.04	0.8	1	39.00
10^{-9}	0.004	0.08	1	3.90
10^{-10}	0.0004	0.008	1	0.39
10^{-8}	0.04	0.8	1	39.00
10^{-8}	0.04	0.8	0.1	3.90
10^{-8}	0.04	0.8	0.01	0.39

C. Density functional theory (DFT) simulations

1. Computational details

All electronic structure calculations were done using the projector augmented wavefunction (PAW) [20, 21] as implemented in Vienna Ab Initio Simulation Package (VASP, v.5.3.5) [22-25]. Generalized Gradient Approximation (GGA) to Density Functional theory (DFT) [26, 27] was used jointly with the Perdew−Burke−Ernzerhof (PBE) exchange correlation functional [28, 29]. DFT(PBE)-D3 corrections with Becke-Johnson damping [30] were employed to account for Van der Waals (VDW) interactions on an empirical basis. Structural relaxations were carried out using the conjugate gradient algorithm, where they were considered converged once all forces deviate less than 0.01 eV Å^{-1} in two consecutive ionic steps. Besides, we used the default accuracy parameters for the FFT grid and real space projectors alongside a Gaussian smearing of 0.1 eV. No constraints have been applied on any atoms during the optimizations. Minimum energy paths (MEPs) along the predefined reaction pathways connecting a reactant-product pair were computed by optimizing several geometries collectively with the climbing-image nudge elastic band (CI-NEB) method [31]. CI-NEB optimizations were done with a looser convergence criterion on forces (0.1 eV Å^{-1}) utilizing the Hessian-based (G)-LBFGS [32] algorithm as implemented in VTST tool set [33].

Due to their rather large size, the supercells (see HfN surface models for DFT simulations, Figure A5.2) could be integrated in reciprocal-space with only one *K*-point coinciding with the *Γ*-point. Relevantly, all the supercells considered here were optimized in terms of size and shape using a rather large kinetic energy cutoff of 520 eV, only containing the HfN surface with various surface functionalization (bare/pristine, hydroxylated or oxygenated). These optimized

supercells are used in the H_2O/O_2 chemisorption or H^+ ion exposure *ab initio* molecular dynamics (AIMD) simulations, as will be reported later.

The AIMD simulations were carried out to elucidate the underlying chemistry taking place on the HfN surface, when exposed to reactive species (H_2O, O_2 or H^+). Unlike the static approach, AIMD can suggest the possible chemical routes for surface reactions. Furthermore, AIMD can also account for dynamic effects, such as the impact of energetic ions (H_3^+, H_2^+, H^+) incident on the surface by tuning the velocities assigned to ions.

2. δ-HfN surface models for DFT simulations

Three distinct bare HfN surface models were considered for simulating thermal adsorption of H_2O and O_2 (Figure A5.2). It should be noted that a -NH termination was found to be unstable (data not shown). The H on the N sites tends to migrate to Hf sites and remain weakly physisorbed, hoping from one Hf site to another. Subsequently, recombination of 2 H is observed leading to liberation of molecular H_2.

Each HfN surface is composed of four layers, where each monolayer is made up of 32 Hf and 32 N atoms, coordinated to form a face-centered-cubic (fcc) crystal structure. The HfN(200) orientation was found to yield a unique termination comprising of equivalent Hf and N atoms, whereas two distinct HfN(111) surfaces were obtained, depending on the termination type (Hf- or N-). These surfaces are in-line with our previous experimental report on the growth of polycrystalline *δ*-HfN_x films exhibiting HfN(200) and HfN(111) textures, when grown at a time-averaged substrate potential (V_{bias}) values of 0V and -130V [10].

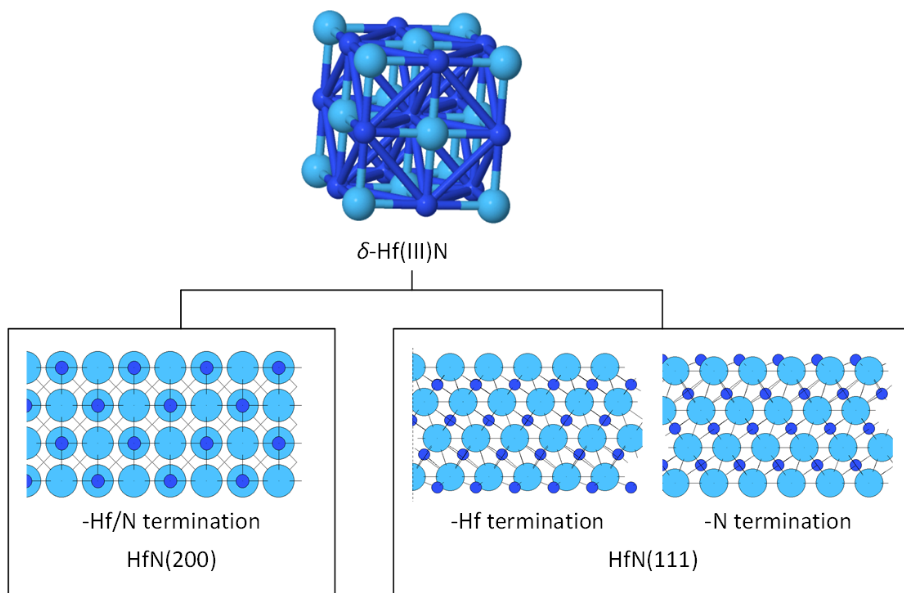

Figure A5.2. Three simulation models of pristine (bare) HfN surfaces, which are predominantly formed upon the cleavage of the bulk δ-HfN fcc crystal (top). Color code: cyan: Hf; blue: N.

D. Chemisorption of reactive H_2O/O_2 on HfN(200) and HfN(111) surface

1. Computational details and simulation model

The spontaneous thermal adsorption of H_2O and O_2 residual gases in the reactor background on the bare HfN surfaces is deemed as the primary reason for O incorporation in the HfN_x films. The underlying surface chemistry of the hydroxylation and oxygenation was studied by using AIMD, as aforementioned. We utilized two model systems containing either 16 H_2O molecules or 16 O_2 molecules, thereby covering the bare HfN surface with a ratio of Hf:O=2:1. Following the proper cell and geometry relaxations, canonical (NVT) AIMD ensembles were created at 1000 K (assigning random initial velocities to the particles in the system according to Boltzmann distribution) and in a vacuum environment. A time step of 1 fs was employed for sampling the model systems for a total of ca. 3.0 ps for each case.

Furthermore, the binding energies of H_2O or O_2 on the HfN(200) and HfN(111) surfaces were computed through physisorption (ΔE_p) or chemisorption (ΔE_c) using Eqn. A1.

$$\Delta E_{p/c}=E_{AS}-E_A-E_S \quad \text{(A1)}$$

where E_{AS} is the total energy of the physisorbed/chemisorbed substrate-adsorbate complex, E_A and E_S are the total energies of an isolated adsorbate and a given substrate surface. As will be shown later, the same procedure is employed to obtain the binding energies of neutral or charged H_2 plasma species (H·, H^+, H_2^+, H^- etc.) on the fully hydroxylated and oxygenated HfN surfaces.

In order to accommodate the corresponding amount of adsorbent molecules (H_2O, O_2) on a given HfN surface and to minimize the resulting interactions through periodic boundary conditions, supercells were kept rather large in the *xy* plane. Particularly, a 4x4 supercell of the HfN(200) surface slab (with the optimized dimensions of 17.8 Å x 17.8 Å x 27.6 Å, $\alpha=\beta=\gamma=90^o$, 256 atoms) and a 4x4 supercell of HfN(111) surface slab (Hf- or N-terminated, 19.3 Å x 19.3 Å x 24.7 Å $\alpha=\beta=90^o$, $\gamma=120^o$). The hydroxylation or oxygenation of the bare HfN surface resulted in only very minor deviations from the original cell dimensions (less than 5%). To limit the computational efforts, we have used four layers of the HfN slab in our model, which turned out to yield binding energy of a single adsorbent molecule within 2 meV of a 6-layer model. For minimizing the image interactions through PBC, the surface slab images in each model were separated along the *z*-axis by 15 Å or more.

2. *Hydroxylation of HfN(200) and HfN(111) surfaces*

H_2O molecules were found to readily bind on the HfN(200) surface. Altogether, 14 out of 16 H_2O molecules adsorbed on the surface leading to selective formation of Hf-OH surface bonds. Furthermore, volatile H_2 is released as the reaction by-product. Figure A5.3 shows the side-view and top-view snapshots of the corresponding AIMD simulations.

In addition to the overall reaction for hydroxylation of bare HfN surface as given in Eqn. 1, we propose a set of redox half reactions in Eqns. A2-A5 in order to better understand the surface chemistry. It is hypothesized that the dissociative adsorption of H_2O molecules proceeds *via* formation of H^+ and OH^- ions, given the high electronegativity of –OH group. Furthermore, judging from the low kinetic barrier (ca. 0.11 eV for route 1) for Hf-OH bond formation and the electronic configuration (e.c.) of Hf(III) oxidation state ([Xe] $4f^{14}5d^16s^0$), the loss of 5d electron (i.e. oxidation to Hf(IV) with e.c. [Xe] $4f^{14}5d^06s^0$) is highly probable. Subsequent to the oxidation of Hf, the liberation of H_2 is likely to occur (Eqns. A3-

A4), in-line with the DFT findings. Furthermore, the binding of OH^- with the Hf(IV) is hypothesized to proceed *via* sharing the extra electron of OH^- for formation of a covalent bond. As a result, the Hf(IV) partially reverts back to Hf(III) state. However, the bond is expected to be highly polarized due to high electronegativity of O. This leads to partial oxidization of $Hf(III)^{\delta+}$ (Eqn. A5), in-line with the previously reported XPS results and the Bader charge analysis mentioned in the main text (see note [34] in the main text for more discussions) [10].

<u>Redox half reaction for H_2O chemisorption on pristine HfN surface</u>

$H_2O_{(g)} \rightarrow H^+ + OH^-$ (A2)

$Hf(III)^* \rightarrow Hf(IV)^* + 1e^-$ (A3)

$H^+ + 1e^- \rightarrow ½H_{2(g)}$ (A4)

$Hf(IV)^* + OH^- \rightarrow Hf(III)^{\delta+}\text{-}OH^{\delta-}{}^*$ (A5)

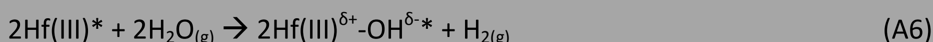

$2Hf(III)^* + 2H_2O_{(g)} \rightarrow 2Hf(III)^{\delta+}\text{-}OH^{\delta-}{}^* + H_{2(g)}$ (A6)

*Denotes surface species, whereas partial charges are represented by $^{\delta+}$,$^{\delta-}$

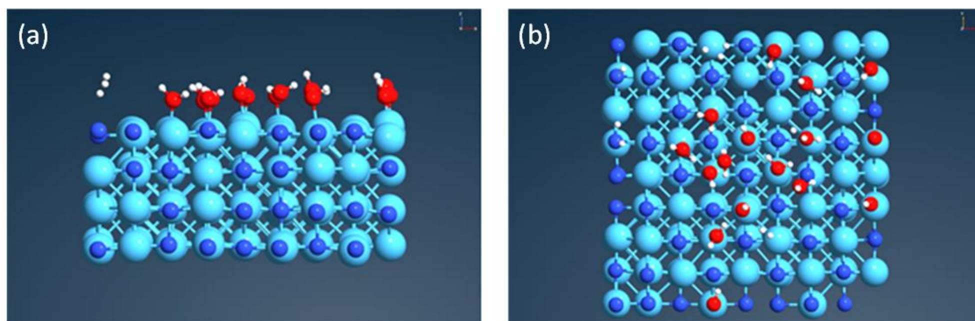

Figure A5.3. (a) Side-view and (b) top-view snapshot from the AIMD simulation of the thermal hydroxylation of bare HfN(200) surface. A total of 16 H_2O molecules were added to provide a coverage ratio of Hf:O=2:1. Color code: cyan: Hf; blue: N; red: O; white: H.

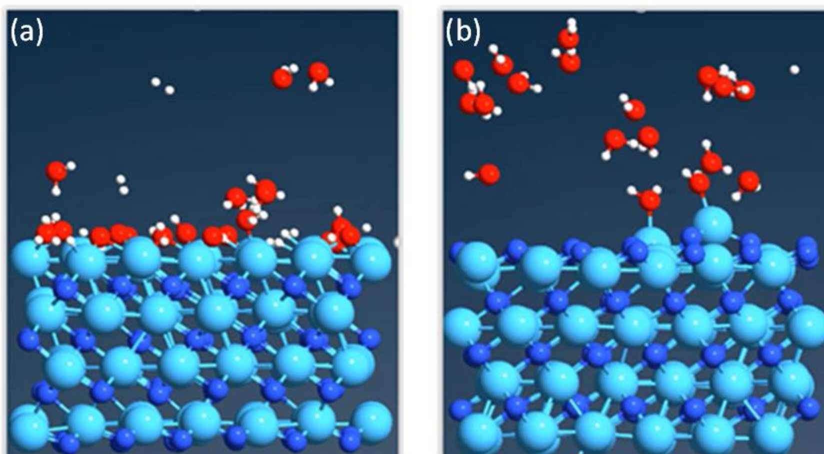

Figure A5.4. Side-view snapshots from the AIMD simulations of the thermal hydroxylation of bare HfN(111) surface with (a) Hf-termination and (b) N-termination. A total of 16 H_2O molecules were added to provide a coverage ratio of Hf:O=2:1. Color code: cyan: Hf; blue: N; red: O; white: H.

Figure A5.4 shows the snapshots of the AIMD simulations performed using the HfN(111) surface. Similar to the HfN(200) surface, H_2O molecules were found to readily bind on the Hf-terminated HfN(111) surface with a total of 11 H_2O molecules being adsorbed. On the other hand, only 2 H_2O molecules adsorbed on N-terminated HfN(111) surface, preventing an efficient H_2O adsorption. Furthermore, the formation of exclusively surface Hf-OH bonds is observed in both the cases, similar to the result of adsorption of H_2O on HfN(200) surface. Formation of volatile H_2 by-products is also observed.

3. Oxygenation of HfN(200) surface

Gaseous O_2 is also found as a residual gas in the reactor background alongside H_2O, even though in trace amounts compared to H_2O [35]. The likelihood of oxygenation of the bare HfN(200) surface was computed by the PBE-D3 level MEP along the designated pathway (as given in Eqn. A7 and Figure A5.5). The predicted MEP suggests that the dissociative binding of O_2 on HfN surface is also thermodynamically driven (ΔE = -3.58 eV) and even more favorable than the binding of a H_2O molecule. However, it is kinetically more hindered (E_a = 0.25 eV) as compared to the chemisorption of H_2O, given in Eqn. 1 (see Figure 5.2a). The pathway comprises of binding of one O_2 molecule on the Hf(200) surface, resulting in two distinct chemisorbed products, which differ in terms of the orientation of the separated O atoms on the surface (Figure A5.5). O_2 is assumed

to be in the singlet form in the calculations. However, the dissociation of O_2 requires an intersystem crossing (ISC) from the triplet ground state of dioxygen to the activated singlet species, which could introduce even higher kinetic barriers. Furthermore, the oxygenated HfN surface is still highly reactive due to the enhanced nucleophilic character of the Hf-O-Hf bonds, and it is predicted to abstract H from the nearby H_2O molecules in the reactor background and form stable surface -OH groups.

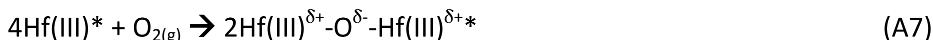

$$4Hf(III)^* + O_{2(g)} \rightarrow 2Hf(III)^{\delta+}\text{-}O^{\delta-}\text{-}Hf(III)^{\delta+*} \quad \text{(A7)}$$

*Denotes surface species, whereas partial charges are represented by $^{\delta+,\delta-}$

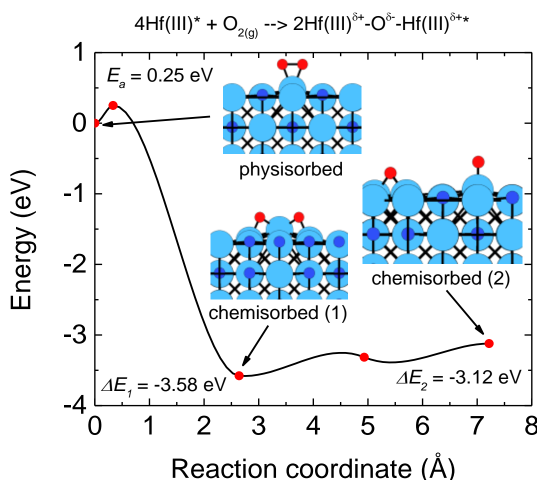

Figure A5.5. DFT/PBE-D3 level energy profile for the thermal adsorption of an O_2 molecule on bare HfN(200) surface following the pathway as described in Eqn. A7. Color code: cyan: Hf; blue: N; red: O; white: H.

E. Effect of ion bombardment on the surface termination of fully hydroxylated/oxygenated HfN(200) surface

1. HfN(200) surface model for probing the effect of ion bombardment

The bare HfN(200) surface was taken as the starting point to create fully hydroxylated and oxygenated HfN surfaces (Figure A5.6) for probing the binding energies of various H_2 plasma species (H·, H^+, H_2^+, H^- etc.) towards the surface –OH

groups and evaluating the underlying surface chemistry during the energetic cation exposure. Hydroxylation and oxygenation of the HfN surface were carried out by attaching 32 -OH and 16 -O groups to the surface Hf sites, yielding a surface coverage ratio of either Hf/O=1:1 or Hf/O=2:1 respectively. These models represent an idealized case, where all the surface Hf sites are hydroxylated or oxygenated, corresponding to the $Hf(III)^{\delta+}$ oxidation state. However, it should be noted that in reality the HfN film contains a mixture of Hf(III) and $Hf(III)^{\delta+}$, as previously reported [10].

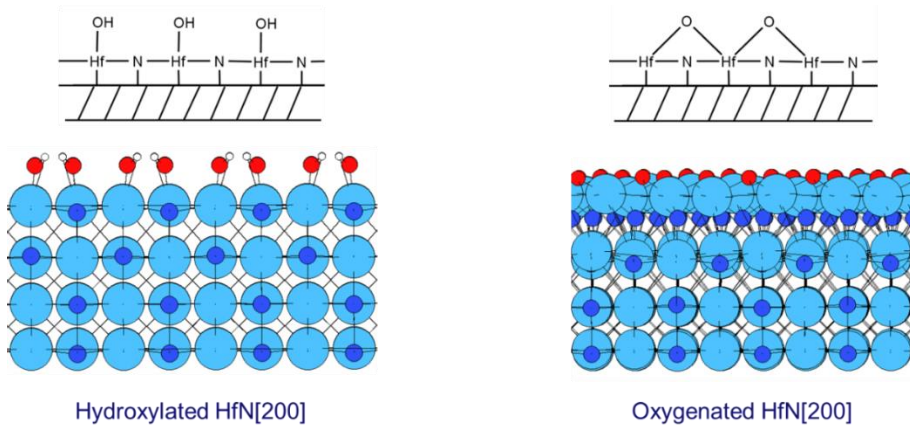

Figure A5.6. Relaxed hydroxylated and oxygenated HfN(200) models used in first-principles DFT simulations, whereby either -OH or -O adatoms are bonded to the surface Hf atoms with a coverage ratio of Hf:O=1:1 and Hf:O=2:1 respectively. For the oxygenated case, each oxygen atom is shared by two neighboring Hf sites (bridging O), and surface reconstruction is also observed (as opposed to the hydroxylated model). Color code: cyan: Hf; blue: N; red: O; white: H.

2. Binding energy of various H_2 plasma species with oxygenated HfN surface

As described in the Table 5.1 and in the main text, the cationic plasma species (H^+, H_2^+ and H_3^+) show the highest affinity towards binding with the surface –OH groups for a fully hydroxylated HfN(200) surface, whereas the anionic (H^-, H_2^- and H_3^-) and neutral (H, H_2 and H_3) species are (energetically) reluctant to react with the surface –OH groups. All the cationic species were found to form H_2O as a product upon reaction with the surface –OH groups.

In the case of the oxygenated HfN(200) surface, a similar affinity of the cationic species towards the surface Hf-O-Hf groups is observed, whereas the neutral or anionic species are again found to have much lower surface reactivity. However, in contrast to the hydroxylated case, cationic species (particularly H^+

and H_3^+) react with the surface Hf-O-Hf groups to yield surface Hf–OH groups, (partly) converting the surface into a more stable hydroxylated termination.

Table A5.3. DFT/PBE-D3 level binding energies (E_b) of various hydrogen-containing plasma species on an oxygenated HfN surface (Hf-O-Hf) and the type of the product(s) formed.

Species	E_b [eV][a]	Product Type
H^- / H / $\mathbf{H^+}$	-1.14 / -2.38 / **-2.61**	All form surface -OH
H_2^- / H_2 / $\mathbf{H_2^+}$	0.57 / -0.46 / **-13.46**	None reacts with surface. Only physisorbed
H_3^- / H_3 / $\mathbf{H_3^+}$	-1.24 / -7.05 / **-15.06**	All decompose into H_2 and H, which forms surface -OH group.

[a]Binding energies are computed using E_b=E_p-E_H-E_s, where E_p is the product energy, E_H and E_s energies of the isolated hydrogen-containing species and isolated oxygenated HfN surface.

3. Redox reactions occurring on fully hydroxylated HfN(200) surface

Based on the static DFT results (i.e. without energetic ions), we propose a set of redox half reactions that likely underlie the binding of H^+ ions on Hf-OH surface groups (Eqns. A8-A12). The energetic H^+ ions may lead to dissociation of surface Hf-OH bonds to yield Hf(IV) and OH^- ions (Eqn. A8, backward reaction of Eqn. A5), if provided with sufficient kinetic energy as will be shown later. Concertedly, the H^+ ions most likely undergo reaction with the released OH^- ions to form H_2O molecules (Eqn. A9). The formation and release of H_2O is seen in DFT. Following the H_2O liberation, H· radicals in the plasma near the surface are hypothesized to restore the pristine HfN surface via reduction of Hf(IV) to Hf(III) in a concerted reaction pathway (Eqns. A10-A11), in-line with the previously reported XPS results [9]. Furthermore, the released H^+ ion in Eqn. A10 most likely undergo recombination with the electrons present on the HfN_x surface to yield surface H· radical (Eqn. A12). The liberation of H_2 molecules is also observed in the dynamic AIMD simulations shown later in the main text (Figure 5.3). Other cationic species (H_2^+, H_3^+) were also evaluated towards the H_2O liberation and the corresponding redox half reactions and overall reactions are provided in Eqns. A14-A25.

Redox half reaction for H_2O liberation during energetic H^+ ion exposure

$Hf(III)^{\delta+}\text{-}OH^{\delta-}* \rightarrow Hf(IV)* + OH^-$ (A8)

$H^+_{(energetic\ ion)} + OH^- \rightarrow H_2O_{(g)}$ (A9)

$H\cdot_{(plasma)} \rightarrow H^+ + 1e^-$ (A10)

$Hf(IV)* + 1e^- \rightarrow Hf(III)*$ (A11)

$H^+ + 1e^-_{(surface)} \rightarrow H\cdot$ (A12)

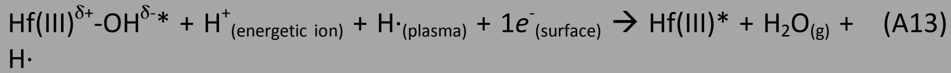
$Hf(III)^{\delta+}\text{-}OH^{\delta-}* + H^+_{(energetic\ ion)} + H\cdot_{(plasma)} + 1e^-_{(surface)} \rightarrow Hf(III)* + H_2O_{(g)} + H\cdot$ (A13)

Redox half reaction for H_2O liberation during energetic H_2^+ ion exposure

$2Hf(III)^{\delta+}\text{-}OH^{\delta-}* \rightarrow 2Hf(IV)* + 2OH^-$ (A14)

$H_2^+{}_{(energetic\ ion)} + OH^- \rightarrow H_2O_{(g)} + H\cdot$ (A15)

$2H\cdot_{(plasma)} \rightarrow 2H^+ + 2e^-$ (A16)

$2Hf(IV)* + 2e^- \rightarrow 2Hf(III)*$ (A17)

$H^+ + 1e^-_{(surface)} \rightarrow H\cdot$ (A18)

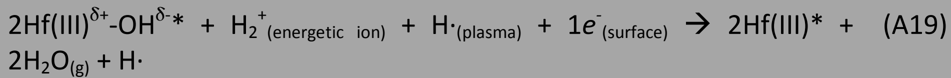
$2Hf(III)^{\delta+}\text{-}OH^{\delta-}* + H_2^+{}_{(energetic\ ion)} + H\cdot_{(plasma)} + 1e^-_{(surface)} \rightarrow 2Hf(III)* + 2H_2O_{(g)} + H\cdot$ (A19)

Redox half reaction for H_2O liberation during energetic H_3^+ ion exposure

$Hf(III)^{\delta+}\text{-}OH^{\delta-}* \rightarrow Hf(IV)* + OH^-$ (A20)

$H_3^+{}_{(energetic\ ion)} + OH^- \rightarrow H_2O_{(g)} + H_2$ (A21)

$H\cdot_{(plasma)} \rightarrow H^+ + 1e^-$ (A22)

$Hf(IV)* + 1e^- \rightarrow Hf(III)*$ (A23)

$H^+ + 1e^-_{(surface)} \rightarrow H\cdot$ (A24)

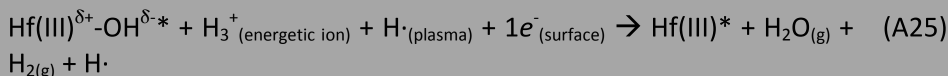

$Hf(III)^{\delta+}\text{-}OH^{\delta-}* + H_3^+{}_{(energetic\ ion)} + H\cdot_{(plasma)} + 1e^-_{(surface)} \rightarrow Hf(III)* + H_2O_{(g)} + H_{2(g)} + H\cdot$ (A25)

4. Effect of the energetic cations on the surface termination

As aforementioned, the AIMD simulations can provide valuable atomistic insights into the reactions occurring at the HfN(200) surface when exposed to energetic H_2 plasma cations at different values of V_{bias}. Several models with 16 H^+ ions placed above the fully hydroxylated HfN(200) surface (see Figures A5.7-A5.8 for visuals of the models) were utilized for simulating the cation exposure. For simplicity, we have considered only the H^+ cations, even though H_2 plasma also contains the other cations (H_2^+ and H_3^+). Using these models, microcanonical ensembles (NVE) were generated, whereby the H^+ ions were manually assigned two sets of initial velocity values to roughly represent the case for the grounded electrode and external rf substrate bias application. Velocities were deduced on the basis of the substrate potential (V_{bias}) (see Table A5.4), obtained from the readout of FlexAL ALD tool. Profijt *et al.* and Faraz *et al.* reported that the E_{ion} is roughly ~30 eV higher than the value of V_{bias} [36, 37]. However, it should be noted that the mean ion velocity (v_i) deduced in the calculations may slightly differ from the actual v_i as the ion energy distribution is also not taken into account in the calculations. Using the mass of H^+ ion (m) = $1.67\cdot10^{-27}$ kg, we can compute the v_i of ions impinging on the surface by using $v_i = \sqrt{2 \cdot E_{ion}/m}$. Velocities of the other atoms (i.e. those of the HfN surface) were assigned randomly to match the initial temperature of 1000 K.

Table A5.4. Based on the typical mean ion energies (E_{ion}), mean ion velocity is computed for H^+ and H_3^+ ions.

	H^+ ion		H_3^+ ion	
	V_{bias} = 0V	V_{bias} = -130V	V_{bias} = 0V	V_{bias} = -130V
Mean ion energy (E_{ion}) (eV)	~30	~160	~30	~160
Mean ion velocity (v_i) (Å fs^{-1})	0.76	1.75	0.44	1.00

Figure A5.7 shows a few snapshots from one of the trajectories (among several diverse ensembles) of the AIMD simulations for the fully hydroxylated HfN(200) surface. An initial ion velocity of 1.75 Å/fs was used in these simulations, corresponding to the V_{bias} value of -130V. From the snapshots, it can be observed that the bombardment of H^+ ions with enough energy leads to dissociation of Hf-OH surface bonds and subsequent formation of volatile H_2O can be seen.

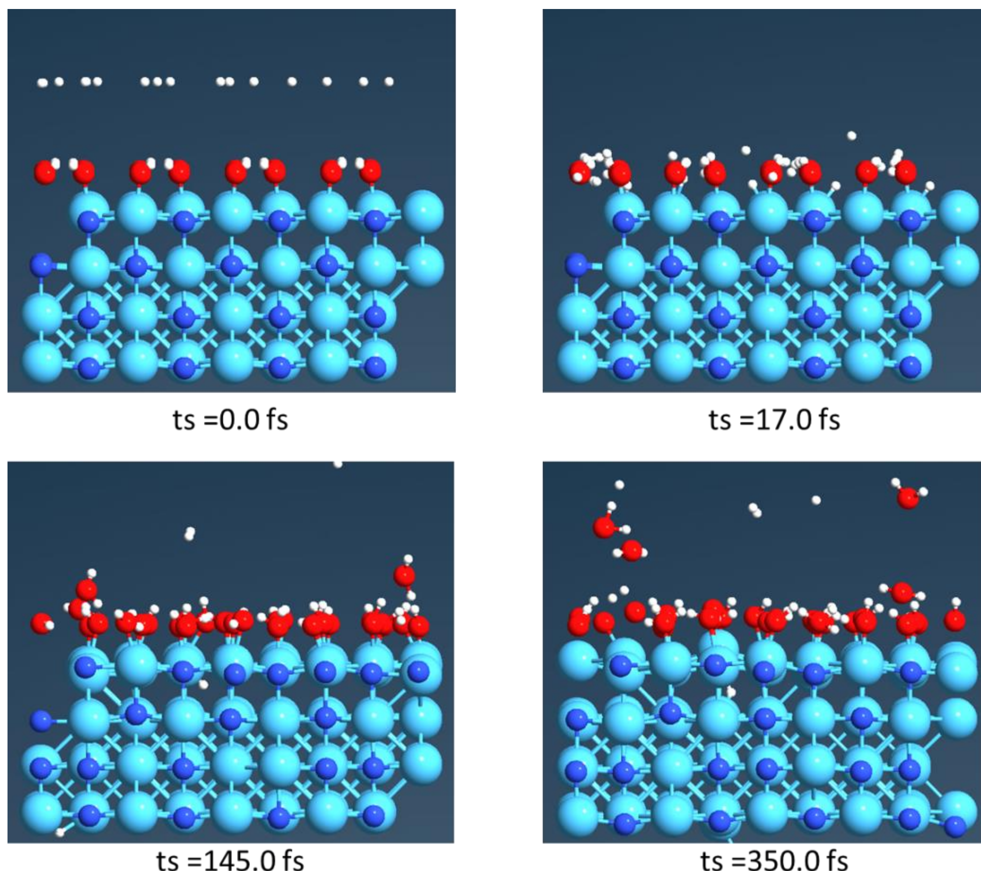

Figure A5.7. Ab initio molecular dynamics (AIMD) simulations for probing the effect of energetic H^+ ion bombardment with higher initial velocity (1.75 Å/fs) on fully hydroxylated HfN(200) surface. Extended version of Figure 5.3, with more time steps being visualized. Color code: cyan: Hf; blue: N; red: O; white: H.

5. *Surface species following the H^+ ion bombardment and complete abstraction of H_2O*

We have previously discussed the surface reactions occurring on the fully hydroxylated HfN(200) surface upon H^+ ion bombardment based on the AIMD simulations. For comparison purposes, we also simulated the H^+ ion bombardment (with assigned velocity of 1.75 Å/fs) on bare HfN(200) surface, supposing that all the surface –OH groups have been dissociated and H_2O has been completely abstracted. The corresponding AIMD simulations (Figure A5.8 depicts several snapshots) suggests that only a very small fraction of the incoming H^+ ions binds on the bare HfN surface and can penetrate into the HfN lattice, whereas most of the ions are deflected off the surface. Only after losing their kinetic energy due to collisions with other particles and/or the HfN surface, the H^+ ions are found to bind preferably on the Hf sites (rather than N). However, the H^+ ions were found to weakly adsorb on the surface (i.e. physisorbed). Furthermore, they can freely hover above the surface, hopping from one Hf site to another. Additionally, the physisorbed H was found to undergo recombination to form molecular H_2.

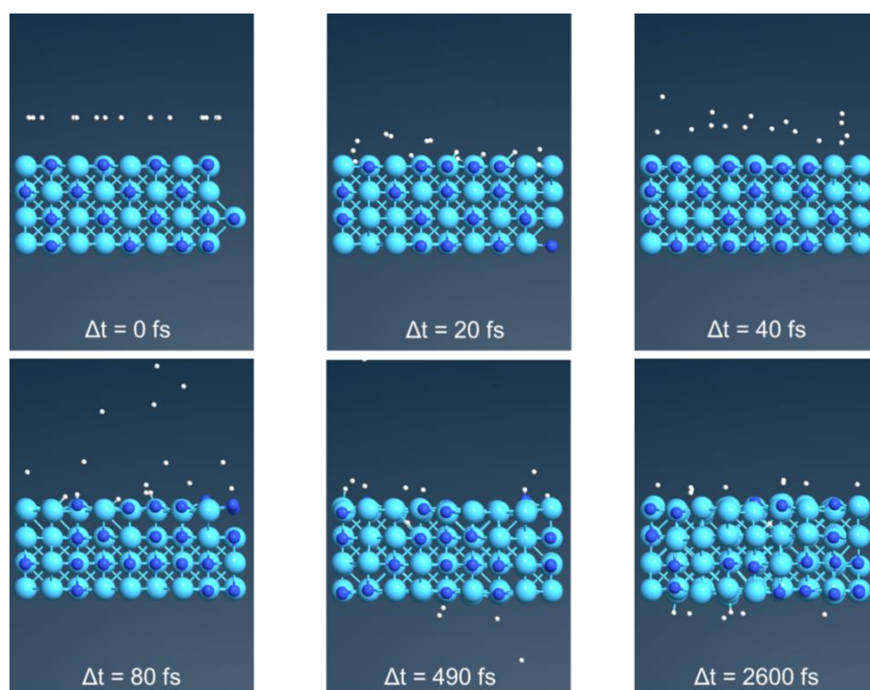

Figure A5.8. AIMD simulations for probing the effect of H^+ ion bombardment with higher kinetic energy on the bare HfN surface. Color code: cyan: Hf; blue: N; white: H.

Subsequently, a hypothetical case was considered, where all the surface Hf sites were hydrogenated and the efficiency of H_2O chemisorption was investigated. The relevant MD simulations (Figure A5.9) showed that the H_2O molecules do undergo chemisorption, but less efficiently (ca. 25% vs. 90% of the 16 H_2O molecules bind). Therefore, it can be inferred that the physisorbed H species might only slightly passivate the surface towards chemisorption of H_2O molecules following the H^+ ion bombardment. However, considering the rather weak binding of H^+ ions on the surface, it is anticipated that these ions are most likely removed during the purging step (with high Ar flow) subsequent to H_2 plasma exposure.

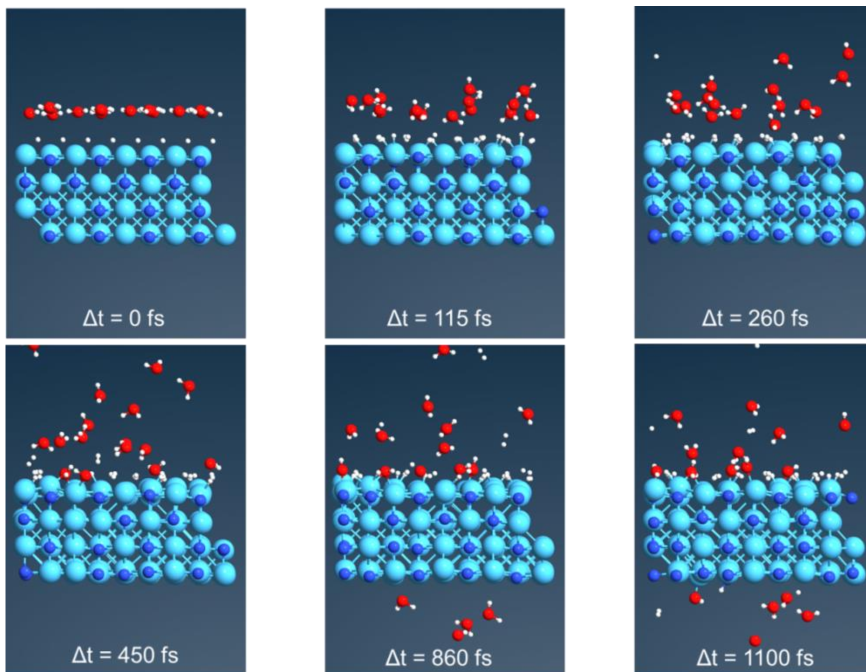

Figure A5.9. AIMD simulations for the H_2O adsorption on hydrogenated HfN surface. Color code: cyan: Hf; blue: N; red: O; white: H.

References

1. Kim, J.Y., et al., *Remote plasma enhanced atomic layer deposition of TiN thin films using metalorganic precursor.* Journal of Vacuum Science and Technology A: Vacuum, Surfaces and Films, 2004. **22**(1): p. 8-12.

2. Musschoot, J., et al., *Atomic layer deposition of titanium nitride from TDMAT precursor.* Microelectronic Engineering, 2009. **86**(1): p. 72-77.

3. Kim, J.Y., et al., *Remote plasma-enhanced atomic-layer deposition of tiN by using TDMAT with a NH 3 plasma.* Journal of the Korean Physical Society, 2004. **45**(6): p. 1639-1643.

4. Heil, S.B.S., et al., *Low-temperature deposition of TiN by plasma-assisted atomic layer deposition.* Journal of the Electrochemical Society, 2006. **153**(11): p. G956-G965.

5. Krylov, I., et al., *Properties of conductive nitride films prepared by plasma enhanced atomic layer deposition using quartz and sapphire plasma sources.* Journal of Vacuum Science & Technology A, 2019. **37**(1): p. 010906.

6. Seungchan, C., et al., *Barrier Characteristics of ZrN Films Deposited by Remote Plasma-Enhanced Atomic Layer Deposition Using Tetrakis(diethylamino)zirconium Precursor.* Japanese Journal of Applied Physics, 2007. **46**(7R): p. 4085.

7. Consiglio, S., et al., *Plasma-assisted atomic layer deposition of conductive hafnium nitride using tetrakis(ethylmethylamino)hafnium for CMOS gate electrode applications.* Journal of the Electrochemical Society, 2008. **155**(3): p. H196-H201.

8. Kim, E.J. and D.H. Kim, *Highly conductive HfN x films prepared by plasma-assisted atomic layer deposition.* Electrochemical and Solid-State Letters, 2006. **9**(8): p. C123-C125.

9. Karwal, S., et al., *Plasma-assisted atomic layer deposition of HfNx: Tailoring the film properties by the plasma gas composition.* Journal of Vacuum Science and Technology A: Vacuum, Surfaces and Films, 2017. **35**(1).

10. Karwal, S., et al., *Low resistivity HfNx grown by plasma-assisted ALD with external rf substrate biasing.* Journal of Materials Chemistry C, 2018. **6**(15): p. 3917-3926.

11. Rampelberg, G., et al., *Low temperature plasma-enhanced atomic layer deposition of thin vanadium nitride layers for copper diffusion barriers.* Applied Physics Letters, 2013. **102**(11): p. 111910.

12. Hinz, J., A.J. Bauer, and L. Frey, *Analysis of NbN thin film deposition by plasma-enhanced ALD for gate electrode application.* Semiconductor Science and Technology, 2010. **25**(7): p. 075009.

13. Langereis, E., et al., *Synthesis and in situ characterization of low-resistivity Ta Nx films by remote plasma atomic layer deposition.* Journal of Applied Physics, 2007. **102**(8).

14. Bertuch, A., et al., *Plasma enhanced atomic layer deposition of molybdenum carbide and nitride with bis(tert-butylimido)bis(dimethylamido) molybdenum.* Journal of Vacuum Science & Technology A: Vacuum, Surfaces, and Films, 2017. **35**(1): p. 01B141.

15. Sowa, M.J., et al., *Plasma-enhanced atomic layer deposition of tungsten nitride.* Journal of Vacuum Science & Technology A: Vacuum, Surfaces, and Films, 2016. **34**(5): p. 051516.

16. Ritala, M. and M. Leskelä, *Chapter 2 - Atomic layer deposition*, in *Handbook of Thin Films*, H. Singh Nalwa, Editor. 2002, Academic Press: Burlington. p. 103-159.

17. Knoops, H.C.M., et al., *Status and prospects of plasma-assisted atomic layer deposition.* Journal of Vacuum Science & Technology A, 2019. **37**(3): p. 030902.

18. Jousten, K. and C.B. Nakhosteen, *Handbook of Vacuum Technology*. 2016: Wiley.

19. Kroll, U., et al., *Origins of atmospheric contamination in amorphous silicon prepared by very high frequency (70 MHz) glow discharge.* Journal of Vacuum Science & Technology A: Vacuum, Surfaces, and Films, 1995. **13**(6): p. 2742-2746.

20. Blöchl, P.E., *Projector augmented-wave method.* Physical Review B, 1994. **50**(24): p. 17953-17979.

21. Kresse, G. and D. Joubert, *From ultrasoft pseudopotentials to the projector augmented-wave method.* Physical Review B, 1999. **59**(3): p. 1758-1775.

22. Kresse, G. and J. Furthmüller, *Efficiency of ab-initio total energy calculations for metals and semiconductors using a plane-wave basis set.* Computational Materials Science, 1996. **6**(1): p. 15-50.

23. Kresse, G. and J. Furthmüller, *Efficient iterative schemes for ab initio total-energy calculations using a plane-wave basis set.* Physical Review B, 1996. **54**(16): p. 11169-11186.

24. Kresse, G. and J. Hafner, *Ab initio molecular dynamics for liquid metals.* Physical Review B, 1993. **47**(1): p. 558-561.

25. Kresse, G. and J. Hafner, *Ab initio molecular-dynamics simulation of the liquid-metal-amorphous-semiconductor transition in germanium.* Physical Review B, 1994. **49**(20): p. 14251-14269.

26. Hohenberg, P. and W. Kohn, *Inhomogeneous Electron Gas.* Physical Review, 1964. **136**(3B): p. B864-B871.

27. Kohn, W. and L.J. Sham, *Self-Consistent Equations Including Exchange and Correlation Effects.* Physical Review, 1965. **140**(4A): p. A1133-A1138.

28. Perdew, J.P., K. Burke, and M. Ernzerhof, *Generalized Gradient Approximation Made Simple.* Physical Review Letters, 1996. **77**(18): p. 3865-3868.

29. Perdew, J.P., K. Burke, and M. Ernzerhof, *Generalized Gradient Approximation Made Simple [Phys. Rev. Lett. 77, 3865 (1996)].* Physical Review Letters, 1997. **78**(7): p. 1396-1396.

30. Grimme, S., et al., *A consistent and accurate ab initio parametrization of density functional dispersion correction (DFT-D) for the 94 elements H-Pu.* The Journal of Chemical Physics, 2010. **132**(15): p. 154104.

31. Henkelman, G., B.P. Uberuaga, and H. Jónsson, *A climbing image nudged elastic band method for finding saddle points and minimum energy paths.* The Journal of Chemical Physics, 2000. **113**(22): p. 9901-9904.

32. Nocedal, J., *Updating quasi newton matrices with limited storage.* Mathematics of Computation, 1980. **35**(151): p. 951-958.

33. *VTST tool set for VASP*. 2015; Available from: http://theory.cm.utexas.edu/vasp/.

34. *Comparison of the Bader charges of the bare and hy-droxylated HfN models reveals that the binding of -OH groups (with a partial charge of ca. -0.52e per -OH moiety) triggers a charge transfer away from the surface Hf atoms (amounting to ca. 0.35e).*

35. Henning, H., *Chapter 2.6 - Turbomolecular Pumps*, in *Handbook of Vacuum Science and Technology*. 1998, Academic Press: San Diego. p. 183-213.

36. Profijt, H.B., M.C.M. Van De Sanden, and W.M.M. Kessels, *Substrate-biasing during plasma-assisted atomic layer deposition to tailor metal-oxide thin film growth.* Journal of Vacuum Science and Technology A: Vacuum, Surfaces and Films, 2013. **31**(1).

37. Faraz, T., et al., *Energetic ions during plasma-enhanced atomic layer deposition and their role in tailoring material properties.* Plasma Sources Science and Technology, 2019. **28**(2): p. 024002.

Chapter 6

Plasma-assisted ALD of highly conductive HfN_x: on the effect of energetic ions on film microstructure*

Abstract

In this work, we report on the atomic layer deposition (ALD) of HfN_x thin films by employing $CpHf(NMe_2)_3$ as the Hf(IV) precursor and Ar-H_2 plasma in combination with external rf substrate biasing as the co-reactant. Following up on our previous results based on an H_2 plasma and external rf substrate biasing, here we address the effect of ions with a larger mass and higher energy impinging on HfN_x film surface during growth. We show that an increase in the average ion energy up to 304 eV leads to a very low electrical resistivity of $4.1 \cdot 10^{-4}$ Ωcm. This resistivity value is achieved for films as thin as ~35 nm, and it is an order of magnitude lower than the resistivity reported in literature for HfN_x films grown by either CVD or ALD, while being comparable to the resistivity of PVD-grown HfN_x films. From the extensive thin film characterization, we conclude that the impinging ions during the film growth lead to the very low electrical resistivity of HfN_x films by suppressing the oxygen incorporation and in-grain nano-porosity in the films.

Saurabh Karwal, Marcel A. Verheijen, Karsten Arts, Tahsin Faraz, Wilhelmus M.M. Kessels and Mariadriana Creatore (submitted)

6.1 Introduction

Conductive transition metal nitride (TMN) films find many applications in nano-electronics. They are used as metal electrodes in metal oxide semiconductor field effect transistors (MOSFETs) [1-4], and as diffusion barriers in inter-connects [5-8]. In view of the continuous scaling of semiconductor devices, the application of TMN films at small dimensions requires ultra-thin films with low resistivity, besides forming stable interfaces, e.g. with the underlying high-k HfO_2 [1, 3, 4, 8]. Specifically, thin films of titanium nitride and tantalum nitride tend to form undesirable oxy-nitrides at the interface with HfO_2 [4, 8]. Low resistivity hafnium nitride (HfN_x) can serve as an effective alternative because of its superior stability when used in combination with HfO_2 [8].

HfN_x predominantly exists in two crystal phases: highly resistive Hf_3N_4 with Hf(IV) oxidation state [9, 10], and low resistivity δ-HfN with Hf(III) oxidation state [11, 12]. The control of the oxidation state of Hf is therefore essential to synthesize conductive HfN_x layers [13-15]. Physical vapor deposition (PVD) methods have been widely adopted for the synthesis of low resistivity HfN_x films [8, 11, 12, 16-19]. Seo *et al.* have reported the growth of stoichiometric and epitaxial 500 nm thick HfN_x layers with a resistivity of $1.4\cdot10^{-5}$ Ωcm, which is the lowest resistivity value reported thus far [18]. Typically, the polycrystalline HfN_x films prepared by PVD exhibit a resistivity of ca. (1-2)$\cdot10^{-4}$ Ωcm for a typical film thickness of ~200 nm [17, 19, 20]. On the other hand, the growth of low resistivity HfN_x films by techniques employing a metal-organic precursor, such as chemical vapor deposition (CVD) or atomic layer deposition (ALD), is very challenging [13, 14, 21-23]. A major challenge is the reduction of Hf(IV) oxidation state in the precursor to Hf(III) oxidation state in the deposited film, as highlighted in our previous work [13, 14]. Kim *et al.* reported the growth of HfN_x films with a resistivity of $1\cdot10^{-3}$ Ωcm, the lowest achieved by means of CVD [21].

The urgent requirement from the field of nano-electronics is the synthesis of ultra-thin films with precise control over film thickness, excellent uniformity and conformality on high aspect ratio 3D nanostructures [24-27]. These requirements motivate the synthesis of low resistivity HfN_x films by ALD. We have recently shown that the δ-HfN phase can be achieved by adopting $CpHf(NMe_2)_3$ as Hf(IV) precursor and H_2 plasma as reducing co-reactant in a plasma-assisted ALD process [13]. We demonstrated that the application of an external rf substrate bias during the H_2 plasma exposure and an increase in the time-averaged substrate potential ($|V_{bias}|$) from 0V to 130V resulted in a major decrease in electrical resistivity (ρ_e) from 0.9 Ωcm to $3.3\cdot10^{-3}$ Ωcm [14]. The decrease in ρ_e was found to be correlated with a major increase in the fraction of Hf(III) oxidation state from 0.65±0.02 to 0.82±0.02 [13, 14]. These results demonstrated that the impingement of energetic

ions during the film growth can significantly improve the chemical and associated electrical properties of HfN_x thin films prepared by ALD. In parallel, Villamayor *et al.* recently showed that an increase in the mass of impinging ions positively affects also the crystallinity of HfN_x films grown by PVD, which contributes to the decrease in electrical resistivity [20].

In the present work, we investigate the effect of Ar-H_2 plasma in combination with external rf substrate biasing during the plasma half cycle as the reducing co-reactant. The impact of impingement of ions with larger mass and higher energy on the chemical and microstructural properties of HfN_x films is addressed here. The motivation to use Ar-H_2 plasma derives from the work of Sode *et al.* [28]. ArH^+ is anticipated to be the most abundant ion in an Ar-H_2 plasma, in contrast to the lighter H_3^+ ion in a H_2 plasma as employed in the previous work [28]. Furthermore, the ion energy measurements carried out in the present work indicate that the growing HfN_x film is subjected to a higher average ion energy ($<E_{ion}>$) in the case of Ar-H_2 plasma with respect to the previously reported H_2 plasma process [14]. The ions with a larger mass and higher $<E_{ion}>$ leads to a minimum in the electrical resistivity of $4.1\cdot10^{-4}$ Ωcm. To best of our knowledge, this value represents the lowest resistivity reported in the literature for HfN_x films grown by either CVD or ALD, and is comparable to the resistivity of PVD grown films [13, 14, 21-23]. This low resistivity is achieved for films as thin as ~35 nm. As a result of impinging ions with a larger mass and higher $<E_{ion}>$, a high Hf(III) fraction of 0.86 is obtained and major suppression of in-grain nano-porosity is observed, in contrast to the H_2 plasma process.

6.2 Experimental section

I. Plasma-assisted ALD of HfN_x

The ALD of HfN_x thin films was conducted in an Oxford Instruments FlexAL ALD reactor [14, 29, 30], equipped with an inductively coupled remote plasma (ICP) source with an alumina dielectric tube. The reactor chamber was pumped to a base pressure of 10^{-6} Torr using a turbo-molecular pump before every deposition. A stage temperature of 450°C was selected for HfN_x ALD. This corresponds to a substrate temperature of about 340°C as verified by spectroscopic ellipsometry (SE) [13, 14]. The onset of precursor decomposition and the start of a CVD regime was observed above 450°C as previously reported [14]. The reactor walls were kept at 145°C during all the depositions.

The Hf precursor $CpHf(NMe_2)_3$ (Air Liquide, >99.99% purity) was contained in a stainless steel bubbler at 60°C and bubbled by an Ar flow of 100 sccm. An Ar flow

of 100 sccm was also injected into the ICP alumina tube during the precursor dosage in order to suppress deposition on the ICP tube walls (a gate valve present between the ICP source and reactor chamber was kept open during the full cycle). Following the precursor dose, the chamber was pumped down to a base pressure of 10^{-6} Torr in order to remove the unreacted precursor and reaction byproducts for 4 s. For the plasma exposure half cycle, an $Ar+H_2$ gas mixture (10 sccm Ar and 40 sccm H_2) was introduced into the chamber from the ICP alumina tube. The valve to the pump was fully opened culminating in a reactor pressure of ~6 mTorr. After stabilization of the gas flows for 4 s, the plasma was ignited with 100W radio frequency (rf) ICP power (13.56 MHz) for the desired time. The purge steps for both half cycles consisted of a flow of 200 sccm Ar through the bubbling lines in addition to the 100 sccm Ar flow from the ICP source and with the valve to the pump fully opened. A $CpHf(NMe_2)_3$ pulse length of 4 s and plasma exposure of 10 s were used, while keeping the purge step of 2 s after every half cycle [13].

II. External rf substrate biasing

Employing the special feature of our Oxford Instruments FlexAL systems, an external substrate bias is applied during the plasma half cycle for the last 5 s using an additional rf power source (13.56 MHz), attached to the substrate table [14]. As a result, a time-averaged negative substrate potential with respect to ground (V_{bias}) develops during the plasma exposure [14]. The magnitude of V_{bias} is tuned by changing the applied rf power as previously reported in detail (appendix, Figure A6.1) [14]. An oscilloscope was connected to the substrate table via a high voltage probe that was used to measure the rf bias voltage waveforms as a function of time [14]. Figure A6.1 also shows the $|V_{bias}|$ values for the applied rf bias power values [14, 31].

The ions are accelerated towards the surface of the growing film as a consequence of the voltage drop over the plasma sheath [31]. The ion flux-energy distribution functions (IFEDFs) of incident ions are measured using an Impedans Semion retarding field energy analyzer (RFEA) [31-33], as described in detail in ref. [34]. As reported by Profijt *et al.*, a mono-modal IFEDF for the grounded electrode ($|V_{bias}|$ = 0V) condition, whereas the application of external rf substrate bias resulted in a bi-modal IFEDF [31]. The shape of the IFEDF for a collisionless sheath is determined by the ratio of ion transit time to the period of rf cycle [32]. The mean ion energy is denoted by E_{ion}, while ΔE_{ion} represents the peak-to-peak separation in a bimodal IFEDF in the text. Furthermore, the RFEA is also used to estimate the flux of incident ions using $\Gamma_i = {I_c}/{e \cdot A_e}$, where I_c is the collector current measured by the RFEA, e is the elementary charge and A_e is the effective

collector area. Ref. [34] describes a detailed procedure to deduce the value of factor A_e, equal to (3.9±1.0)·10^{-3} cm^2 for the RFEA probe used in this work. Moreover, a slightly lower value of $|V_{bias}|$ was obtained during the IFEDF measurements using RFEA than during the growth of HfN_x films on a substrate, for a particular rf bias power application (appendix, Figure A6.1c).

III. Substrates and material characterization

The HfN_x films are deposited on planar Si(100) substrates with a diameter of 100 mm and with 450 nm SiO_2 atop.

The growth per cycle (GPC) and the dielectric functions of the HfN_x films were examined using spectroscopic ellipsometry (SE, J.A. Woollam, Inc., M2000U). The dielectric functions ($0.75 \leq h\nu \leq 5.0$ eV) of HfN_x films could be modelled using one Drude and two Lorentz oscillators as demonstrated by Hu *et al.* (appendix, Table A6.1 for details and discussion on the selected optical model) [11]. Additionally, the optical film resistivity (ρ_{op}) was deduced from the free-carrier Drude parameterization, given by $\rho_{op} = (\Gamma_D/\varepsilon_o) \cdot \omega_p^2$, where Γ_D is the damping factor for the Drude oscillator, ε_o is the permittivity of free space, and ω_p is the screened plasma frequency. The electrical resistivity (ρ_e) was obtained via the four-point probe measurements using a Keithley 2400 SourceMeter and a Signaton probe by multiplying the sheet resistance of the HfN_x films with the film thickness as derived from SE. All resistivities reported in this work are for room temperature.

X-ray photoelectron spectroscopy (XPS) measurements were performed using a Thermoscientific K-Alpha KA1066 system equipped with a monochromatic Al Kα ($h\nu$ = 1486.6 eV) source in order to study the chemical bonding and the oxidation states of elements present in the film. The chemical composition and the mass density of the films was evaluated via Rutherford backscattering spectrometry (RBS) and elastic recoil detection (ERD) using 1900 keV $^4He^+$ ions (Detect99). For the ERD measurements, the recoil angle was 30° and the angle of incidence with the sample surface was kept at 15° whereas for the RBS, two detectors were used with scattering angles of 170° and 150°.

The surface morphology and the lateral grain sizes of thick HfN_x films (t > 30 nm) were studied using a Zeiss Sigma field emission scanning electron microscope (FE-SEM) operated at an acceleration voltage of 2 kV.

The crystallinity of the HfN_x films was examined with a PANalytical X'pert PRO MRD X-ray diffractometer using a Cu Kα (λ = 1.542 Å) X-ray source. The X-ray diffractograms were obtained in a θ-2θ configuration and were compared with the powder HfN patterns [35, 36]. High-angle annular dark-field scanning

transmission electron microscopy (HAADF-STEM) studies were conducted using a JEOL ARM 200F operated at 200kV in order to analyze: 1) the lateral grain sizes of thin HfN_x films ($t \leq 10$ nm), defined by the low atomic density grain boundary regions in the top-view images and 2) the microstructure and the nano-porosity of thick HfN_x films ($t > 30$ nm), obtained from the cross-sectional samples. These cross-sectional samples were prepared using a Focused Ion Beam (FIB), following a standard lift-out sample preparation procedure. Prior to FIB milling, a protective layer was deposited on the HfN_x layers. In case of the Ar-H_2 plasma sample, a stack of Electron Beam Induced Deposited (EBID) SiO_2, EBID Pt/C and Ion Beam Induced Deposited (IBID) Pt was used. In case of the H_2 plasma sample, only EBID Pt/C and IBID Pt was used, as can be recognized from the TEM images below.

6.3 Results and discussion

I. Ion energy characterization

The IFEDF measurements were carried out at various values of $|V_{bias}|$ for Ar-H_2 plasma and are presented in Figure 6.1. The IFEDFs for the H_2 plasma process were also measured and are shown for comparison. It is noted that the energy distribution of ions with a specific mass cannot be resolved and rather a cumulative distribution of all the ions impinging on the surface is obtained. However, from literature [37-39] and a recent report from Sode *et al.* [28], it can be expected that an Ar-H_2 plasma contains ArH^+, Ar^+, H_3^+, H_2^+ and H^+ ions, with ArH^+ being the most abundant ion under a similar experimental conditions. In a pure H_2 plasma discharge, H_3^+ is the most abundant ion, in combination with H_2^+ and H^+ ions [28].

A mono-modal IFEDF with an average ion energy ($\langle E_{ion} \rangle$) of 24 eV was obtained for the grounded electrode ($|V_{bias}|$ = 0V) for the Ar-H_2 plasma as shown in Figure 6.1a. The application of 10W rf bias power resulted in an asymmetrical IFEDF with a $|V_{bias}|$ = 102V, $\langle E_{ion} \rangle$ = 126 eV and an outermost peak-to-peak width (ΔE_{ion}) of 47 eV. Upon increasing the rf bias power to 60W, the value of $|V_{bias}|$ increased to 246V, the $\langle E_{ion} \rangle$ increased to 308 eV and an ΔE_{ion} of 77 eV was obtained. The increase in ΔE_{ion} with $|V_{bias}|$ is a consequence of an increase in the peak-to-peak sheath voltage [32]. Furthermore, when closely inspecting the IFEDFs, they appear to be a superposition of multiple bi-modal IFEDFs of individual cationic species with different masses (i.e. ArH^+, Ar^+, H_3^+, H_2^+ and H^+), that have different transit times through the plasma sheath as described by Manenschijn *et al.* [40]. This may be expected at low operating pressures used, where there are less ion-neutral collisions in the plasma sheath and ions are essentially unidirectional towards the surface of growing film.

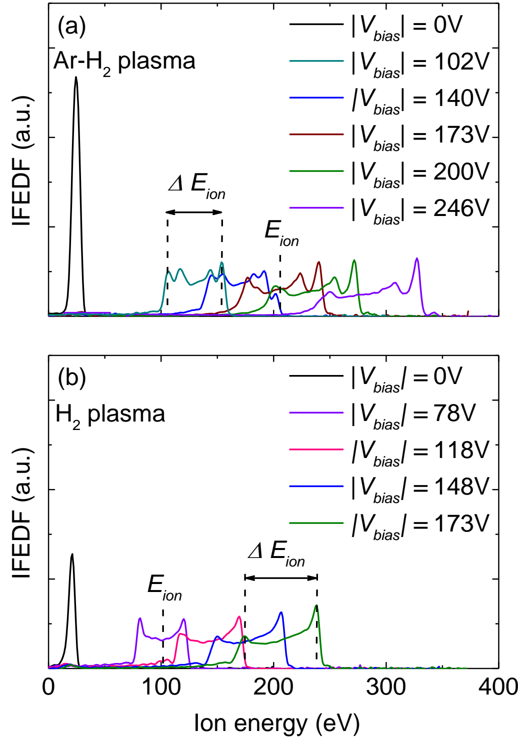

Figure 6.1. Ion flux-energy distribution functions (IFEDFs) for ions in a (a) Ar-H_2 plasma operated at 6 mTorr and (b) H_2 plasma operated at 30 mTorr for various values of $|V_{bias}|$.

Figure 6.1b shows the IFEDFs at various values of $|V_{bias}|$ for the previously reported H_2 plasma process at 30 mTorr. Similar to the Ar-H_2 plasma, a mono-modal IFEDF was obtained for the grounded electrode ($|V_{bias}|$ = 0V), centered at $\langle E_{ion} \rangle$ of 19 eV. Upon the application of external rf substrate bias, the IFEDF became bi-modal and an $\langle E_{ion} \rangle$ of 98 eV with ΔE_{ion} of 39 eV was obtained at $|V_{bias}|$ = 78V (rf bias power = 10W). Furthermore, the $\langle E_{ion} \rangle$ and ΔE_{ion} increases with $|V_{bias}|$ in a similar fashion as for Ar-H_2 plasma.

The flux of impinging ions (Γ_i) was calculated from the total ion current (I_c) recorded by the RFEA, since the flux of impinging ions is also expected to influence the film growth and related properties, as shown by Adibi *et al.* [41]. In our case, a constant Γ_i of $(9.0\pm2.1)\cdot10^{14}$ cm^{-2} s^{-1} was calculated independent of $|V_{bias}|$ for the Ar-H_2 plasma, whereas a slight increase in Γ_i from $(3.1\pm0.7)\cdot10^{14}$ cm^{-2} s^{-1} at $|V_{bias}|$ = 0V to $(9.5\pm2.2)\cdot10^{14}$ cm^{-2} s^{-1} at $|V_{bias}|$ = 173V was observed for the H_2

plasma process. Based on these results, we can conclude that the values of Γ_i' for both the processes are relatively similar in the entire range of $|V_{bias}|$ investigated, whereas a significant increase in E_{ion} is observed in the case of the Ar-H_2 plasma.

II. Opto-electrical properties of HfN_x

The ALD process was extensively characterized in terms of growth-per-cycle (GPC) and material properties. A detailed discussion can be found in the appendix and here, only a few aspects are highlighted. The GPC was found to be constant at 0.35±0.04 Å/cycle (Figure A6.2), independent of the increase in the $|V_{bias}|$ from 0V to 255V. Above the $|V_{bias}|$ value of 255V, a slight increase in the GPC was observed. The previously reported data for the H_2 plasma process is also included in Figure A6.2 for comparison. Furthermore, based on our previous studies on the ALD process employing H_2 plasma, it is anticipated that the application of external rf substrate bias does not affect the saturation behavior of the ALD process [14].

Figure 6.2a shows the ρ_e and the ρ_{op} resistivity values for HfN_x films as a function of $|V_{bias}|$. The HfN_x films grown at $|V_{bias}|$ = 0V using an Ar-H_2 plasma exhibit values of ρ_e of $(2.0\pm0.1)\cdot10^{-1}$ Ωcm and of $\rho_{op} = (5.2\pm0.1)\cdot10^{-3}$ Ωcm. When increasing the $|V_{bias}|$ value up to 255V, a substantial decrease in ρ_e to $(4.1\pm0.1)\cdot10^{-4}$ Ωcm and in ρ_{op} to $(2.4\pm0.1)\cdot10^{-4}$ Ωcm was observed. A subsequent increase in $|V_{bias}|$ value to 367V led to an increase in ρ_e to $(6.5\pm0.1)\cdot10^{-4}$ Ωcm and ρ_{op} to $(3.5\pm0.1)\cdot10^{-4}$ Ωcm. Figure 6.2a also contains the previously reported ρ_e and ρ_{op} data for the H_2 plasma process for comparison [14].

It should be noted that the very low ρ_e achieved at $|V_{bias}|$ = 255V is for HfN_x films as thin as ~35 nm. To best of our knowledge, this resistivity value is the lowest reported for HfN_x films grown by either CVD or ALD, and is comparable to values reported for PVD-grown films [13, 14, 21-23]. The $|V_{bias}|$ value that yields the minimum in ρ_e and ρ_{op} is here referred to as *optimum condition* for the corresponding ALD process and the rest of the manuscript will address the film characterization mainly at the *optimum conditions*.

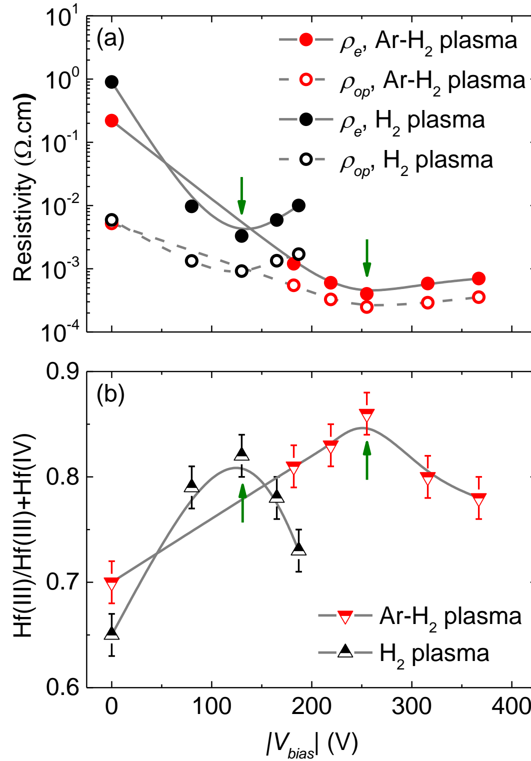

Figure 6.2. (a) Electrical (ρ_e) and optical resistivity (ρ_{op}) values for ~35 nm HfN_x films grown using Ar-H_2 plasma compared with previously reported ~80 nm HfN_x films grown using H_2 plasma and (b) the corresponding Hf(III) oxidation state fractions as a function of $|V_{bias}|$. Lines serve as a guide to the eye and the (green) arrows indicate the *optimum condition* in terms of minimum in resistivity achieved in both ALD processes.

By considering that the interaction distance of the incident light with the HfN_x films is rather small, it can be expected that only the crystalline quality within 3-4 nm is probed by SE for determining the ρ_{op} (see Table A6.1 and the discussion underneath). Therefore, the difference between the ρ_e and ρ_{op} (Δρ) provides insights into the amount of electronic scattering in the HfN_x films, as we previously described [13, 14, 42]. A very low *Δρ* is achieved at the *optimum condition* for Ar-H_2 plasma. It is relevant here to underline that *Δρ* is an order of magnitude smaller than in the case of the previously reported H_2 plasma process. This suggests that the application of Ar-H_2 plasma has greatly contributed to reduce the amount of electronic scattering in the HfN_x films. In order to comprehend the reason behind the very low scattering and the low value of ρ_e

achieved at the *optimum condition*, the chemical composition and microstructure of the HfN_x films was studied [14].

III. Chemical properties of HfN_x

The chemical composition of the HfN_x films was investigated by means of XPS and RBS. The binding energy values attributed to each spectral line for a specific chemical element in the XPS spectrum can be found in the appendix (Table A6.2). Figure 6.2b shows the Hf(III) oxidation state fraction as a function of $|V_{bias}|$. For comparison, the previously reported Hf(III) fraction data for H_2 plasma is also shown. The Hf(III) fraction increased from 0.70±0.02 to 0.86±0.02 upon increasing the $|V_{bias}|$ from 0V up to the *optimum condition* (see the deconvolution of Hf 4f XPS spectrum in Figure A6.3a-b). Interestingly, the high Hf(III) fraction achieved at the *optimum condition* for Ar-H_2 plasma is comparable to the previously reported H_2 plasma (i.e. 0.86±0.02 vs. 0.82±0.02).

Table 6.1 gives an overview of the material properties of HfN_x films grown at the *optimum condition* using Ar-H_2 plasma, whereas the film properties as a function of $|V_{bias}|$ can be found in the appendix (Table A6.3). The aforementioned increase in Hf(III) fraction upon increasing the $|V_{bias}|$ from 0V to 255V is correlated with a major suppression in O content from 19.9±0.9 at.% to <2 at.%. In our previous report on H_2 plasma [14], we also concluded that this increase in Hf(III) fraction with $|V_{bias}|$ is associated with a major decrease in O content in the HfN_x films. Additionally, the H content (and presumably Hf-H bonds) at the *optimum condition* appears to limit the Hf(III) fraction from reaching unity [14]. The latter suggestion is further corroborated by the fact that an increase in $|V_{bias}|$ beyond the *optimum condition* leads to an increase in H at.%, while a simultaneous decrease in Hf(III) fraction is observed (Table A6.3). It should be noted that the O content stays below <2 at.% at $|V_{bias}|$ of 255V or higher. Furthermore, the C concentration was found to increase upon increasing the $|V_{bias}|$ up to the *optimum condition* (see Figure A6.3d). This increase in carbon is similar to previously reported H_2 plasma process and is thought to arise from enhanced cracking of ligands on the film surface by energetic ions, followed by their re-deposition [14, 30].

Based on these results, it can be concluded that a high Hf(III) fraction and a very low O content is achieved at the *optimum condition* for the HfN_x films grown using Ar-H_2 plasma, which is comparable to the previously reported H_2 plasma process.

Table 6.1. Properties of the HfN_x films prepared at *optimum conditions* using an Ar-H_2 plasma compared with previously reported properties of HfN_x films deposited using a H_2 plasma. The electrical resistivity was obtained by a combination of four-point probe (FPP) and spectroscopic ellipsometry (SE) whereas the optical resistivity and thickness were determined using SE. X-ray photoelectron spectroscopy (XPS) was used to obtain the Hf(III) oxidation state fraction whereas the chemical composition was determined via Rutherford backscattering (RBS). The H content was measured using elastic recoil detection (ERD). The mass density was calculated by dividing the total areal mass density (obtained via RBS and ERD) with the film thickness. The measurement errors for electrical and optical resistivities are less than 3% and 2% of their absolute values, respectively.

Plasma $\lvert V_{bias} \rvert$	FPP	SE		XPS	RBS				ERD
	Electrical resistivity (Ωcm)	Optical resistivity (Ωcm)	Thickness (nm)	Hf(III) / Hf(III)+Hf(IV)	N/Hf	C (at.%)	O (at.%)	Mass density (g cm^{-3})	H (at.%)
Ar-H_2 255V	$4.1\cdot10^{-4}$	$2.4\cdot10^{-4}$	35	0.86±0.02	0.84±0.08	8.4±0.4	<2.0	10.0±0.3	11.8±0.6
H_2 130	$3.3\cdot10^{-3}$	$9.0\cdot10^{-4}$	81	0.82	1.00±0.07	11.0±1.2	<2.0	8.6	12.6±0.6

IV. Microstructural properties of HfN_x

The crystallinity and microstructure of the HfN_x films were also investigated. In fact, we have previously shown that the ρ_e is also related to the film microstructure [14]. The crystallinity of 35 nm thick film grown using Ar-H_2 plasma and 80 nm thick film grown using H_2 plasma was examined using XRD (θ-2θ mode) (appendix, Figure A6.4). Conductive δ-HfN phase was observed for the *optimum condition* of the Ar-H_2 plasma, exhibiting HfN(111), HfN(200) and HfN(220) reflections in a similar peak intensity ratio as the powder δ-HfN pattern [14], indicating no preferred growth direction.

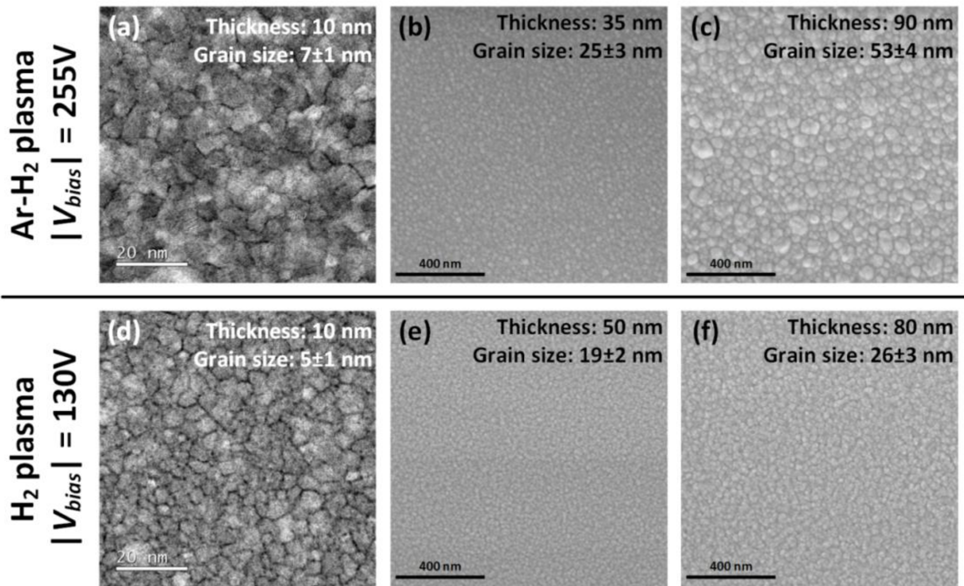

Figure 6.3. Top-view high-angle annular dark-field scanning transmission electron microscopy (HAADF-STEM) and scanning electron microscopy (SEM) images for HfN_x films prepared at the *optimum conditions* using Ar-H_2 plasma and H_2 plasma with an approximate thickness of (a and d) 10 nm; (b and e) 35 nm and 50 nm; (c and f) 90 nm and 80 nm, respectively.

The lateral grain sizes of the HfN_x films were subsequently investigated. Figure 6.3 shows top-view high-angle annular dark-field scanning transmission electron microscopy (HAADF-STEM) and scanning electron microscopy (SEM) images of HfN_x layers grown at the *optimum condition* of Ar-H_2 plasma, allowing evaluation of the lateral grain size as a function of film thickness. The images for H_2 plasma process are also shown for comparison purposes. It can be concluded from the data in HAADF-STEM and SEM images that the rate of lateral grain growth is

higher for Ar-H_2 plasma as compared to the H_2 plasma (Figure 6.4). Importantly, the lateral grain size for the relevant ~35 nm thick film grown using the Ar-H_2 plasma is similar to that of previously reported ~80 nm thick HfN_x film prepared with H_2 plasma (green circles in Figure 6.4).

The lateral grain sizes of the HfN_x films were subsequently investigated. Figure 6.3 shows top-view high-angle annular dark-field scanning transmission electron microscopy (HAADF-STEM) and scanning electron microscopy (SEM) images of HfN_x layers grown at the *optimum condition* of Ar-H_2 plasma, allowing evaluation of the lateral grain size as a function of film thickness. The images for H_2 plasma process are also shown for comparison purposes. It can be concluded from the data in HAADF-STEM and SEM images that the rate of lateral grain growth is higher for Ar-H_2 plasma as compared to the H_2 plasma (Figure 6.4). Importantly, the lateral grain size for the relevant ~35 nm thick film grown using the Ar-H_2 plasma is similar to that of previously reported ~80 nm thick HfN_x film prepared with H_2 plasma (green circles in Figure 6.4).

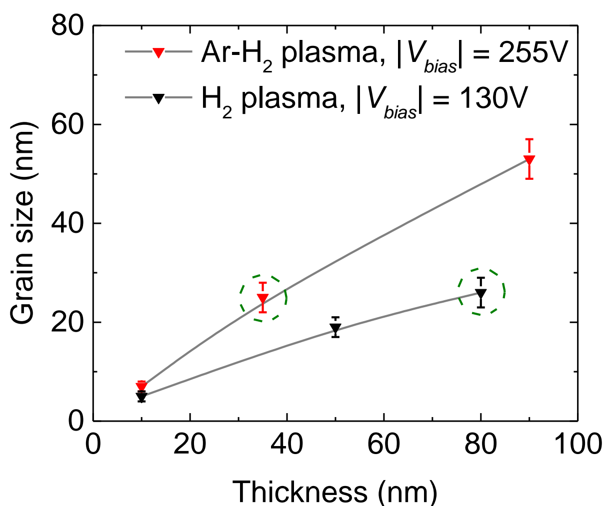

Figure 6.4. Lateral grain sizes for the HfN_x films prepared at the *optimum conditions* of the Ar-H_2 plasma and H_2 plasma as a function of film thickness. The points with the (green) circles indicate the grain sizes of HfN_x films that are discussed in more detail in terms of resistivity for the corresponding ALD process.

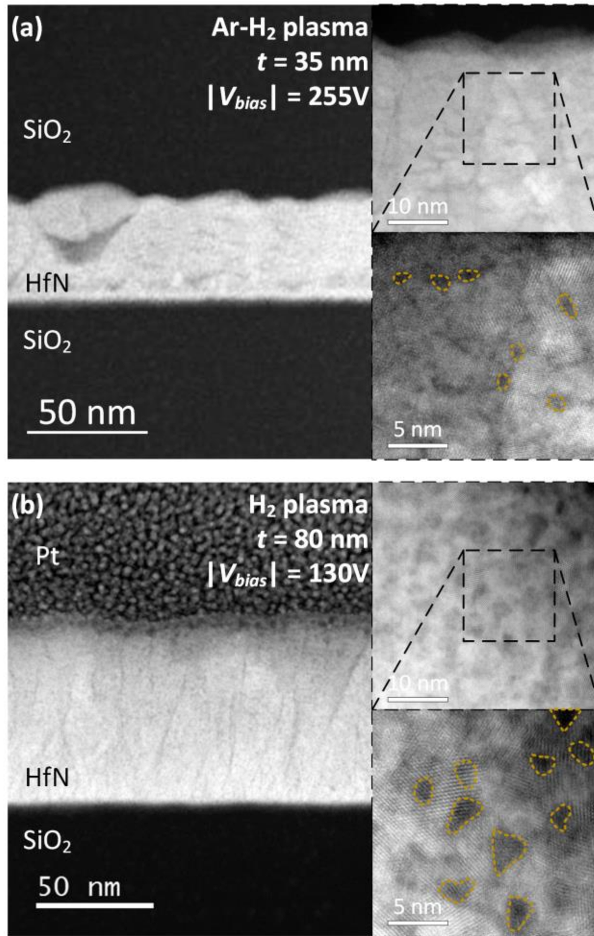

Figure 6.5. Cross-sectional high-angle annular dark-field scanning transmission electron microscopy (HAADF-STEM) images for (a) ~35 nm thick film grown at $|V_{bias}|$ = 255V using Ar-H_2 plasma and (b) ~80 nm thick film prepared using H_2 plasma at $|V_{bias}|$ = 130V. The insets show magnified views of the micro-structure displaying the nano-scale porosity in the film as indicated by the highlighted (yellow) areas.

The in-grain crystal quality of the HfN_x films grown at the *optimum conditions* was investigated by studying its micro-structure. Figure 6.5 shows the HAADF-STEM image of cross-sectional samples for the Ar-H_2 plasma (35 nm thick) and the H_2 plasma (80 nm thick) cases. Dark regions in the films indicate the presence of lighter elements and/or porosity. The images with a 50 nm scale display the lateral development of crystal grains as a function of height, yielding similar grain size values on the top surfaces of the film as measured from the aforementioned top-view HAADF-STEM and SEM studies of Figure 6.3. The higher magnification

insets reveal that the HfN_x film grown using Ar-H_2 plasma are quite dense, i.e. displaying much less nano-porosity than the case of H_2 plasma. Specifically, non-uniform contrast variations and dark patches can be observed within the crystal grains of the HfN_x film grown using H_2 plasma, suggesting the presence of lower density regions such as nano-pores. These results agree with the higher mass density obtained for HfN_x films grown using Ar-H_2 plasma in comparison with the H_2 plasma (Table 6.1).

The in-grain crystal quality of the HfN_x films grown at the *optimum conditions* was investigated by studying its micro-structure. Figure 6.5 shows the HAADF-STEM image of cross-sectional samples for the Ar-H_2 plasma (35 nm thick) and the H_2 plasma (80 nm thick) cases. Dark regions in the films indicate the presence of lighter elements and/or porosity. The images with a 50 nm scale display the lateral development of crystal grains as a function of height, yielding similar grain size values on the top surfaces of the film as measured from the aforementioned top-view HAADF-STEM and SEM studies of Figure 6.3. The higher magnification insets reveal that the HfN_x film grown using Ar-H_2 plasma are quite dense, i.e. displaying much less nano-porosity than the case of H_2 plasma. Specifically, non-uniform contrast variations and dark patches can be observed within the crystal grains of the HfN_x film grown using H_2 plasma, suggesting the presence of lower density regions such as nano-pores. These results agree with the higher mass density obtained for HfN_x films grown using Ar-H_2 plasma in comparison with the H_2 plasma (Table 6.1).

In addition, we observed the presence of V-shaped pyramidal voids for the Ar-H_2 plasma in the initial phase of film growth (Figure 6.5a). The cause for this phenomenon is not known yet. Although the voids can be observed in several areas of the whole TEM cross-section of the Ar-H_2 sample (appendix, Figure A6.5), it appears that their presence does not affect the film electrical properties.

6.4 Conclusions

Plasma-assisted ALD of HfN_x has been studied using $CpHf(NMe_2)_3$ as the Hf(IV) precursor and Ar-H_2 plasma in combination with an external rf substrate bias application as the co-reactant. Ion energy characterization reveals that the average energy of the impinging ions ($<E_{ion}>$) on the HfN_x surface at the *optimum condition* of the lowest film resistivity of $4.1 \cdot 10^{-4}$ Ωcm for Ar-H_2 plasma is 304 eV and the ion flux (Γ_i) is $(9.0 \pm 2.1) \cdot 10^{14}$ cm^{-2} s^{-1}. Such a low resistivity is achieved for films as thin as ~35 nm. From the extensive thin film characterization, we show that a very low O content (<2 at.%) and a correlated high Hf(III) oxidation state fraction of 0.86±0.02 is obtained for the HfN_x films grown at the *optimum*

condition. Furthermore, the HfN_x films exhibit a very low in-grain nano-porosity. The high in-grain crystalline quality and low in-grain nano-porosity is also in line with the aforementioned observation on the very low electronic scattering (i.e. small $\Delta\rho$) in the HfN_x films (Figure 6.2a). Altogether, these excellent material properties lead to the very low ρ_e of the HfN_x films grown using Ar-H_2 plasma with energetic ion bombardment.

Impinging ions during plasma processes are known to initiate several interactions with the growing films, for example, enhanced adatom surface diffusion leading to decrease in the defect density; bulk lattice atom displacements resulting in a collision cascade; sputtering and ion-induced damage; ion implantation at higher ion energies [20, 43-51]. In regards to the material properties, Hultman *et al.* and Petrov *et al.* showed that energetic ions in a N_2 and Ar-N_2 plasma discharges respectively with $|V_{bias}|$ value in the range of 150V - 250V can lead to annihilation of defects and reduction in nano-porosity in sputtered TiN films [52, 53], and attributed the decrease in defect density to the near-surface and sub-surface diffusion processes [44, 45].

Next to the ion energy, the mass of impinging ions is of importance. In our case, from the ion energy results and from literature reports [28], it is concluded that the HfN_x film surface at the *optimum conditions* is subjected to energetic ions with significantly higher ion energy and larger mass when using an Ar-H_2 plasma (mainly ArH^+) instead of a H_2 plasma ($\langle E_{ion} \rangle$ = 159 eV, mainly H_3^+), while the Γ'_i remains comparable ($\Gamma'_i = (8.2 \pm 1.9) \cdot 10^{14}$ cm^{-2} s^{-1} for H_2 plasma). It is further noted that the ρ_e value for HfN_x films grown at the *optimum conditions* using Ar-H_2 plasma is an order of magnitude lower than the H_2 plasma. This major decrease in the ρ_e value is primarily attributed to the improvement in the HfN_x film microstructure, enabled by the impingement of ions with a larger mass and higher energy. Relevantly, Villamayor *et al.* also recently showed that an increase in the mass of impinging ions by adopting Kr-N_2 plasma, instead of Ar-N_2 plasma, led to an improvement in the crystalline quality of the sputtered HfN_x films [20]. The above results can be understood from the fact that the nature of ion-surface interaction depends on the extent of energy and momentum transfer. As highlighted by Gago *et al.* [48], the system can be approximated by the simple case of an elastic binary atom(ion)-atom collision. Using this model, the kinematic factor (k) for energy transfer can be easily calculated using $k = {}^{4Mm}/_{(M+m)^2} \cdot cos^2\varphi$, where M and m are the masses of incoming ion and target atom respectively and φ is the scattering angle [48]. It should be noted that the value of k is approximately an order of magnitude higher for the impinging heavy ArH^+ ions in comparison to the light H_3^+ ions, when Hf is considered as the target atom. Altogether, it is expected that the impinging ions with a higher energy (304 eV vs.

159 eV) and larger mass (ArH^+ vs. H_3^+) may lead to a greater extent of energy and momentum transfer to the HfN_x film surface [20, 43-51].

So to conclude, the obtained results demonstrate how energy and mass of impinging ions and the associated energy and momentum transfer during plasma ALD can contribute to the fine tuning of the chemical and microstructural properties of HfN_x thin films. The results may be applicable to wide range of ALD processes including for the growth of other transition metal nitrides [54].

References

1. Liu, Y., et al., *Channel shape and interpoly dielectric material effects on electrical characteristics of floating-gate-type three-dimensional fin channel flash memories.* Japanese Journal of Applied Physics, 2015. **54**(4).
2. Pierson, H.O., *Handbook of Refractory Carbides and Nitrides: Properties, Characteristics, Processing and Apps*. 1996: Elsevier Science.
3. Franklin, A.D., et al., *Carbon Nanotube Complementary Wrap-Gate Transistors.* Nano Letters, 2013. **13**(6): p. 2490-2495.
4. Yu, H.Y., M.F. Li, and D.L. Kwong, *Thermally robust HfN metal as a promising gate electrode for advanced MOS device applications.* IEEE Transactions on Electron Devices, 2004. **51**(4): p. 609-615.
5. Hu, C.K. and J.M.E. Harper, *Copper interconnections and reliability.* Materials Chemistry and Physics, 1998. **52**(1): p. 5-16.
6. Jeong, W., et al., *Characteristics of HfN films deposited by using remote plasma-enhanced atomic layer deposition.* Journal of the Korean Physical Society, 2010. **56**(3): p. 905-910.
7. Kim, H., et al., *Diffusion barrier properties of transition metal thin films grown by plasma-enhanced atomic-layer deposition.* Proceedings of the 29th Conference on the Physics and Chemistry of Semiconductor Interfaces, 2002. **20**(4): p. 1321-1326.
8. Yu, H.Y., et al., *Robust High-Quality HfN-HfO 2 Gate Stack for Advanced MOS Device Applications.* IEEE Electron Device Letters, 2004. **25**(2): p. 70-72.
9. Xu, M., et al., *Optical properties of cubic Ti3N4, Zr3N4, and Hf3N4.* Applied Physics Letters, 2006. **89**(15).

10. Becker, J.S., E. Kim, and R.G. Gordon, *Atomic Layer Deposition of Insulating Hafnium and Zirconium Nitrides.* Chemistry of Materials, 2004. **16**(18): p. 3497-3501.

11. Hu, C., et al., *Nature of tunable optical reflectivity of rocksalt hafnium nitride films.* Journal of Physical Chemistry C, 2014. **118**(35): p. 20511-20520.

12. Farrell, I.L., et al., *Tunable electrical and optical properties of hafnium nitride thin films.* Applied Physics Letters, 2010. **96**(7).

13. Karwal, S., et al., *Plasma-assisted atomic layer deposition of HfNx: Tailoring the film properties by the plasma gas composition.* Journal of Vacuum Science and Technology A: Vacuum, Surfaces and Films, 2017. **35**(1).

14. Karwal, S., et al., *Low resistivity HfNx grown by plasma-assisted ALD with external rf substrate biasing.* Journal of Materials Chemistry C, 2018. **6**(15): p. 3917-3926.

15. Knoops, H.C.M., et al., *Reaction mechanisms of atomic layer deposition of TaNx from Ta(NMe2)5 precursor and H2-based plasmas.* Journal of Vacuum Science & Technology A, 2012. **30**(1): p. 01A101.

16. Johansson, B.O., et al., *Reactively magnetron sputtered Hf-N films. I. Composition and structure.* Journal of Applied Physics, 1985. **58**(8): p. 3104-3111.

17. Johansson, B.O., J.E. Sundgren, and U. Helmersson, *Reactively magnetron sputtered Hf-N films. II. Hardness and electrical resistivity.* Journal of Applied Physics, 1985. **58**(8): p. 3112-3117.

18. Seo, H.S., et al., *Growth and physical properties of epitaxial HfN layers on MgO(001).* Journal of Applied Physics, 2004. **96**(1): p. 878-884.

19. Shinkai, S. and K. Sasaki, *Influence of sputtering parameters on the formation process of high-quality and low-resistivity HfN thin film.* Japanese Journal of Applied Physics, Part 1: Regular Papers and Short Notes and Review Papers, 1999. **38**(4 A): p. 2097-2102.

20. Villamayor, M.M.S., et al., *Low temperature (Ts/Tm < 0.1) epitaxial growth of HfN/MgO(001) via reactive HiPIMS with metal-ion synchronized substrate bias.* Journal of Vacuum Science & Technology A, 2018. **36**(6): p. 061511.

21. Kim, Y., et al., *Metal-organic CVD of conductive and crystalline hafnium nitride films.* Chemical Vapor Deposition, 2005. **11**(6-7): p. 294-297.

22. Consiglio, S., et al., *Plasma-assisted atomic layer deposition of conductive hafnium nitride using tetrakis(ethylmethylamino)hafnium for CMOS gate electrode applications.* Journal of the Electrochemical Society, 2008. **155**(3): p. H196-H201.

23. Kim, E.J. and D.H. Kim, *Highly conductive HfN x films prepared by plasma-assisted atomic layer deposition.* Electrochemical and Solid-State Letters, 2006. **9**(8): p. C123-C125.

24. Elam, J.W., et al., *Atomic layer deposition of aluminum oxide in mesoporous silica gel.* Journal of Physical Chemistry C, 2010. **114**(41): p. 17286-17292.

25. Haukka, S., et al., *Dispersion and distribution of titanium species bound to silica from TiCl4.* Langmuir, 1993. **9**(12): p. 3497-3506.

26. Lakomaa, E.L., A. Root, and T. Suntola, *Surface reactions in Al2O3 growth from trimethylaluminium and water by atomic layer epitaxy.* Applied Surface Science, 1996. **107**: p. 107-115.

27. Keranen, J., et al., *Surface-controlled gas-phase deposition and characterization of highly dispersed vanadia on silica.* Journal of Physical Chemistry B, 2003. **107**(39): p. 10773-10784.

28. Sode, M., T. Schwarz-Selinger, and W. Jacob, *Ion chemistry in H2-Ar low temperature plasmas.* Journal of Applied Physics, 2013. **114**(6).

29. Knoops, H.C.M., et al., *Atomic Layer Deposition of Silicon Nitride from Bis(tert-butylamino)silane and N<inf>2</inf> Plasma.* ACS Applied Materials and Interfaces, 2015. **7**(35): p. 19857-19862.

30. Knoops, H.C.M., K. De Peuter, and W.M.M. Kessels, *Redeposition in plasma-assisted atomic layer deposition: Silicon nitride film quality ruled by the gas residence time.* Applied Physics Letters, 2015. **107**(1).

31. Profijt, H.B., M.C.M. Van De Sanden, and W.M.M. Kessels, *Substrate-biasing during plasma-assisted atomic layer deposition to tailor metal-oxide thin film growth.* Journal of Vacuum Science and Technology A: Vacuum, Surfaces and Films, 2013. **31**(1).

32. Gahan, D., et al., *Ion energy distribution measurements in rf and pulsed dc plasma discharges.* Plasma Sources Science and Technology, 2012. **21**(2).

33. Gahan, D., B. Dolinaj, and M.B. Hopkins, *Retarding field analyzer for ion energy distribution measurements at a radio-frequency biased electrode.* Review of Scientific Instruments, 2008. **79**(3).

34. Faraz, T., et al., *Energetic ions during plasma-enhanced atomic layer deposition and their role in tailoring material properties.* Plasma Sources Science and Technology, 2019. **28**(2): p. 024002.

35. Timofeeva, I.I. and L.K. Shvedova, *Microhardness and thermal expansion of transition metal nitrides within the 80-300K temperature range.* Izvestiya Akademii Nauk SSSR, Neorganicheskie Materialy, 1972. **8**(6): p. 1169-1170.

36. Wang, W., T. Nabatame, and Y. Shimogaki, *Preparation of conductive HfN by post rapid thermal annealing-assisted MOCVD and its application to metal gate electrode.* Microelectronic Engineering, 2008. **85**(2): p. 320-326.

37. Rennick, C.J., et al., *Measurement and modeling of a diamond deposition reactor: Hydrogen atom and electron number densities in an Ar/H2 arc jet discharge.* Journal of Applied Physics, 2005. **97**(11): p. 113306.

38. Meulenbroeks, R.F.G., et al., *Argon-hydrogen plasma jet investigated by active and passive spectroscopic means.* Physical Review E, 1994. **49**(5): p. 4397-4406.

39. Jiménez-Redondo, M., et al., *Ion kinetics in Ar/H2 cold plasmas: the relevance of ArH+.* RSC advances, 2014. **4**(107): p. 62030-62041.

40. Manenschijn, A., et al., *Measurement of ion impact energy and ion flux at the rf electrode of a parallel plate reactive ion etcher.* Journal of Applied Physics, 1991. **69**(3): p. 1253-1262.

41. Adibi, F., et al., *Effects of high-flux low-energy (20–100 eV) ion irradiation during deposition on the microstructure and preferred orientation of Ti0.5Al0.5N alloys grown by ultra-high-vacuum reactive magnetron sputtering.* Journal of Applied Physics, 1993. **73**(12): p. 8580-8589.

42. Knoops, H.C.M., et al., *Optical modeling of plasma-deposited ZnO films: Electron scattering at different length scales.* Journal of Vacuum Science & Technology A, 2015. **33**(2): p. 021509.

43. Insepov, Z., I. Yamada, and M. Sosnowski, *Sputterring and smoothing of metal surface with energetic gas cluster beams.* Materials Chemistry and Physics, 1998. **54**(1): p. 234-237.

44. Wang, L.P., et al., *Influence of temperature and ion kinetic energy on surface morphology of CeO2 films prepared by dual plasma deposition.* Materials Science and Engineering: A, 2002. **336**(1): p. 75-80.

45. Gottlieb, S.O. and H. Satoshi, *Foundations of low-temperature plasma enhanced materials synthesis and etching.* Plasma Sources Science and Technology, 2018. **27**(2): p. 023001.

46. Nastasi, M., J. Mayer, and J.K. Hirvonen, *Ion stopping*, in *Ion-Solid Interactions: Fundamentals and Applications*. 1996, Cambridge University Press: Cambridge. p. 88-114.

47. Insepov, Z. and I. Yamada, *Molecular dynamics simulation of cluster ion bombardment of solid surfaces.* Nuclear Instruments and Methods in Physics Research Section B: Beam Interactions with Materials and Atoms, 1995. **99**(1): p. 248-252.

48. Gago, R., I. Jiménez, and J. Albella, *Thin Film Growth by Ion-Beam-Assisted Deposition Techniques*. 2006. p. 345-382.

49. Anders, A., *A structure zone diagram including plasma-based deposition and ion etching.* Thin Solid Films, 2010. **518**(15): p. 4087-4090.

50. Auciello, O. and R. Kelly, *Ion bombardment modification of surfaces: fundamentals and applications*. 1984: Elsevier Science Publishers.

51. Greene, J.E. and S.A. Barnett, *ION-SURFACE INTERACTIONS DURING VAPOR PHASE CRYSTAL GROWTH BY SPUTTERING, MBE, AND PLASMA-ENHANCED CVD: APPLICATIONS TOSEMICONDUCTORS.* PROC OF THE ANNU CONF ON THE PHYS AND CHEM OF SEMICOND INTERFACES, 9TH, 1982. **V 21**(N 2): p. 285-302.

52. Hultman, L., et al., *Low-energy ion irradiation during film growth for reducing defect densities in epitaxial TiN(100) films deposited by reactive-magnetron sputtering.* Journal of Applied Physics, 1987. **61**(2): p. 552-555.

53. Petrov, I., et al., *Microstructure modification of TiN by ion bombardment during reactive sputter deposition.* Thin Solid Films, 1989. **169**(2): p. 299-314.

54. Faraz, T., et al., *Tuning Material Properties of Oxides and Nitrides by Substrate Biasing during Plasma-Enhanced Atomic Layer Deposition on Planar and 3D Substrate Topographies.* ACS Applied Materials & Interfaces, 2018. **10**(15): p. 13158-13180.

Appendix 6

A. Substrate potential waveform and RFEA measurements

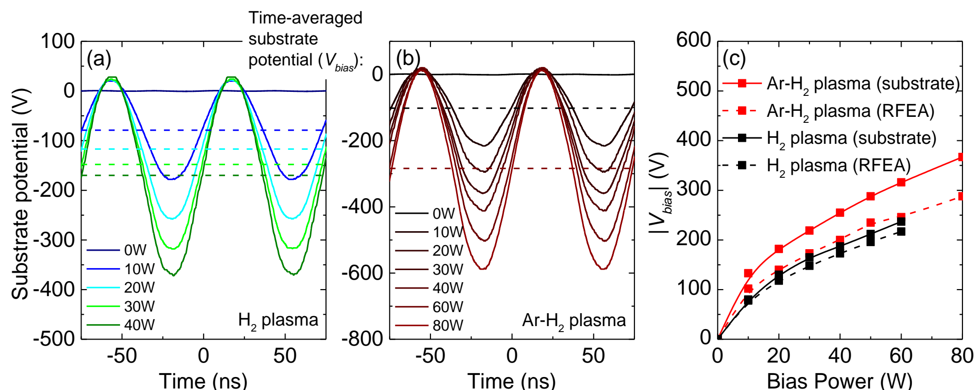

Figure A6.1. Substrate potential waveforms obtained via high voltage probe measurements and an oscilloscope for (a) H_2 plasma at 30 mTorr and (b) Ar-H_2 plasma at 6 mTorr. They reveal the development of the time-averaged negative substrate potential (V_{bias}) with respect to ground (shown by horizontal dashed lines) (c) absolute values of the time-averaged substrate potential ($|V_{bias}|$) as a function of the applied rf bias power for Ar-H_2 plasma at 6 mTorr and H_2 plasma at 30 mTorr measured during the HfN_x film deposition (with a 100 mm SiO_2/Si substrate on the substrate stage) and RFEA measurements (with the RFEA [1], made from aluminium, on the substrate stage).

A small difference in $|V_{bias}|$, as measured by a high voltage probe and oscilloscope, is observed between RFEA measurements and performing the HfN_x ALD, for any given rf bias power value. This may be a consequence of a difference in the impedance of the substrate stage when using a substrate and when using RFEA.

B. HfN_x ALD process characterization

The effect of the application of external rf substrate bias on the GPC in terms of thickness (Å) and areal density of Hf atoms deposited per cycle (Hf atoms nm^{-2})[a] is presented in Figure A6.2. We have previously shown that the application of external rf substrate bias does not affect the saturation of the ALD process for H_2 plasma process [2]. The GPC(Å) for the growth of HfN_x films using Ar-H_2 plasma was found to be constant independent of an increase in the $|V_{bias}|$ from 0V to 255V, beyond which a slight increase in GPC(Å) was observed. This is in contrast to

the previously reported H_2 plasma process, where a consistent increase in the GPC(Å) with the increase in $|V_{bias}|$ was observed [2].

By means of RBS,[b] we found that the areal density of Hf atoms per cycle remained constant at roughly ~1.30±0.04 atoms nm^{-2} $cycle^{-1}$ for the Ar-H_2 plasma in the whole range of $|V_{bias}|$. On the contrary, the areal density of Hf atoms per cycle increased with increasing $|V_{bias}|$ values for H_2 plasma process, signifying enhanced precursor adsorption that led to an increase in the aforementioned GPC(Å) [2].

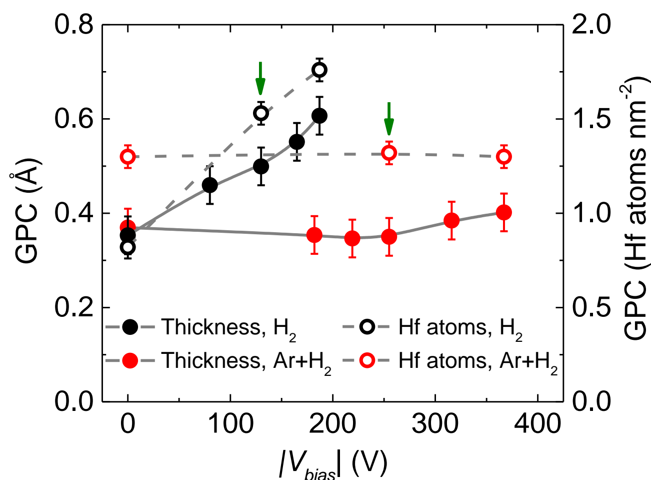

Figure A6.2. Growth per cycle (GPC) in terms of thickness and number of Hf atoms deposited per nm^2 for the Ar-H_2 plasma case and the previously reported H_2 plasma case as a function of $|V_{bias}|$. Lines serve as guides to the eye and (green) arrows indicate the *optimum condition* in terms of resistivity for both ALD processes.

A similar GPC(Å) was obtained at $|V_{bias}|$ = 0V using Ar-H_2 plasma as for the earlier reported H_2 plasma. However, we found a much higher areal density of Hf atoms deposited per cycle at $|V_{bias}|$ = 0V using Ar-H_2 plasma, as compared to the H_2 plasma. Based on the results, we can conclude that a similar GPC(Å) and yet higher GPC (Hf atoms nm^{-2}) at $|V_{bias}|$ = 0V can be explained in terms of higher mass density of HfN_x films grown using Ar-H_2 plasma (10.4±0.3 g/cm^3) as compared to the H_2 plasma (8.2±0.2 g/cm^3) (Table A6.3).[c] On the other hand, the values for the GPC (Hf atoms nm^{-2}) are quite comparable at the *optimum condition*[d] of both the processes, while the GPC(Å) is lower for the Ar-H_2 plasma as compared to the H_2 plasma. This is again a consequence of the higher mass

density of HfN_x films grown using Ar-H_2 plasma (10.0±0.3 g/cm^3) in comparison to the H_2 plasma (8.6±0.2 g/cm^3). Furthermore, the slight increase in the GPC(Å) at $|V_{bias}|$ = 367V for Ar-H_2 plasma is thought to stem from the decrease in HfN_x film mass density to 8.4±0.2 g/cm^3, since the GPC(Hf atoms nm^{-2}) is not affected by increase in $|V_{bias}|$.

C. Dielectric function from spectroscopic ellipsometry (SE) and notes on the electronic scattering

The dielectric function of conductive δ-HfN_x can be modelled using one Drude and two Lorentz oscillators:

$$\varepsilon(E) = \varepsilon_1(E) + i\varepsilon_2(E) = \varepsilon_\infty - \overbrace{\frac{E_p^2}{E^2 - i\Gamma_D E}}^{Drude} + \sum_{j=1}^{2} \overbrace{\frac{S_j E_{0j}^2}{E_{0j}^2 - E_j^2 + iE_j\Gamma_j}}^{Lorentz} \quad (1)$$

where, ε_∞ represents transitions at higher energy which are not accounted in Lorentz oscillators, E_p is plasma energy and Γ_D is the damping factor for Drude oscillator. The Lorentz oscillators are centered at E_o which corresponds to the resonance frequency, while S indicates the strength of the oscillators and Γ is the damping factor for the Lorentz oscillators.

[a,b,c]The areal density of Hf atoms deposited per cycle (Hf atoms nm^{-2}) and the mass density of HfN_x films is computed by Rutherford backscattering measurements (RBS) reported later in the main text of manuscript.
[d]The *optimum condition* refers to $|V_{bias}|$ value of 255V for Ar-H_2 plasma and 130V for H_2 plasma process, where a minimum in electrical and optical resistivity is obtained for the respective process (see manuscript).

Table A6.1. SE fitting parameter values for one Drude and two Lorentz oscillators for δ-HfN_x film grown using Ar-H_2 plasma at $|V_{bias}|$ = 255V and H_2 plasma at $|V_{bias}|$ = 130V.

Plasma gas composition		**Ar-H_2**	**H_2**
$\|V_{bias}\|$ (V)		**255**	**130**
ε_∞		3.67	4.15
E_p (eV)		2.33	1.70
Γ_D (eV)		0.44	0.53
Lorentz oscillator 1	S	19.4	34.0
	Γ (eV)	1.2	0.9
	E_o (eV)	1.1	0.9
Lorentz oscillator 2	S	5.4	4.9
	Γ (eV)	4.3	5.0
	E_o (eV)	5.7	6.2

Langereis *et al.* and Knoops *et al.* described that insights into electronic scattering can be gained by probing opto-electronic properties using SE [3, 4]. The Drude parameterization of the imaginary part of the dielectric function ε_2 was used to deduce the optical resistivity (ρ_{op}) of the HfN_x films. An ρ_{op} of $(2.4\pm0.2)\cdot10^{-4}$ Ωcm was obtained for the HfN_x film grown at $|V_{bias}|$ = 255V using Ar-H_2 plasma. Similarly, an ρ_{op} of $(9.0\pm0.2)\cdot10^{-4}$ Ωcm was deduced for the HfN_x film grown at $|V_{bias}|$ = 130V using H_2 plasma as previously reported [2]. In addition, the interaction distance (d_{int}) of the incident light with the HfN_x films was calculated using the electron effective mass of 0.88 in HfN [5], the Fermi velocity $\left(\nu_e = \hbar(3\pi^2 N)^{1/3}/m^*\right)$ and a photon energy of 0.75 eV in the same manner as described by Knoops *et al* [4]. An d_{int} of 4.6 nm and 3.2 nm were deduced for HfN_x films grown at the *optimum conditions* of Ar-H_2 plasma and H_2 plasma, respectively. In-view of the small interaction distance as compared to the lateral grain size of ~25 nm of the HfN_x films of relevant thickness (as elucidated by

microstructural characterization in Figure 6.3), the optical resistivity delivers information only on the in-grain electronic scattering at extremely small distances. Therefore, the difference between electrical and optical resistivity can be used to evaluate the uniformity of in-grain crystalline quality and the extent of electronic scattering.

D. Chemical composition analysis using X-ray photoelectron spectroscopy

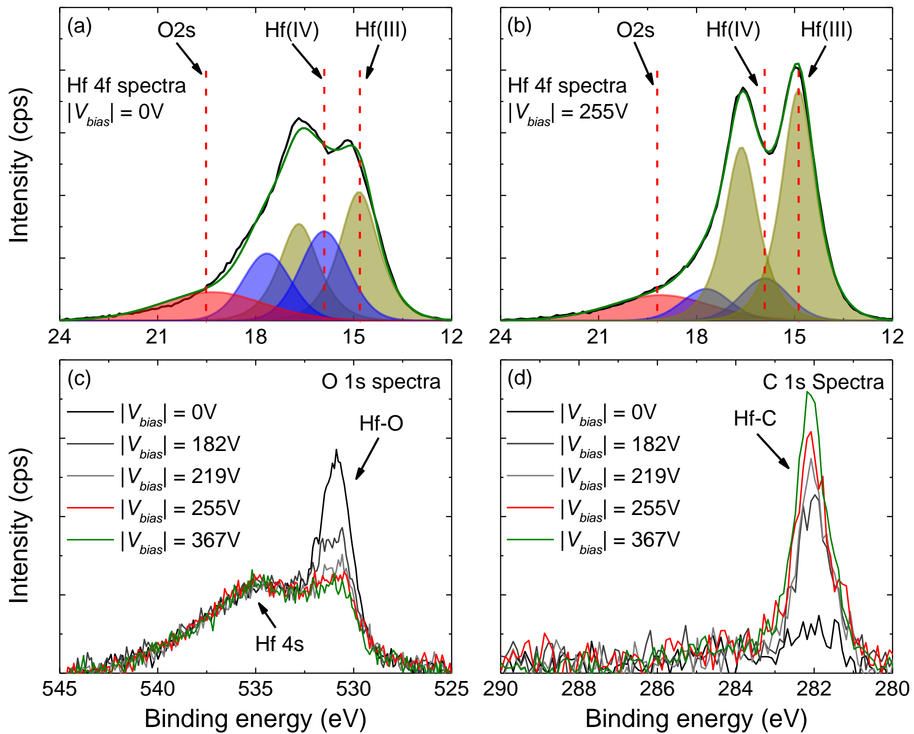

Figure A6.3. Deconvoluted Hf 4f XPS spectra for HfNx films prepared at (a) $|V_{bias}|$ = 0V and (b) $|V_{bias}|$ = 255V with Hf(III) and Hf(IV) oxidation states (c) O 1s XPS spectra as a function of $|V_{bias}|$ depicting a decrease in Hf-O peak intensity with an increase in $|V_{bias}|$ (d) C 1s XPS spectra as a function of $|V_{bias}|$ showing an increase in Hf-C peak intensity with an increase in $|V_{bias}|$.

Table A6.2. Corresponding peak assignment, binding energies and full width half maximum for the Hf, N, O and C spectral lines used to deconvolute the peaks as measured by XPS.

Spectral line	Peak designation	Binding energy (eV)	FWHM (eV)	Reference
Hf $4f_{7/2}$	Hf(IV)	16.0	1.6	[6, 7]
Hf $4f_{7/2}$	Hf(III)	14.9	1.6	[8]
N 1s	Hf(III)N	397.5	1.5	[9]
N 1s	Hf(IV)N	396.5	1.6	[10]
O 1s	HfO_x	530.8	1.9	[11]
C 1s	HfC_x	282	1.2	[12]

E. Material properties of HfN_x films as a function of $|V_{bias}|$ for Ar-H_2 plasma and H_2 plasma processes

Table A6.3. The properties of the HfN_x films prepared using Ar-H_2 plasma compared with previously reported H_2 plasma at various values of $|V_{bias}|$, as determined by four-point probe (FPP), spectroscopic ellipsometry (SE), X-ray photoelectron spectroscopy (XPS), Rutherford backscattering (RBS) and elastic recoil detection (ERD). The electrical resistivity was obtained by a combination of FPP and SE whereas the optical resistivity, GPC and thickness were determined using SE. XPS was used to obtain the Hf(III) oxidation state fraction whereas the chemical composition and the GPC in terms of the number of deposited Hf (in terms of atoms nm^{-2} cycle^{-1}) were determined *via* RBS. The H content was measured using ERD. The mass density was calculated by dividing the total areal atomic density (obtained via RBS and ERD) with the film thickness. The errors for electrical resistivities and optical resistivities are less than 3% and 2% of their absolute values, respectively. The errors for the GPC, the Hf(III) fraction and the mass densities are mentioned in the first line unless otherwise mentioned.

Plasma	FPP	SE			XPS	RBS					ERD
$\lvert V_{bias}\rvert$ (V)	Electrical resistivity (Ωcm)	Optical resistivity (Ωcm)	GPC (Å)	Thickness (nm)	Hf(III) / Hf(III)+Hf(IV)	GPC (Hf at. nm^{-2} cycle^{-1})	N/Hf	C (at.%)	O (at.%)	Mass density (g cm^{-3})	H (at.%)
Ar-H_2 0V	$2.0\cdot10^{-1}$	$5.2\cdot10^{-3}$	0.37±0.04	37	0.70±0.02	1.30±0.04	0.86±0.09	<2.0	19.9±0.9	10.4±0.3	4.7±0.3
Ar-H_2 255V	$4.1\cdot10^{-4}$	$2.4\cdot10^{-4}$	0.35	35	0.86	1.32±0.06	0.84±0.08	8.4±0.4	<2.0	10.0	11.8±0.6
Ar-H_2 367V	$6.5\cdot10^{-4}$	$3.5\cdot10^{-4}$	0.40	40	0.78	1.30±0.06	0.68±0.08	14.6±0.6	<2.0	8.4	15.0±0.7
H_2	$9.0\cdot10^{-1}$	$5.9\cdot10^{-3}$	0.35	71	0.65	0.82±0.04	0.86±0.05	<2.0	20.1±0.7	8.2±0.2	7.0±0.3

0V											
H_2 130V	$3.3 \cdot 10^{-3}$	$9.0 \cdot 10^{-4}$	0.50	81	0.82	1.53±0.06	1.00±0.07	11.0±1.2	<2.0	8.6	12.6±0.6
H_2 187V	$1.0 \cdot 10^{-2}$	$1.7 \cdot 10^{-3}$	0.60	83	0.73	1.76±0.06	0.98±0.06	10.3±1.1	<2.0	8.0	18.5±0.9

F. Crystallinity analysis using X-ray diffraction

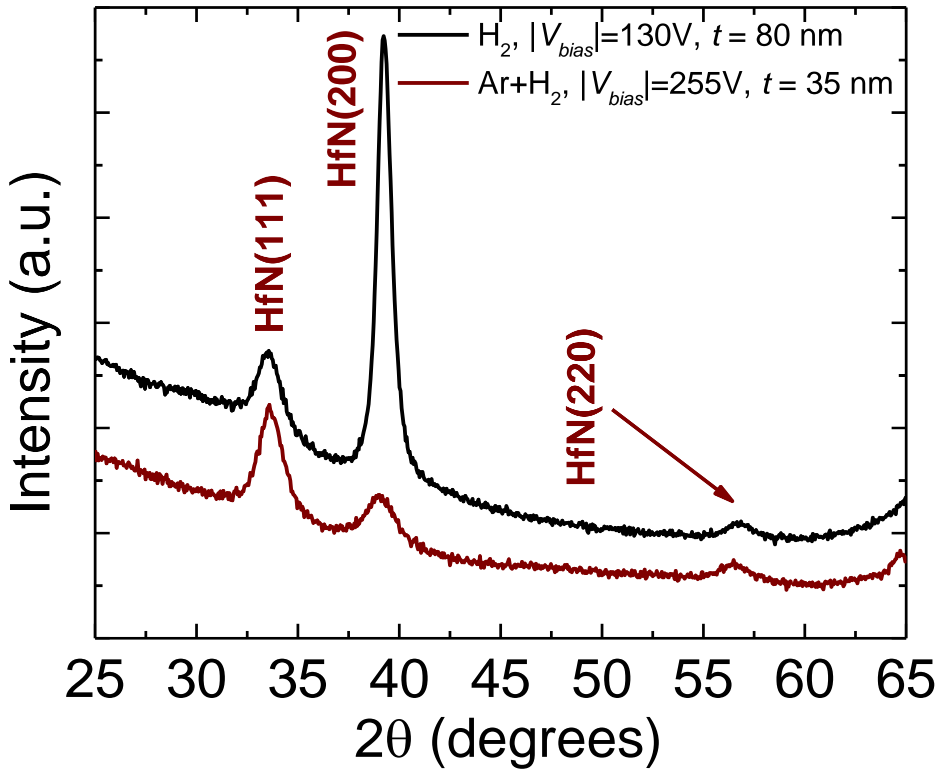

Figure A6.4. X-ray diffractograms (XRD) for ~35 nm thick film prepared at $|V_{bias}|$ = 255V using Ar-H_2 plasma and ~80 nm thick film prepared at $|V_{bias}|$ = 130V using H_2 plasma.

G. HfN_x film microstructural analysis using HAADF-STEM and XRD

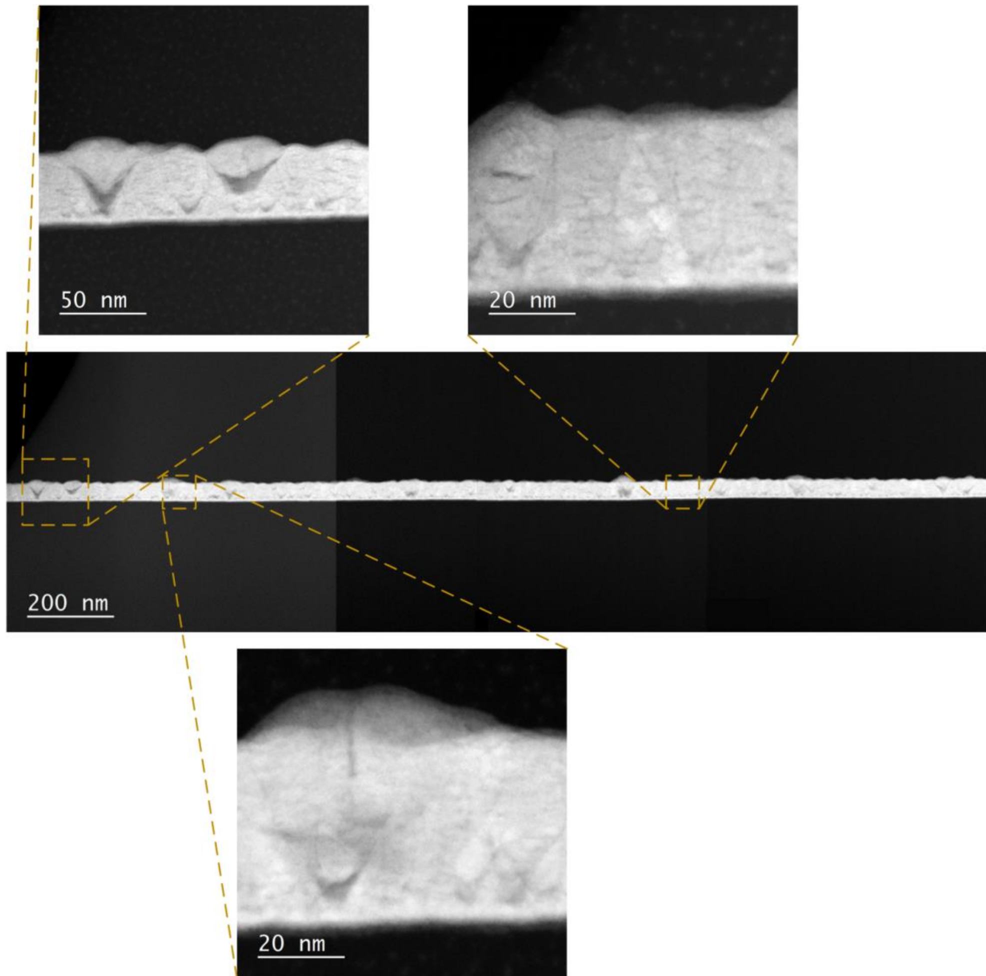

Figure A6.5. Low magnification cross-sectional high-angle annular dark-field scanning transmission electron microscopy (HAADF-STEM) image of a ~35 nm thick HfN_x film grown at $|V_{bias}|$ = 255V using Ar-H_2 plasma, displaying V-shaped voids near the onset of HfN_x film growth along the entire TEM sample. The higher magnification images acquired at the positions indicated in the overview image display the voids in more detail. The TEM sample is thinner at the left than at the right, allowing for a clearer view on the shape of the voids in the upper-left image.

References

1. Gahan, D., et al., *Ion energy distribution measurements in rf and pulsed dc plasma discharges.* Plasma Sources Science and Technology, 2012. **21**(2).

2. Karwal, S., et al., *Low resistivity HfNx grown by plasma-assisted ALD with external rf substrate biasing.* Journal of Materials Chemistry C, 2018. **6**(15): p. 3917-3926.

3. Langereis, E., et al., *In situ spectroscopic ellipsometry study on the growth of ultrathin TiN films by plasma-assisted atomic layer deposition.* Journal of Applied Physics, 2006. **100**(2): p. 023534.

4. Knoops, H.C.M., et al., *Optical modeling of plasma-deposited ZnO films: Electron scattering at different length scales.* Journal of Vacuum Science & Technology A, 2015. **33**(2): p. 021509.

5. Strømme, M., R. Karmhag, and C.G. Ribbing, *Optical constants of sputtered hafnium nitride films. Intra- and interband contributions.* Optical Materials, 1995. **4**(5): p. 629-639.

6. Kang, C.S., et al., *Bonding states and electrical properties of ultrathin HfOxN y gate dielectrics.* Applied Physics Letters, 2002. **81**(14): p. 2593-2595.

7. Arranz, A., *Synthesis of hafnium nitride films by 0.5-5 keV nitrogen implantation of metallic Hf: An X-ray photoelectron spectroscopy and factor analysis study.* Surface Science, 2004. **563**(1-3): p. 1-12.

8. Wang, W., T. Nabatame, and Y. Shimogaki, *Preparation of conductive HfN by post rapid thermal annealing-assisted MOCVD and its application to metal gate electrode.* Microelectronic Engineering, 2008. **85**(2): p. 320-326.

9. Shinkai, S. and K. Sasaki, *Influence of sputtering parameters on the formation process of high-quality and low-resistivity HfN thin film.* Japanese Journal of Applied Physics, Part 1: Regular Papers and Short Notes and Review Papers, 1999. **38**(4 A): p. 2097-2102.

10. Wang, W., T. Nabatame, and Y. Shimogaki, *Interface structure of HfNx/SiO2 stack grown by MOCVD using TDEAHf precursor.* Surface Science, 2005. **588**(1-3): p. 108-116.

11. Kirsch, P.D., et al., *Electrical and spectroscopic comparison of HfO 2/Si interfaces on nitrided and un-nitrided Si(100).* Journal of Applied Physics, 2002. **91**(7): p. 4353-4363.

12. Jang, J.H., et al., *Role of Carbon on Resistivity and Structure of Hf Cx Ny Films Grown by Low Temperature MOCVD.* Journal of the Electrochemical Society, 2009. **156**(1): p. H76-H79.

Chapter 7

Conclusions and Outlook

Conductive transition metal nitride (TMN) films are essential in the nanoelectronic industry, and their use span over various applications. For example, they have played a pivotal role in the manufacturing line of the state-of-the-art MOSFET devices. They are employed as gate metals in the FEOL and as diffusion barriers in the BEOL fabrication steps. Advanced FET devices and novel device architectures necessitate highly conformal and uniform growth of low-resistivity TMN films ($\rho < 4{\cdot}10^{-4}$ Ω·cm) on 3D nanostructures with a high aspect ratio of more than 5:1. These challenges motivate the synthesis of TMN films by the atomic layer deposition (ALD) technique. The latter enables the growth of ultra-thin films with precise control over uniformity, thickness and step coverage on high surface area substrates.

The synthesis of low-resistivity TMN films ($\rho < 4{\cdot}10^{-4}$ Ω·cm) requires the presence of a high +3 oxidation state fraction (> 0.8) of the metal atoms in the grown films, together with high film crystallinity and low nanoporosity. The growth of low-resistivity TMN films by ALD is confronted with various challenges. These include 1) an efficient reduction of the metal atoms present in a higher oxidation state in the metal precursor in order to yield a high fraction of +3 oxidation state in the grown films by selecting an appropriate reducing co-reactant and 2) achieving high crystallinity and dense microstructure at typically low ALD growth temperatures of $T < 500$.

This dissertation uses plasma-assisted ALD of conductive HfN_x as a case study to address the aforementioned challenges. Specifically, the effects of various process and plasma parameters, such as gas composition, ion energy and ion mass, on the chemical and microstructural properties of HfN_x films are investigated. Furthermore, a correlation between the chemical and microstructural properties of HfN_x films with its electrical properties is established. In addition, fundamental understanding is developed, by employing both experimental as well as theoretical methods, on the surface reactions that enable the growth of low-resistivity HfN_x films when the HfN_x surface is exposed to energetic ions. The key results obtained in this thesis may be applicable to a wide range of ALD processes and also promote the growth of other TMN films

with low-resistivity. The following general conclusions can be drawn from this dissertation:

- **Chapter 2** reviews the literature works on the reduction of different transition metal atoms by various reducing co-reactants. In particular, it has been observed that the reduction of some metal atoms from a higher oxidation state, for eg. Ti(IV) or Nb(V), to +3 oxidation state in the deposited films is enabled even by the adoption of NH_3 gas as the co-reactant, leading to the conductive phases of the respective TMN films. In contrast, the reducing potential of NH_3 gas is insufficient to enable the reduction of Ta(V), Zr(IV) and Hf(IV) oxidation states to +3 oxidation state and insulating phases of TMN films are obtained. Co-reactants with a higher reducing potential, such as that of a H_2 plasma, are required to enable the synthesis of the conductive phases of TMN films. In this regard, **Chapter 3** investigates the adoption of plasma (N_2 plasma vs. H_2 plasma) as co-reactant in combination with the Hf precursor $CpHf(NMe_2)_3$. As anticipated, the use of N_2 plasma was found to be insufficient to reduce Hf(IV) oxidation state and therefore insulating Hf_3N_4 phase was obtained. In contrast, highly reducing H_2 plasma enabled the reduction of Hf(IV) to Hf(III) and thus allowed the synthesis of conductive HfN_x phase. These results demonstrate that the selection of an appropriate reducing co-reactant is essential and depends on the reduction potential of metal atoms in the precursor. The obtained results are consistent with the findings of Langereis *et al.* for the growth of conductive TaN_x films and Vos *et al.* for the growth of metallic Co films by employing H_2 plasma, instead of N_2-containing plasma [1, 2]. Therefore, it is concluded that the obtained results can also be extended to other technologically relevant metal and metal nitride films prepared by ALD, where the reduction of metal atom is essential.
- Even though H_2 plasma can lead to the synthesis of conductive HfN_x phase, a high film resistivity of 0.9 Ωcm and a low Hf(III) fraction of 0.65 was obtained. A high concentration of oxygen (~20 at.%) in the form of Hf-O bonds was found to be present in the films, which increased the oxidation state of Hf to +4. This resulted in a low Hf(III) oxidation state fraction and high film resistivity. It is concluded that the oxygen incorporation in the films occurs during the film growth itself suggesting that Hf(III) oxidation state is highly reactive towards H_2O/O_2 (present as residual gases in reactor background). In contrast, the oxygen incorporation was found to be minimal in the Hf_3N_4 films grown using N_2 plasma, signifying that the presence of Hf(IV) makes the surface unreactive towards H_2O/O_2 residual gases and thus averts the oxygen incorporation. Figure 7.1 provides an overview of the key results in terms of the fraction of Hf(III) oxidation state, oxygen content, film crystallinity and surface morphology as a function of the plasma gas composition (N_2 plasma

vs. H_2 plasma). From the obtained results, it is concluded that oxygen incorporation has profound adverse effects on the film conductivity. In particular, the oxygen incorporation in the films occurs when the reactivity of the growth surface (for e.g., presence of Hf(III) or Ti(III) on the surface) is high towards H_2O/O_2. In such a case, significant oxygen incorporation can take place even at a very low vacuum base pressure of 10^{-6} Torr. Furthermore, the oxygen incorporation is expected to be even more pronounced for longer ALD cycle times and/or for ALD processes with low growth per cycle (GPC). Therefore, it is essential to identify the source of oxygen incorporation in the prepared films in order to device novel approaches to avert it and produce high quality metal and metal nitride films that can be employed in respective applications.

- One of the important plasma parameter that can be tuned during the film growth in plasma-assisted ALD is the energy of impinging ions, enabled by the application of external rf substrate biasing technique, as addressed in **Chapter 4**. An increase in the substrate potential (i.e. ion energy) resulted in quantitative suppression of oxygen in the film. This significantly increased the Hf(III) oxidation state fraction in the films from 0.65 to 0.82, accompanied by a decrease in film resistivity by two orders of magnitude down to $3.3 \cdot 10^{-3}$ Ωcm. **Chapter 6** investigates Ar-H_2 plasma as co-reactant, instead of H_2 plasma. The application of Ar-H_2 plasma in combination of rf substrate biasing led to another order of decrease in the film resistivity down to $4.1 \cdot 10^{-4}$ Ωcm. This value of film resistivity is comparable to the highly crystalline and pure HfN_x films grown by physical vapour deposition (PVD) technique. Ion flux energy distribution functions (IFEDFs) and literature studies reveal that the ion energy and ion mass in the case of Ar-H_2 plasma are significantly higher than in H_2 plasma. Furthermore, the HfN_x films exhibit a high Hf(III) fraction of 0.86, similar to the H_2 plasma process. In contrast, microstructural analysis reveals that the film undergoes a major improvement. Specifically, the in-grain nano-porosity is significantly suppressed. The latter effect is attributed to an efficient transfer of energy and momentum to the HfN_x film surface in the presence of ions with a higher energy and larger mass. The impinging ions with a higher momentum may facilitate near-surface diffusion of atoms and therefore may lead to may lead to annihilation of defects and reduction in nano-porosity in the HfN_x films. Figure 7.2 presents an overview of the impact of co-reactant plasma gas and substrate potential (i.e. energetic ions) on the chemical, microstructural and electrical properties of HfN_x films. The obtained results signify how energy and mass of impinging ions can impact both the chemical and microstructural properties of grown films. These material properties have direct influence on the electronic properties of the grown

HfN_x films and, in general, other TMN films. The insights obtained and the key concepts established in these chapters can enable further improvements in the material properties of also other related technologically-relevant metal nitride and metallic films and enable their efficient use in various applications. For instance, Faraz *et al.* and Grady *et al.* have respectively reported a similar decrease in the oxygen content and the resistivity of TiN_x and MoC_x films upon the application of external rf substrate biasing [3, 4].

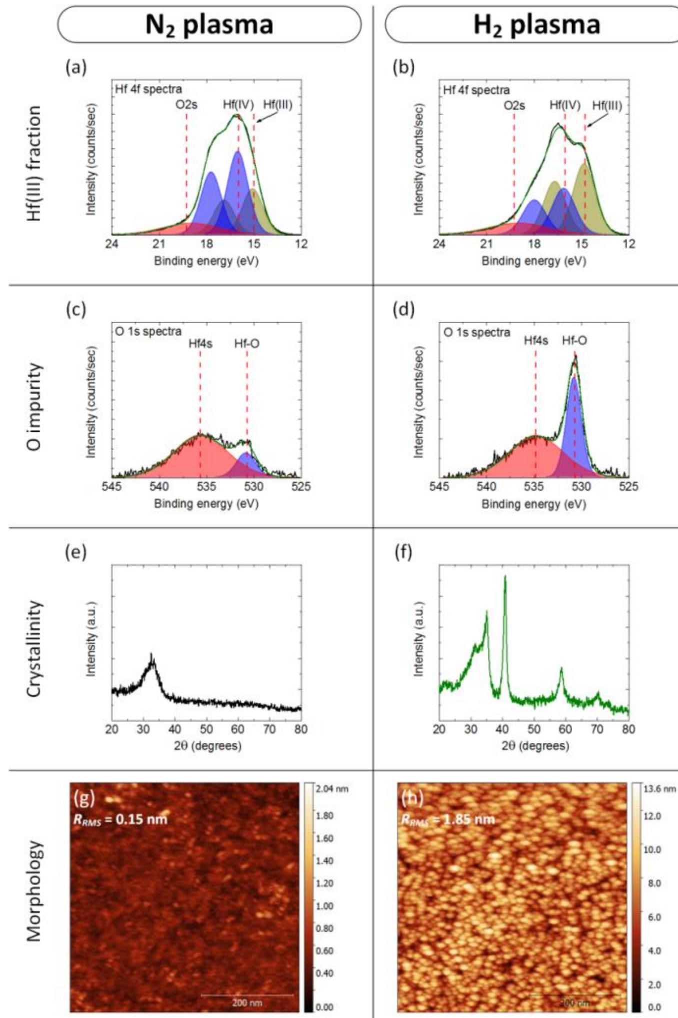

Figure 7.1. An overview of the key HfN_x film properties achieved by using either N_2 plasma or H_2 plasma as the co-reactant. (a and b) Hf 4f XPS spectra depicting a higher Hf(III) oxidation state fraction for the H_2 plasma than for N_2 plasma; (c and d) O 1s XPS spectra showing a higher

concentration of Hf-O bonds for the H_2 plasma; (e and f) grazing incidence XRD patterns illustrating the synthesis of conductive δ-HfN phase with H_2 plasma and (g and h) 500x500 nm AFM surface scans showing a higher surface roughness for the HfN_x films grown using H_2 plasma, the signature of the growth of crystalline films.

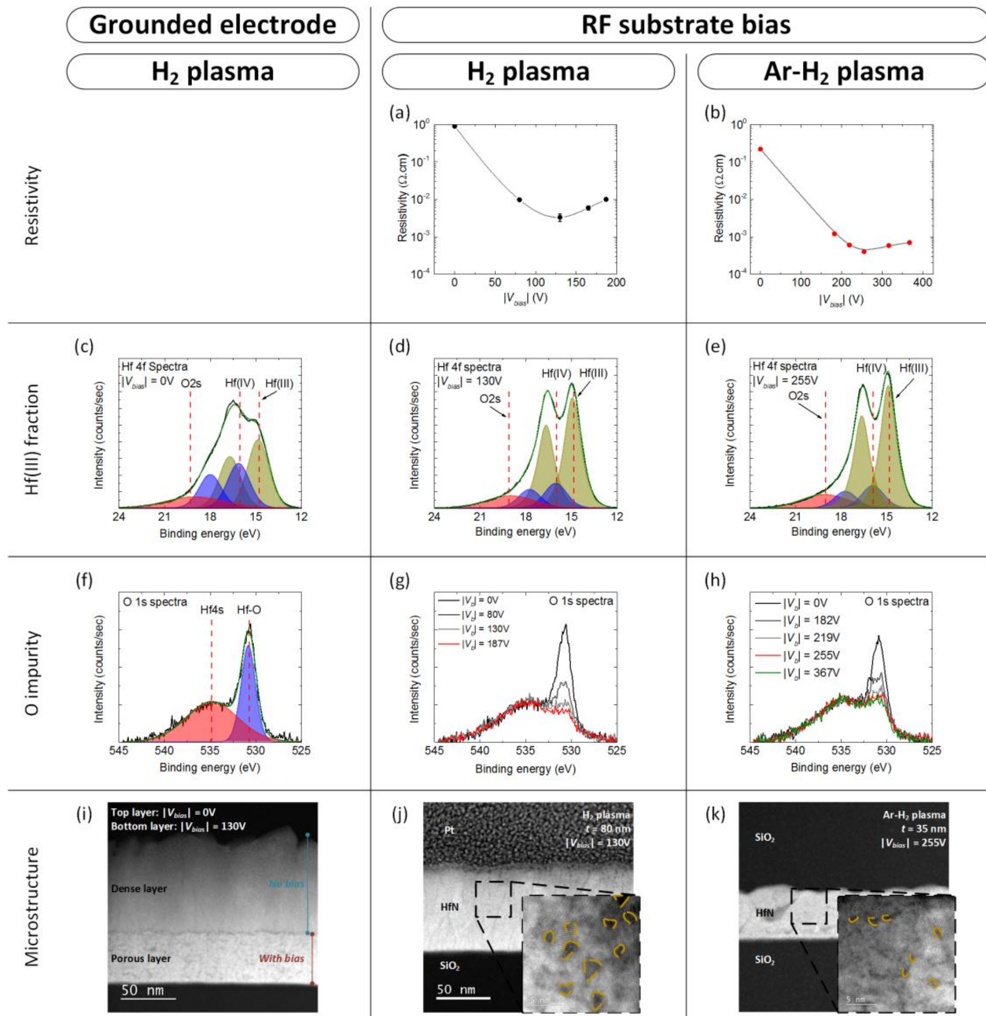

Figure 7.2. An overview of the effects on the key HfN_x film properties when an external rf substrate bias is applied during the H_2 and Ar-H_2 plasma half cycle. (a and b) Electrical resistivity values of the prepared HfN_x films as a function of the substrate potential ($|V_{bias}|$) for both H_2 plasma and Ar-H_2 plasma; (c, d and e) Hf 4f XPS spectra depicting an increase in Hf(III) oxidation state fraction upon application of an external rf substrate bias; (f, g and h) O 1s XPS spectra showing a gradual decrease in concentration of Hf-O bonds due to the external rf substrate bias ; (i, j and k) high-angle annular dark-field scanning transmission electron microscopy (HAADF-STEM) images for HfN_x films depicting a suppression of nano-porosity by employing Ar-H_2 plasma, instead of H_2 plasma, as the co-reactant.

- **Chapter 5** employs first principles density functional theory calculations (DFT) to unravel the underlying surface chemistry that takes place during the impingement of energetic ions. In other words, it is possible to explain the major modification in the chemical composition that the film undergoes during impingement of energetic ions by studying the reactions taking place on the surface of growing HfN_x film. The DFT calculations suggested that the chemisorption of H_2O (residual gas present in the reactor background) on a pristine HfN surface is highly favoured and leads to the formation of surface Hf-OH bonds. This results in the partial oxidation of Hf(III) to $Hf(III)^{\delta+}$. Furthermore, the bombardment of energetic cations (H^+, H_2^+ and H_3^+) triggers the dissociation of surface Hf-OH bonds and leads to H_2O formation and desorption. Subsequently, the H· radicals present in the H_2 plasma are hypothesized to reduce the Hf(IV) to Hf(III). These results have led to a better insight into the relation between the oxygen incorporation and reactivity of the growth surface and can also be extended to other ALD processes. Such analyses will be useful in devising new approaches for preventing oxygen incorporation with the aid of energetic ions. This can serve as a platform for synthesizing highly pure and functional films with desired material properties, which can be efficiently used in various nanoscale applications.

Based on the insights and results obtained in this work, some recommendations are made for future research:

- In this work, external rf substrate biasing has been employed in the co-reactant plasma step in a so-called AB type ALD process. However, the application of substrate biasing could be very well extended to a multi-step plasma ALD processes, where substrate biasing could be implemented as the C step in a ABC type ALD process. This could be of particular interest for discerning between the chemical effects and physical effects of energetic ions in the case where the B step uses reactive plasma (for e.g., H_2) and the C step consists of plasma of an inert gas (for e.g., Ar), thus imparting another degree of control over the material properties of the grown films. In addition, the external rf substrate bias may be applied for the entire duration of the plasma half cycle in a AB type ALD process or a small part of it. This is the so-called 'duty cycle' of substrate bias application. In this setup, the duration of bias application and the sequence of bias application (i.e., first part, intermediate part or last part of the plasma half cycle) can be varied. Such variations could induce differences in material properties as a function of substrate biasing. Relevantly, Faraz *et al.* reported on different trends of various material

properties, such as refractive index, density and stress, for TiO_x films as a function of the bias duty cycle [3].

- With respect to the substrate biasing, it would be interesting to explore the effect of voltage bias waveforms with a higher frequency, as compared to 13.56 MHz that has been employed in this work, on the TMN film properties prepared by plasma-assisted ALD [5]. The latter would enable a decrease in the peak-to-peak width of IFEDF (ΔE_{ion}) and a narrower distribution of ion energies can be obtained. In addition to higher frequency operation, pulse-shaped biasing may also allow to generate IFEDF with a narrower distribution [6]. In principle, a narrower distribution of ion energies could enable an accurate measurement of ion energy and thus allow a higher degree of control on the material properties of films prepared by plasma-assisted ALD.
- As highlighted in **Chapter 6**, the microstructural properties of the HfN_x films can be improved by employing ions with higher energy and larger mass. This effect, in principle, can be further enhanced by the use of heavier inert gases, such as Krypton or Xenon instead of Argon, in combination with H_2 gas as the feed gas for the co-reactant plasma step. The ions with larger mass may more effectively transfer their momentum to the surface of the growing film and thus may lead to further decrease in the film nano-porosity and therefore the film resistivity.
- As highlighted in this dissertation, the growth of TMN films with low-impurity is very challenging. The latter is primarily due to the susceptibility of TMN films towards oxidation from residual gases. In addition to the oxygen, carbon impurities are also usually present in the TMN films due to the incomplete abstraction of ligands by a non-oxygen containing plasma (H_2 and/or N_2 plasma). Ion bombardment that leads to an efficient removal of O from the TMN films may also lead to the enhanced cracking of ligands (attached to the metal atom adsorbed on the surface) during the plasma exposure, which may subsequently get redeposited on the surface of the growing film. One method to circumvent this issue could be the use of 'softer' techniques such as the application of vacuum ultraviolet (VUV) photons or H· radicals to first liberate the ligands, followed by the exposure of energetic ions in order to obtain films with the desired properties in a 3-step ABC type ALD process.
- The conductivity of the TMN films is known to improve with an increase in deposition temperature due to enhanced film crystallinity. Usually, the choice of deposition temperature in ALD is dictated by the decomposition temperature of the metal-organic precursor. As discussed in **Chapter 3**, the use of precursors with cyclopentadienyl, benzene or similar ligands may help to increase the decomposition temperature of the precursor. The latter would

allow an increase in the ALD temperature and further improvement in film conductivity.

- Since the key to obtain conductive TMN films is to achieve +3 oxidation state of metal atoms in the deposited films, it would be extremely useful to synthesize ALD precursors with metal atoms already present in +3 oxidation state. The latter may greatly diminish the efforts devoted towards reducing the metal atoms and would promote for deposition of low-resistivity TMN films even with thermal ALD processes (for e.g., employing NH_3). This would be particularly interesting, in the view of applications in the nanoelectronics, as the conformality of thermal ALD grown films is expected to be high also on the sidewalls of 3D trench structures.

- Since HfN_x forms a seemingly perfect interface with the high-*k* HfO_x, the former can serve as gate metal in advanced MOSFET devices. The results presented in this dissertation demonstrate that the energetic ions can significantly improve the material properties of HfN_x films. As the impinging ions are incident normally on the surface of growing film due to the presence of plasma sheath, one of the major challenges for plasma-assisted ALD is the growth of high-quality and low-resistivity HfN_x films also on the sidewalls of high-aspect ratio 3D nanostructures. **Chapter 4** briefly addresses this issue and also provides a plausible solution, i.e., an increase in the operating pressure of plasma may allow ions to also reach the sidewalls of the 3D trenches. However, an increase in plasma pressure will surely impact the energy and flux of impinging ions and hence the film properties. In-view of the implementation of low-resistivity HfN_x films, and in general, other related nitrides in 3D MOSFET technology, future research could focus on collecting more experimental results on the conformality and film properties of the grown TMN films. Furthermore, the evaluation of angular distribution and energy of impinging ions by employing advanced retarding field energy analyser (RFEA) setups can prove to be very useful.

- Low resistivity TMN films are highly reflective in the IR region ($1 \text{ eV} \leq h\nu \leq 2.5$ eV) and are potential candidates for the back contact of thin-film copper-indium-gallium-selenium (CIGS) solar cells, thus enabling an increase in the optical absorption of low energy photons. In particular, thick and opaque HfN_x films grown by PVD exhibit a reflectivity of c.a. 85% in the IR region. In addition, chemical inertness and thermal stability towards the harsh growth conditions of the CIGS layer makes the TMN films lucrative candidate as the back contacts, in comparison to Ag or Au films. Initial experiments (data is not reported in this thesis) show a consistent increase in the EQE, especially in the low energy photon regime, and a correlated enhancement in the short circuit

current (J_{sc}) with a decrease in the CIGS absorber thickness down to 250 nm by using HfN_x as back electrode, instead of conventional Mo. Furthermore, as elucidated in this work, the growth of low resistivity HfN_x, and in general TMN films, by ALD can be particularly interesting for the deposition of highly reflective films on textured substrates. The use of textured substrates may allow for an even higher enhancement in the optical absorption of low energy photons.

References

1. Langereis, E., et al., *Synthesis and in situ characterization of low-resistivity Ta Nx films by remote plasma atomic layer deposition.* Journal of Applied Physics, 2007. **102**(8).
2. Vos, M.F.J., et al., *Atomic Layer Deposition of Cobalt Using H2-, N2-, and NH3-Based Plasmas: On the Role of the Co-reactant.* The Journal of Physical Chemistry C, 2018. **122**(39): p. 22519-22529.
3. Faraz, T., et al., *Tuning Material Properties of Oxides and Nitrides by Substrate Biasing during Plasma-Enhanced Atomic Layer Deposition on Planar and 3D Substrate Topographies.* ACS Applied Materials & Interfaces, 2018. **10**(15): p. 13158-13180.
4. Grady, E., et al., *Tailored Molybdenum Carbide Properties and Graphitic Nano Layer Formation by Plasma and Ion Energy Control during Plasma Enhanced ALD.* arXiv:1911.05046, 2019.
5. Gahan, D., B. Dolinaj, and M.B. Hopkins, *Retarding field analyzer for ion energy distribution measurements at a radio-frequency biased electrode.* Review of Scientific Instruments, 2008. **79**(3).
6. Economou, D.J., *Tailored ion energy distributions on plasma electrodes.* Journal of Vacuum Science & Technology A, 2013. **31**(5): p. 050823.

Thesis appendix

A. Comparison of thermal and plasma-assisted ALD

As highlighted in chapter 1, a typical atomic layer deposition (ALD) process comprises of a metal (-organic or -halide) precursor dose followed by a co-reactant (gas vapours or plasma) exposure. These two half-cycles are separated by purge steps that enable complete removal of unreacted reactants and/or reaction by-products from the reactor and ensures non-CVD-like layer-by-layer growth. Figure TA.1 shows one complete ALD cycle for both the thermal and plasma-assisted ALD routes. A thermal ALD process typically employs NH_3 or N_2H_4 gases as reducing co-reactants for the growth of TMN films [1-8]. On the other hand, typical plasmas used for the growth of TMN films are those generated in H_2, N_2 or NH_3 gases or their combinations [1, 9-22]. Due to the greater reducing potential of plasma species as compared to gaseous molecules, the fraction of M(III) oxidation state in the prepared films is expected to be higher in the case of plasma-assisted ALD.

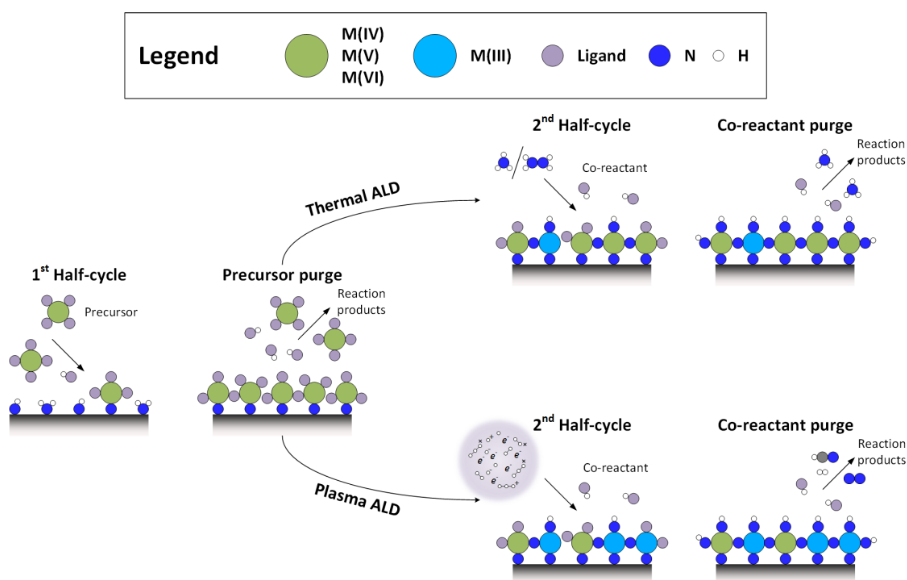

Figure TA.1. Schematic representation of thermal and plasma-assisted ALD. The surface of the growing film is either exposed to gaseous molecules or to species generated in a plasma during the co-reactant half cycle. The latter is expected to yield higher fraction of M(III) oxidation state in the grown films.

B. General plasma aspects

It is relevant here to describe a few important aspects of plasma that are relevant for this dissertation. A plasma is a collection of electrons, charged ions and neutral atomic or molecular gas-phase species. A plasma is quasi-neutral on a macroscopic scale, that is, the electron density (n_e) is equal to the ion density (n_i). Plasmas are created by accelerating and heating of the electrons in the presence of electric fields, that leads to ionization of gas-phase species through electron impact collisions. As a result of electron impact collisions, gas-phase species can also undergo dissociation and/or excitation which leads to the formation of radicals and/or photons *via* de-excitation. The kinetic energy of electrons (also referred to as electron temperature, T_e) in a plasma has a Maxwellian distribution and only the electrons in high energy tail are able initiate to the above mentioned processes. In an inductively coupled plasma (ICP), the T_e is typically 3-5 eV (or ~$4 \cdot 10^4$ K). Typically, the processing plasmas belong to the 'cold' plasma category, where the gas temperature (T_g) of 300-500K is much lower than T_e.

The density of ions (n_i) in an ICP plasma (also referred to as plasma density) is approximately 10^{16}-10^{17} m^{-3}. The degree of ionization (X_i) in a typical ICP plasma is very low (~10^{-5}-10^{-3}), implying that the surface of growing film or reactor walls receive much higher flux of reactive radicals as compared to the ions. Therefore, it is thought that the surface chemistry during the film growth is mainly driven by the interactions of plasma radicals with the moieties on the film surface. However, as described in chapter 2, the flux and energy of impinging ions has significant implications on the material properties of the prepared films. Due to the much higher thermal velocity of electrons as compared to the ions, the electrons are immediately lost to the walls and/or surfaces interacting with the plasma. In order to compensate for the loss of plasma electrons, a space charge region (also referred to plasma sheath) is setup between the plasma and the surfaces as schematically depicted in Figure TA.2. As a result of the formation of plasma sheath, the positive ions are accelerated towards the surfaces such that the flux of impinging ions on the surface balances the flux of incident electrons. Within the sheath region, both n_i and n_e decrease with different rates such that n_i is always larger than n_e. In fact, n_i already exceed n_e at the sheath edge and the ions enter the sheath region with a minimum velocity, known as the Bohm velocity ($u_B \geq (kTe/M)^{1/2}$). This means that a pre-sheath region develops between quasi-neutral plasma and the sheath, where the ions are accelerated to a velocity of at least u_B.

In a collisionless plasma sheath, the ions are incident normally on the surface. The potential drop across the plasma sheath can be used to determine the mean energy of impinging ions (E_{ion})

$$E_{ion} = e \cdot V_s = e \cdot (V_p - V_{sub}) \tag{1}$$

where e is the elementary charge, V_p is the plasma potential and V_{sub} is the substrate potential (0 V for the grounded electrode and V_f for floating electrode). The $<E_{ion}>$ is approximately ~20-30 eV for a grounded substrate electrode. At higher operating pressures, the ions may undergo collisions with the background gas, each collision defined by a collision cross-section (σ). In case of ion-neutral collisions in the plasma sheath, the ion mean free path ($\lambda_i = 1/n_g \cdot \sigma$) [23] gets reduced and may become comparable or smaller than the sheath thickness (l_s). As a consequence, the $<E_{ion}>$ is reduced and depends on the l_s [24, 25]. Furthermore, the ion flux (Γ_i) to the surfaces may also be affected.

$$l_s = \frac{2}{3} \cdot \left(\frac{\varepsilon_0}{e \cdot \Gamma_i}\right)^{\frac{1}{2}} \cdot \left(\frac{2e}{M_i}\right)^{\frac{1}{4}} \cdot V_s^{\frac{3}{4}} \tag{2}$$

where ε_o is the permittivity of free space, M_i is the mass of the ion.

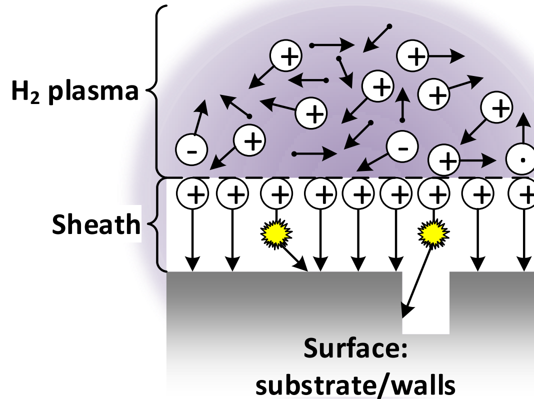

Figure TA.2. A schematic representation of the presence of plasma sheath near a surface in an H_2 plasma discharge. The potential drop across the sheath enables the bombardment of energetic positive ions. In a collision less plasma sheath, ions are anisotropic with normal incidence. In a collisional plasma sheath, ion may lose their energy and directionality.

C. ALD reactor

1. Precursor dose and plasma exposure

The plasma-assisted ALD of HfN_x thin films was conducted in Oxford Instruments FlexAL reactor and is schematically illustrated in Figure TA.3. The reactor can accommodate 200 mm wafers and has a load-lock for loading and unloading samples. The wafers are transported into the main chamber for the growth of thin films by a loading arm. Both the loadlock and main chamber are pumped by turbo-molecular pumps to a base pressure of 10^{-6} Torr.

The $CpHf(NMe_2)_3$ precursor (Air Liquide, >99.99% purity) is contained in a stainless steel bubbler at 60°C and is transported to the main chamber by Argon using stainless steel delivery lines. The dosage is controlled by pneumatic ALD valves (Swagelok). The FlexAL reactor is equipped with an inductively coupled plasma (ICP) source with an inductive coil wrapped around an Al_2O_3 dielectric tube. The plasma source is spatially separated from the substrate such that the substrate is not involved in the plasma generation and therefore it is a 'remote' plasma ALD reactor. Various inlet gases (i.e. Ar, O_2, N_2, H_2, NH_3, SF_6 of combination thereof) can be used for generation of plasma.

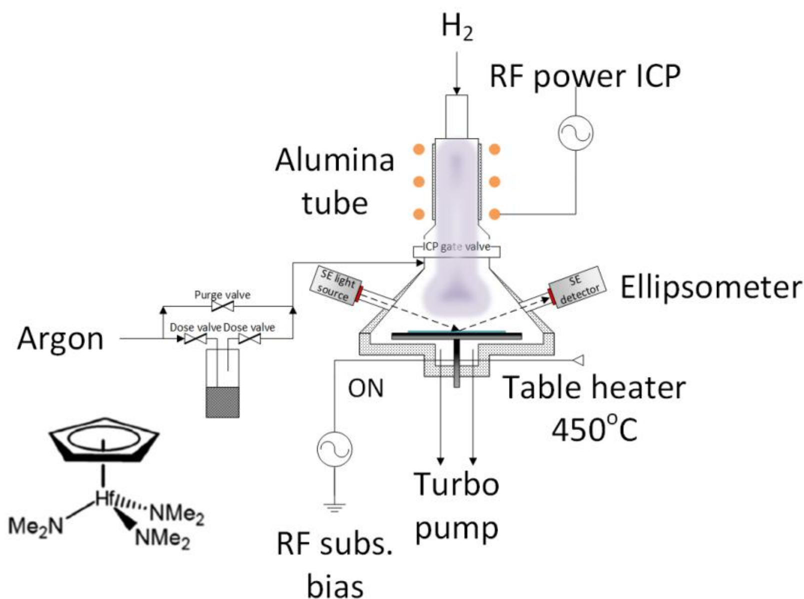

Figure TA.3. Schematic illustration of the Oxford Instruments FlexAL ALD reactor.

The temperature of precursor delivery lines is 20-30°C higher than the bubbler in order to prevent any condensation of precursor in the lines. The stage temperature can be increased to 600°C, however CVD-type HfN_x growth was observed at a stage temperature of 550°C and above. The wall temperature was maintained at 145°C. The reactor is equipped with few optical ports which can used for in-situ characterization of the ALD process. For instance, an optical port is located above the ICP tube in order to monitor the de-excitation spectrum of plasma radicals via optical emission spectroscopy (OES). Furthermore, quadruple mass spectrometry (QMS) and spectroscopic ellipsometry (SE) measurements can be performed. The in-situ measurements allow for better understanding of the ALD processes and associated chemistry and growth mechanisms.

2. *External rf substrate biasing*

In a remote plasma ALD reactor, which has been used for performing the experiments in this dissertation, the plasma source and the substrate stage are spatially separated such that the substrate is not involved in the generation of the plasma species. Therefore, the plasma parameters (ion flux, radical density) can be varied fairly independently from the substrate conditions (ion energy). Profijt *et al.* showed that, for an O_2 plasma, the ion flux can be increased by increasing the power of the radio-frequency inductively coupled plasma source [26]. On the other hand, an increase in the operating pressure of the O_2 plasma led to a gradual decrease in both the flux and energy of impinging ions. When considering the energetic ions, Profijt *et al.* introduced the aspect of external rf substrate bias application during the plasma half cycle [27]. A remote plasma reactor, therefore, may allow for enhancing the ion energies quite independently from the ion flux by externally biasing the substrate with an additional rf power source. As a result of rf substrate biasing, time-varying sinusoidal voltage with respect to ground (V_{bias}) develops at the substrate with a frequency of 13.56 MHz. While the light electrons can respond to the rapidly varying voltages, the ions can only respond to the time-averaged substrate potential. This gradually results in the development of a time-invariant negative potential ($-V_{bias}$) with respect to the ground at the substrate (Figure TA.4), thereby balancing the fluxes of ions and electrons reaching the substrate. In one complete rf cycle, the electrons gets collected at the substrate in the positive part of the cycle whereas ions are collected in the negative part. Furthermore, the magnitude of V_{bias} can be regulated by the applied rf power to the substrate. The voltage waveform in Figure TA.4a are measured using an oscilloscope connected to the substrate table *via* a high voltage probe.

For rf substrate bias application, $<E_{ion}>$ is given by $<E_{ion}> = e(V_p - V_{bias})$ for a collisionless plasma sheath. Furthermore, the shape of ion flux energy distribution functions (IFEDF) is determined by the τ_{ion}/τ_{rf}, where τ_{ion} is the time an ion takes to traverse the plasma sheath and τ_{rf} is the rf period. When $\tau_{ion}/\tau_{rf} >> 1$, the ions cannot respond to the high frequency of instantaneous sheath voltage and essentially a mono-modal IFEDF is obtained [28]. On the other hand, when $\tau_{ion}/ \tau_{rf} << 1$, ions can respond to the instantaneous sheath voltage and cross the sheath in a small fraction of the rf cycle. This leads to a broad and bimodal IFEDF [28], where the peak separation (ΔE) is a function of peak-to-peak sheath voltage (V_{pp}) and the ratio of τ_{rf}/τ_{ion}, as elucidated in Eqn. 3. Chapter 2 describes the implication of $<E_{ion}>$ on the material properties of films prepared by various vapour-based deposition techniques.

$$\Delta E = \frac{2eV_{pp}}{\pi}\left(\frac{\tau_{rf}}{\tau_{ion}}\right) \quad (3)$$

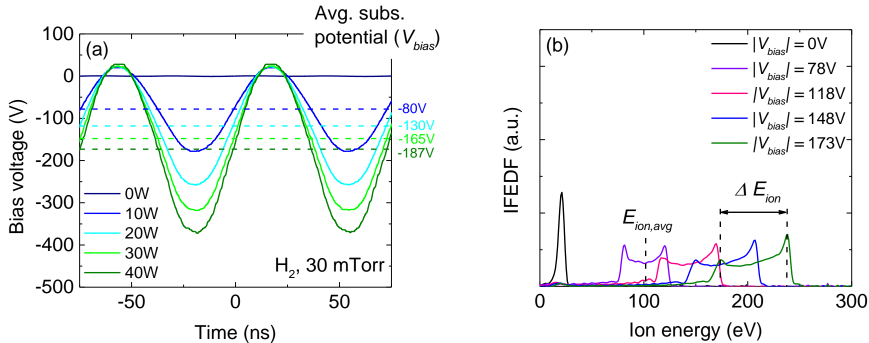

Figure TA.4. (a) Substrate potential waveforms as a function of time for H_2 plasma operated at 30 mTorr measured using an oscilloscope. The development of time-averaged substrate potential $|V_{bias}|$ with respect to ground can be observed. (b) Ion flux-energy distribution functions (IFEDFs) for ions in a H_2 plasma operated at 30 mTorr for various values of $|V_{bias}|$.

Figure TA.4b shows the IFEDFs for the ions in a H_2 plasma operated at 30 mTorr. A mono-modal IFEDF is obtained with a grounded electrode ($|V_{bias}| = 0V$), whereas rf substrate biasing results in a bi-modal IFEDF which is centred at the mean ion energy of $<E_{ion}>$ and has a peak-to-peak width of ΔE_{ion}. As can be observed, both the $<E_{ion}>$ and ΔE_{ion} increase upon increasing the $|V_{bias}|$, thereby exploring the ion energy parameter space of Figure 2.6. It should be noted here

that rf substrate biasing is one of the many ways to increase the energy of impinging ions and <E_{ion}>, ion flux and ion mass are the essential parameters that effects the material properties, as will be shown later.

D. Material characterization

The material properties of the HfN_x films prepared by plasma-assisted ALD has been extensively investigated using various methods.

1. Spectroscopic ellipsometry

Spectroscopic ellipsometry (SE) was used to determine the optical dispersion of the HfN_x films and the thickness. A linearly polarized light is incident on to the sample at an angle θ with respect to the sample surface normal as shown in Figure TA.5. The light-matter interaction alters the polarization of light, which is measured by the detector in terms of the ellipsometric angles ψ and Δ. ψ and Δ represent the amplitude ratio and the phase difference of the p-polarized and s-polarized light upon reflection. These two quantities were measured in a photon energy range of 0.75 eV to 5 eV. For the data analysis, a model was set up for HfN_x films on SiO_2 (450 nm)/c-Si substrates. Key material parameters such as optical resistivity, screened plasma frequency and carrier mobility could be extracted by parametrizing the complex dielectric function $\varepsilon=\varepsilon_1+i\varepsilon_2$. The dielectric functions can be modelled using one Drude and two Lorentz oscillators:

$$\varepsilon(E) = \varepsilon_1(E) + i\varepsilon_2(E) = \varepsilon_\infty - \overbrace{\frac{E_p^2}{E^2 - i\Gamma_D E}}^{Drude} + \sum_{j=1}^{2} \overbrace{\frac{S_j E_{0j}^2}{E_{0j}^2 - E_j^2 + iE_j\Gamma_j}}^{Lorentz} \quad (4)$$

where, ε_∞ represents transitions at higher energy which are not accounted in Lorentz oscillators, E_p is plasma energy and Γ_D is the damping factor for Drude oscillator. The Lorentz oscillators are centered at E_o which corresponds to the resonance frequency, while S indicates the strength of the oscillators and Γ is the damping factor for the Lorentz oscillators. The optical resistivity (ρ_{op}) was deduced from the free-carrier Drude parameterization, given by $\rho_{op} = \Gamma_D/\varepsilon_o \cdot \omega_p^2$, where Γ_D is the damping factor for the Drude oscillator, ε_o is the permittivity of free space, and ω_p is the screened plasma frequency.

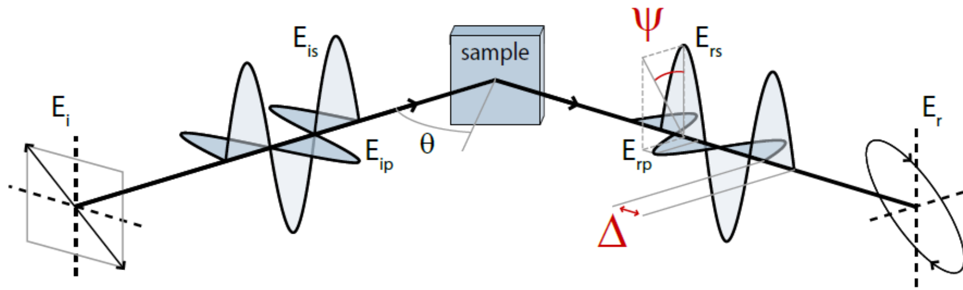

Figure TA.5. Schematic illustration of the working principle of spectroscopic ellipsometry. Polarized light is incident onto the sample at an angle θ with respect to the surface normal. Changes in light polarization are measured upon reflection on the sample as the ellipsometric angles ψ and Δ.

2. X-ray photoelectron spectroscopy

X-ray photoelectron spectroscopy (XPS) is used to determine the chemical composition of the prepared films and the environment of chemical bonding. The sample is irradiated with X-ray photons that leads to the emission of core electrons from the sample. Since the mean free path of the emitted electrons is limited due to scattering events, the information on chemical composition can be derived only from the region <10 nm below the surface. The emitted electrons travel through energy analyser with a certain pass energy and their kinetic energy (E_k) is recorded by the detector. The E_k depends on the binding energy (E_b) of the electrons in one of the core levels and the energy of incident photons (hv).

$$E_b = h\nu - E_k - \varphi \quad (5)$$

where φ is the work function of the material. The chemical environment and the oxidation states of the atoms in the sample can therefore be extracted from the measured E_b. Furthermore, the relative quantitative estimation of the different elements in the films can be performed by determining the area under the peak and dividing it by the sensitivity factor (SF) corresponding to the different elements. It should be noted that the calibration of the SF should be performed before the quantitative estimation of elements. In this work, the fraction of Hf(III) oxidation state, i.e. Hf(III)/Hf(III)+Hf(IV), in the HfN_x films has been determined by using 4f orbital spectra of Hf atoms. In addition to extracting the chemical

environment of Hf, the chemical bonding of O and C impurity atoms was also probed.

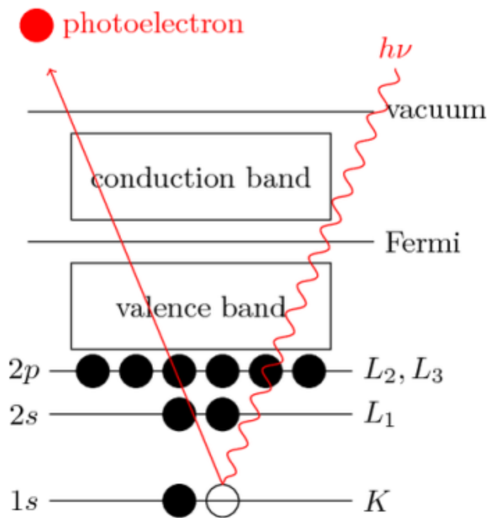

Figure TA.6. A schematic illustration of the emission of a core electron by incidence of high energy X-ray photons. The kinetic energy of emitted electron is used to determine the binding energy of the core electron.

The XPS measurements were carried out by first sputtering the HfN_x for 500s by Ar^+ ions with low energy of 200 eV. This was done in order to eliminate the chemical contribution of impurities from the first few layers of HfN_x films and to ensure the measurement of relevant quantities of the HfN_x bulk film precisely.

3. *Rutherford backscattering*

The absolute chemical composition in terms of areal density of atoms and the mass density of the HfN_x films was evaluated by Rutherford backscattering spectrometry (RBS) and elastic recoil detection (ERD) measurements. An RBS instrument generally includes an alpha particles ($^4He^+$ ions) source, a linear particle accelerator capable of accelerating incident ions up to 1900 keV and a detector capable of measuring the energies of backscattered ions over some range of angles.

The $^4He^+$ source is connected to an acceleration tube with a high positive potential applied to the ion source, and the ground at the end of the acceleration

tube. The detectors that are used to measure backscattered energy usually consist of a ~100 nm thick p-type Si layer on an n-type Si substrate, thus forming a p-n junction. The $^{4}He^{+}$ ions lose some of their energy due to inelastic scattering from the electrons, and some of these electrons gain enough energy to overcome the band gap of Si. This means that each ion incident on the detector produces some electron-hole pairs and it's number is dependent on the energy of the ion. These pairs can be detected by applying a voltage across the detector and measuring the current, providing an effective measurement of the ion energy. Furthermore, angular dependence of detection can be achieved by using a movable detector, covering some range of angles around direct (180 degrees) back-scattering. Angular dependence of the incident beam is controlled by using a tilting sample stage.

The energy loss of a backscattered ion is dependent on two processes 1) the energy lost in the scattering events with sample nuclei and 2) the energy lost to small-angle scattering from the sample electrons. The first process is dependent on the scattering cross-section of the nucleus and thus on its mass and atomic number. For a given measurement angle, nuclei of two different elements will therefore scatter incident ions to different degrees and with different energies, producing separate peaks on a measurement counts as a function of energy. These peaks are characteristic of the elements contained in the material, providing a means of analysing the composition of a sample by matching scattered energies to known scattering cross-sections. The second energy loss process, the stopping power of the sample electrons, does not result in large discrete losses such as those produced by nuclear collisions. Instead it creates a gradual energy loss dependent on the electron density and the distance traversed in the sample. This energy loss will lower the measured energy of ions which backscatter from nuclei inside the sample in a continuous manner dependent on the depth of the nuclei. The result is that instead of the sharp backscattered peaks, a gradual trail off in the peaks is observed towards lower energy as the ions pass through the depth occupied by that element.

ERD is very similar to RBS, but instead of detecting the projectile at the back angle, the recoils are detected in the forward direction by maintaining an angle of incidence with the sample surface at 15°. ERD was originally developed for detection of light elements (H, He, Li, C, O, Mg, K), thereby overcoming some of the limitations of RBS.

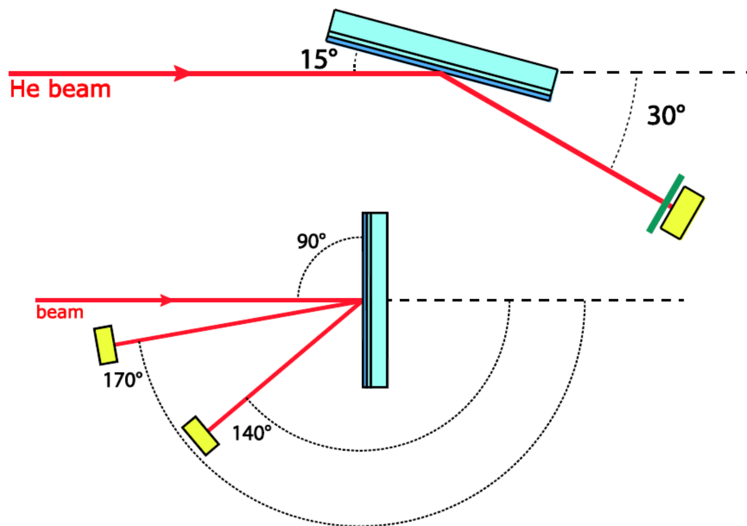

Figure TA.7. A schematic for ERD (top) and RBS (bottom) measurements. The ERD measurements are carried out using He^+ beam with the detector at a recoil angle of 30°. RBS was performed with the detectors at scattering angles of 140° and 170°. The angles may vary depending on the measurement.

4. X-ray diffraction

X-ray diffraction (XRD) is used to determine the crystalline structure of the prepared films by detecting the constructive interference patterns of the X-rays that are elastically scattered from the crystal lattice. Figure TA.8 schematically shows an illustration of the Bragg reflection condition that has to be met in order to achieve the constructive interference from a set of lattice planes. The induced path difference amounts to 2dsinθ, where θ is the incidence angle of the X-ray beam and *d* is the spacing between the two lattice planes. The condition for the Bragg reflection is $2dsin\theta = n\lambda$, where λ is the wavelength of the X-ray photons emitted from Cu Kα source.

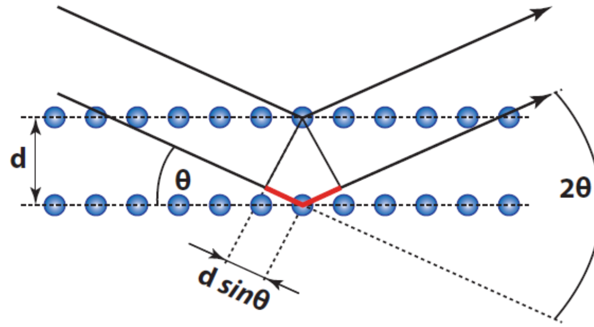

Figure TA.8. Representative illustration of a set of lattice planes hit by X-rays. The difference in distance covered by the two X-rays reflected by the top and bottom lattice planes is indicated in red. is the angle of incidence of the X-ray radiation and d the spacing between the lattice planes.

In a θ/2θ scan, both the incident X-ray beam and the detector make an angle θ with respect to the sample surface. In this measurement configuration, only the coherent lattice planes oriented parallel to the sample surface of a polycrystalline films contribute to the diffraction spectra and therefore this configuration enables the detection of texture, if any, in the prepared films. Furthermore, such a measurement also allows for determining the vertical crystallite size, that coherently contributes to the diffraction, as shown in Figure TA.9.

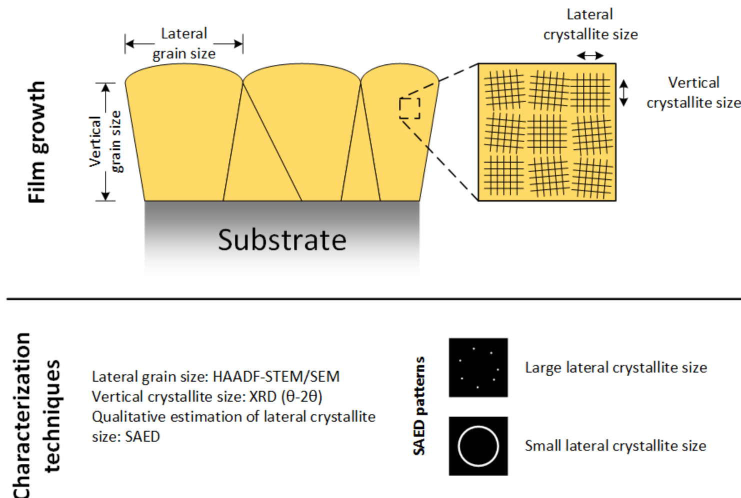

Figure TA.4. A schematic illustration of the growth of polycrystalline thin film with laterally developing grains with film thickness. The determination of grain sizes and crystallite sizes by different crystallographic techniques is also shown.

1. *Transmission electron microscopy and selected area electron diffraction*

In a transmission electron microscopy (TEM) experiment, highly energetic electrons (up to 300 keV) are transmitted through an ultra-thin sample (<100-200 nm) in order to obtain high-resolution images of the crystalline microstructure of the sample. In either the bright-field (BF)-TEM or dark-field (DF)-TEM imaging, the electron beam is collimated by a set of condenser lenses. After the transmission through the sample, both the un-scattered primary and the diffracted electron beams are then condensed by the objective lens. In the back focal plane, the primary and diffracted beams are spatially separated, forming the electron diffraction pattern. An objective aperture can be inserted in the back focal plane in order to choose between the beams that will form the image. Projector lenses are then used to highly magnify the image which is then projected on a fluorescent screen and recorded by a CCD camera.

In BF-TEM, the direct primary beam is selected for the image formation. The regions with a higher average atomic number result in a darker contrast. Furthermore, the contrast also depends on the crystalline structure of the sample. A crystal lattice that is oriented in a strongly diffracting orientation will result in a darker contrast. On the other hand, DF-TEM employs one or more diffracted beams in the back focal plane to form the image. Therefore, the regions of the sample which contribute to that specific diffracted beam will contribute to the brightness in the image. This technique can be employed to resolve single-crystalline grains or to identify grains with the same crystallographic orientation.

High-Angle Annular Dark Field Scanning TEM (HAADF-STEM) is a technique that is used to provide images with a contrast that is also set by the atomic number. In contrast to the BF-TEM and DF-TEM where the images are produced by the projection of the sample, STEM forms images by scanning the sample by a focused electron beam. For HAADF imaging an annular DF detector is placed at a high angle with respect to the direct beam in order to collect electrons scattered by the sample. The atomic number contrast generally dominates HAADF images since the angular distribution of the scattered electrons strongly depends on the atomic number of the atom from which they are incoherently scattered. Moreover, the amount of scattered electrons also depends on the local atomic density (e.g. film thickness, grain boundaries and nano-porosity).

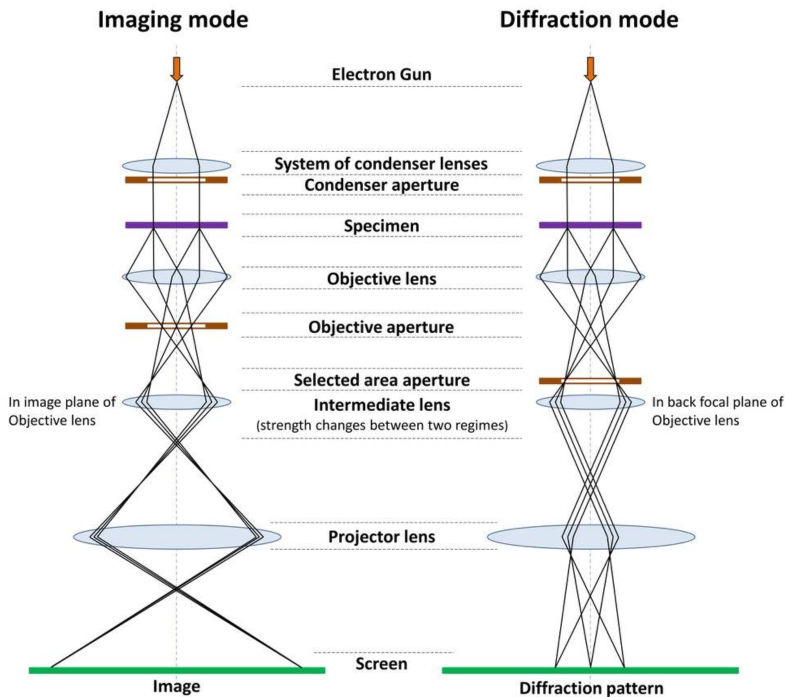

Figure TA.5. Schematic illustration of the positions of the objective aperture used to select the direct beam (a) or a diffracted beam (b) in order to obtain BF-TEM or DFTEM images, respectively.

Selected area electron diffraction (SAED) makes use of the collimated electron beam in order to form a diffraction pattern in the back focal plane. SAED is used to determine the crystal structure and possible texture of the sample. In case the selected area aperture is much larger than the dimensions of the crystallites, the diffraction pattern constitutes of continuous diffraction rings whereas SAED of a single crystal will result in a single crystalline diffraction pattern, the pattern depending on the crystallographic axis used for imaging. The distance of the diffraction ring (or spot) to the centre of the reciprocal space corresponds to the inter-planar distance. Furthermore, information on the texture of thin films can be gained that corresponds to the intensity of the rings or discrete spots.

For the analysis of HfN_x thin films by HAADF-STEM and SAED, ~10-15 nm thick films were deposited on Si_3N_4 TEM membranes. On the other hand, the cross-sectional TEM analysis on ~70-80 nm thick samples was performed on a thin (50-100 nm) lamella taken from a $Pt/HfN_x/SiO_2$ film stack prepared by Focused Ion Beam preparation.

References

1. Musschoot, J., et al., *Atomic layer deposition of titanium nitride from TDMAT precursor.* Microelectronic Engineering, 2009. **86**(1): p. 72-77.

2. Tetsuro, H., et al., *Investigation of Thermal Stability of TiN Film Formed by Atomic Layer Deposition Using Tetrakis(dimethylamino)titanium Precursor for Metal-Gate Metal–Oxide–Semiconductor Field-Effect Transistor.* Japanese Journal of Applied Physics, 2010. **49**(4S): p. 04DA16.

3. Becker, J.S., E. Kim, and R.G. Gordon, *Atomic Layer Deposition of Insulating Hafnium and Zirconium Nitrides.* Chemistry of Materials, 2004. **16**(18): p. 3497-3501.

4. Mayumi, B.T., et al., *Atomic Layer Deposition of Thin VN x Film from Tetrakis(diethylamido)vanadium Precursor.* Japanese Journal of Applied Physics, 2011. **50**(5S1): p. 05EA06.

5. Burton, B.B., A.R. Lavoie, and S.M. George, *Tantalum nitride atomic layer deposition using (tert-butylimido) tris(diethylamido)tantalum and hydrazine.* Journal of the Electrochemical Society, 2008. **155**(7): p. D508-D516.

6. Miikkulainen, V., M. Suvanto, and T.A. Pakkanen, *Atomic Layer Deposition of Molybdenum Nitride from Bis(tert-butylimido)-bis(dimethylamido)molybdenum and Ammonia onto Several Types of Substrate Materials with Equal Growth per Cycle.* Chemistry of Materials, 2007. **19**(2): p. 263-269.

7. Klaus, J.W., S.J. Ferro, and S.M. George, *Atomic layer deposition of tungsten nitride films using sequential surface reactions.* Journal of the Electrochemical Society, 2000. **147**(3): p. 1175-1181.

8. Becker, J.S., et al., *Highly Conformal Thin Films of Tungsten Nitride Prepared by Atomic Layer Deposition from a Novel Precursor.* Chemistry of Materials, 2003. **15**(15): p. 2969-2976.

9. Kim, J.Y., et al., *Remote plasma enhanced atomic layer deposition of TiN thin films using metalorganic precursor.* Journal of Vacuum Science and Technology A: Vacuum, Surfaces and Films, 2004. **22**(1): p. 8-12.

10. Kim, J.Y., et al., *Remote plasma-enhanced atomic-layer deposition of tiN by using TDMAT with a NH 3 plasma.* Journal of the Korean Physical Society, 2004. **45**(6): p. 1639-1643.

11. Muneshwar, T. and K. Cadien, *Low temperature plasma enhanced atomic layer deposition of conducting zirconium nitride films using tetrakis (dimethylamido) zirconium and forming gas (5% H2 + 95% N2) plasma.* Journal of Vacuum Science & Technology A: Vacuum, Surfaces, and Films, 2015. **33**(3): p. 031502.

12. Seungchan, C., et al., *Barrier Characteristics of ZrN Films Deposited by Remote Plasma-Enhanced Atomic Layer Deposition Using Tetrakis(diethylamino)zirconium Precursor.* Japanese Journal of Applied Physics, 2007. **46**(7R): p. 4085.

13. Consiglio, S., et al., *Plasma-assisted atomic layer deposition of conductive hafnium nitride using tetrakis(ethylmethylamino)hafnium for CMOS gate electrode applications.* Journal of the Electrochemical Society, 2008. **155**(3): p. H196-H201.

14. Kim, E.J. and D.H. Kim, *Highly conductive HfN x films prepared by plasma-assisted atomic layer deposition.* Electrochemical and Solid-State Letters, 2006. **9**(8): p. C123-C125.

15. Jeong, W., et al., *Characteristics of HfN films deposited by using remote plasma-enhanced atomic layer deposition.* Journal of the Korean Physical Society, 2010. **56**(3): p. 905-910.

16. Rampelberg, G., et al., *Low temperature plasma-enhanced atomic layer deposition of thin vanadium nitride layers for copper diffusion barriers.* Applied Physics Letters, 2013. **102**(11): p. 111910.

17. Mario, Z., et al., *Superconducting niobium nitride thin films deposited by metal organic plasma-enhanced atomic layer deposition.* Superconductor Science and Technology, 2013. **26**(2): p. 025008.

18. Sowa, M.J., et al., *Plasma-enhanced atomic layer deposition of superconducting niobium nitride.* Journal of Vacuum Science & Technology A: Vacuum, Surfaces, and Films, 2017. **35**(1): p. 01B143.

19. Langereis, E., et al., *Synthesis and in situ characterization of low-resistivity Ta Nx films by remote plasma atomic layer deposition.* Journal of Applied Physics, 2007. **102**(8).

20. Bertuch, A., et al., *Plasma enhanced atomic layer deposition of molybdenum carbide and nitride with bis(tert-butylimido)bis(dimethylamido) molybdenum.* Journal of Vacuum Science & Technology A: Vacuum, Surfaces, and Films, 2017. **35**(1): p. 01B141.

21. Jang, Y., et al., *Highly-conformal nanocrystalline molybdenum nitride thin films by atomic layer deposition as a diffusion barrier against Cu.* Journal of Alloys and Compounds, 2016. **663**(Supplement C): p. 651-658.

22. Sowa, M.J., et al., *Plasma-enhanced atomic layer deposition of tungsten nitride.* Journal of Vacuum Science & Technology A: Vacuum, Surfaces, and Films, 2016. **34**(5): p. 051516.

23. Lieberman, M.A. and A.J. Lichtenberg, *Atomic Collisions*, in *Principles of Plasma Discharges and Materials Processing*. 2005, John Wiley & Sons, Inc. p. 43-85.

24. Baloniak, T., R. Reuter, and A. Von Keudell, *Fundamental aspects of substrate biasing: Ion velocity distributions and nonlinear effects.* Journal of Physics D: Applied Physics, 2010. **43**(33).

25. Lieberman, M.A. and A.J. Lichtenberg, *Direct Current (DC) Sheaths*, in *Principles of Plasma Discharges and Materials Processing*. 2005, John Wiley & Sons, Inc. p. 165-206.

26. Profijt, H.B., et al., *Ion and photon surface interaction during remote plasma ALD of metal oxides.* Journal of the Electrochemical Society, 2011. **158**(4): p. G88-G91.

27. Profijt, H.B., M.C.M. Van De Sanden, and W.M.M. Kessels, *Substrate-biasing during plasma-assisted atomic layer deposition to tailor metal-oxide thin film growth.* Journal of Vacuum Science and Technology A: Vacuum, Surfaces and Films, 2013. **31**(1).

28. Gahan, D., et al., *Ion energy distribution measurements in rf and pulsed dc plasma discharges.* Plasma Sources Science and Technology, 2012. **21**(2).

Summary

Conductive transition metal nitride (TMN) films are of fundamental importance to the semiconductor industry as they play a pivotal role in the fabrication of advanced nano-electronic devices. They are used as gate metals in the state-of-the-art metal-oxide-semiconductor field-effect transistors (MOSFETs) because of their low electrical resistivity. They are also employed as diffusion barriers in the interconnect technology. At the same time, the decrease of dimensions in emerging device technologies and the use of high-aspect ratio 3D architectures demands that the growth of TMN films occurs with precise thickness control and excellent step coverage. These requirements have made atomic layer deposition (ALD) the preferred deposition technique for the growth of ultra-thin films. However, the growth of conductive TMN films by vapour-based deposition methods, such as ALD, faces several challenges. One of them is to synthesize TMN films with a high fraction of the metal present in oxidation state III ($0.8 < M(III) < 1.0$). Specifically, the metal precursors adopted in ALD contain metal atoms in oxidation state either IV or V, which has to be effectively reduced to oxidation state III in order to deposit conductive TMN films. In this respect, the choice of the reducing co-reactant is vital.

This dissertation addresses the synthesis of conductive hafnium nitride (δ-HfN) by plasma-assisted ALD. Low-resistivity δ-HfN is a material of interest due to its superior stability when used in combination with high-*k* HfO_2. When adopting thermal ALD, the use of NH_3 gas as reducing co-reactant leads to the growth of insulating Hf_3N_4 films, suggesting that the reduction potential of NH_3 gas is insufficient to achieve a high fraction of Hf(III) in the deposited film. At the same time, the adoption of plasma in combination with ALD opens up opportunities, as it offers the high chemical and physical reactivity in the form of radicals and energetic ions. The first part of this dissertation, therefore, focuses on the importance of selecting the plasma feed gas (H_2 plasma versus N_2 plasma), in combination with the Hf precursor ($CpHf(NMe_2)_3$), for enabling the growth of conductive HfN_x films. Whereas the use of N_2 plasma leads to insulating Hf_3N_4 films, the resistivity decreases down to 0.9 Ωcm when employing H_2 plasma. This resistivity value is accompanied by the presence of 20 at.% of oxygen and a Hf(III) fraction of 0.65 in the film.

One of the important parameters that can be manipulated during the plasma exposure step is the energy of ions impinging on the surface of the growing film. Therefore, the effect of an external rf substrate bias applied during the H_2 plasma

exposure on the material properties of HfN_x films is investigated. An increase in the substrate potential from 0V to |130| V leads to two order of magnitude decrease in electrical resistivity of the HfN_x films, down to $3.3 \cdot 10^{-3}$ Ωcm. The latter results from a major decrease in the O content down to ≤ 2 at.% and increase in Hf(III) fraction up to 0.82. In parallel, the crystalline quality of XRD coherent domains for δ-HfN(200) improves. These results demonstrate that energetic ions play a major role in affecting the chemical composition and microstructure of HfN_x films.

The above-reported experimental observations motivate the application of density functional theory (DFT) calculations in order to unravel the underlying surface chemistry for O incorporation in HfN_x films and the role of energetic ions in decreasing film resistivity. DFT calculations show that the dissociative binding of H_2O (present in the reactor background) on a HfN surface is highly favoured, resulting in the formation of Hf-OH groups and concomitant oxidation of Hf(III) to Hf(IV). On the other hand, highly energetic cations (H^+, H_2^+ and H_3^+) trigger the dissociation of surface Hf-OH bonds, leading to H_2O formation and subsequent desorption. Following the desorption of H_2O, we hypothesize that plasma H radicals reduce Hf(IV) to Hf(III).

Finally, this dissertation investigates the HfN_x film properties when an Ar-H_2 plasma is adopted, again in combination with an external rf substrate bias. Ion flux energy distribution functions (IFEDFs) measured by a retarding field energy analyser (RFEA) reveal that the ion energy and mass in the case of Ar-H_2 plasma are significantly higher than in H_2 plasma. As a result, an electrical resistivity as low as $4.1 \cdot 10^{-4}$ Ωcm is achieved for HfN_x films as thin as 35 nm. This resistivity value is the lowest reported for the HfN_x films grown by either ALD or CVD, and is comparable to the case of PVD grown films. Next to a high Hf(III) fraction of 0.86, the film undergoes a major improvement in terms of microstructural properties, specifically in-grain nano-porosity is suppressed. The latter effect is attributed to an efficient transfer of energy and momentum to the HfN_x film surface in the presence of ions with a higher energy and larger mass.

The results achieved in this dissertation contribute to the fundamental understanding of the underlying mechanisms in the ALD synthesis of highly conductive HfN_x and, in general, transition metal nitrides.

List of publications

Peer-reviewed articles

1. **Saurabh Karwal**, Benjamin L. Williams, Janne-P Niemelä, Marcel A. Verheijen, Wilhelmus M. M. Kessels and Mariadriana Creatore, Plasma-assisted atomic layer deposition of HfN_x: Tailoring the film properties by the plasma gas composition, J. Vac. Sci. Technol. A 35, 01B129 (2017); doi: 10.1116/1.4972208
2. **Saurabh Karwal**, Marcel A. Verheijen, Benjamin L. Williams, Tahsin Faraz, Wilhelmus M. M. Kessels and Mariadriana Creatore, Low resistivity HfN_x grown by plasma-assisted ALD with external rf substrate biasing, J. Mater. Chem. C 6, 3917 (2018); doi: 10.1039/C7TC05961B
3. **Saurabh Karwal**, Tao Li, Angel Yanguas-Gil, Christian P. Canlas, Yu Lei, Anil U. Mane, Joseph A. Libera, Soenke Seifert, Randall E. Winans and Jeffrey W. Elam, Tailoring nanopore formation in atomic layer deposited ultra-thin films, J. Vac. Sci. Technol. A 36, 01A103 (2018); doi: 10.1116/1.5003360
4. Akhil Sharma, Marcel A. Verheijen, Longfei Wu, **Saurabh Karwal**, Vincent Vandalon, Harm C. M. Knoops, Ravi S. Sundaram, Jan P. Hofmann, Wilhelmus M. M. Kessels and Ageeth A. Bol, Low-temperature plasma-enhanced atomic layer deposition of 2-D MoS2: large area, thickness control and tuneable morphology, Nanoscale 18, 8615 (2018); doi: 10.1039/C8NR02339E
5. Tahsin Faraz, Harm C. M. Knoops, Marcel A. Verheijen, Cristian A. A. van Helvoirt, **Saurabh Karwal**, Akhil Sharma, Vivek Beladiya, Adriana Szeghalmi, Dennis M. Hausmann, Jon Henri, Mariadriana Creatore and Wilhelmus M. M. Kessels, Tuning material properties of oxides and nitrides by substrate biasing during plasma-enhanced atomic layer deposition on planar and 3d substrate topographies, ACS applied materials & interfaces 15, 13158 (2018); doi: 10.1021/acsami.8b00183
6. Tahsin Faraz, Karsten Arts, **Saurabh Karwal**, Harm C. M. Knoops and Wilhelmus M. M. Kessels, Energetic ions during plasma-enhanced atomic layer deposition and their role in tailoring material properties, Plasma Sources Science and Technology 28, 024002 (2019); doi: 10.1088/1361-6595/aaf2c7
7. Yinghuan Kuang, Valerio Zardetto, Roderick van Gils, **Saurabh Karwal**, Dibyashree Koushik, Marcel A. Verheijen, Lachlan E. Black, Christ

Weijtens, Sjoerd Veenstra, Ronn Andriessen, Wilhelmus M.M. Kessels and Mariadriana Creatore, Low-temperature plasma-assisted ALD SnO2 as electron transport layer in planar perovskite solar cells, ACS applied materials & interfaces 10, 30367 (2018); doi: 10.1021/acsami.8b09515

To be published

1. **Saurabh Karwal**, Bora Karasulu, Harm C. M. Knoops, Vincent Vandalon, Wilhelmus M.M. Kessels and Mariadriana Creatore, Atomic insights into oxygen incorporation in atomic-layer deposited conductive nitrides and its mitigation by energetic ions (submitted)
2. **Saurabh Karwal**, Marcel A. Verheijen, Karsten Arts, Tahsin Faraz, Wilhelmus M.M. Kessels and Mariadriana Creatore, Plasma-assisted ALD of highly conducting HfN_x: on the effect of ion bombardment on film microstructure (submitted)

Acknowledgements

‘Life isn’t about finding yourself. It is about creating yourself’ and ‘Calibre of a person is not defined by how well he prepares for everything to go right, but how he bounces back when everything has gone wrong’. These two quotes adequately summarize the journey of a PhD candidate as he/she goes through moments of joy, sorrow, excitement, enthusiasm and despair in these 4 years. More often than not, he/she is trying to convince himself/herself that: ‘Yes! I can do it’. In these 4 years, I have had the opportunity to meet some exceptional humans and researchers that believed in me and also inspired me to bring this voyage to a successful end.

My foremost appreciation is for my first promotor, **Adriana**, who gave me the opportunity to carry out my research in form of a PhD dissertation in the PMP group. Adriana, your quest for an in-depth understanding of any result that I presented to you is remarkable. During the course of my PhD, I wanted to explore new ideas/research topics but you always kept my feet on ground and taught me that a good research cannot be carried out without developing an understanding of the obtained results. These are the signs of a great mentor. I appreciate your critical views and feedback on my results, which also helped me to gain a better understanding of them. My next words of gratitude are for my second promotor, **Erwin**. I remember how Jeff Elam was happy to know that I am going to pursue my PhD with you at PMP. Your dedication, hard work and time management is what makes PMP a great group. I appreciate the time you have spent on motivating me to ‘better my best’ and teaching me how to position my work and effectively communicate it in form of publications or presentations. At the same time, you are critical about details as well as one who readily comprehends the bigger message. I hope I was able to inculcate these attributes into myself through our discussions. My next thanks goes to another pillar of PMP and my co-promotor, **Marcel**. Your knowledge on material science and characterization is exceptional. Your constructive criticism on (almost) every paper has been highly valuable. Furthermore, your availability and flexibility for discussion on the material properties also greatly appreciated. Due to this, I was also able to witness the TEM facility at Philips, which has helped (almost) every PhD/Post-doc to publish great results. I would also like to express my gratitude to **Fred**, whom I first met during my interview for PhD position at PMP. It is always amazing to see your excitement and enthusiasm towards science. While talking to you, it never occurred to me that you are one of the faculty members (in positive sense). It is

great to observe how you modulate your level and allow PhD students to communicate (personal or professional) with you without hesitation.

PMP is blessed to have an excellent pool of technicians. **Cristian**, besides being an excellent problem-solver and teaching me various aspects of XPS and XRD, you have been a great friend. Working in cleanroom was always fun when you were around. Thank you for being highly accommodating with all the requests that I produced. You never made me feel that **Wytze** was not around ;). Besides helping me on the professional front, you always cared about how I was doing on a personal level. Thanks for that and I am sure we will keep in contact for future. **Jeroen**, you have been equally helpful towards my issues and requests. You were always eager to help PhD/Post-doc with issues related to reactors with an immediate effect. **Casper, Joris** and **Janneke**, thanks for your help also on innumerable occasions. Outside PMP, a big thanks goes to the Nanolab staff: **Beatriz, Frank, Nando, Barry** and **Erik**. Thanks Frank for also teaching me some more basics on XRD, Barry for helping me with my requests on using new chemicals, Erik for helping me with e-beam lithography training that was extremely useful and Beatriz for preparing TEM lamellas on numerous occasions.

I would like to extend my warm gratitude to **Jeanne** and **Lianne**. Not only did you help me with all the official matters required to materialize my PhD thesis and with organizing travel requests, but also sharing some light moments from time to time.

Next in the list are the people who made my PhD journey joyful in form of fruitful collaborations and/or friendship. **Srinath**, thanks for being such a good friend and a motivator. I felt I could always come to you with any sort of scientific/non-scientific query. You have been always eager (sometime more than myself) to address my issues in the most practical manner possible. Thanks for being there for me in my tough times and also to share my joys! The time we spent as house mates is unforgettable. **Chaitanya**, you have been a great friend, an excellent career advisor and peer reviewer of one of my paper. You are always someone I look up to if I have to seek any pragmatic advice on (almost) anything. It is just great to see you now having two bundle of joys – Ishan and Uday. I will always cherish the trip that we did together. **Akhil**, we have shared many light moments together. You have been a great support both professionally and personally. Seeing you work tirelessly and the amount of enthusiasm and energy you put in every discussion has always been very inspiring. You are a great researcher and a very good friend. I am happy that you found a great job just after your PhD. **Alfredo**, I think we have shared (almost) all the miseries and joys in our lives during the time of PhD. It was great to see that is such a small span of 1.5 – 2 years, you almost mastered the field of area-selective ALD and actually produced

many nice papers. You are a great scientist and I am happy that we again share the same job. It was great to see you also getting your own bundle of joy – Amelia Marie. **Tahsin**, the sheer hard work and efforts that you put in towards research are commendable. You are very thorough and always interested in any scientific topic that we discussed. Thanks for the peer-review of my papers and the help with collecting the biasing data. **Bora**, your contribution to my PhD thesis and also in my personal life has been immense! Thank you for being such a nice friend. I felt I could share almost anything with you and you never ceased to crack spontaneous jokes. You set a completely different level for one-liners. I will forever cherish the road trip we had in Ireland. **Vincent**, your self-less attitude to help everybody/anytime is exemplary. You are always passionate, irrespective of the subject of conversation. Your knowledge on every theme is immense. You were a great sparring partner in squash and your efforts to do better is infectious, which also motivates the opponent to better himself. Thank you so much for helping me with moving to Leiden! I wish you all the best for own career.

I would also like to extend my thanks to other colleagues. **Morteza**, in the last days of PhD, we were actually going through exactly the same phase. It was great to see that you also joined me in Delft and we can share much more light moments in future. **Eldad**, you are a very nice human. Even when you were going through lot of stressful days, the smile that you wore on your face was very encouraging. I wish you all the best for your career in future. **Saravana**, you have a very nice friend to chat with. You are quite passionate about research and it is amazing to see that you believe in TiS_3 even if it doesn't exist ;). Jokes apart, I wish you all the best for your own PhD and success! **Shashank**, you are quite competitive on court and off court. Further, your comments on political discussions are often hilarious. It is great to see you building your career with some nice publications. Good luck with your own PhD! **Reyhaneh**, I really wish that I had some noise cancellation headphones when you were around ;P. Whenever I was stressed due to the long day of work, I always wanted to chat with you and Akhil to release stress. Although the conversation was always reduced to me and Akhil listening to you, it was joyful. Good luck with your own PhD. **Karsten**, you are a very nice person and great colleague. Although always soft spoken, you were very critical on the ion energy and flux calculations. Thanks for peer reviewing my paper and also verifying my calculations from time to time. **Harm**, you seemed to be a mobile remote plasma source. Your knowledge and experience on the subject of plasma ALD is immense and it is always great to see you helping new PMP members to get familiar with various aspects of plasma ALD. Thanks for helping me with the calculations for one of my paper and also helping me with structuring my talks. **Janne**, I very much enjoyed our collaboration on CIGS solar cells. Even though the project was short lived, your

enthusiasm and interest kept my motivation high. In addition, I very much liked your calm and relaxed attitude to approach issues. I wish I could instil a part of it into myself. **Yinguan**, my Chinese bhai. Thanks for including me also in your research on perovskite solar cells. In that short time of few month, I learned quite some aspects on PSCs from you. Also thanks for encouraging me to carry out calculations that could be used in your own paper. **Dibya**, another perovskite genius. Thanks for being a good friend and to share some light moments. I wish you best of luck with your own PhD and future job. **Ben**, **Valerio Z** and **Alberto**, thanks for incorporating me into the WeMo team and also helping me in every possible way during the initial phase of my PhD.

I would like to also thank colleagues with whom I had limited conversations but were truly great to have them around – **Valerio DP, Yizhi, Ilker, Roy, Lachlan, Gerben, Jimmy, Maria, Mahdi, Martijn, Tijn, Mark, Claire, Vivek, Bart, Leo, Maarten** and **Rochan**. I wish you all good luck with your own career. I extend my gratitude to also the TNO collaborators – **Bas, Marcel** and **Mirjam**. I appreciate your hard work and enthusiasm that kept the CIGS collaboration going. Together, we had some nice results which (hopefully) may get published.

Next in the list are the humans of Delft who indirectly kept my morale high during the tough times of the PhD journey – the mini-van group. **Nakul, Sujaya, Ramu, Aritra, Abhi, Darwin, Varun, Pandey, PKG, Cuckoo, Akshay, Bhattu, Utteya, Ashish, Nikhil** and **Saudi**. You guys have been exceptional. We have shared all the ins and outs of our lives, dined together and partied together. My PhD journey would have been incomplete without your contributions. Thank you for making Netherlands my second home as I never felt away from home when you guys were around. It is great to see each one of you develop into a more mature and professional individual after completion of masters. I wish you good luck and happiness in every stage of life.

My next words of appreciation is for my BHU family – the chempions group. **4co, Handa, Deepu, JP da, Shasha, Thakraal, Rajoo, Chussu, Ecko, Bhind, Kaana, Bhookali, Baba, Jogi, Bacha, DVD, Pandey, Tidu** and **Neta**. The 4 years that we spent together at the university and the successive reunions in Delhi, Lucknow and (sometimes) in Europe are unforgettable. I often recall and cherish the fond memories that we made during the bachelors. Thanks for staying in touch and for the fun times!

Last but definitely not the least, the people who saw me grow and also started their professional life in parallel – my school mates. **Shakul, Devkant, Ritesh, Ayush, Ishita, Kaveri, Sachin, Yugal, Divyanshu** and **Priyanka**. It has been so many years that we have been together and yet our conversations don't finish

whenever we talk ;). It has been so nice to see all of you grow into more mature individuals. Hopefully, we can still organize reunions in Delhi as we used to.

To the most important people in my life – my family. **Bhai** and **Bhabhi**, I am highly indebted to you for all the endeavours you have made for the family when I was not around. Further, thanks for taking care of me and **Chandrita** and fulfilling all our needs. It is just inspiring to see you manage not only your professional lives but also your personal lives. Bhabhi, it was great to see you successfully complete your own PhD amidst all the struggles and also giving birth to the most beautiful damsel I know – **Mishu**.

To my late **father-in-law** and **mother-in-law**, I am thankful to you for all your love and support and treating me as your own son. **Mummy g**, your hard work and devotion is an example to many of the young generation. Even in the toughest situations, you did not lose hope and maintained your calm. The time I and Chandrita spent with you when you were here in Europe with us is something we will always treasure.

Papa and **mummy**, I cannot express the unconditional love and support that you have given to me in words. Even though it was very tough, I am extremely indebted to you for taking the arduous decision to send me to fulfil my dreams – I cannot forget that. I also cannot forget the struggles/sleepless nights that you have went through in raising me and making what I am today. This thesis is dedicated to you.

Anup sir and **Rekha** mam, you have been fatherly and motherly figure in lives of both Chandrita and me. You are a source of wisdom, knowledge and selflessness. Thank you so much for blessing us with your everlasting love. I cannot express your support in words and I enthusiastically look forward to the years to come.

Lastly, I want to thank my wife – Chandrita. Thanks for bearing with me the ups and downs in my life and supporting me in all the odd working hours in the final stages of my PhD. This thesis wouldn't have been possible without your contributions and understanding. At the same time, it was also inspiring to see your strong character during the toughest phase of your life in the last few years.

Saurabh Karwal

Curriculum vitae

Sep 01, 1988	Born in Delhi, India
Jul 2007 – May 2011	Bachelor of Technology Department of Chemical Engineering Indian Institute of Technology, Banaras Hindu University, India
Aug 2011 – Dec 2013	Master of Science in Sustainable Energy Technology Faculty of Applied Sciences Delft University of Technology, Netherlands
May 2013 – Dec 2013	Master thesis at Argonne National Labs Argonne, United States of America
Apr 2014 – May 2018	PhD candidate Department of Applied Physics Plasma & Materials Processing group, Eindhoven University of Technology, Netherlands
Jun 2018 – Present	Research Scientist TNO, The Netherlands